

NORTHWESTERN UNIVERSITY

PbQ–NaSbQ₂ (Q = Te, Se, S) and SnTe–NaPnTe₂ (Pn = Sb, Bi) Thermoelectric Alloys

A DISSERTATION

SUBMITTED TO THE GRADUATE SCHOOL
IN PARTIAL FULFILLMENT OF THE REQUIREMENTS

for the degree

DOCTOR OF PHILOSOPHY

Field of Chemistry

By

Tyler J. Slade

EVANSTON ILLINOIS

June 2020

©Copyright Tyler Slade 2020

All rights Reserved

ABSTRACT**PbQ–NaSbQ₂ (Q = Te, Se, S) and SnTe–NaPnTe₂ (Pn = Sb, Bi) Thermoelectric Alloys**

Tyler J. Slade

Thermoelectric modules that convert heat into electrical energy are attractive for improving global energy management. This thesis reports the synthesis and characterization of two new families of lead and tin chalcogenide alloys and focuses on the impact of the grain boundaries, phase segregation, and atomic vacancies on the electronic and thermal transport properties.

Alloying NaSbQ₂ (Q = Te, Se, S) into PbQ forms new quaternary semiconductors NaPb_mSbQ_{m+2} where the three cations randomly occupy the same crystallographic position. NaSbQ₂ enhances phonon scattering and favorably changes the electronic structure, resulting in high thermoelectric performance in the telluride and selenide families. The synthetic procedure has a profound impact on the microstructure and physical properties of NaPb_mSbTe_{m+2}. As-cast ingots form two phase composites, with nano to micron-scale phase segregation depending on the NaSbTe₂ fraction and exhibit degenerate p-type conduction. On the contrary, sintered pellets form single phase solid solutions with weakly n-type transport.

The selenide and sulfide families exhibit irregular charge transport behavior, with thermally activated electrical conductivity below 500 K and a change to metallic transport above. This work demonstrates the thermally activated conduction stems from scattering of charge carriers by the grain boundaries and furthermore proposes a chemical framework that explains the magnitude of the scattering in PbQ–NaSbQ₂ alloys and other thermoelectric compounds.

The tin-analogues, SnTe–NaPnTe₂ (Pn = Sb, Bi), are found to have distinct thermoelectric properties that are determined by the intrinsic defects. Addition of NaSbTe₂, but not NaBiTe₂, to

SnTe enhances the concentration of native Sn vacancies. The vacancies both strengthen phonon scattering and raise the charge carrier concentration, which suppresses detrimental intrinsic conduction. Therefore, the Sn vacancies allow superior thermoelectric performance in SnTe–NaSbTe₂ than SnTe–NaBiTe₂.

The final chapter explores the Fermi–level dependence of the sound velocities (acoustic phonon velocities) in eight thermoelectric semiconductors. Raising the charge carrier concentration, in both p– and n–type directions, to highly degenerate values over 10^{20} cm^{-3} suppresses the sound velocity by up to 16 percent, demonstrating charge carriers play an important and previously unrecognized role in determining the phonon transport properties of heavily doped semiconductors.

Thesis Advisor: Professor Mercuri G. Kanatzidis

Acknowledgements

I am deeply grateful to my advisor, Professor Mercouri G. Kanatzidis, for his guidance, patience, and continuous support during my time as a graduate student. Mercouri's immense knowledge and ever-present enthusiasm served as steady inspiration throughout my graduate career. I am particularly thankful that Mercouri always gave me the freedom to pursue my own questions and interests, and in doing so challenged and taught me to become a more critical thinker and independent researcher. I also express thanks to my committee members, Professors Kenneth R. Poeppelmeier, Vinayak P. Dravid, and Dana E. Freedman for their thoughtful and helpful feedback during my qualifying exam, research proposal, and thesis examination.

The support and mentorship of my friends and colleagues in the Kanatzidis group made coming to work each day something to look forward to. I particularly want to thank Jason Khoury and Daniel Chica, whom I was fortunate enough to join the group in parallel with. We have enjoyed close friendship, support, and oftentimes good-natured rivalry over the last five years, and our friendship has been a highlight of my time at Northwestern. I furthermore thank Drs. James Hodges, Sumanta Sarkar, and Gangjian Tan for their mentorship, training, and regular insightful conversations. I made numerous good friends with the others in the group and want to thank all my lab mates for their comradery, particularly my officemates with whom frequent discussions were a highlight of each day.

A substantial portion of the work presented in this thesis would not have been possible without the help of my excellent collaborators. I thank Professors Vinayak P. Dravid, G. Jeffrey Snyder, Chris Wolverton, and Ctirad Uher for their expertise and advice. I especially thank Jann A. Grovogui, who collected most of the TEM images found in this thesis, and whose ideas, advice,

and friendship were of great importance during my graduate career. I want to furthermore thank the members of the Snyder group, with whom I had frequent discussions and who contributed significantly to the ideas and work found in the latter chapters of this thesis.

Most importantly, I could not have made it here without the love and support of my family and close friends. My parents, Sam and Chris have enthusiastically supported all my ambitions and pursuits, and their encouragement and love have truly been invaluable. They are each role models to whom I still aspire. I further thank my brother Andrew for his lifelong friendship and camaraderie. I look forward to future collaborations, both in our joint musical aspirations and otherwise. Lastly, I am endlessly grateful to my wonderful fiancéé, Erin Young, whose boundless love, friendship, support, and companionship are truly the most cherished parts of my life. I look forward to many more happy years together and am excited for what the future may bring.

Table of Contents

	Page
Abstract.....	3
Acknowledgements.....	5
Table of Contents.....	7
List of figures and tables.....	14
Chapter One	
Introduction to thermoelectric materials and motivation.....	36
1.1 A short history of thermoelectrics.....	37
1.2 Thermoelectric energy conversion and cooling.....	39
1.3 Breaking down the thermoelectric figure of merit.....	42
1.4 Thermoelectric design principles: strategies to improve ZT	44
1.4.1 General material considerations.....	44
1.4.2 Minimizing the thermal conductivity.....	45
1.4.3 Raising the electronic power factor.....	48
1.5 PbQ–NaSbQ ₂ (Q = Te, Se, S) as potential thermoelectric materials.....	52
1.6 Chapter summaries.....	54
Chapter Two	
Absence of nanostructuring in NaPb _m SbTe _{m+2} : solid solutions with high thermoelectric performance in the intermediate temperature regime.....	60
2.1. Introduction.....	61
2.2. Results and Discussion.....	64

2.2.1	Major differences between ingots and SPS-processed samples.....	64
2.2.2	Powder X-ray diffraction	68
2.2.3	Scanning Electron Microscopy	75
2.2.4	TEM characterization: absence of nanostructuring and its origins	78
2.2.5	Optimizing the thermoelectric properties after SPS: off-stoichiometric NaPb _m SbTe _{m+2}	81
2.2.6	High average <i>ZT</i> in optimized NaPb _m SbTe _{m+2}	93
2.3	Summary and Conclusions	95
2.4	Experimental Section	96
2.4.1	Synthesis and processing.....	96
2.4.2	Electrical properties.....	98
2.4.3	Total thermal conductivities.....	101
2.4.4	Lattice thermal conductivity.....	102
2.4.5	Calculation of the Lorenz number.....	103
2.4.6	Calculation of effective masses.....	103
2.4.7	Powder X-ray diffraction	104
2.4.8	Infrared spectroscopy	104
2.4.9	Scanning electron microscopy	106
2.4.10	Transmission electron microscopy.....	107
2.4.11	Hall effect measurements	107
2.4.12	Density functional theory (DFT) calculations.....	108

Chapter 3

High thermoelectric performance in PbSe–NaSbSe ₂ alloys from valence band convergence and low thermal conductivity	109
3.1 Introduction.....	110
3.2 Results and Discussion	112
3.2.1 Structural and optical characterization.....	112
3.2.2 Microstructural characterization of NaPb _m SbSe _{m+2}	115
3.2.3 Thermoelectric properties of p-type NaPb _m SbSe _{m+2}	117
3.2.4 Low lattice thermal conductivity in NaPb _m SbSe _{m+2}	123
3.2.5 Role of NaSbSe ₂ in modifying the electronic structure of PbSe.....	124
3.2.6 Thermoelectric figure of merit	132
3.2.7 Unorthodox charge transport below 500 K and future directions.....	134
3.3 Summary and Conclusions	138
3.4 Experimental Section.....	139
3.4.1 Synthesis and processing.....	139
3.4.2 Thermoelectric Measurement.....	140
3.4.3 Calculation of the Lorenz number and estimation of the lattice thermal conductivity.....	141
3.4.4 Hall Effect	143
3.4.5 Microscopy characterization	147
3.4.6 Photoemission spectroscopy	148
3.4.7 Electronic structure calculations	149

3.4.8 Powder X-ray diffraction	149
3.4.9 Fourier transformed infrared spectroscopy (FT-IR).....	150
3.4.10 Impact of the grain boundary charge carrier scattering on the estimated lattice thermal conductivity.....	150
3.4.11 Pisarenko plots	151
3.4.11 Debye-Callaway model for theoretical lattice thermal conductivity	153

Chapter Four

Understanding the thermally activated charge transport in $\text{NaPb}_m\text{SbQ}_{m+2}$ (Q = S, Se, Te)

thermoelectrics: weak dielectric screening leads to grain boundary dominated charge carrier

scattering..... 156

4.1 Introduction.....	157
4.2 Results and Discussion	161
4.2.1 Experimental evidence for grain boundary charge carrier scattering in $\text{NaPb}_m\text{SbSe}_{m+2}$	161
4.2.2 Microscopic characterization of the grain boundaries in $\text{NaPb}_m\text{SbQ}_{m+2}$.	167
4.2.3 Charge carrier trapping at the grain boundaries	171
4.2.4 Relationship between polarizability and GB charge carrier scattering ...	173
4.2.5 Broader Scope: relevance of dielectric screening to GB scattering in emerging thermoelectric materials.....	184
4.3 Summary and conclusions	189
4.4 Experimental details.....	190
4.4.1 Synthesis and processing.....	190

4.4.2	Electrical conductivity and Seebeck Coefficient	192
4.4.3	Hall effect.....	192
4.4.4	Microscopy characterization	193
4.4.5	Calculations of the dielectric constants.....	194

Chapter Five

NaSn _m SbTe _{m+2} and NaSn _m BiTe _{m+2} thermoelectric alloys: high performance facilitated by cation vacancies and lattice softening.....		196
5.1	Introduction.....	197
5.2	Results and Discussion	199
5.2.1	Structural characterization.....	199
5.2.2	Comparing the thermoelectric properties of NaSn _m SbTe _{m+2} and NaSn _m BiTe _{m+2}	204
5.2.3	Impact of NaSbTe ₂ and NaBiTe ₂ on the electronic structure of SnTe....	208
5.2.4	The role of cation vacancies in NaSn _m SbTe _{m+2}	215
5.2.5	Analysis of the sound velocities of NaSn _m BiTe _{m+2} (SnTe–NaBiTe ₂)	221
5.2.6	Potential mechanism of vacancy formation in NaSn _m SbTe _{m+2}	222
5.3	Summary and Conclusions	228
5.4	Experimental details.....	229
5.4.1	Synthesis and SPS processing	229
5.4.2	Electrical conductivity and Seebeck coefficient	230
5.4.3	Hall effect.....	231
5.3.4	Thermal Conductivity	231

5.4.5	Model for theoretical lattice thermal conductivity	234
5.4.6	Powder X-ray diffraction	237
5.4.7	Sound velocity.....	238
5.4.8	Measurement of heat capacity and Debye temperature	238
5.4.9	Electron microscopy.....	239
5.4.10	Electronic structure calculations	240

Chapter Six

Electron Count Mediated Lattice Softening in Semiconductors.....		242
6.1	Introduction.....	243
6.2	Results and Discussion	245
6.3	Summary and Conclusions	257
6.4	Experimental Details.....	257
6.4.1	Synthesis and sample preparation	258
6.4.2	Hall effect.....	259
6.4.3	Sound velocity measurements.....	260
6.4.4	Powder X-ray diffraction	260
6.5	Additional and raw data	261

Chapter Seven

Conclusions, future work, and outlook.....		265
7.1	Summary and conclusions	266
7.1.1	Absence of nanostructuring in $\text{NaPb}_m\text{SbTe}_{m+2}$: solid solutions with high thermoelectric performance in the intermediate temperature regime	266

7.1.2	High thermoelectric performance in PbSe–NaSbSe ₂ alloys from valence band convergence and low thermal conductivity.....	266
7.1.3	Understanding the thermally activated charge transport in NaPb _m SbQ _{m+2} (Q = S, Se, Te) thermoelectrics: weak dielectric screening leads to grain boundary dominated charge carrier scattering	267
7.1.4	NaSn _m SbTe _{m+2} and NaSn _m BiTe _{m+2} thermoelectric alloys: high performance facilitated by cation vacancies and lattice softening.....	268
7.1.5	Electron count mediated lattice softening in semiconductors.....	269
7.2	Future work.....	270
7.2.1	Mixed chalcogenide forms of NaPb _m SbQ _{m+2}	270
7.2.2	Potential cation ordering in NaPb _m SbQ _{m+2}	270
7.2.3	Exploration of SnSe–NaSbSe ₂ and GeTe–NaSbTe ₂	271
7.2.4	Optimizing large grained forms of NaPb _m SbQ _{m+2} (Q = Se, S) and other ionic semiconductors	272
7.2.5	Investigating the mechanism of electron count lattice softening	272
7.3	Outlook	273
	References.....	274
	Curriculum Vita	292

List of figures and tables

Figure 1.1	Simplified diagrams of thermoelectric modules configured for (a) power generation using the Seebeck effect and (b) cooling through the Peltier effect	40
Figure 1.2	Maximum energy conversion efficiency of a thermoelectric module as a function of temperature. Each curve corresponds to a different ZT_{avg} for the device. The calculations assume a constant cold side $T_C = 300$ K.....	41
Figure 1.3	Electrical conductivity σ , Seebeck coefficient S , total thermal conductivity κ_{tot} , and thermoelectric figure of merit ZT plotted as functions of charge carrier concentration n . The curves are calculated with a single parabolic band (SPB) model. The scale is arbitrary to emphasize the differences in doping dependence of each property	44
Figure 1.4	Defect engineering at different length scales to enhance phonon scattering and produce materials with low lattice thermal conductivity	46
Figure 1.5	Illustration of the electronic band structure of PbTe. The primary band gap is at the L-point of the Brillouin zone, and there is a second heavier valence band at the Σ -point. Alloying with 2+ cations decreases the energy of the valence band edge at the L-point, allowing the Σ -band to contribute to charge transport. PbSe and PbS have qualitatively analogous band structure ...	49
Figure 1.6	Illustration of resonance levels in the density of states. (a) Typical density of states for a single band semiconductor. (b) A resonance level giving a localized spike in the DOS	51
Figure 1.7	Mixing PbQ and NaSbQ ₂ (Q = Te, Se, S) to form quaternary solid solution NaPb _m SbQ _{m+2} . The Na, Sb, and Pb are statistically disordered in NaSbQ ₂ and NaPb _m SbQ _{m+2} to maintain the cubic symmetry	53

Figure 2.1 Thermoelectric properties of SPSed and as-cast ingot $\text{NaPb}_m\text{SbTe}_{m+2}$ samples. (a) SPSed electrical conductivity, (b) SPSed Seebeck coefficient, (c) SPSed total thermal conductivity, (d) ingot electrical conductivity, (e) ingot Seebeck coefficients, and (f), ingot total thermal conductivity 65

Figure 2.2 Laboratory powder X-ray diffraction (PXRD) patterns for $\text{NaPb}_m\text{SbTe}_{m+2}$ obtained on (a) SPS processed samples and (b) as-cast ingots. (c) Lattice parameters refined from the patterns shown in (a) and (b). The pink line is a guide to the eye showing the linear trend. The ingots with $m < 1$ (over 50% NaSbTe_2) show small peaks corresponding to Sb_2Te_3 69

Figure 2.3 High resolution synchrotron PXRD patterns collected for $\text{NaPb}_m\text{SbTe}_{m+2}$ (a) SPS processed samples and (b) as-cast ingots. (c) and (d) are close up images of several higher angle peaks for SPSed and ingot samples respectively showing significant peak broadening in patterns collected with the ingots 70

Figure 2.4 SEM images and electron backscatter diffraction (EBSD) orientation maps with accompanying EDS elemental maps for Pb, Sb, Na and Te in a NaPbSbTe_3 as-cast ingot (a) and SPSed sample (b). Upper left and right images for each are the electron and EBSD images, respectively. The EDS images show that there is clear chemical segregation in the ingot sample (Na/Sb-rich and Pb-rich phases) and that Spark Plasma Sintering results in a more homogeneous elemental distribution. The Na map for SPSed shows minor Na segregation along the crack seen in the electron image. Na segregation along cracks and GBs is frequently found in PbQs..... 71

Figure 2.5 (a) EDS elemental maps of Pb, Sb, Te, and Na in a NaPbSbTe_3 ($m = 1$, 50% NaSbTe_2) as-cast ingot showing severe elemental inhomogeneity consistent with the results shown

in Figure 2.4. (b) and (c) are the spectra for the EDS point scans of region 1 and 2, showing Pb-rich and Na/Sb-rich regions, respectively..... 72

Figure 2.6 (a) Scanning electron image and EDS elemental maps of Pb, Sb, Na, and Te in a SPSed sample of $\text{NaPb}_8\text{SbTe}_{10}$ ($m = 8$, 11% NaSbTe_2). (b) Average EDS spectra extracted from the EDS map of the entire area shown in the electron image. (c) The EDS line scan extracted from the map data is denoted by the arrows on the Sb map and electron image. The line scan passes over an area of potential inhomogeneity revealed in the Sb map. The change in composition is not greater than the noise level of the EDS scan (as is seen in areas of inhomogeneity). Because the synchrotron diffraction patterns of the SPSed samples also reveal no secondary phases, we believe it is safe to consider the SPSed samples single phase..... 73

Figure 2.7 TEM images of SPSed (a) NaPbSbTe_3 , (c) $\text{Na}_{1.10}\text{Pb}_{9.90}\text{Sb}_{0.85}\text{Te}_{12}$, and (e) $\text{Na}_{1.15}\text{Pb}_{19.85}\text{Sb}_{0.85}\text{Te}_{22}$. (b), (d), and (f) show selected area electron diffraction patterns for each respective sample. All images reveal a single phase and homogeneous microstructure with no evidence of nanostructures..... 79

Figure 2.8 (a) Electrical conductivities and (b) Seebeck coefficients of SPSed $\text{NaPb}_{10}\text{Sb}_{1-y}\text{Te}_{12}$ indicating that introducing Sb vacancies allows p-type transport to survive SPS. The increase in σ and decrease in S with greater y indicates that the hole concentration increases with increasing fraction of Sb vacancies 82

Figure 2.9 Laboratory powder X-ray diffraction patterns for doped $\text{NaPb}_m\text{SbTe}_{m+2}$. (a) $\text{Na}_{1+x}\text{Pb}_{8-x}\text{Sb}_{0.85}\text{Te}_{12}$, (c) $\text{Na}_{1+x}\text{Pb}_{10-x}\text{Sb}_{0.85}\text{Te}_{12}$, (e) $\text{Na}_{1.10}\text{Pb}_{9.90}\text{Sb}_y\text{Te}_{12}$, and (g) $\text{Na}_{1+x}\text{Pb}_{20-x}\text{Sb}_{0.85}\text{Te}_{22}$. (b), (d), (f), and (h) are the respective lattice parameters of each compound..... 83

- Figure 2.10** Thermoelectric properties of SPSed $\text{Na}_{1+x}\text{Pb}_{8-x}\text{Sb}_{0.85}\text{Te}_{10}$. (a) Electrical conductivities, (b) Seebeck coefficients, (c) power factors, (d) lattice thermal conductivities ($\kappa_{\text{tot}} - \kappa_{\text{elec}}$), (e) total thermal conductivities, and (f) ZT 84
- Figure 2.11** Thermoelectric properties of SPSed $\text{Na}_{1+x}\text{Pb}_{10-x}\text{Sb}_{0.85}\text{Te}_{12}$. (a) Electrical conductivities, (b) Seebeck coefficients, (c) power factors, (d) lattice thermal conductivities ($\kappa_{\text{tot}} - \kappa_{\text{elec}}$), (e) total thermal conductivities, and (f) ZT 85
- Figure 2.12** Thermoelectric properties of SPSed $\text{Na}_{1.10}\text{Pb}_{9.90}\text{Sb}_{1-y}\text{Te}_{12}$ ($y = 0.05-0.25$). (a) Electrical conductivities, (b) Seebeck coefficients, (c) power factors, (d) lattice thermal conductivities ($\kappa_{\text{tot}} - \kappa_{\text{elec}}$), (e) total thermal conductivities, and (f) ZT . The thermal conductivity of $y = 0.05$ sample was not measured due to the lower power factor 86
- Figure 2.13** Thermoelectric properties of SPSed $\text{Na}_{1+x}\text{Pb}_{20-x}\text{Sb}_{0.85}\text{Te}_{22}$. (a) Electrical conductivities, (b) Seebeck coefficients, (c) power factors, (d) lattice thermal conductivities, (e) total thermal conductivities ($\kappa_{\text{tot}} - \kappa_{\text{elec}}$), and (f) ZT 87
- Figure 2.14** (a) Hall carrier densities for the $\text{Na}_{1+x}\text{Pb}_{m-x}\text{Sb}_{0.85}\text{Te}_{m+2}$ derived from variable temperature Hall effect measurements. (b) Room temperature effective masses estimated from the carrier densities and Seebeck coefficients. (c) Infrared absorption spectra for SPSed $\text{NaPb}_m\text{SbTe}_{m+2}$ ($m = 4-20$). Dashed lines show the tangents used to estimate the band gaps. (d) Band gaps estimated from the FTIR spectra showing an increase in E_g with increasing NaSbTe_2 fraction (larger x or smaller m) 89
- Figure 2.15** Calculated band structures for (a) $\text{Pb}_{27}\text{Te}_{27}$, (b) $\text{NaPb}_{25}\text{SbTe}_{27}$, (c) $\text{Na}_2\text{Pb}_{25}\text{Sb}_2\text{Te}_{27}$, and (d) $\text{Na}_3\text{Pb}_{21}\text{Sb}_3\text{Te}_{27}$, or equivalently $m = \infty, 25, 11.5, 7, (\sim 0, 4, 8, \text{ and } 12 \text{ percent } \text{NaSbTe}_2)$

respectively. The calculations reveal both an increase in the band gap and a significant flattening of the bands (increase in m^*) with greater NaSbTe_2 fraction..... 90

Figure 2.16 (a) Comparison of ZTs for high performing SPSed $\text{Na}_{1+x}\text{Pb}_{m-x}\text{Sb}_{1-y}\text{Te}_{m+2}$ compositions developed in this work with the state-of-the-art low and high temperature thermoelectrics $\text{Bi}_{0.4}\text{Sb}_{1.6}\text{Te}_3$ ¹⁰⁴ and $\text{PbTe}-8\%\text{SrTe}$,⁴⁹ respectively. (b) The average ZT for materials shown in (a) over temperature ranges 323–523, 323–673, and 323–823 K..... 94

Figure 2.17 Summary of the work on $\text{NaPb}_m\text{SbTe}_{m+2}$ compounds. The as-cast ingots are inhomogeneous and behave as p-type semiconductors. Spark plasma sintering results in dissolution of the secondary phases to form more homogeneous solid solutions, which exhibit nearly intrinsic n-type behavior. Optimizing the cation stoichiometry in SPSed $\text{NaPb}_m\text{SbTe}_{m+2}$ results in p-type compounds with excellent average ZT of 1.1 over 323–673 K..... 95

Figure 2.18 (a) A typical pellet of $\text{NaPb}_m\text{SbTe}_{m+2}$ after SPS sintering. (b) Schematic showing how the samples were cut from the SPS pellet for thermoelectric characterization. (c) Final samples for ZEM-3 (left) and LFA-457 (right) 97

Figure 2.19 Comparison of the electrical conductivity and Seebeck coefficient for $\text{Na}_{1.10}\text{Pb}_{9.90}\text{Sb}_{0.85}\text{Te}_{12}$ with no annealing (a, b) and after annealing the SPS pellet prior to measurements for 24 h at 673 K (c, d). In each case, 3 heating/cooling cycles between 300–900 K were conducted with a 50 K step size. Large hysteresis is observed without annealing; however, after annealing, the thermoelectric properties show significantly improved thermal stability and little to no changes are observed after the initial heating profile. Black arrows denote the beginning of the first heating cycle..... 99

Figure 2.20 Measured thermal diffusivities for (a) $\text{NaPb}_m\text{SbTe}_{m+2}$ ($m = 1-20$), (b) $\text{Na}_{1+x}\text{Pb}_{8-x}\text{Sb}_{0.85}\text{Te}_{10}$, (c) $\text{Na}_{1+x}\text{Pb}_{10-x}\text{Sb}_{0.85}\text{Te}_{12}$, (d) $\text{Na}_{1.10}\text{Pb}_{9.90}\text{Sb}_{1-y}\text{Te}_{12}$, and (e) $\text{Na}_{1+x}\text{Pb}_{20-x}\text{Sb}_{0.85}\text{Te}_{22}$. (f) Calculated values for C_p . All samples shown above were sintered by SPS 100

Figure 2.21 Calculated temperature-dependent Lorenz numbers for (a) $\text{Na}_{1+x}\text{Pb}_{8-x}\text{Sb}_{0.85}\text{Te}_{10}$, (b) $\text{Na}_{1+x}\text{Pb}_{10-x}\text{Sb}_{0.85}\text{Te}_{12}$, (c) $\text{Na}_{1.10}\text{Pb}_{9.90}\text{Sb}_{1-y}\text{Te}_{12}$, and (e) $\text{Na}_{1+x}\text{Pb}_{20-x}\text{Sb}_{0.85}\text{Te}_{22}$ 105

Figure 2.22 Electronic contribution to the thermal conductivity (κ_{elec}) for (a) $\text{Na}_{1+x}\text{Pb}_{8-x}\text{Sb}_{0.85}\text{Te}_{10}$, (b) $\text{Na}_{1+x}\text{Pb}_{10-x}\text{Sb}_{0.85}\text{Te}_{12}$, (c) $\text{Na}_{1.10}\text{Pb}_{9.90}\text{Sb}_{1-y}\text{Te}_{12}$, and (e) $\text{Na}_{1+x}\text{Pb}_{20-x}\text{Sb}_{0.85}\text{Te}_{22}$... 106

Table 2.1 Qualitative atomic percentages from the EDS point spectra 1 and 2 taken on NaPbSbTe_3 shown in Figure 2.5. The point spectra show that the Te is uniformly distributed while the Pb and Na/Sb are segregated, confirming the phase segregation in the ingots and suggesting that the similarity of Sb and Te elemental maps is due to the nearly overlapping L_α EDS peaks. 74

Table 2.2 Qualitative atomic percentages of each element obtained from the EDS elemental maps of the SPSed $\text{NaPb}_8\text{SbTe}_{10}$ sample shown in Figure 2.6. The atomic percentages are in good agreement with the nominal $\text{NaPb}_8\text{SbTe}_{10}$ stoichiometry 74

Table 2.3 DFT-calculated Mixing Energies of $\text{Pb}(\text{NaSb})_{0.5}\text{Te}_2$ ($\text{NaPb}_2\text{SbTe}_4$), $\text{Pb}(\text{AgSb})_{0.5}\text{Te}_2$ ($\text{AgPb}_2\text{SbTe}_4$), and $\text{Pb}(\text{AgSb})_{0.5}\text{Se}_2$ ($\text{AgPb}_2\text{SbSe}_4$) solid solutions 81

Table 2.4 Measured densities and corresponding fractions of the theoretical densities for the SPSed $\text{NaPb}_m\text{SbTe}_{m+2}$ and doped $\text{Na}_{1+x}\text{Pb}_{m-x}\text{Sb}_{1-y}\text{Te}_{m+2}$ (nominal compositions of $m = 6-20$, $x = 0.02-0.15$, $y = 0.10-0.25$, all SPS processed). Theoretical densities were obtained from the Rietveld refinements of the PXRD data..... 101

Figure 3.1 a) Powder X-ray diffraction patterns for $\text{NaPb}_m\text{SbSe}_{m+2}$ ($m = 2-30$). b) Refined lattice parameters for $\text{NaPb}_m\text{SbSe}_{m+2}$, represented as $\text{PbSe} + x\% \text{NaSbSe}_2$. c) Fourier transformed

infrared spectroscopy spectra for the same $\text{NaPb}_m\text{SbSe}_{m+2}$ compounds (the dashed lines show the extrapolation used to estimate the bandgaps) and d) the estimated bandgaps. The dashed blue lines in (b) and (d) are guides to the eye showing the approximately linear trends in lattice parameter and bandgap as functions of NaSbSe_2 content. Unless noted, the data shown above was obtained from samples after SPS sintering..... 114

Figure 3.2 (a) A characteristic high-resolution TEM image of a sample with nominal composition $\text{Na}_{1.15}\text{Pb}_{9.85}\text{SbSe}_{12}$ and (b) a selected area electron diffraction pattern, both confirming a clean rocksalt structure with no nanoscale precipitates. (c) Backscattered electron image showing noticeable micron-level Z-contrast, and (d-g) EDS elemental maps over the region shown in (c). The EDS maps confirm minor segregation into Pb- and Na/Sb-rich regions..... 116

Figure 3.3 (a) PXRD patterns for $\text{Na}_{1+x}\text{Pb}_{m-x}\text{SbSe}_{m+2}$ and (b) refined lattice parameters 118

Figure 3.4 Temperature-dependent (a) electrical conductivities, (b) Seebeck coefficients, (c) Hall carrier densities, and (d) Hall carrier mobilities for $\text{Na}_{1+x}\text{Pb}_{10-x}\text{SbSe}_{12}$. The inset in (d) shows a close up of the mobilities of samples for which $x = 0.05$ and 0.15 , emphasizing the positive temperature dependence of μ below 500 K 119

Figure 3.5 Temperature-dependent (a) total thermal conductivities, (b) estimated lattice thermal conductivities $\kappa_{\text{tot}} - \kappa_{\text{elec}}$ and (c) ZTs for $\text{Na}_{1+x}\text{Pb}_{10-x}\text{SbSe}_{12}$ 121

Figure 3.6 Temperature-dependent thermoelectric properties of $\text{Na}_{1+x}\text{Pb}_{10}\text{Sb}_{1-x}\text{Se}_{12}$. (a) electrical conductivity, (b) Seebeck coefficient, (c) Hall carrier concentration for $x = 0.10$, (d) power factors, (e) total thermal conductivities, and (f) ZT 122

Figure 3.7 Experimentally determined lattice thermal conductivity for $\text{NaPb}_m\text{SbSe}_{m+2}$ for $m = 2-30$ and PbSe , plotted as % NaSbSe_2 in PbSe , compared with the theoretical curve generated from the simplified Debye-Callaway model. The error bars are 8% 124

Figure 3.8 (a) DFT calculated band structures for $\text{NaPb}_m\text{SbSe}_{m+2}$ (shown as $\text{Na}_n\text{Sb}_n\text{Pb}_{27-2n}\text{Se}$ and representing 0, 4, and 8 percent NaSbSe_2 respectively). (b) DFT calculated energy differences between L and Σ bands for the band structures shown in (a). (c) Pisarenko plots for $\text{NaPb}_{10}\text{SbSe}_{12}$ at 323 K and 623 K. The theoretical lines were calculated with both a single band (SKB) and two-band model, shown as dashed and solid lines respectively. (d) Temperature-dependent Hall coefficients for p-type doped $\text{NaPb}_{10}\text{SbSe}_{12}$ 126

Figure 3.9 (a) Photoemission yield spectroscopy in air (PYSA) spectra for nominally undoped samples of $\text{NaPb}_m\text{SbSe}_{m+2}$ ($m = 10-30$, and pure PbSe). (b) Energies of the valence band edges (work functions) and conduction band edges for each sample extracted from the linear regions of the photoemission spectra, shown as red and blue points respectively. 9% NaSbSe_2 corresponds to the $m = 10$ sample discussed most thoroughly in the text. (c) Experimentally estimated energy differences between L - and Σ - valence band for each sample 130

Figure 3.10 Temperature-dependent power factors of two differently doped $\text{NaPb}_{10}\text{SbSe}_{12}$ samples compared with those of PbSe-2\%Na and band engineered PbSe-2\%HgSe (2% Na doped). The PbSe-HgSe exhibits a record high power factor $\sim 20 \mu\text{W}\cdot\text{cm}^{-1}\cdot\text{K}^{-2}$ above 900 K; however, the $\text{NaPb}_{10}\text{SbSe}_{12}$ have superior power factors below ~ 700 K that contribute to outstanding average ZTs. Considering each of the compounds shown above has comparable carrier densities $\sim 2 \times 10^{20} \text{cm}^{-3}$, we attribute the high power factors below 700 K in $\text{NaPb}_{10}\text{SbSe}_{12}$ to the greater contribution of the Σ -band. Namely, in $\text{NaPb}_{10}\text{SbSe}_{12}$ both L - and Σ -bands participate in the charge transport

even near room temperature, which should improve the power factors at low and moderate temperatures due to the high valley degeneracy 132

Figure 3.11 (a) Traces of the temperature-dependent ZT values for $\text{Na}_{1.10}\text{Pb}_{10}\text{Sb}_{0.90}\text{Se}_{12}$ (this work, denoted as $\text{NaPb}_{10}\text{SbSe}_{12}$), PbSe-SrSe , and PbSe-CaS , PbSe-HgSe . The line for $\text{Na}_{1.10}\text{Pb}_{10}\text{Sb}_{0.90}\text{Se}_{12}$ was obtained from the averages of 5 separate samples. (b) Comparison of the average (device) ZT s estimated for the same materials 134

Figure 3.12 Temperature-dependent (a) electrical conductivity, (b) Seebeck coefficient, (c) variable-temperature powder X-ray diffraction patterns of a p-type $\text{NaPb}_m\text{SbSe}_{m+2}$ sample with nominal composition $\text{Na}_{1.10}\text{Pb}_{9.90}\text{Sb}_{0.90}\text{Se}_{12}$, and (d) refined lattice parameters from first four patterns shown in (c). The PXRD patterns show no clear changes upon heating and cooling, and the lattice parameters increase nearly linearly with heating as expected. These results suggest the unorthodox semiconducting-like electrical conductivity and turnover to metallic charge transport above in (a) is not from a change in phase or change in dopant solubility..... 135

Figure 3.13 Temperature-dependent thermoelectric properties of nominally undoped of $\text{NaPb}_m\text{SbSe}_{m+2}$ ($m = 2-30$). (a) electrical conductivity, (b) Seebeck coefficients, (c) total thermal conductivity, and (d) estimated lattice thermal conductivity ($\kappa_{\text{tot}}-\kappa_{\text{elec}}$). The $m = 8, 10$, and 30 samples have slightly higher p-type electrical conductivities, potentially arising from cation vacancies or slight off-stoichiometry during the synthesis; the other compounds behave as undoped semiconductors as expected. All compounds show strong bipolar diffusion above 600 K, consistent with low charge carrier densities 144

Figure 3.14 Temperature-dependent (a) thermal diffusivities, (b) estimated specific heats, (c) and calculated electronic thermal conductivities of nominally undoped $\text{Na}_{1+x}\text{Pb}_{10-x}\text{SbSe}_{12}$ ($m = 2-30$). For all samples shown above we used $L = 1.485 \times 10^{-8} \text{ V}^2 \cdot \text{K}^{-2}$ 145

Figure 3.15 Temperature-dependent (a) thermal diffusivities, (b) estimated specific heats, (c) Lorentz numbers, and (d) calculated electronic thermal conductivities of $\text{Na}_{1+x}\text{Pb}_{10-x}\text{SbSe}_{12}$... 146

Figure 3.16 Temperature-dependent (a) thermal diffusivities, (b) estimated specific heats, (c) Lorentz numbers, and (d) calculated electronic thermal conductivities of $\text{Na}_{1+x}\text{Pb}_{10}\text{Sb}_{1-x}\text{Se}_{12}$.. 147

Table 3.1 Measured densities and fraction of the theoretical density (obtained by refinement of the powder XRD patterns) of $\text{NaPb}_m\text{SbSe}_{m+2}$, $\text{Na}_{1+x}\text{Pb}_{10-x}\text{SbSe}_{12}$, and $\text{Na}_{1+x}\text{Pb}_{10}\text{Sb}_{1-x}\text{Se}_{12}$. The densities were measured from the masses and volumes of the $\sim 6 \times 6 \times 2 \text{ mm}^2$ squares used for the LFA measurements 141

Table 3.2 Room temperature Hall coefficients and Hall carrier densities for $\text{Na}_{1+x}\text{Pb}_{10-x}\text{SbSe}_{12}$ and $\text{Na}_{1.10}\text{Pb}_{10}\text{Sb}_{0.90}\text{Se}_{12}$ 143

Table 3.3 Constants and parameters used in the Debye-Callaway lattice thermal conductivity calculations for $\text{NaPb}_m\text{SbSe}_{m+2}$ 155

Figure 4.1 (a) Illustration of the unusual temperature dependence of the electrical conductivity observed in thermoelectric materials such as PbSe-NaSbSe_2 ($\text{NaPb}_m\text{SbSe}_{m+2}$), Mg_3Sb_2 , SnSe , and Zintl antimonides. At low temperatures, charge carriers are scattered at the grain boundaries, leading to thermally activated conduction. Above a threshold temperature, the expected phonon scattering dominates the electronic transport. (b) Variable-temperature electrical conductivities for PbSe alloyed with $\sim 4, 9$, and 14 percent NaSbSe_2 . The electrical conductivities are increasingly

suppressed under ~ 600 K for greater NaSbSe₂ fraction. (c) Estimated energy barriers at the GBs for the samples in (b). As the more ionic NaSbSe₂ is added to PbSe, the charge carrier screening is weakened (decreased ϵ) and the barrier heights increase. The inset in (c) is a cartoon illustration of alloying NaSbSe₂ into PbSe to form NaPb_mSbSe_{m+2}..... 159

Figure 4.2 Comparison of the powder X-ray diffraction patterns of SPS-processed and as-cast ingots of p-type doped Na_{1+x}Pb_{10-x}SbSe₁₂. (a) is for $x = 0.15$ and (b) for $x = 0.03$. In both cases, the PXRD patterns show the expected peaks characteristic of the rocksalt structure with no evidence for secondary phases. These patterns suggest negligible chemical changes between SPS-processed and ingot forms 162

Figure 4.3 Electron backscatter diffraction (EBSD) images showing the grain structure of Na_{1.15}Pb_{9.85}SbSe₁₂ samples prepared by (a) water quenching followed by powdering and SPS sintering and (b) slow cooling of ingots. Each individually colored region represents a single grain. Comparison of the (c) electrical conductivities and (d) Seebeck coefficients for large grained (slow cooled ingots), and small grained (SPS sintered pellets) Na-doped Na_{1+x}Pb_{10-x}SbSe₁₂. The closed and open points represent data for the large and small grained samples respectively..... 164

Figure 4.4 Powder X-ray diffraction patterns of SPS-processed samples prepared with different mesh sieves. All samples have the same nominal composition Na_{1.10}Pb_{9.90}Sb_{0.90}Se₁₂. The diffraction patterns all suggest each is phase pure with negligible chemical differences 165

Figure 4.5 Electrical transport properties of samples with nominal composition of Na_{1.10}Pb_{9.90}Sb_{0.90}Se₁₂ prepared to have different sized grains by passing powdered ingots through different mesh sieves. (a) Electrical conductivities, (b) Seebeck coefficients. The sample passed

through a 53 μm sieve likely has a somewhat smaller charge carrier concentration than the other samples, as evidenced by the greater Seebeck coefficient over the full temperature range 166

Figure 4.6 (a) A characteristic high resolution TEM image of a grain boundary in a $m = 10$ selenide sample with nominal composition $\text{Na}_{1.15}\text{Pb}_{9.85}\text{SbSe}_{12}$. The image shows a clean boundary with no evidence for secondary phase segregation. The inset displays a selected area electron diffraction pattern showing only the expected rocksalt spots. (b) A HAADF-STEM image of another GB in the same sample also showing a clean boundary. (c) and (d) are the same for telluride samples with nominal composition $\text{Na}_{1.10}\text{Pb}_{9.90}\text{Sb}_{0.85}\text{Te}_{12}$ 168

Figure 4.7 EDS maps over the GB region of the $\text{Na}_{1.15}\text{Pb}_{9.85}\text{SbSe}_{12}$ sample whose TEM and STEM images are discussed in Figure 4.6. The EDS maps also show a homogeneous distribution of elements supporting that there is negligible phase or dopant segregation at the GBs..... 170

Figure 4.8 EDS maps over the GB region of a telluride sample with nominal composition $\text{Na}_{1.15}\text{Pb}_{9.85}\text{Sb}_{0.85}\text{Te}_{12}$ whose TEM and STEM images are discussed in Figure 4. The EDS maps also show a homogeneous distribution of elements supporting that there is negligible phase or dopant segregation at the GBs 171

Figure 4.9 Powder X-ray diffraction patterns for p-type doped $\text{NaPb}_m\text{SbSe}_{m+2}$ for $m = 20$ and $m = 6$ (equivalently $\sim 4\%$ and 14% NaSbSe_2 in PbSe respectively). Nominal compositions are $\text{Na}_{1+x}\text{Pb}_{20-x}\text{SbSe}_{22}$ and $\text{Na}_{1.10}\text{Pb}_{5.90}\text{Sb}_x\text{Se}_8$. (a) and (c) are the PXRD patterns, and (b) and (d) are the respective lattice parameters. In general, all patterns show the expected peaks characteristic of the rocksalt structure and the lattice parameters change (approximately) linearly with doping, indicating successful Na incorporation. A very small amount of secondary phase is found for the pattern for $m = 6$, $x = 0.95$ in (c)..... 175

Figure 4.10 Comparison of the electrical properties for p-type doped $\text{NaPb}_m\text{SbSe}_{m+2}$ for $m = 20$ and $m = 6$ (equivalently $\sim 4\%$ and 14% NaSbSe_2 in PbSe respectively). Nominal compositions are $\text{Na}_{1+x}\text{Pb}_{20-x}\text{SbSe}_{22}$ and $\text{Na}_{1.10}\text{Pb}_{5.90}\text{Sb}_x\text{Se}_8$. (a) Electrical conductivities and (b) Seebeck coefficients for the $m = 20$ compounds. (c) Electrical conductivities and (d) Seebeck coefficients for the $m = 6$ phases. Clearly, comparing (a) and (c) shows that the $m = 6$ compounds have qualitatively stronger GB scattering, manifesting in a greater degree of suppression of σ under ~ 600 K..... 176

Figure 4.11 Comparison of the electrical transport properties of comparably doped samples of $\text{NaPb}_m\text{SbSe}_{m+2}$ for $m = 20, 10,$ and 6 (equivalently $\sim 4, 9,$ and 14 percent NaSbSe_2 in PbSe). (a) Electrical conductivities and (b) Seebeck coefficients, (c) variable temperature Hall charge carrier concentrations, and (d) plots of $\ln\sigma$ vs. $1/k_B T$ showing linear temperature dependence over the low temperature GB dominated regime. The solid lines in (d) are the fits used to extract E_b 178

Figure 4.12 Plots of $\ln\mu$ against $1/k_B T$ for the $m = 20, 10,$ and 6 $\text{NaPb}_m\text{SbSe}_{m+2}$ discussed in Figure 4.11. The extracted energy barriers from the slopes agree well with the values estimated from the plots of $\ln\sigma$ vs $1/k_B T$ 179

Figure 4.13 (a) Temperature-dependent electrical conductivities for three $\text{NaPb}_m\text{SbSe}_{m+2}$ ($m = 20, 10, 6$) samples that have similar bulk electrical conductivities σ_G . The room-temperature charge carrier concentrations measured for each are given in the legend. (b) Temperature-dependent Seebeck coefficients for the same samples. (c) Plots of $\ln\sigma$ vs. $1/k_B T$ for each sample, showing that the barrier height increases with NaSbSe_2 amount, consistent with the data discussed in Figure 4.11 and 4.12 above. Nominal compositions for each sample are as follows: $\text{Na}_{1.05}\text{Pb}_{19.95}\text{SbSe}_{22}$ ($m = 20$), $\text{Na}_{1.05}\text{Pb}_{9.95}\text{SbSe}_{12}$ ($m = 10$), and $\text{Na}_{1.10}\text{Pb}_{5.90}\text{Sb}_{0.90}\text{Se}_8$ ($m = 6$).... 181

Figure 4.14 Electrical transport properties of p-type doped $m = 20$ $\text{NaPb}_m\text{SbS}_{m+2}$ (nominally $\text{Na}_{1+x}\text{Pb}_{20-x}\text{SbS}_{22}$). (a) Electrical conductivities, (b) Seebeck coefficients, and (c) plots of $\ln\sigma$ vs. $1/k_{\text{B}}T$ showing linear temperature dependence over the low temperature GB dominated regime. The solid lines in (c) show the linear fits used to extract E_{b} 182

Figure 4.15 Powder X-ray diffraction patterns for p-type doped $\text{Na}_{1+x}\text{Pb}_{20-x}\text{SbS}_{22}$ ($m = 20$, equivalently $\sim 4\%$ NaSbS_2). The powder patterns show only peaks corresponding to the expected rocksalt reflections. No reflections corresponding to secondary phases are observed 183

Figure 4.16 (a) Power factors, (b) total thermal conductivities, (c) estimated lattice thermal conductivity, and (d) ZT for as-cast ingots (large grained samples) and SPS-processed (small grains) $\text{Na}_{1+x}\text{Pb}_{10-x}\text{SbSe}_{12}$. Because of the improved charge carrier mobility, the power factors are enhanced in the large grained samples. The figures of merit for the $x = 0.03$ (lightly doped) sample is significantly improved for the larger grained sample. The enhancement is more modest in the large-grained forms of the more heavily doped $x = 0.15$ samples 187

Figure 4.17 (a) Power factors, (b) total thermal conductivities, (c) estimated lattice thermal conductivity, and (d) ZT for samples with nominal composition of $\text{Na}_{1.10}\text{Pb}_{9.90}\text{Sb}_{0.90}\text{Se}_{12}$. The samples were prepared by SPS-sintering powders that were first passed through sieves with different mesh sizes. The electronic properties for these samples are discussed in Figure 4.5. Because of the improved charge carrier mobility, the power factors are increasingly enhanced as the grain size increases. The figures of merit are likewise modestly enhanced at low temperature as the grain size is raised..... 188

Table 4.1 DFT calculated relative isotropic dielectric constants for each PbQ and NaSbQ_2 ($Q = \text{S, Se, Te}$), as well as Mg_3Sb_2 , NbFeSb , TiCoSb , Mg_2Si 185

Table 4.2 Room temperature Hall coefficients and Hall charge carrier densities for $\text{NaPb}_m\text{SbSe}_{m+2}$ $m = 6, 20$ and $\text{NaPb}_m\text{SbSe}_{m+2}$ $m = 20$. Nominal compositions are $\text{Na}_{1.10}\text{Pb}_{5.90}\text{Sb}_x\text{Se}_8$ and $\text{Na}_{1+x}\text{Pb}_{20-x}\text{SbSe}_{22}$, and $\text{Na}_{1+x}\text{Pb}_{20-x}\text{SbS}_{22}$ 193

Figure 5.1 (a) Powder X-ray diffraction patterns for SnTe-NaSbTe_2 ($\text{NaSn}_m\text{SbTe}_{m+2}$) alloys for $m = 50-3$ (or equivalently up to 25% NaSbTe_2 in SnTe). (b) Rietveld refined lattice parameters obtained from diffraction patterns in (a). (c) and (d) are respectively the same for SnTe-NaBiTe_2 ($\text{NaSn}_m\text{BiTe}_{m+2}$) over $m = 50 - 5$ (0–16% NaBiTe_2). The dashed blue lines in (c) and (d) are guides to the eye showing the linear trends of a as function of alloy fraction. In the $\text{NaSn}_m\text{PnTe}_{m+2}$ notation, high m corresponds to SnTe -rich compositions 200

Figure 5.2 (a) High resolution TEM image of a sample with nominal composition $\text{NaSn}_5\text{SbTe}_7$) showing a clean matrix and no evidence of nanoscale precipitation. (b) SEM image of the same sample. (c-f) display EDS spectra obtained over the SEM image shown in (b). The EDS spectra for each element are uniform over the full images, indicating the sample is single phase on the micron scale 202

Figure 5.3 (a) A characteristic SEM image of a $\text{NaSn}_m\text{BiTe}_{m+2}$ sample with nominal composition $\text{NaSn}_5\text{BiTe}_7$ ($m = 5$). (b-e) are the corresponding energy dispersive spectroscopy (EDS) elemental maps of each element. The data shows a nearly uniform distribution of elements indicating a single-phase microstructure 203

Figure 5.4 Thermoelectric properties for SnTe-NaSbTe_2 ($\text{NaPb}_m\text{SbTe}_{m+2}$) alloys over $m = 50-3$ (2–25 % NaSbTe_2). (a) Electrical conductivities, (b) Seebeck coefficients, (c) power factors, (d) total thermal conductivities, (e) lattice thermal conductivities, and (f) figure of merit ZT 204

Figure 5.5 Thermoelectric properties for SnTe–NaBiTe₂ (NaPb_mBiTe_{m+2}) alloys over $m = 50$ – 5 (2–16 % NaBiTe₂). (a) Electrical conductivities, (b) Seebeck coefficients, (c) power factors, (d) total thermal conductivities, (e) lattice thermal conductivities, and (f) figure of merit ZT 205

Figure 5.6 (a) Traces of the ZT vs. temperature curves for NaSn_mSbTe_{m+2} ($m = 4, 5$) presented in this work with several examples of high-performance thermoelectric systems recently reported in the literature.^{178, 180, 184-185} (b) Average ZTs calculated over 300–873 K corresponding to the materials in (a) 207

Figure 5.7 DFT calculated electronic energy band structures of SnTe–NaSbTe₂ (NaSn_mSbTe_{m+2}) for pure SnTe and approximately 4, 7.5, and 11 percent NaSbTe₂ or respectively $m = 25, 11.5,$ and 7 . The compositions are denoted Na_xSn_{27-2x}Sb_xTe₂₇ to reflect the supercells used in the calculations. The band along the Γ – K line is the Σ -band..... 209

Figure 5.8 DFT calculated electronic energy band structures for SnTe–NaBiTe₂ (NaSn_mBiTe_{m+2}) for pure SnTe and approximately 4, 7.5, and 11 percent NaBiTe₂ or respectively $m = 25, 11.5,$ and 7 . The compositions are denoted Na_xSn_{27-2x}Bi_xTe₂₇ to reflect the supercells used in the calculations. The band along the Γ – K line is the Σ -band 210

Figure 5.9 Variable temperature Hall coefficients measured for (a) NaSn_mSbTe_{m+2} ($m = 50, 15, 5$) and (b) NaSn_mBiTe_{m+2} ($m = 50, 5$) 211

Figure 5.10 Pisarenko plot showing the Seebeck coefficients plotted against charge carrier concentration for NaSn_mSbTe_{m+2} (red) and NaSn_mBiTe_{m+2} (green). The solid blue line is the theoretical curve calculated for pure SnTe 213

Figure 5.11 (a) Room temperature hall charge carrier concentrations for SnTe–NaSbTe₂ (NaSn_mSbTe_{m+2}) and SnTe–NaBiTe₂ (NaSn_mBiTe_{m+2}). (b) Room temperature (average) sound velocities for SnTe–NaSbTe₂ (NaSn_mSbTe_{m+2}). The dashed line in (b) shows the linear fit 216

Figure 5.12 (a-c) Temperature-dependent specific heats measured for NaSn_mSbTe_{m+2} for m = 50, 15, 5 (equivalently ~2, 6, 16.6 percent NaSbTe₂ in SnTe respectively). (d-f) Low-temperature plots of C_p/T vs. T² corresponding to C_p data displayed in (a-f). The slopes (β) and estimated Debye temperatures (θ_D) are also shown for each..... 218

Figure 5.13 Debye temperatures SnTe–NaSbTe₂ (NaSn_mSbTe_{m+2}) estimated from the specific heat data and plotted vs. NaSbTe₂ fraction..... 219

Figure 5.14 (a) Comparison of the experimental and theoretical lattice thermal conductivities of SnTe–NaSbTe₂ measured at 323 K. The solid lines are the thermal conductivities predicted by the Debye-Callaway model using the sound velocity and Sn vacancies concentration found in pure SnTe (blue) and the measured values (red). (b) Lattice thermal conductivities of SnTe–NaSbTe₂ over the full temperature range of the study. The points are the measured values and the lines are calculated from our model. The dashed lines exclude the softening and phonon–vacancy scattering and the solid lines include each 220

Figure 5.15 (a) Measured sound velocities for SnTe alloys with NaBiTe₂ and NaSbTe₂. While the SnTe–NaSbTe₂ soften monotonically and approximately linearly with NaSbTe₂ fraction, the SnTe–NaBiTe₂ samples show little dependence on the alloy fraction under ~ 10% NaBiTe₂ and then soften at higher concentrations. (b) Room temperature lattice thermal conductivities for SnTe–NaBiTe₂ and model calculations with and without the reduced v_s shown in (a). Both curves provide reasonably satisfactory fits to the experimental data..... 222

Figure 5.16 (a) Simplified molecular orbital (MO) diagram for a SnTe_6 octahedron. (b) The same MO diagram considering the lattice contraction induced by NaSbTe_2 . The contraction increases orbital overlap and destabilizes the VB edge. The diagram in (b) overlays the original (for pure SnTe) in faded color to emphasize the change after NaSbTe_2 addition. (c) DFT calculated partial density of states for pure SnTe . (d) DFT calculated COHP plot for pure SnTe 224

Figure 5.17 Partial density of states (pDOS) for (a–c) $\text{NaSn}_m\text{SbTe}_{m+2}$ (SnTe – NaSbTe_2) and (d–f) $\text{NaSn}_m\text{BiTe}_{m+2}$ (SnTe – NaBiTe_2) materials. The compositions reflect the supercells used for the DFT calculations. The calculations show the valence band edge primarily originates from interactions between Sn – $5s$ and Te – $5p$ orbitals, agreeing with the MO framework 226

Figure 5.18 Crystal orbital Hamilton population plots for (a–c) $\text{NaSn}_m\text{SbTe}_{m+2}$ (SnTe – NaSbTe_2) and (d–f) $\text{NaSn}_m\text{SbTe}_{m+2}$ (SnTe – NaBiTe_2) materials showing bonding/antibonding interactions for the Na – Te , Sb – Te , and Sn – Te interactions. The compositions reflect the supercells used for the DFT calculations. The calculations show the valence band edge remains antibonding in character after alloying with NaSbTe_2 or NaBiTe_2 227

Figure 5.19 The room temperature Hall hole densities plotted against the lattice constants for our $\text{NaSn}_m\text{SbTe}_{m+2}$ and $\text{NaSn}_m\text{BiTe}_{m+2}$ samples as well as for the $\text{AgSn}_m\text{SbTe}_{m+2}$ previously reported by Tan et al.¹⁷⁶ The graph shows a nearly linear dependence of n_H on a 228

Figure 5.20 (a) Measured thermal diffusivities, (b) estimated heat capacities used to calculate κ_{tot} , (c) estimated temperature-dependent Lorenz numbers, and (d) estimated electronic contribution to the thermal conductivities for $\text{NaSn}_m\text{SbTe}_{m+2}$ ($m = 50$ – 3), equivalently ~ 2 – 25 percent NaSbTe_2 233

Figure 5.21 (a) Measured thermal diffusivities, (b) estimated heat capacities used to calculate κ_{tot} , (c) estimated temperature-dependent Lorenz numbers, and (d) estimated electronic contribution to the thermal conductivities for $\text{NaSn}_m\text{BiTe}_{m+2}$ ($m = 50-5$), equivalently 2–16 percent NaBiTe_2 234

Table 5.1 Measured densities and fraction of the theoretical density (obtained by refinement of the powder XRD patterns) of $\text{NaSn}_m\text{SbTe}_{m+2}$ and $\text{NaSn}_m\text{BiTe}_{m+2}$. The densities were measured from the masses and volumes of the $\sim 6 \times 6 \times 2 \text{ mm}^2$ squares used for the LFA measurements. ... 232

Table 5.2 Constants and fitted parameters used in our model lattice thermal conductivity calculations for $\text{NaSn}_m\text{SbTe}_{m+2}$ and $\text{NaSn}_m\text{BiTe}_{m+2}$ 237

Figure 6.1 Sound velocities plotted against Hall charge carrier concentration for SnTe, PbTe, Nb_xCoSb , CoSb_3 , La_3Te_4 , Pr_3Te_4 , Mg_3Sb_2 , Mg_3Sb_2 , and Mo_3Sb_7 . All materials show a negative linear dependence of v_s on n_H . The sound velocities are all normalized the by the highest measured value (v_0) for each respective compound. 246

Figure 6.2 Measured average sound velocities plotted against Hall charge carrier concentration for p-type SnTe based samples. The legend shows the different dopants and alloys (b) DFT calculated sound velocities as a function of charge carrier concentration. The values of v_s are normalized to the calculated results for zero charge carriers (v_0). The blue line shows the calculated results using Na as a dopant, and the grey line the calculated results using Sn vacancies to modulate n_H 247

Figure 6.3 (a) Refined lattice parameters for the variably doped SnTe alloys discussed in Figure 6.2. (b) Measured densities for the same SnTe samples..... 248

Figure 6.4 Hall charge carrier concentrations plotted against nominal composition x for (a) Nb_xCoSb and (b) Pr_xTe_4 . (c) and (d) are the measured sound velocities plotted against carrier concentration for the same samples 250

Figure 6.5 (a) Hall charge carrier concentrations plotted against nominal La stoichiometry x in La_xTe_4 . The blue line is a linear fit to the experimental points. (b) Debye temperatures of La_xTe_4 plotted against x . The data shown here was obtained from references 210 and 212..... 251

Figure 6.6 (a) DFT calculated sound velocities (normalized to the undoped value v_0) plotted against charge carrier concentration for skutterudite CoSb_3 doped with different filler atoms. (b) Experimental sound velocities and carrier concentrations for Yb-filled CoSb_3 (nominally..... 252

Figure 6.7 (a) Normalized lattice thermal conductivity as a function of charge carrier concentration. The red line is the traditional picture, where κ_{lat} is insensitive to the charge carriers. The blue line shows the relative change of the lattice thermal conductivity assuming that v_s is reduced linearly with n . (b) Thermoelectric properties plotted against charge carrier concentration assuming a single parabolic band (SPB) model with $m^* = 5m_e$. The dashed blue line shows the total thermal conductivity assuming v_s is independent of n , while the solid blue line considers v_s to be linearly dependent on n . If the charge carriers drive lattice softening, κ_{lat} is increasingly suppressed at high n and the total thermal conductivity is reduced, shifting the optimal carrier density needed to maximize ZT to higher values. The scale in (b) is arbitrary 256

Figure 6.8 Powder X-ray diffraction patterns for the doped/alloyed SnTe samples. Nominal compositions are indicated to the side of each pattern and are as follows: (a) Sn_xTe , (b) $\text{Na}_x\text{Sn}_{1.02-x}\text{Te}$, (c) $\text{Ag}_x\text{Sn}_{1-x}\text{Te}$, (d) $\text{Sn}_{1-x}\text{Sb}_x\text{Te}$, (e) $\text{Sn}_{1-x}\text{Bi}_x\text{Te}$, $\text{Sn}_{0.98}\text{Te}_{1-x}\text{I}_x$. The lattice parameters listed in Table 6.3 are refined from the above powder patterns using the Rietveld method 264

- Table 6.1** Data from the pulse-echo measurements of the sound velocity and Hall effect measurements of the charge carrier concentration for PbTe. Compositions are nominal and p- and n-type doping is denoted by (p or n respectively). The refined lattice parameters and measured sample densities are also given. The uncertainty in v_L and v_T are the standard deviations of 3 measurements obtained on each sample 261
- Table 6.2** Compiled results from the pulse-echo measurements of the sound velocity and Hall effect measurements of the charge carrier concentration for Yb-filled CoSb_3 ($\text{Yb}_x\text{Co}_4\text{Sb}_{12}$). Compositions are nominal. The data was previously published in a Ph.D. thesis (thesis.library.caltech.edu/9681/55/Tang_Yinglu_2015_thesis_04212016). The original work attributed the softening to the filler alone, not the changed charge carrier density 261
- Table 6.3** Compiled results from the pulse-echo measurements of the sound velocity and Hall effect measurements of the charge carrier concentration for SnTe based alloys. The compositions are nominal. The refined lattice parameters and measured sample densities are also given. The uncertainty in v_L and v_T are the standard deviations of 3 measurements on each sample..... 262
- Table 6.4** Data from the pulse-echo measurements of the sound velocity and Hall effect measurements of the charge carrier concentration for Nb_xCoSb (nominal x) 263
- Table 6.5** Data from the pulse-echo measurements of the sound velocity and Hall effect measurements of the charge carrier concentration for Pr_xTe_4 . The uncertainty in v_L and v_T are the standard deviations of three measurements obtained on each sample. Due to the very high charge carrier concentrations, the Hall effect measurement of n_H for Pr_3Te_4 has high uncertainty, but independent measurements of the Seebeck coefficient and electrical conductivity confirm the higher charge carrier concentration 263

Table 6.6	Data from the pulse-echo measurements of the sound velocity and Hall effect measurements of the charge carrier concentration for $\text{Mg}_{3.2}\text{Sb}_{2-x}\text{Te}_x$	263
------------------	--	-----

Chapter One

Introduction to thermoelectric materials and motivation

1.1 A short history of thermoelectrics

Heat and electricity are among the most familiar and important aspects of contemporary life. While everyday experience indirectly connects electricity and heating; for example, a light bulb becomes hot after continuous operation, and fuel is burned to produce electricity, it is perhaps more surprising that a temperature differential applied across a material will alone produce an electrical voltage. Despite being less intuitive, this direct relationship between thermal and electrical energy has been known for nearly two centuries, when in 1821, German physicist Thomas Johann Seebeck discovered the effect which bears his name. In a presentation to the Berlin Academy, Seebeck demonstrated that a compass needle will be deflected when placed in a closed loop of different wires that are subjected to a temperature gradient.¹ While Seebeck incorrectly attributed his discovery to a thermomagnetic effect,² Hans Christian Ørsted later corrected this mistake,³ identifying that the needle is deflected from a magnetic field which is induced by the electrical current passing through the wires, thus indicating a direct electrical response from the temperature gradient that he defined as “thermoelectricity.” Several years later, in 1834, Jean Charles Athanase Peltier discovered the inverse of the Seebeck effect, showing that an electrical current passed through a circuit of dissimilar materials causing heating and cooling at the ends.⁴

The development of quantum mechanics and subsequent establishment of semiconductor physics in the early twentieth century gave scientists and engineers the tools to achieve a microscopic understanding of thermoelectricity. Beginning in the 1930s, researchers showed how the Seebeck and Peltier effects could be used to construct modules which directly convert thermal to electrical energy and provide precise solid-state, refrigerant-free cooling.⁵ Owing to their high

robustness, scalability, and reliability, thermoelectric devices are attractive for numerous applications ranging from waste-heat recover to remote power generation.⁶ Despite the promise, thermoelectric generators and coolers are unfortunately limited by their relatively poor energy conversion efficiencies, costly materials, and complex manufacturing challenges, and for much of the last 60 years, thermoelectric modules have largely been restricted to niche applications where reliability outweighs efficiency and financial concerns. To date, the greatest successes of thermoelectric technology are in deep space exploration, where crafts such as Voyager I and II and the Curiosity Mars rover are all powered by thermoelectric generators.

While the field of thermoelectrics lay nearly dormant for nearly half a century, with only modest advancements in fundamental theoretical understanding and subsequently minor gains achieved in device efficiency, thermoelectric research experienced a renaissance in the 1990's which rapidly accelerated into the twenty-first century. New conceptual ideas regarding manipulation of both the nanoscale features of materials as well as their electronic structures funneled fresh insight into the field.⁷⁻¹⁴ At the same time, the global energy crisis spurred intense demand for more efficient means of energy generation and conservation. Because nearly 60 percent of the world's energy is lost as waste heat, thermoelectric technology has potential to play an important role in harvesting this lost thermal energy and therefore contribute to more efficient energy management.¹⁵ Driven by novel scientific advances and growing societal need for green technology, thermoelectricity experienced rapid progress in the mid 2000's, achieving a near doubling in the efficiencies of several classic materials as well as discovery of numerous new and promising alternative thermoelectric compounds. Despite the success, the efficiencies of even the best materials are still too low compared to other renewable energy sources for thermoelectrics to

achieve widespread usage. A crucial restriction on thermoelectric technologies remains the high cost and relatively poor performance of the materials themselves. As such, discovery of alternative materials, as well as new approaches to improving efficiency are paramount issues. Such findings necessitate new insights into the microscopic charge and thermal transport properties that ultimately determine material performance, and these topics form the bulk of this thesis.

1.2 Thermoelectric energy conversion and cooling

Thermoelectric modules utilize the Seebeck effect to directly convert heat into electrical energy or the Peltier effect to achieve solid-state refrigeration. Simple illustrations of modules configured for power generation and cooling are shown in Figure 1.1. Devices are composed of p- and n-type semiconductor legs connected in series, and when a temperature gradient is applied, the free charge carriers in the semiconductors diffuse from hot to cold sides, analogous to the behavior of particles in a gas. The diffusion of charge carries from hot to cold produces an electric field in each leg, and the resulting voltage V between each end is proportional to the temperature differential to give the Seebeck coefficient S .

$$S = \frac{\Delta V}{\Delta T} \quad (1.1)$$

Where the sign of S is determined by the dominant charge carrier type in the semiconductors. In a p-type material, the Seebeck coefficient is positive, indicating that current flows from cold to hot sides, and n-type materials give negative values of S , indicating that current flows from hot to cold. To understand the efficiency η of a thermoelectric module, we need to find the electrical power w that is delivered to the load (with resistance R_L) and the rate at which heat q is drawn from the source.^{5, 16} The Seebeck effect produces an electromotive force that is related to the

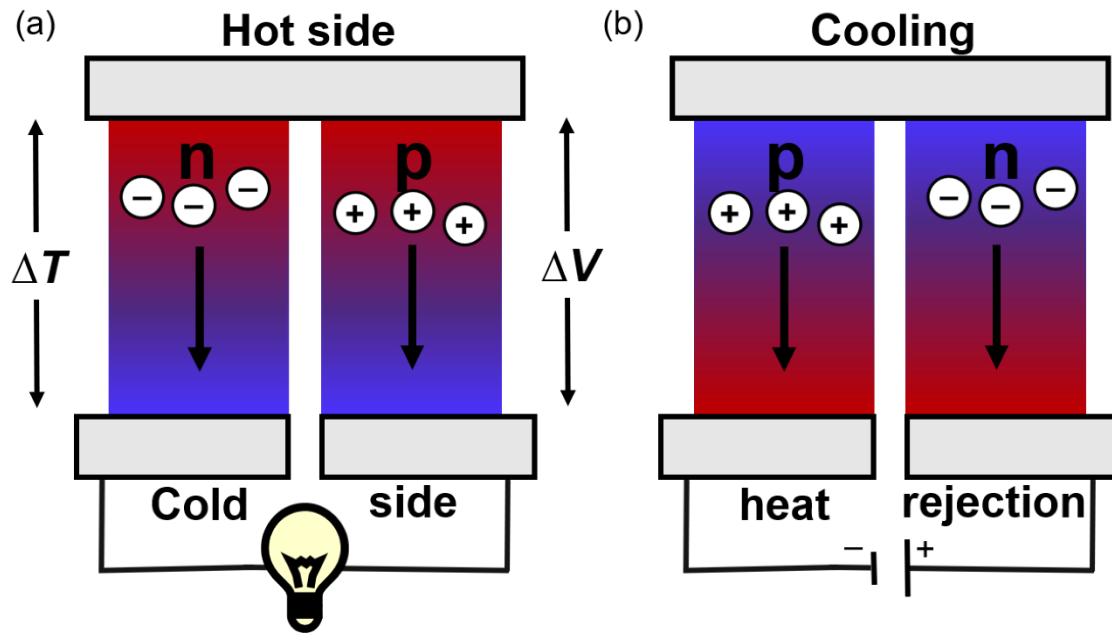


Figure 1.1 Simplified diagrams of thermoelectric modules configured for (a) power generation using the Seebeck effect and (b) cooling through the Peltier effect.

Seebeck coefficients of the p- and n-type legs, S_p and S_n respectively. The resulting current I is given as:

$$I = \frac{(S_p - S_n) \cdot (T_H - T_C)}{R_p + R_n + R_L} \quad (1.2)$$

Where T_H and T_C are the temperatures at the hot and cold sides, and R_p and R_n are the resistances of the legs. From here, the power delivered to the load is

$$w = I^2 R = \left[\frac{(S_p - S_n) \cdot (T_H - T_C)}{R_p + R_n + R_L} \right]^2 \cdot R_L \quad (1.3)$$

The flow of current through the device produces Peltier cooling across the semiconductor legs, which draws some of the heat from the source. The flow of heat through the device is

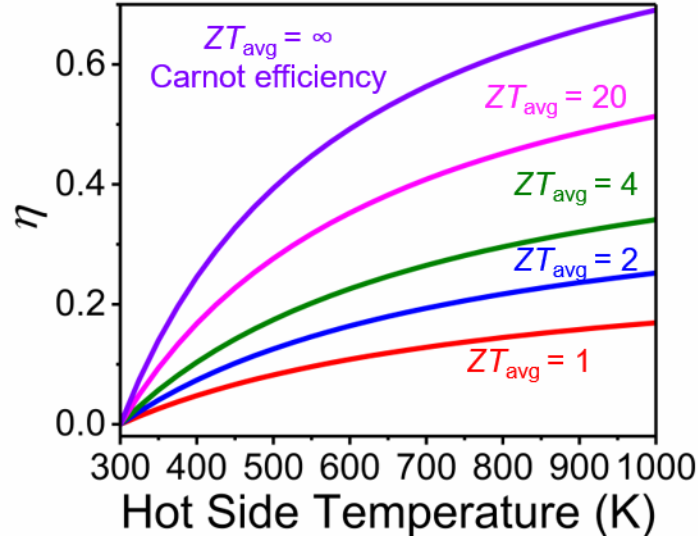


Figure 1.2 Maximum energy conversion efficiency of a thermoelectric module as a function of temperature. Each curve corresponds to a different ZT_{avg} for the device. The calculations assume a constant cold side $T_C = 300$ K.

furthermore determined by both the thermal conductivity κ_p and κ_n of each leg and the Joule heating from the current. The total heat flow from the hot side therefore is expressed as

$$q = (S_p - S_n) \cdot IT_H + (\kappa_p - \kappa_n) \cdot (T_H - T_C) - \frac{I^2 R_L}{2} \quad (1.4)$$

The efficiency is the ratio of the work and heat flow, w/q , which can be calculated by the ratio of equations 1.3 and 1.4. If we define M as the ratio of the load resistance to the total resistance of the legs, $M = \frac{R_L}{R_p + R_n}$, then the maximum efficiency η_{max} of the module occurs when

$\partial\eta/\partial M = 0$. Further defining $Z = \frac{S^2}{(\sqrt{\kappa_p \rho_p} + \sqrt{\kappa_n \rho_n})^2}$, where ρ is the electrical resistivity, we find

$$\eta_{max} = \frac{\sqrt{1+ZT_{avg}}-1}{\sqrt{1+ZT_{avg}}+T_C/T_H} \cdot \frac{T_H-T_C}{T_H} \quad (1.5)$$

where $T_{avg} = \frac{T_H - T_C}{2}$. The term ZT_{avg} is referred to as the thermoelectric figure of merit of the device, and as shown in the above equation, practically determines the fraction of the Carnot efficiency that the module can access. Figure 1.2 shows theoretical values of thermoelectric plotted against hot side temperature for several increasing values of ZT_{avg} . Clearly, the efficiency of a module can be increased either by raising the temperature gradient across which the module operates, or by increasing ZT_{avg} . Therefore, the central task of thermoelectric research is to understand the fundamental physics which gives rise to high ZT_{avg} and use this knowledge to design new and improved materials with superior performance.

1.3 Breaking down the thermoelectric figure of merit

The figure of merit defined above is representative of the energy conversion efficiency of a device. When assessing a specific compound for its potential in thermoelectric applications, the material figure of merit ZT becomes the primary factor of interest. The material ZT is defined as:

$$ZT = \frac{\sigma S^2}{\kappa_{tot}} T \quad (1.6)$$

where σ is the electrical conductivity ($1/\rho$), S is the Seebeck coefficient, κ_{tot} is the total thermal conductivity, and T is the absolute temperature. The total thermal conductivity is further decomposed into the sum of lattice κ_{lat} and electronic κ_{elec} components ($\kappa_{tot} = \kappa_{elec} + \kappa_{lat}$), which parameterize the heat transported respectively by lattice vibrations (phonons) and charge carriers.

The joint requirements for high electrical conductivity and low thermal conductivity indicate that thermoelectricity appears to rest upon a fundamental contradiction, as thermal and electrical conductivity are often directly correlated. For example, metals are good conductors of heat and electricity, while insulators are typically poor conductors of both. More detailed

examination expands upon the complexity. In a single parabolic band (SPB) model, the Seebeck coefficient is determined by the charge carrier effective mass m^* and charge carrier concentration n as follows:

$$S = \frac{8\pi^2 k_B^2}{3eh^2} m_{DOS}^* T \left(\frac{\pi}{3n} \right)^2 \quad (1.7)$$

Here k_B is the Boltzmann constant, e is the electron charge, h is the Plank constant, and m_{DOS}^* is the density of states effective mass ($m_{DOS}^* = N_v^{2/3} m_b^*$) where m_b^* is the band effective mass. The electrical conductivity is likewise related to the same parameters and is given by:

$$\sigma = ne\mu \quad (1.8)$$

Where μ is the charge carrier mobility defined as:

$$\mu = \frac{e\tau}{m_b^*} \quad (1.9)$$

in which τ is the charge carrier relaxation time. The thermal conductivity is also related to the electronic properties through κ_{elec} , which is determined by the Wiedemann–Franz law:

$$\kappa_{elec} = \sigma LT \quad (1.10)$$

The proportionality constant L between the electrical conductivity and electronic component of the thermal conductivity is known as the Lorenz number. The above equations reveal that the three material properties that determine ZT are deeply interconnected to the electronic structure, through m^* , and to the Fermi level through the charge carrier concentration. Unfortunately, the above analysis shows that optimization of any one property generally comes at the cost of the others, and overcoming the contradictory relationship between σ , S , and κ is the central problem in thermoelectric research.

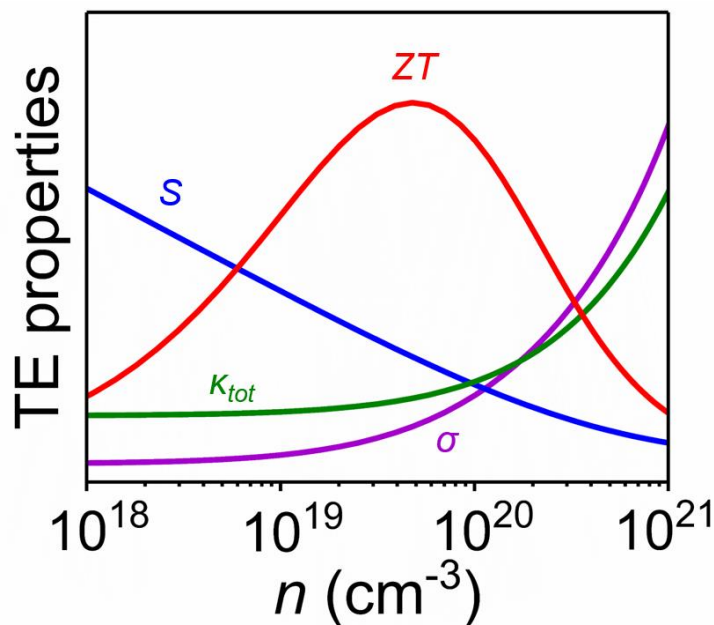


Figure 1.3 Electrical conductivity σ , Seebeck coefficient S , total thermal conductivity κ_{tot} , and thermoelectric figure of merit ZT plotted as functions of charge carrier concentration n . The curves are calculated with a single parabolic band (SPB) model. The scale is arbitrary to emphasize the differences in doping dependence of each property.

1.4 Thermoelectric design principles: strategies to improve ZT

1.4.1 General material considerations

Figure 1.3 shows the primary thermoelectric properties plotted as function of charge carrier concentration within the single parabolic band model. This simple analysis provides significant insight into the proper choice of quality thermoelectric materials. Metals possess high charge carrier densities over 10^{22} cm^{-3} , giving very poor Seebeck coefficients, high thermal conductivity, and correspondingly low ZT . Likewise, intrinsic and wide band gap semiconductors lie on the low n side and are too electrically resistive to reach appreciable figures of merit. Good thermoelectric

materials must therefore be semiconductors that can be doped to degenerate, but not metallic, charge carrier concentrations in the range of 10^{19} – 10^{20} cm^{-3} in order to optimize the tradeoff between each property. In addition to doping, there are many specific material features and properties that can be engineered to achieve high figures of merit. We outline the most common and historically successful strategies below.

1.4.2 Minimizing the thermal conductivity

Because the lattice vibrations are largely independent of the electronic structure, minimize the lattice thermal conductivity is a requirement to achieve the highest thermoelectric performance. In the Debye–Callaway model, the lattice thermal conductivity is given by¹⁷

$$\kappa_{\text{lat}} = \int_0^{\omega_{\text{max}}} C_s v_g^2 \tau d\omega \quad (1.11)$$

where, C_s is the frequency dependent specific heat, v_g is the phonon group velocity, and τ is the phonon relaxation time. Traditional routes to suppress the lattice thermal conductivity primarily aim to increase phonon scattering to reduce τ . Figure 1.4 illustrates engineering phonon scattering at different length scales.

Complex crystal structures, such as the $\text{Yb}_{14}\text{MnSb}_{11}$ Zintl compound shown in Figure 1.4a, intuitively provide a frustrated path for phonon transport. In $\text{Yb}_{14}\text{MnSb}_{11}$, the 104 atoms per unit give rise to numerous low-lying optical phonon modes, which yields a very high number of available states space for phonon scattering. Materials with structurally complicated, many atom unit cells therefore hosts intrinsically strong phonon-phonon scattering and generally low lattice thermal conductivity.¹⁸ Alternatively, introducing impurity atoms (point defects) into simple structures enhances phonon scattering, and alloying to lower the lattice thermal conductivity is

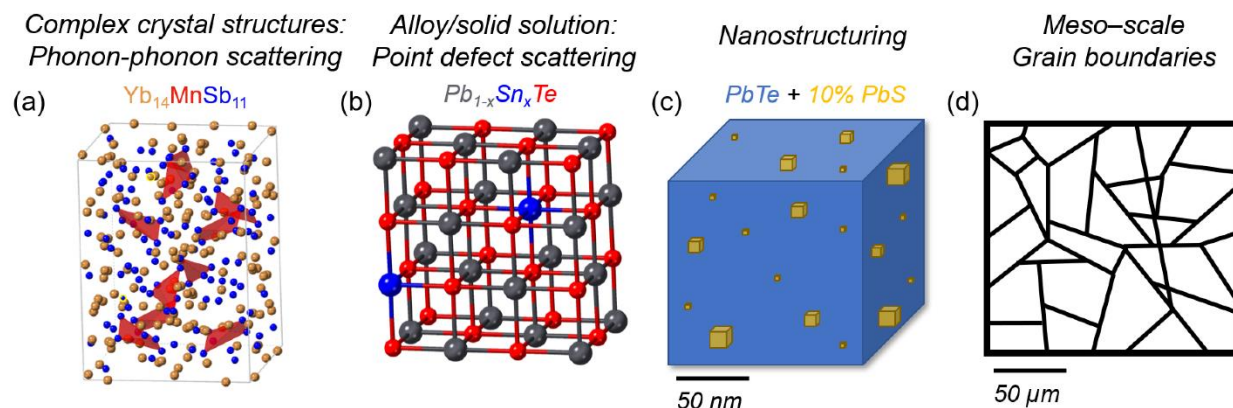


Figure 1.4 Defect engineering at different length scales to enhance phonon scattering and produce materials with low lattice thermal conductivity.

among the most exhaustively utilized strategy to achieve improved thermoelectric performance. For example, Figure 1.4b shows an illustration of cubic PbTe with a small fraction of Sn alloyed onto the cation sites. The mass and size contrast between impurity and host atoms provides a local perturbation to the crystal lattice and facilitates the scattering of high frequency (low wavelength) phonons.¹⁹⁻²² Introducing weakly bonded filler atoms into the void sites of clathrate and skutterudite structures (among others) induces a “rattling effect,” which likewise can provide strong phonon scattering and exceptionally low lattice thermal conductivity.^{14, 23-24}

Moving up in length scales, nanoscale precipitates embedded in a bulk matrix can enhance the scattering of medium wavelength phonons. Figure 1.4c demonstrates this in PbTe–PbS. Here, proper heat treatment of PbS introduced in quantities just above the solubility limit allows for growth of PbS nano-precipitates endotaxially embedded and dispersed throughout the bulk PbTe matrix.²⁵ When the precipitate size is properly selected, the boundaries between matrix and precipitate can give exceptionally strong phonon scattering and very low lattice thermal

conductivity.²⁶⁻³¹ Engineering of nanoscale structural features into bulk thermoelectric materials played a central role in the renaissance of thermoelectric research that occurred during the 2000s.^{28,}

32-33

Lastly, as illustrated in Figure 1.4d the grain boundaries in polycrystalline materials can scatter longer wavelength phonons. Engineering the grain boundary morphology, i.e. dislocation density, grain size, etc., can provide significant phonon scattering, particularly in materials with intrinsically long phonon mean free path.³⁴⁻³⁷ Integrating defects at multiple length scales, often called “all-scale hierarchical engineering” provides a broad spectrum of phonon scattering and correspondingly very low thermal conductivity and is a robust strategy of achieving high thermoelectric performance.³⁸⁻⁴²

While introducing defects to bolster phonon scattering is historically well established and applicable to many thermoelectric semiconductors, these approaches are most useful at low and moderate temperatures, as intrinsic phonon-phonon scattering dominates the relaxation time at high temperatures in most compounds. On the other hand, the lattice thermal conductivity is also sensitive to the phonon velocity, and the impact of v_g on κ_{lat} is largely temperature independent.¹⁷

Above the Debye temperature, Equation 1 reduces to $\kappa_{lat} \sim A \frac{v_g^3}{T}$, where A is a constant, indicating that lattice softening, or reduction of the phonon velocity, may provide a powerful means of accessing low thermal conductivity beyond what can be achieved through increasing phonon scattering alone. The latter chapters in this thesis explore new routes towards lattice softening in several promising thermoelectric semiconductors.

1.4.3 Raising the electronic power factor

As discussed above, the lattice thermal conductivity is largely independent of the other thermoelectric properties, making crystal and microstructural engineering to minimize κ_{lat} rather straightforward means of improving ZT . Conversely, the inverse relationship between S and σ through both the charge carrier density and effective mass make improving the electronic properties considerably more challenging. Nevertheless, while there is a theoretical (amorphous) limit to the minimal lattice thermal conductivity,⁴³⁻⁴⁴ the product $S^2\sigma$, or power factor, has no maximum value, making robust strategies to enhance $S^2\sigma$ highly sought after.

Both the Seebeck coefficient and electrical conductivity are fundamentally determined by the electronic band structure through the effective mass. The band effective mass m_b^* is related to the curvature of the electronic band extrema as shown below:

$$m_b^* = \hbar^2 \left(\frac{\partial^2 E}{\partial k^2} \right)^{-1} \quad (1.12)$$

where E is the electronic energy and k the crystal momentum. The above relationship shows that dispersive bands will give light charge carriers, while flat bands host heavy electrons/holes. Equations 1.7–1.9 indicate that while modifying the band structure to flatten the bands will raise the Seebeck coefficient, the charge carrier mobility and electrical conductivity will be reduced. As such, alloying to raise the band mass is generally of little benefit, and more dispersive bands are often preferred to maintain appreciable charge carrier mobility.⁴⁵ In semiconductors where only a single band contributes to charge transport, the charge carrier concentration should be raised to the optimal level determined by Equations 1.7–1.9.

Multi-band semiconductors offer substantially more exciting possibilities for improving the power factor. As shown in Equation 1.7, enhancing the valley degeneracy N_v can improve

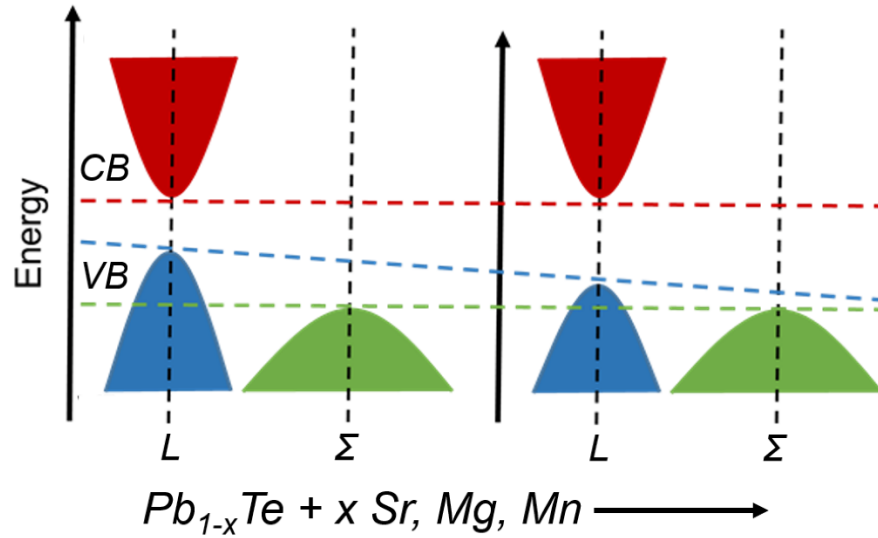


Figure 1.5 Illustration of the electronic band structure of PbTe. The primary band gap is at the L -point of the Brillouin zone, and there is a second heavier valence band at the Σ -point. Alloying with 2+ cations decreases the energy of the valence band edge at the L -point, allowing the Σ -band to contribute to charge transport. PbSe and PbS have qualitatively analogous band structure.

m_{DOS}^* without changing m_b^* . Therefore, raising N_v is a robust means of decoupling S and σ to improve the thermoelectric performance.⁴⁶ The valley degeneracy effectively parameterizes how many carrier pockets contribute to the charge transport. High N_v occurs when either a single band is degenerate in k -space, as determined by the symmetry of the Brillouin zone, or when multiple different bands participate in the electronic transport.

Lead chalcogenides are the premier example of thermoelectrics where high N_v which gives rise to excellent thermoelectric properties. As illustrated in Figure 1.5, PbTe is a direct gap semiconductor with primary valence and conduction bands at the L -point of the Brillouin zone. The L -band is itself fourfold degenerate in k -space ($N_v = 4$). Furthermore, there is a second,

heavier valence band ~ 0.15 eV below the L -band edge and located at the Σ -point. The Σ -band has outstanding valley degeneracy of 12, and critically, as the temperature is increased, the L -band moves down in energy while the Σ -band energy stays approximately constant. Furthermore, alloying 2+ cations onto the Pb sites pushes the L -band down in energy without changing the energetic position of the Σ -band. In p-type PbTe, band convergence facilitates high $N_v \sim 16$ to produce exceptional power factors and high ZT .^{40-41, 47-49} The chalcogenide analogues, PbSe and PbS, have qualitatively similar electronic structure and promising thermoelectric figures of merit.⁵⁰⁻⁵¹ Electronic structure engineering to enhance N_v is among the most important routes to improving ZT , and the vast majority of high quality thermoelectric materials, such as Bi₂Te₃, Mg₃Sb₂, CoSb₃, SnSe, GeTe, Mg₂Si, and the half Heuslers, among others, feature multi-band electronic structures.⁵²⁻⁵⁹

Another means of manipulating the band structure to improve the electronic properties is the introduction of resonance states. The basis of this strategy is comes from the Mott equation, which provides an alternative view of the Seebeck coefficient.⁶⁰

$$S = \frac{\pi^2}{3} \cdot \frac{k_B^2 T}{e} \cdot \left. \frac{d \ln \sigma(E)}{dE} \right|_{E=E_F} \quad (1.13)$$

The energy dependence of the electrical conductivity $\sigma(E)$ is primarily determined by the density of states, meaning that $\frac{d \ln \sigma(E)}{dE}$ is effectively a measure of the slope of the density of states at the Fermi level. Based on this formulation, Mahan and Soho demonstrated the ideal electronic structure for a thermoelectric material consists of a delta function in the density of states (DOS) at the Fermi level.⁷ Motivated by this insight, Hicks and Dresselhaus proposed that reduced dimensional materials, such as quantum wires and wells or superlattices, may exhibit such features in their electronic structure.^{8, 61-63} While these ideas have been heavily pursued, most work to

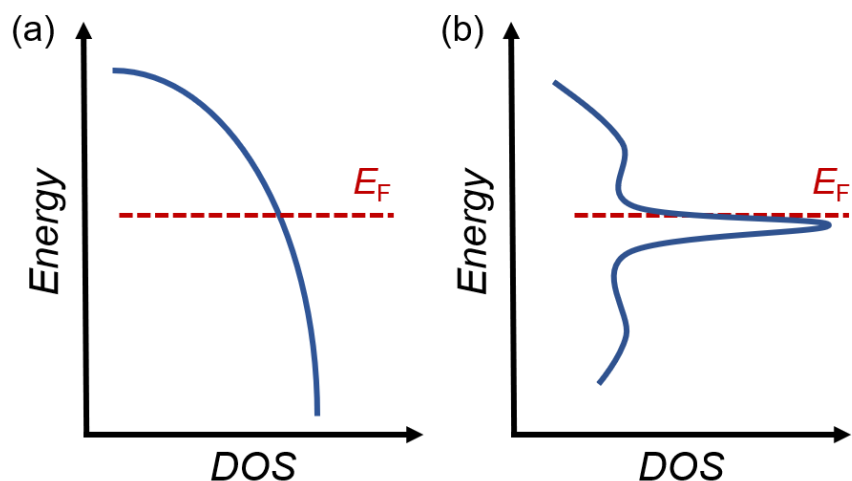


Figure 1.6 Illustration of resonance levels in the density of states. (a) Typical density of states for a single band semiconductor. (b) A resonance level giving a localized spike in the DOS.

realize high thermoelectric performance in low dimensional and superlattice structures is complicated by serious experimental challenges and has largely been unsuccessful.

Despite mixed results in low dimensional materials, similar effects can be achieved in bulk materials. Doping certain atoms into bulk semiconductors can lead to distortions in the electronic structure and cause a sharp spike in the density of states, generally referred to as a resonance level.⁶⁴ An illustration of resonance levels is given in Figure 1.6. As shown in Figure 1.6, if the Fermi level can be tuned to the proper energy, the spike in the density of states approximates the delta function described by Mahan and Soho and can yield significantly enhanced thermoelectric performance. Successful examples of resonance levels leading to improved thermoelectric properties in bulk thermoelectrics include Tl-doped PbTe,⁶⁵ In-doped SnTe,⁵⁴ Sn-doped Bi₂Te₃.⁶⁶ One drawback of using resonance states to improve the thermoelectric properties is that the Fermi

level is often temperature dependent, and can move away from the ideal energy, eliminating any beneficial effects of the altered density of states.

1.5 PbQ–NaSbQ₂ (Q = Te, Se, S) as potential thermoelectric materials

Based on the above discussion, novel thermoelectric materials should be semiconductors that can be heavily doped to degenerate p- and/or n-type charge carrier concentrations. Furthermore, materials should have complex, multi-valley electronic band structures that ideally can be chemically manipulated through strategic alloying. Materials composed of heavy atoms such as Pb and Bi facilitate low phonon velocities and low thermal conductivity. Complex crystal structures or compounds with nanoscale phase separation are also desired for achieving minimal lattice thermal conductivity.

A largely unexplored class of materials that matches these considerations is PbQ–NaSbQ₂ (Q = Te, Se, S), which is interchangeably described using the notation NaPb_mSbQ_{m+2}. Figure 1.7 illustrates stoichiometrically mixing a lead chalcogenide with the ternary NaSbQ₂ to form a new quaternary compound NaPb_mSbQ_{m+2}. In the final alloy, Na, Pb, and Sb randomly occupy the cation sublattice to maintain the cubic $Fm\bar{3}m$ symmetry. By integrating Na⁺ and Sb³⁺ in equimolar quantities, NaSbQ₂ may feasibly mimic the Pb²⁺ and give NaSbQ₂ high solubility in the respective lead chalcogenides. These factors could allow for a very wide range of fertile phase space over which to explore and optimize the thermoelectric properties. High NaSbQ₂ solubility will naturally produce double the concentration of point defects (from Na and Sb) than alloying with binary 2+ tellurides such as SrQ and MnQ. As such, NaPb_mSbQ_{m+2} compounds are anticipated to intrinsically exhibit very low lattice thermal conductivities. Furthermore, if the rocksalt structure

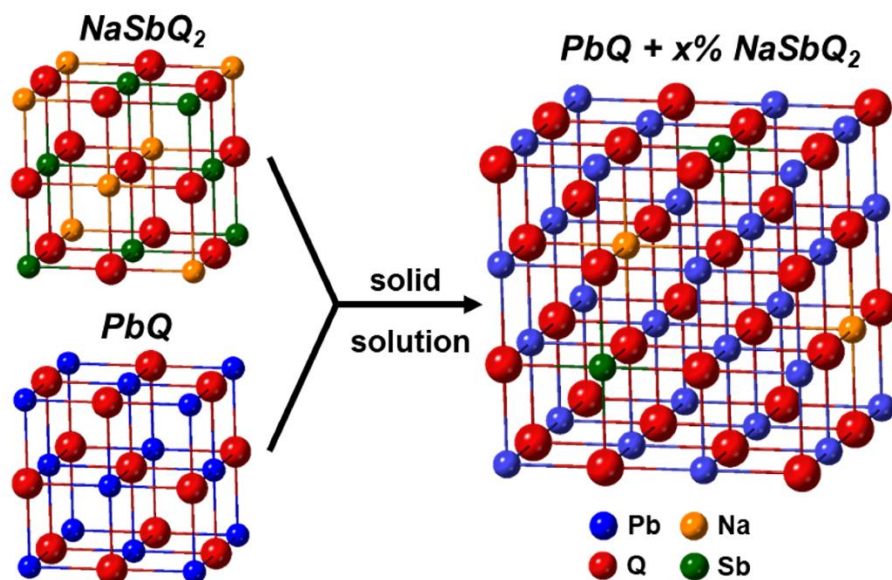


Figure 1.7 Mixing PbQ and NaSbQ_2 ($Q = \text{Te, Se, S}$) to form quaternary solid solution $\text{NaPb}_m\text{SbQ}_{m+2}$. The Na, Sb, and Pb are statistically disordered in NaSbQ_2 and $\text{NaPb}_m\text{SbQ}_{m+2}$ to maintain the cubic symmetry.

is maintained, $\text{NaPb}_m\text{SbQ}_{m+2}$ may likewise preserve the favorable electronic band structure of the host lead chalcogenides.

To date, there is very little work investigating the thermoelectric properties of PbQ – NaSbQ_2 alloys; however, the Ag–based analogues, $\text{AgPb}_m\text{SbTe}_{m+2}$, are classic nanostructured materials with low lattice thermal conductivity and high figures of merit ~ 1.7 at 700 K. Preliminary work on the tellurides, PbTe – NaSbTe_2 (or $\text{NaPb}_m\text{SbTe}_{m+2}$) conducted by our group reported very promising results. PbTe –rich phases were reported to have a microstructure rich with nanoscale precipitates, possibly nucleating from locally Na/Sb rich regions of the bulk PbTe matrix. These compounds exhibit exceptionally low lattice thermal conductivity under $1 \text{ W}\cdot\text{m}^{-1}\cdot\text{K}^{-1}$ between room temperature and near 700 K and likewise reach high ZT values near 1.6 at 700

K.⁶⁷ Limited investigation of more NaSbTe₂-rich phases also indicate promising thermoelectric properties with even lower thermal conductivity and figures of merit over 1. Despite the encouraging results, most work on PbTe–NaSbTe₂ alloys was abandoned in the early 2010's, largely because as-cast ingots are extraordinarily brittle and challenging to handle for measurements and other alloys based on Sr, Mg, and other 2+ cations took precedence. The chalcogenide analogues, PbSe–NaSbSe₂ and PbS–NaSbS₂ remain entirely unexplored.

The PbQ–NaSbQ₂ systems therefore represent a broad phase space ripe for thermoelectric characterization. These materials are anticipated to feature rich structural chemistry at the nano and micron scale as well as favorable electronic-band structures. The different chalcogenides will likely impart unique effects on the electronic structure and may alter the microstructure in differing manners.

1.6 Chapter summaries

This thesis reports the synthesis, structural characterization, and thermoelectric properties of the PbQ–NaSbQ₂ families. Much of the work seeks to elucidate the role microstructural features, including grain boundaries (GBs), phase separation, and intrinsic vacancies, play in determining the charge and thermal transport properties. The latter chapters branch out from the lead chalcogenide families and study the tin analogues, SnTe–NaSbTe₂ and SnTe–NaBiTe₂.

Chapter Two is a study of the complete PbTe–NaSbTe₂ system that addresses the impact synthetic conditions have on the nano and microscale phase segregation, as well as the thermoelectric properties. At low NaSbTe₂ fractions, as-cast ingots exhibit nanoscale phase separation, degenerate p-type electrical properties, and promising figures of merit near 1.4. As the

NaSbTe₂ fraction approaches 50%, the phase separation becomes more pronounced and the samples are better described as two-phase composites of Na/Sb-rich (low m) and Pb-rich (high m) NaPb _{m} SbTe _{$m+2$} members. Surprisingly, spark plasma sintering (SPS) to prepare more mechanically robust pellets causes the secondary Na/Sb-rich phases to dissolve into the bulk matrix, yielding single phase solid solutions without nanostructures. High resolution synchrotron X-ray diffraction and electron microscopy indicate the samples remain single phase alloys even at 50% NaSbTe₂. Dissolution of the secondary precipitates changes the charge transport from degenerate p-type to weakly n-type behavior characteristic of intrinsic semiconductors. Density functional theory calculations indicate the formation energy of single phase PbTe–NaSbTe₂ alloys is significantly lower than the analogous nanostructured Ag containing analogues (PbTe–AgSbTe₂), in agreement with the experimental observations. To improve the thermoelectric properties, Na-rich and off stoichiometric forms (i.e. Na_{1+x}Pb _{$m-x$} Sb_{1-y}Te _{$m+2$}) are investigated and shown to recover the metallic p-type conduction. The heavy cation disorder facilitates very low lattice thermal conductivities in the range 1–0.5 W·m⁻¹·K⁻¹, and optimal compositions reach high maximum ZT of 1.6 at 673 K. Compared to other forms of PbTe, the figures of merit measured for Na_{1+x}Pb _{$m-x$} Sb_{1-y}Te _{$m+2$} are enhanced at low and intermediate temperatures, giving rise to excellent $ZT_{\text{avg}} \sim 1.1$ estimated between 300 and 673 K. The unusually high performance at moderate temperatures indicate Na_{1+x}Pb _{$m-x$} Sb_{1-y}Te _{$m+2$} may be particularly promising for low to intermediate temperature thermoelectric applications.

Chapter Three reports the PbSe–NaSbSe₂ materials (NaPb _{m} SbSe _{$m+2$}), with specific focus on the impact of NaSbSe₂ on the electronic structure and phonon transport properties. Sintered pellets of PbSe–NaSbSe₂ form single phase solid solutions without evidence for nanoscale phase

separation. Alloying NaSbSe₂ into PbSe has two beneficial effects on the electronic structure: (1) reduction of the energy separation between L - and Σ -valence band raises the density of states effective mass and boosts the power factors, and (2) flattens the L -band edge, further boosting the Seebeck coefficients and shifting the optimal doping level to higher charge carrier density. Hall effect and photoemission yield spectroscopy provide firm experimental evidence confirming the valence band convergence. NaSbSe₂ furthermore sharply lowers the lattice thermal conductivity of PbSe. The joint augmentation of the electronic structure and phonon transport allows NaPb₁₀SbSe₁₂ (~9% NaSbSe₂) to reach a maximum ZT of 1.4 near 900 K and critically, a record estimated ZT_{avg} for p-type PbSe of 0.64 over 400–873 K, marking a significant improvement on existing tellurium free p-type PbSe-based thermoelectrics.

Despite having high charge carrier concentrations ($\sim 10^{20} \text{ cm}^{-3}$), the PbSe–NaSbSe₂ alloys reported in Chapter Two exhibit thermally activated transport below 600 K and metallic behavior at higher temperatures. At such high doping levels, the observed behavior is very unusual, as phonon scattering is expected to dominate the charge carrier mobility and yield a negative temperature dependence. While irregular, similar behavior is increasingly common in the thermoelectrics literature, many newly reported materials exhibiting analogous charge transport properties. Examples include Mg₃Sb₂,⁶⁸⁻⁶⁹ KAlSb₄,⁷⁰ (Hf,Zr)CoSb,⁷¹ Sr₃GaSb₃,⁷² NbFeSb,⁷³ Ca₅Al₂Sb₆,⁷⁴ Ca₃AlSb,⁷⁵ and Mg₂Si.⁷⁶ In all of these materials, suppression of the electrical conductivity ultimately degrades the thermoelectric performance on the cold side and limits the device energy conversion efficiency. Therefore, establishing the origin of the low temperature scattering and developing strategies to mitigate its effect are paramount issues.

Chapter four is a fundamental study addressing the origin of the irregular thermally activated charge transport in PbSe–NaSbSe₂. Measurements of samples prepared with differing grain size and identical chemical composition show the expected metallic electrical conductivity can be recovered by preparing large grained samples with reduced density of grain boundaries (GBs), thus providing unambiguous evidence that the thermally activated transport is due to scattering of charge carriers by the GBs. The electrical properties of PbSe–NaSbSe₂ studied as a function of NaSbSe₂ fraction, as well as those of the chalcogenide analogues, PbTe–NaSbTe₂ and PbS–NaSbS₂, demonstrate how the presence and strength of GB scattering can be understood with simple chemical principles. The magnitude of GB scattering is dependent on the relative degree of charge carrier screening in each material, which can be predicted by considering the polarizability of the host atoms. This intuitive chemical argument elegantly explains the strong GB scattering in the other thermoelectric materials discussed above. By uniting the deleterious charge transport properties exhibited by many different compounds into a common picture, this study gives new design principles for proper microstructure engineering in emerging thermoelectric materials.

Chapter five explores the SnTe–NaSbTe₂ and SnTe–NaBiTe₂ analogues to the lead chalcogenide systems discussed above (NaPb_mSbSe_{m+2} and NaPb_mBiTe_{m+2} respectively). Density functional theory (DFT) calculations indicate the addition of either NaSbTe₂ or NaBiTe₂ into SnTe 1) promotes convergence of the *L*- and Σ -valence bands and 2) sharply decreases the band gap. While the former effect improves the Seebeck coefficients and power factors, the reduced band gaps make each compound increasingly prone to detrimental bipolar diffusion. Indeed, while the room temperature Seebeck coefficients of both materials are enhanced upon alloying, the

thermoelectric properties in the Bi-containing compounds are strongly limited by bipolar charge transport above 600 K. Surprisingly however, this effect is less pronounced in the SnTe–NaSbTe₂ family. The DFT calculations account for some of this discrepancy, indicating that SnTe–NaBiTe₂ becomes a semimetal at high alloying fraction, while the gap remains finite in the SnTe–NaSbTe₂ system. Hall effect measurements moreover show that the introduction of NaSbTe₂, but not NaBiTe₂, to SnTe nearly doubles the charge carrier concentration, which is attributed to an increased number of intrinsic cation vacancies. In NaSn_mSbTe_{m+2}, the higher hole carrier concentration partially offsets the decreased band gap and suppresses bipolar diffusion, allowing the Sb-containing samples to maintain high power factor at elevated temperature. The vacancies significantly enhance the phonon scattering in NaSn_mSbTe_{m+2}. Lastly, NaSbTe₂ incorporation reduces the sound velocity of SnTe by nearly six percent, helping to achieve glasslike thermal conductivity. The joint effects of the vacancies and the lattice softening in NaSn_mSbTe_{m+2} result in superior maximum $ZT \sim 1.2$ at 800 K and excellent $ZT_{\text{avg}} \sim 0.7$ between 323 and 873 K, while the NaSn_mBiTe_{m+2} family has significantly poorer performance with maximum ZT s near 0.85.

The correlation between enhanced concentration of cation vacancies and reduced sound velocity observed in SnTe–NaSbTe₂ suggests the vacancies may drive lattice softening. Even greater reduction in the speed of sound with enhanced vacancy concentration was reported in SnTe–AgSbTe₂. However, because the Sn vacancies necessarily each introduce two holes into the valence band to maintain charge balance, the lattice softening could also be due to the altered charge carrier concentration. In fact, because changing the charge carrier density will alter the number of electrons available for atomic bonding, the controlling the electron count may change the interatomic forces and vibrational physics.

Chapter six is a fundamental investigation of the doping dependence of the phonon velocities in heavily doped thermoelectric semiconductors including SnTe, PbTe, CoSb₃, NbCoSb, La₃Sb₄, Pr₃Sb₄, and Mo₃Sb₇. Each of these compounds significantly softens when the electron and/or hole concentration is raised. The greatest degree of lattice softening is found in SnTe, where the sound velocities are reduced by up to 16 percent when the hole concentration is increased from 10¹⁹ to 10²¹ cm⁻³. This work demonstrates a direct link between the electron count and phonon transport physics in heavily doped semiconductors. Because the traditional picture of lattice dynamics treats the atomic vibrations independently of the electrons, this finding is anticipated to have wide-reaching implications. In the context of engineering high performance thermoelectrics, electron count driven lattice softening may provide a new means of suppressing the thermal conductivity at high charge carrier concentrations, and this is anticipated to be most effective in materials with higher charge carrier effective mass. Finally, chapter seven summarizes the key findings of this thesis and future directions are discussed.

Chapter Two

Absence of nanostructuring in $\text{NaPb}_m\text{SbTe}_{m+2}$: solid solutions with high thermoelectric performance in the intermediate temperature regime

Portions of this chapter were previously published and are reprinted (adapted) with permission from (*J. Am. Chem. Soc.* 2018, 140 (22), 7021-7031). Copyright © 2018, American Chemical Society.

2.1. Introduction

Considering the large fraction of global energy lost as wasted heat, the development of efficient and affordable thermoelectric materials, which directly convert thermal into electrical energy, is highly desirable. High performance thermoelectrics require materials with high Seebeck coefficient, S , and electrical conductivity, σ , while jointly having low thermal conductivity, κ . These parameters determine the dimensionless figure of merit $ZT = \frac{S^2\sigma}{\kappa_{tot}}T$, which governs the fraction of the Carnot efficiency able to be converted to electrical energy for a given temperature differential.^{29,57} Here, κ_{tot} is the sum of the lattice and electronic thermal conductivities, $\kappa_{lat} + \kappa_{elec}$, and T is the absolute temperature. Because thermoelectric modules operate across a temperature gradient, the average ZT (ZT_{avg}) over the temperature differential will determine the device efficiency, making the focus of thermoelectric research to develop materials with high ZT s over broad temperature ranges.⁷⁷ While there is no theoretical upper bound to ZT , the thermoelectric properties σ , S , and κ_{elec} are all strongly coupled through both the carrier concentration and effective mass, making the optimization of ZT a nontrivial task.^{5, 78-80} This challenge limits the maximum ZT in practice to values near 1 at 300 K and 800 K for commercial Bi_2Te_3 and PbTe devices, respectively, and to 2–2.6 at 800–923 K for state-of-the-art PbTe and single crystal SnSe materials found in laboratories.^{38, 49, 81-84}

The past decade and a half was extremely fruitful for thermoelectric research with deeper understanding and new strategies emerging, such as nanostructuring^{13, 26, 28, 48, 85-89} and band structure engineering.^{46-47, 90} Both proved to be highly effective in raising thermoelectric performance and led to the development of materials with maximum ZT s up to 1.8 at 800–900 K. Moreover, integration of both nanostructures and band structure modifications into materials such

as PbTe-SrTe,^{38, 49} PbTe-MgTe,⁴⁰ and PbTe-PbS⁸¹ achieved outstanding ZT s of 2–2.5 at temperatures of ~900 K. While these results represent tremendous progress, a remaining challenge facing the field is improving the ZT s at low and intermediate temperatures. Indeed, for many of the exciting potential applications of thermoelectricity such as waste heat recovery, hot side temperatures are typically at more moderate temperatures under 600 K.⁹¹ Unfortunately, for many of the high ZT (> 2) materials developed in recent years, the enhancement of the figure of merit is primarily achieved at elevated temperatures above 700 K, while the room and intermediate temperature ZT s remain low. For example, in the state-of-the-art PbTe compounds,^{40, 49, 81} typical average ZT s are in the range 1–1.5 over 300–900 K, but under 1 over the more moderate interval of 300–600 K. The lack of improvement at lower temperatures limits the enhancement of the average ZT and, therefore, curtails the potential for higher overall device efficiency. If PbTe based thermoelectrics are to see widespread application, attention must be further directed towards improving the low and intermediate temperature ZT to develop materials with improved average ZT .¹⁵

A class of materials that may show promise as intermediate temperature thermoelectrics is the $\text{NaPb}_m\text{SbTe}_{m+2}$ system. As illustrated in Figure 1.7 (Chapter one), $\text{NaPb}_m\text{SbTe}_{m+2}$ can be envisioned as a solid solution between two cubic compounds, NaSbTe_2 and PbTe , in which the Na, Pb and Sb ions are randomly distributed across the cation sites in the $Fm\bar{3}m$ structure. The value of m in the chemical formula determines where in the $\text{NaSbTe}_2\text{--}(\text{PbTe})_m$ phase space a given composition lies, with higher m implying a more PbTe rich compound. $\text{NaPb}_m\text{SbTe}_{m+2}$ is the Na analogue to the classic nanostructured $\text{AgPb}_m\text{SbTe}_{m+2}$ system, and preliminary investigations of $\text{NaPb}_m\text{SbTe}_{m+2}$ achieved a high ZT of 1.6 at ~700 K when $m = 20$.⁶⁷ Despite these promising early

results, investigations of the NaSbTe₂–PbTe solid solution to date are been limited to a very narrow compositional range of $m = 19$ – 20 , leaving a broad span of unexplored phase space ripe for study. Unfortunately, polycrystalline ingots of NaPb_{*m*}SbTe_{*m*+2} are extremely brittle, and become increasingly so as one progresses towards the NaSbTe₂-rich side of the solid solution (lower m values). The poor mechanical toughness of NaPb_{*m*}SbTe_{*m*+2} makes sample preparation for thermoelectric characterization extremely challenging and practically limits the feasibility of more thorough exploration.

Here, we study NaPb_{*m*}SbTe_{*m*+2} over the range $m = 1$ – 20 , representing a much greater scope of the NaSbTe₂–PbTe solid solution than previously investigated. To improve the mechanical toughness, we used spark plasma sintering (SPS) to consolidate powders prepared from polycrystalline ingots into dense pellets. SPS is routinely utilized in thermoelectric research to quickly consolidate powders into highly dense and robust pellets, and while the impact of SPS processing on the meso-scale grain boundaries has been well studied as a means of achieving low thermal conductivity,^{38, 81, 92} the chemical changes occurring during the sintering process are typically unaddressed. In fact, because SPS is relatively fast on the timescale of solid-state transformations (occurring in under 30 minutes), it is usual practice to assume negligible changes occur during sintering.

Surprisingly, we find that SPS processing of NaPb_{*m*}SbTe_{*m*+2} results in a dramatic change in the electronic properties from degenerate p-type charge transport for the as-cast ingots to weakly n-type behavior after SPS. This result is highly unexpected and to our knowledge unique to NaPb_{*m*}SbTe_{*m*+2}. High resolution synchrotron X-ray diffraction and scanning electron microscopy reveal that the as-cast ingots phase separate upon cooling into two NaPb_{*m*}SbTe_{*m*+2} members, a

primary phase rich in PbTe and a secondary phase rich in Na and Sb. The X-ray diffraction and microscopy data both suggest that the secondary phase diffuses into the primary matrix during the SPS process, resulting in more homogenous and nearly charge compensated compounds that exhibit intrinsic n-type behavior. Unlike the related nanostructured $\text{AgPb}_m\text{SbTe}_{m+2}$ materials, TEM studies show that the SPSed $\text{NaPb}_m\text{SbTe}_{m+2}$ compounds are single phase at the nanoscale, showing that PbTe and NaSbTe_2 form a true solid solution with property synthetic preparation. To achieve the desired p-type behavior in the SPSed samples, we investigated the impact of varying the stoichiometry of Na, Pb and Sb ($\text{Na}_{1+x}\text{Pb}_{m-x}\text{Sb}_{1-y}\text{Te}_{m+2}$) on the thermoelectric properties for $m = 6, 8, 10, 20$ and found that introducing Sb vacancies and substituting Na for Pb (increasing x) successfully yields p-type samples after SPS. Despite the lack of nanostructures, the lattice thermal conductivities of SPSed $\text{Na}_{1+x}\text{Pb}_{m-x}\text{Sb}_{1-y}\text{Te}_{m+2}$ are found to be exceptionally low, ranging from $1\text{--}0.5 \text{ W}\cdot\text{m}^{-1}\cdot\text{K}^{-1}$ over $300\text{--}900 \text{ K}$ which results in maximum ZT s up to 1.6 at 673 K and excellent average ZT of 1.1 between $323\text{--}673 \text{ K}$ when $m = 10, 20$, making $\text{Na}_{1+x}\text{Pb}_{m-x}\text{Sb}_{1-y}\text{Te}_{m+2}$ among the best performing PbTe based thermoelectrics under 650 K.

2.2. Results and Discussion

2.2.1 Major differences between ingots and SPS-processed samples

Initially, we prepared $\text{NaPb}_m\text{SbTe}_{m+2}$ with compositions $m = 1, 6, 10, 18$ as representative of the entire series in order to gain a general understanding of the trends in electrical and thermal properties across the system. These compositions respectively correspond to 50, 14, 9, and 5 percent NaSbTe_2 in PbTe. The thermoelectric data for the $\text{NaPb}_m\text{SbTe}_{m+2}$ samples prepared by SPS are shown in Figure 2.1a–c. In all cases, the electrical conductivities are low, under $100 \text{ S}\cdot\text{cm}^{-1}$

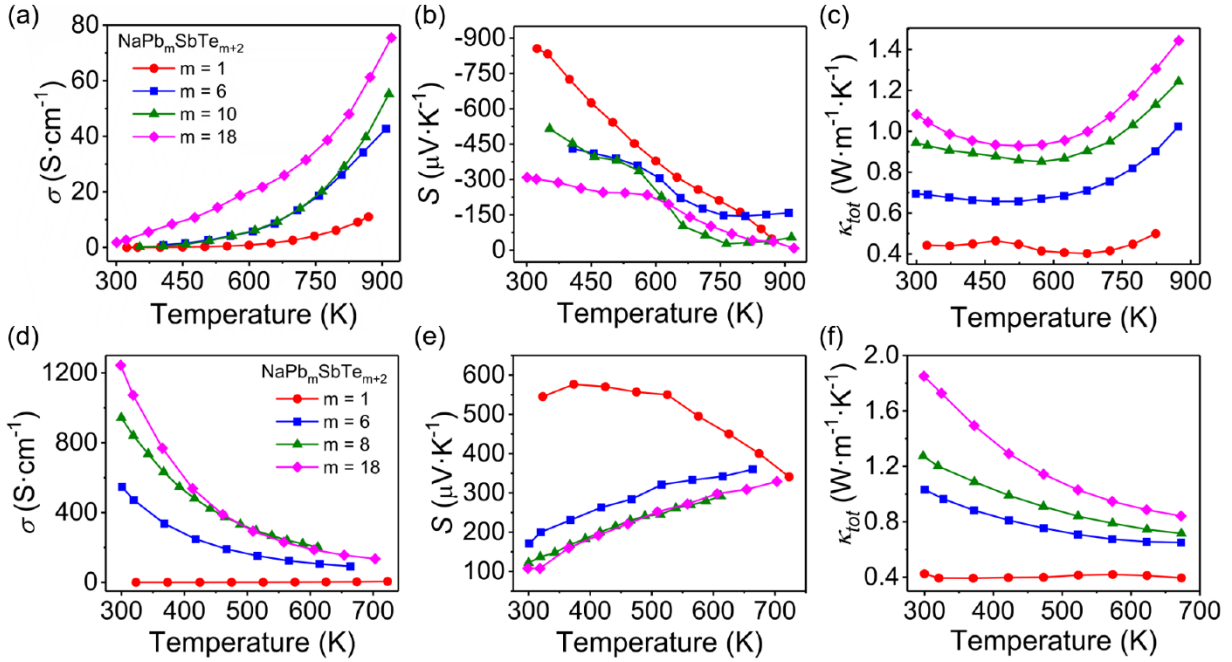


Figure 2.1 Thermoelectric properties of SPSed and as-cast ingot $\text{NaPb}_m\text{SbTe}_{m+2}$ samples. (a) SPSed electrical conductivity, (b) SPSed Seebeck coefficient, (c) SPSed total thermal conductivity, (d) ingot electrical conductivity, (e) ingot Seebeck coefficients, and (f), ingot total thermal conductivity.

and increase with temperature while the Seebeck coefficients are negative with large values of -300 to $-900 \mu\text{V}\cdot\text{K}^{-1}$ at 300 K that decrease with temperature. Taken together, these electronic properties are characteristic of nearly intrinsic n-type semiconductors with low charge carrier concentrations. The total thermal conductivities of these samples decrease with decreasing m (i.e., greater NaSbTe_2 fraction), and are low in the range of $1.4\text{--}0.4 \text{ W}\cdot\text{m}^{-1}\cdot\text{K}^{-1}$ over 300–900 K. Typically, degenerate carrier concentrations in the range $10^{19}\text{--}10^{20} \text{ cm}^{-3}$ are desired to optimize the power factor ($\sigma\cdot S^2$);⁹³ therefore, the essentially intrinsic semiconductor behavior of the $\text{NaPb}_m\text{SbTe}_{m+2}$ samples shown here results in low ZT s below 0.10 for all compositions.

The negative Seebeck coefficients of the SPSed samples indicate n-type charge transport, which is quite surprising since the corresponding polycrystalline ingots were decisively p-type. The previous work on as-cast ingots of $\text{NaPb}_m\text{SbTe}_{m+2}$ reported degenerate p-type conduction for the compositions $m = 19\text{--}20$,²⁸ and preliminary measurements done by our group prior to this work on ingot samples where $m = 6\text{--}10$ also showed degenerate p-type conduction. The explanation of this strange discrepancy between the as-prepared ingots and the SPSed samples was not clear. To further investigate this phenomenon, we prepared polycrystalline ingots of $\text{NaPb}_m\text{SbTe}_{m+2}$ and directly measured the thermoelectric properties (bypassing the SPS step, as described in the Experimental Section).

Figure 2.1d–f shows the thermoelectric data for the as-cast ingots when $m = 1, 6, 8, 18$. For samples with $m = 6\text{--}18$, the electrical conductivities are considerably higher than those of the respective SPSed samples and decrease monotonically with temperature from $600\text{--}1200 \text{ S}\cdot\text{cm}^{-1}$ at 300 K to $\sim 100 \text{ S}\cdot\text{cm}^{-1}$ at 700 K. The Seebeck coefficients are positive and increase with temperature from ~ 100 to $300 \mu\text{V}\cdot\text{K}^{-1}$ over the interval 300–700 K. These charge transport properties show that $\text{NaPb}_m\text{SbTe}_{m+2}$ ($m = 6\text{--}18$) ingots behave as degenerate p-type semiconductors with hole concentrations that appear to decrease as one progresses towards the NaSbTe_2 side of the system, reaching behavior characteristic of nearly intrinsic semiconductors by $m = 1$. Because of the increased κ_{elec} , the thermal conductivities of the ingots are higher than in the corresponding SPSed samples and decrease from $\sim 1\text{--}1.8 \text{ W}\cdot\text{m}^{-1}\cdot\text{K}^{-1}$ at 300 K to $0.9\text{--}0.7 \text{ W}\cdot\text{m}^{-1}\cdot\text{K}^{-1}$ at 700 K when $m = 6\text{--}18$. The higher carrier concentrations lead to considerably better performance compared to the SPSed samples, with ZT s reaching maxima of 1.2–1.4 at 650 K when $m = 6\text{--}18$. These results show that ingots of $\text{NaPb}_m\text{SbTe}_{m+2}$ exhibit reasonably high thermoelectric

performance across a much wider range of the NaSbTe₂-PbTe solid solution than previously explored.

While the NaPb_mSbTe_{m+2} ingots indeed show promising *ZT*s when *m* is greater than or equal to 6, their poor mechanical toughness limits the practicality of further optimization. Additionally, the properties of the ingots were found to be very sensitive to the synthetic conditions, with even small differences in melting and cooling conditions resulting in large fluctuations of the thermoelectric properties. As a result, the sample-to-sample consistency and repeatability of the as-cast ingots is limited, which further curtails their potential for thermoelectric application. Despite this, the significant differences in the electrical properties of the as-cast ingots and SPSed samples is very unusual and warrants further investigation. Typically, SPS is considered to be fast on the timescale of solid-state transformations, occurring in 30 min or less with no changes expected in the material. In the case of NaPb_mSbTe_{m+2}, however, SPS appears to result in a transition from degenerate p-type semiconductors with high *ZT* as ingots to weakly n-type materials with poor thermoelectric properties. This observation is to our knowledge unique to NaPb_mSbTe_{m+2}, making explanation of this phenomenon crucial to understanding the fundamental chemistry of the system and to enhance the thermoelectric properties of the SPSed samples. Furthermore, because SPS is widely used in the field of thermoelectrics to consolidate powders into high-density samples, understanding the chemical changes that occur during SPS processing of common thermoelectric materials such as PbTe-based compounds is of significant practical interest.

2.2.2 Powder X-ray diffraction

To gain more insight into the behavior of the $\text{NaPb}_m\text{SbTe}_{m+2}$ system and the impact of SPS on the physical properties, we prepared samples with compositions $m = 0.25\text{--}20$ spanning the full $\text{NaSbTe}_2\text{-PbTe}$ solid solution ($\sim 4\text{--}80\%$ NaSbTe_2). Figure 2.2a and 2.2b shows respectively the laboratory powder X-ray diffraction (PXRD) patterns for the SPSed and ingot samples of each composition. The experimental diffraction data correspond very well to the projected NaSbTe_2 ($m = 0$) pattern and show that each member (m) of $\text{NaPb}_m\text{SbTe}_{m+2}$ has the expected $Fm\bar{3}m$ structure and contains no detectable secondary phases. As shown in Figure 2.2b, the lattice parameters for the ingots decrease linearly with decreasing PbTe fraction, closely following the trend predicted by Vegard's law and supporting the notion that NaSbTe_2 and PbTe form a solid solution across all compositions. Interestingly, however, for all compositions the lattice parameters of the SPSed samples are smaller than those of their respective ingots and deviate significantly from the trend predicted by Vegard's law. This unusual result is particularly pronounced at intermediate ratios of $(\text{PbTe})_{1-x}\text{-(NaSbTe}_2)_x$ ($x = 0.5$ or equivalently $m = 1$) and will be further explored in the following discussion.

To further explore the structural differences of the two sample forms, we performed high resolution synchrotron powder diffraction at APS-11BM at the Argonne National Laboratory. The full diffraction patterns are shown in Figure 2.3a and 2.3b, and close-up views of several high-angle reflections are shown in Figure 2.3c and 2.3d for ingot and SPSed samples respectively. In the case of the SPSed samples, both Figures 2.3a and 2.3c reveal sharp diffraction peaks corresponding to the expected rock salt structure and are in excellent agreement with the laboratory diffraction data, indicating that the SPSed samples remain phase-pure even to $m = 1$ (50:50 PbTe:

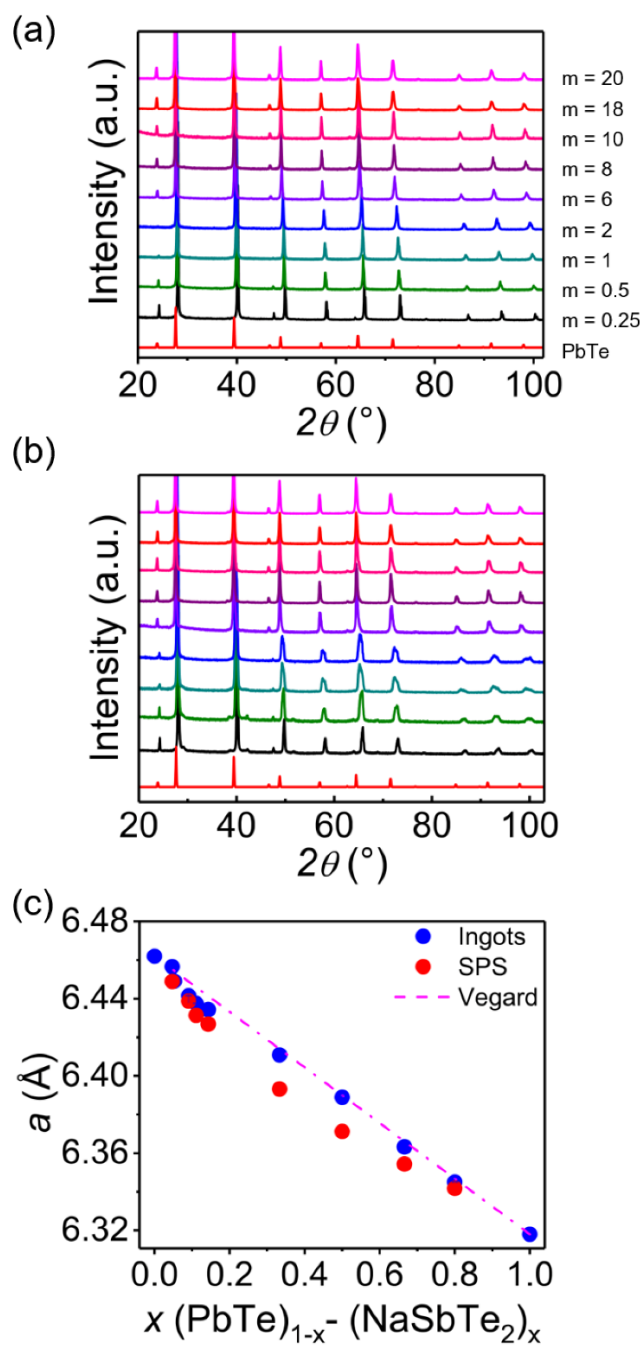


Figure 2.2 Laboratory powder X-ray diffraction (PXRD) patterns for $\text{NaPb}_m\text{SbTe}_{m+2}$ obtained on (a) SPS processed samples and (b) as-cast ingots. (c) Lattice parameters refined from the patterns shown in (a) and (b). The pink line is a guide to the eye showing the linear trend. The ingots with $m < 1$ (over 50% NaSbTe_2) show small peaks corresponding to Sb_2Te_3 .

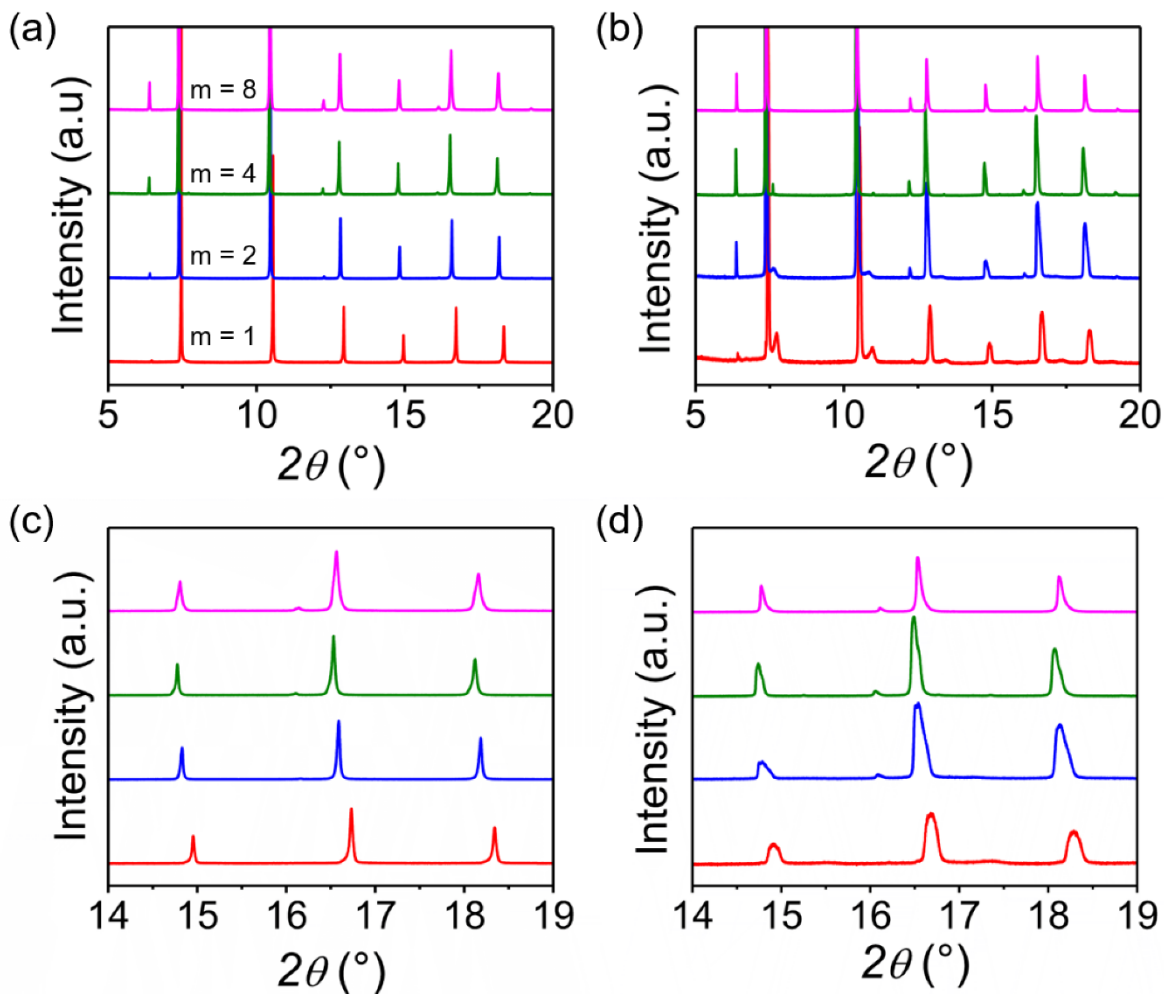


Figure 2.3 High resolution synchrotron PXRD patterns collected for $\text{NaPb}_m\text{SbTe}_{m+2}$ (a) SPS processed samples and (b) as-cast ingots. (c) and (d) are close up images of several higher angle peaks for SPSed and ingot samples respectively showing significant peak broadening in patterns collected with the ingots.

NaSbTe_2). Interestingly however, the diffraction patterns for the ingots (Figure 2.3b and 2.3d) show significant peak broadening when compared with the corresponding SPSed data, an effect that becomes more pronounced at lower values of m . The broader peaks for the ingots suggest that

they are not phase pure, and instead contain a second cubic phase with very similar lattice parameter to that of the primary $\text{NaPb}_m\text{SbTe}_{m+2}$ such that the synchrotron diffraction cannot fully resolve the individual phases. These results suggest that despite following Vegard's law, $\text{NaSbTe}_2\text{-PbTe}$ ingots do not form a perfect solid solution. We believe the phase separation in the as-cast ingots is the origin of the surprising behavior described above and has major consequences

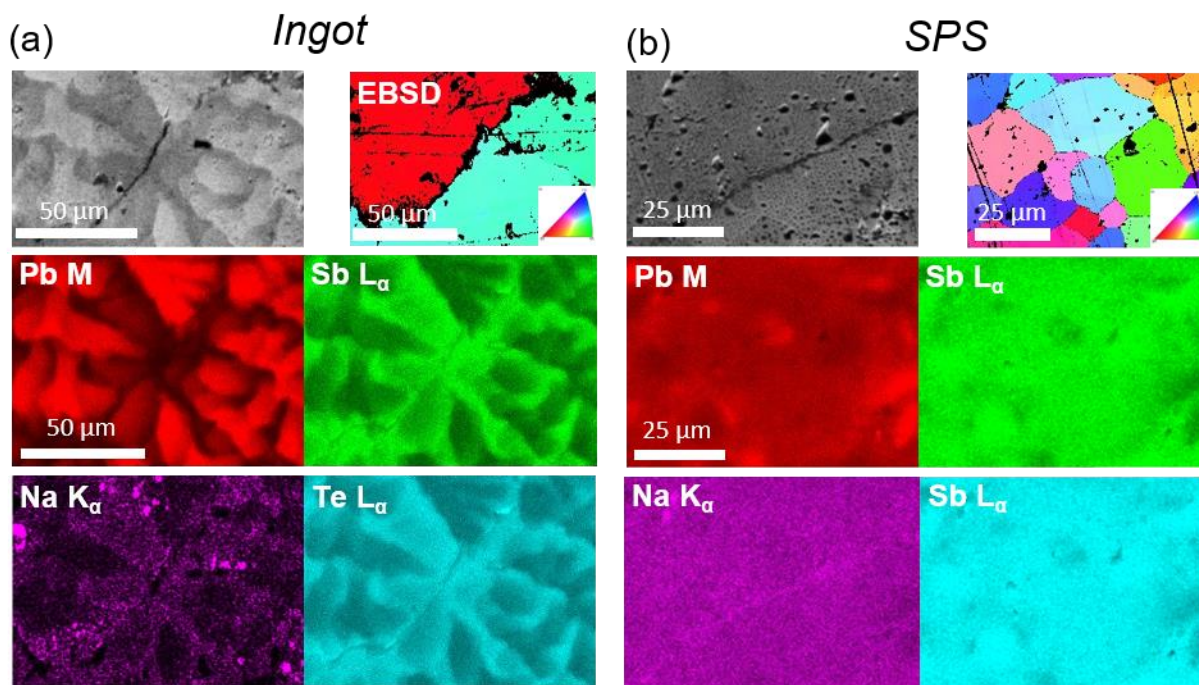


Figure 2.4 SEM images and electron backscatter diffraction (EBSD) orientation maps with accompanying EDS elemental maps for Pb, Sb, Na and Te in a NaPbSbTe_3 as-cast ingot (a) and SPSed sample (b). Upper left and right images for each are the electron and EBSD images, respectively. The EDS images show that there is clear chemical segregation in the ingot sample (Na/Sb-rich and Pb-rich phases) and that Spark Plasma Sintering results in a more homogeneous elemental distribution. The Na map for SPSed shows minor Na segregation along the crack seen in the electron image. Na segregation along cracks and GBs is frequently found in PbQs.

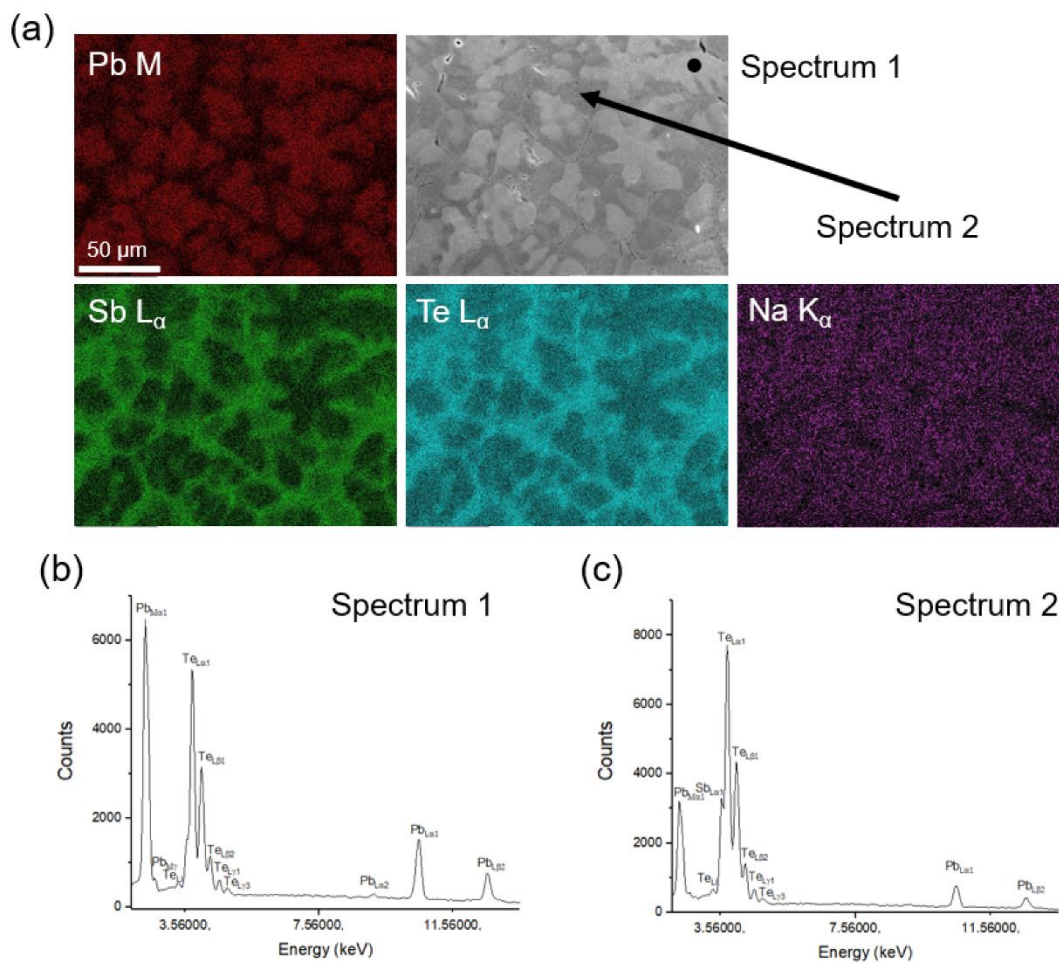


Figure 2.5 (a) EDS elemental maps of Pb, Sb, Te, and Na in a NaPbSbTe_3 ($m = 1$, 50% NaSbTe_2) as-cast ingot showing severe elemental inhomogeneity consistent with the results shown in Figure 2.4. (b) and (c) are the spectra for the EDS point scans of region 1 and 2, showing Pb-rich and Na/Sb-rich regions, respectively.

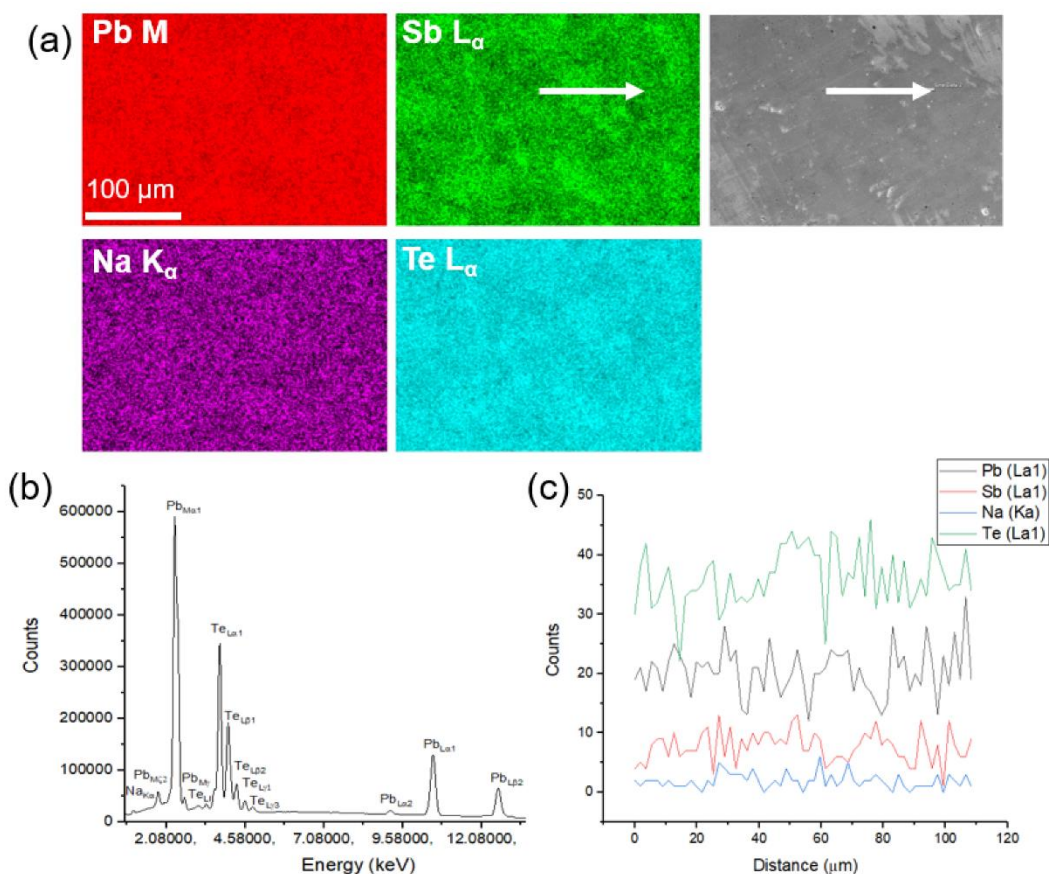


Figure 2.6 (a) Scanning electron image and EDS elemental maps of Pb, Sb, Na, and Te in a SPSed sample of $\text{NaPb}_8\text{SbTe}_{10}$ ($m = 8$, 11% NaSbTe_2). (b) Average EDS spectra extracted from the EDS map of the entire area shown in the electron image. (c) The EDS line scan extracted from the map data is denoted by the arrows on the Sb map and electron image. The line scan passes over an area of potential inhomogeneity revealed in the Sb map. The change in composition is not greater than the noise level of the EDS scan (as is seen in areas of inhomogeneity). Because the synchrotron diffraction patterns of the SPSed samples also reveal no secondary phases, we believe it is safe to consider the SPSed samples single phase.

Table 2.1 Qualitative atomic percentages from the EDS point spectra 1 and 2 taken on NaPbSbTe₃ shown in Figure 2.5. The point spectra show that the Te is uniformly distributed while the Pb and Na/Sb are segregated, confirming the phase segregation in the ingots and suggesting that the similarity of Sb and Te elemental maps is due to the nearly overlapping L_α EDS peaks.

Spectrum 1		Spectrum 2	
Element	Atomic %	Element	Atomic %
Na	10.09	Na	18.81
Sb	9.77	Sb	19.01
Pb	31.30	Pb	12.75
Te	48.84	Te	49.35

Table 2.2 Qualitative atomic percentages of each element obtained from the EDS elemental maps of the SPSed NaPb₈SbTe₁₀ sample shown in Figure 2.6. The atomic percentages are in good agreement with the nominal NaPb₈SbTe₁₀ stoichiometry.

Element	Atomic %
Na	4.96
Sb	5.02
Te	49.08
Pb	40.94

for the electrical properties, resulting in the large discrepancies between the ingots and SPSed samples. These issues will be expanded upon below.

2.2.3 Scanning Electron Microscopy

To more thoroughly investigate the phase separation, scanning electron microscopy (SEM) and energy dispersive spectroscopy (EDS) were used to analyze both ingot and SPSed samples. Figure 2.4a shows a representative SEM image of the $m = 1$ (50% NaSbTe₂) ingot whose powder diffraction data is discussed above. The EDS elemental maps obtained over this region reveal severe inhomogeneity with Pb-rich regions and Na/Sb-rich regions. While Te appears to also be segregated, point scans shown in Figure 2.5 and Table 2.1 show a uniform distribution of Te while retaining the Pb/Na/Sb separation, indicating that the similarity between Te and Sb elemental maps stems from the nearly overlapping L_{α} peaks for these two elements. These results are in good agreement with the synchrotron X-ray diffraction data, revealing clear phase separation in the ingots and suggesting that the detected second phase is rich in Na and Sb. The electron backscatter diffraction (EBSD) images show that the phase separation is not confined to the grain boundaries but is pervasive throughout the whole sample. As shown in Figure 2.4d, the two phases are not fully resolved by the synchrotron powder diffraction, suggesting that both phases are cubic materials with similar lattice parameters. These factors indicate that the as-cast ingots phase separate upon cooling into different NaPb_{*m*}SbTe_{*m*+2} members with slightly different compositions (*m*), one of which is rich in Na and Sb and the other rich in Pb.

Figure 2.4b shows the elemental maps of the $m = 1$ SPSed sample. These maps are strikingly different than those for the as-cast ingot, revealing a significantly more uniform and

homogenous elemental distribution. While there still appears to be minor inhomogeneity in the SPSed sample for 50% NaSbTe₂, the elemental segregation is clearly significantly reduced compared to the ingot, and this minor inhomogeneity vanishes for higher m compositions (more PbTe rich) as evidenced by Figure 2.6. For example, EDS elemental maps of a SPSed NaPb₈SbTe₁₀ ($m = 8$, 11% NaSbTe₂) sample reveal a uniform elemental distribution within the uncertainty of the measurement. Therefore, based on both the EDS results and synchrotron diffraction data, we believe that the SPSed samples are effectively phase pure solid solutions. The single-phase nature of the SPSed samples is further verified by transmission electron microscopy (TEM), as will be discussed in the following sections.

Together, the diffraction and microscopy data suggest an elegant explanation for the unusual electrical properties. Clearly, the NaPb _{m} SbTe _{$m+2$} ingots are not perfect solid solutions and instead phase separate upon cooling into two NaPb _{m} SbTe _{$m+2$} members (different m), a primary phase rich in Pb and a secondary phase rich in Na and Sb. Based on both the width of the ingots' synchrotron diffraction peaks and the relative change in lattice parameters between ingots and SPSed samples, the degree of phase separation is clearly most severe in ingots with intermediate ratios of NaSbTe₂ and PbTe (m near 1). It should be noted that the composition of the second phase will change for different values of m due to the different overall stoichiometries; however, the secondary phase will be rich in Na and Sb for all compositions. On the contrary, both the synchrotron diffraction data and SEM demonstrate that the corresponding SPSed samples are single phase. Based on these observations, we believe that the secondary Na/Sb-rich phase dissolves into the primary matrix during SPS, forming a solid solution. Because Na⁺ and Sb³⁺ have smaller ionic radii than Pb²⁺, the dissolution of the Na/Sb-rich secondary phase into the

primary matrix also explains the origin of the shrinking lattice parameters after SPS (Figure 2.2c). Most importantly, we believe the phase separation leaves the primary phase with a significant fraction of cation vacancies, which would be expected to yield strong p-type charge transport in line with the measured electrical properties for the ingots. Lastly, dissolution of the secondary phase into the primary matrix would leave the final material very close to the stoichiometric composition of $\text{NaPb}_m\text{SbTe}_{m+2}$. In PbTe , Na is typically an acceptor and Sb a donor; therefore, a perfectly stoichiometric $\text{NaPb}_m\text{SbTe}_{m+2}$ compound would be completely charge compensated. The measured electronic properties, displayed in Figure 2.1a and 2.1b, strongly support almost full charge compensation, with temperature-dependent electrical conductivities and Seebeck coefficients characteristic of nearly intrinsic semiconductors for the SPSed samples.

In summary, the synchrotron powder diffraction and SEM-EDS studies both revealed that the as-cast ingots phase separate upon cooling into two $\text{NaPb}_m\text{SbTe}_{m+2}$ phases, a primary phase rich in Pb and a secondary phase rich in Na and Sb. The resulting cation vacancies in the primary phase yield degenerate p-type charge transport. As evidenced by both the synchrotron diffraction and microscopy analysis, the secondary phase dissolves into the primary matrix during SPS, yielding single phase samples with compositions very close to the ideal $\text{NaPb}_m\text{SbTe}_{m+2}$ stoichiometry which exhibit charge transport characteristic of charge compensated and nearly intrinsic n-type semiconductors. It is likely that the dissolution of the Na/Sb-rich phase occurs during sintering because of the shorter diffusion lengths found in the finely ground and sieved powder ($< 53 \mu\text{m}$) used to prepare the samples for SPS, as opposed to the much larger grains of the polycrystalline ingots. The difference in grain size is clearly observed in the electron backscatter diffraction (EBSD) images shown in Figure 2.5. These results show that significant

chemical changes can occur during SPS sintering of PbTe based materials and suggest attention should be directed towards investigating if similar events occur while sintering other common thermoelectric systems.

2.2.4 TEM characterization: absence of nanostructuring and its origins

The synchrotron powder diffraction and SEM results discussed above indicate that the as-cast ingots are in-truth multi-phase composites of different $\text{NaPb}_m\text{SbTe}_{m+2}$ compounds at the microscale, despite appearing as single-phase rocksalt compounds by laboratory PXRD. After SPS-processing, the diffraction and SEM data suggest that the second phases dissolve to form single-phase materials that behave as n-type semiconductors with nearly intrinsic charge carrier concentrations. To further characterize the microstructure and determine if the SPSed samples of $\text{NaPb}_m\text{SbTe}_{m+2}$ remain solid solutions at the nanoscale, we conducted transmission electron microscopy on several samples with compositions of $\text{Na}_{1.10}\text{Pb}_{9.90}\text{Sb}_{0.85}\text{Te}_{12}$, $\text{Na}_{1.15}\text{Pb}_{19.85}\text{Sb}_{0.85}\text{Te}_{22}$, and $\text{NaPb}_m\text{SbTe}_{m+2}$ ($m = 1, 10, \text{ and } 20$, or $\sim 50, 9, \text{ and } 4$ percent NaSbTe_2 in PbTe respectively). The thermoelectric properties of these samples will be discussed in the following sections. Representative TEM images are shown in Figure 2.7 and show no evidence of phase separation or nanostructuring even down to $m = 1$ (50% NaSbTe_2). Instead, all samples investigated exhibit a homogeneous microstructure. These results are consistent with the SEM and synchrotron X-ray diffraction data discussed earlier and confirm the single-phase nature of $\text{NaPb}_m\text{SbTe}_{m+2}$ after SPS.

Because the closely related Ag analogues $\text{AgPb}_m\text{SbTe}_{m+2}$ ⁹⁴ and $\text{AgPb}_m\text{SbSe}_{m+2}$ ⁹⁵ are reported to be nanostructured, it is intriguing that the SPSed $\text{NaPb}_m\text{SbTe}_{m+2}$ materials are not. It

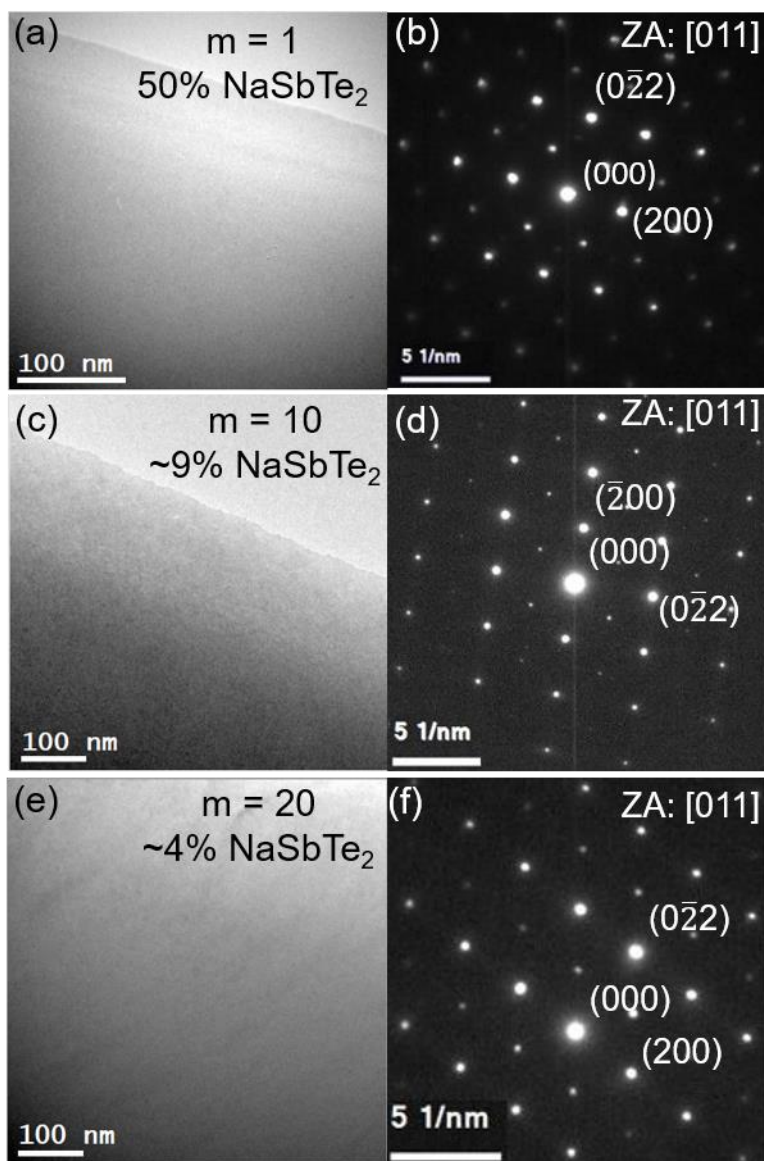


Figure 2.7 TEM images of SPSed (a) NaPbSbTe_3 , (c) $\text{Na}_{1.10}\text{Pb}_{9.90}\text{Sb}_{0.85}\text{Te}_{12}$, and (e) $\text{Na}_{1.15}\text{Pb}_{19.85}\text{Sb}_{0.85}\text{Te}_{22}$. (b), (d), and (f) show selected area electron diffraction patterns for each respective sample. All images reveal a single phase and homogeneous microstructure with no evidence of nanostructures.

should be noted here that Ag analogues were studied in as-cast ingot form, while the $\text{NaPb}_m\text{SbTe}_{m+2}$ ingots in this work were shown to be phase separated and therefore may also be nanostructured. In the Ag systems, coulombic interactions between the negatively charged Ag ions (relative to the primarily Pb^{2+} sublattice) and positively charged Sb ions are suggested to drive the nucleation of Ag- and Sb-rich nanoscale precipitates.⁹⁶⁻⁹⁷ Considering the similarities between $\text{AgPb}_m\text{SbTe}_{m+2}$ and $\text{NaPb}_m\text{SbTe}_{m+2}$, one would expect similar driving forces for the formation of Na- and Sb-rich precipitates in SPSe $\text{NaPb}_m\text{SbTe}_{m+2}$. Yet, the nanostructures found in $\text{AgPb}_m\text{SbTe}_{m+2}$ and $\text{AgPb}_m\text{SbSe}_{m+2}$ —two very similar systems—are quite different in terms of both size (larger precipitates in the selenides), and composition, with Ag_2Te a primary second phase in the tellurides, and separate Ag_2Se and mixed Ag/Sb/Pb nanoprecipitates in the selenides.⁹⁵ Evidently, the thermodynamics of the nanostructure formation differs even between $\text{AgPb}_m\text{SbTe}_{m+2}$ and $\text{AgPb}_m\text{SbSe}_{m+2}$, suggesting that $\text{NaPb}_m\text{SbTe}_{m+2}$ may also be unique.

To explore this, we used DFT to calculate the mixing energies of $\text{Pb}(\text{NaSb})_{0.5}\text{Te}_2$ ($\text{NaPb}_2\text{SbTe}_4$, $m = 2$, 33% NaSbTe_2), $\text{Pb}(\text{AgSb})_{0.5}\text{Te}_2$ ($\text{AgPb}_2\text{SbTe}_4$), and $\text{Pb}(\text{AgSb})_{0.5}\text{Se}_2$ ($\text{AgPb}_2\text{SbSe}_4$) solid solutions, with PBEsol exchange-correlation functional.⁹⁸ We simulated the solid solutions using special quasi-random structures (SQS),⁹⁹ and calculated mixing energies with respect to PbTe and NaSbTe_2 ($L1_1$) for $\text{Pb}(\text{NaSb})_{0.5}\text{Te}_2$, PbTe and NaAgTe_2 ($D4$) for $\text{Pb}(\text{AgSb})_{0.5}\text{Te}_2$, and PbSe and NaAgSe_2 ($L1_1$) for $\text{Pb}(\text{AgSb})_{0.5}\text{Se}_2$. $L1_1$ and $D4$ are ordered rocksalt-based structures found with the lowest energy for NaSbTe_2 and AgSbSe_2 , and for AgSbTe_2 , respectively.⁹⁷ The data is shown in Table 2.3, and reveals that the mixing energy of $\text{NaPb}_2\text{SbTe}_4$ is considerably smaller than that of both $\text{AgPb}_2\text{SbTe}_4$, and $\text{AgPb}_2\text{SbSe}_4$, indicating that the driving force for phase separation is much smaller in the Na compound. These results

Table 2.3 DFT-calculated Mixing Energies of $\text{Pb}(\text{NaSb})_{0.5}\text{Te}_2$ ($\text{NaPb}_2\text{SbTe}_4$), $\text{Pb}(\text{AgSb})_{0.5}\text{Te}_2$ ($\text{AgPb}_2\text{SbTe}_4$), and $\text{Pb}(\text{AgSb})_{0.5}\text{Se}_2$ ($\text{AgPb}_2\text{SbSe}_4$) solid solutions.

Compound	Number of atoms	ΔE_{mix} (meV/cation)
$\text{Pb}(\text{NaSb})_{0.5}\text{Te}_2$	32	24.10
$\text{Pb}(\text{AgSb})_{0.5}\text{Te}_2$	32	92.02
$\text{Pb}(\text{AgSb})_{0.5}\text{Se}_2$	32	52.66

agree with the experimental finding that SPSed $\text{NaPb}_m\text{SbTe}_{m+2}$ forms a solid solution while $\text{AgPb}_m\text{SbTe}_{m+2}$ and $\text{AgPb}_m\text{SbSe}_{m+2}$ phase separate.

2.2.5 Optimizing the thermoelectric properties after SPS: off-stoichiometric $\text{NaPb}_m\text{SbTe}_{m+2}$

Having uncovered the origin of the unusual change in electronic properties between ingot and SPSed samples and verified that SPS processed $\text{NaPb}_m\text{SbTe}_{m+2}$ are single phase solid solutions of PbTe and NaSbTe_2 , we turned to optimization of the thermoelectric properties. Ideally, p-type charge transport is desirable for $\text{NaPb}_m\text{SbTe}_{m+2}$ because of the favorable valence band structure of PbTe -based materials.⁴⁶ As discussed above, while the data for the ingots indeed show promising p-type thermoelectric performance with the maximum ZT s reaching 1.4, further study and tuning of their thermoelectric properties is constrained by the severe mechanical brittleness of these materials. However, SPS can be used to prepare more mechanically robust samples; therefore, we focused on a strategy to preserve the desired p-type transport throughout the SPS process.

Accordingly, we sought to tune the stoichiometry of the cations by substituting additional Na for Pb and introducing Sb vacancies into the matrix ($\text{Na}_{1+x}\text{Pb}_{m-x}\text{Sb}_{1-y}\text{Te}_{m+2}$), each of which should increase the number of hole carriers. We first studied Sb vacancies and display the electrical properties for the SPSed $\text{NaPb}_{10}\text{Sb}_{1-y}\text{Te}_{12}$ ($m = 10$, $y = 0.05\text{--}0.15$) samples Figures 2.8a

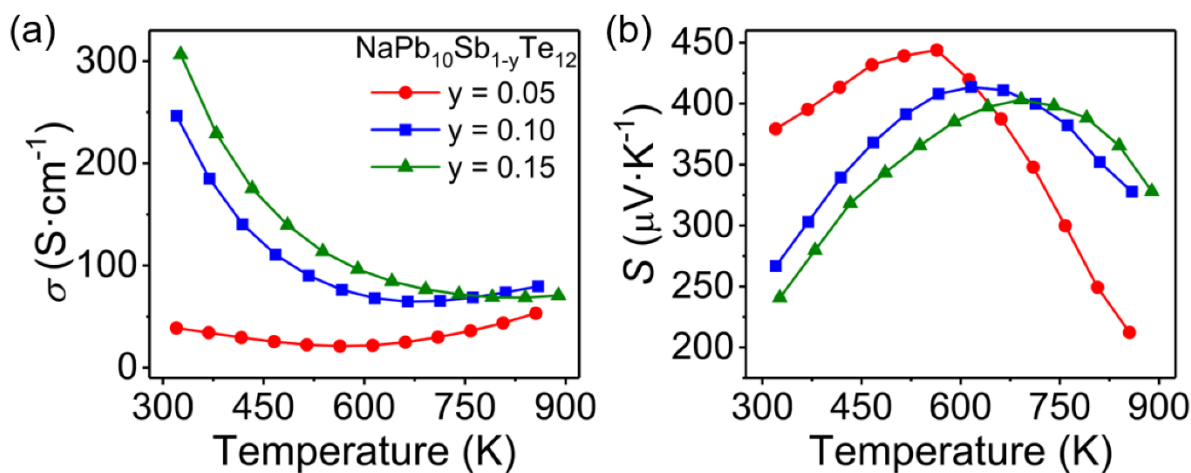


Figure 2.8 (a) Electrical conductivities and (b) Seebeck coefficients of SPSed $\text{NaPb}_{10}\text{Sb}_{1-y}\text{Te}_{12}$ indicating that introducing Sb vacancies allows p-type transport to survive SPS. The increase in σ and decrease in S with greater y indicates that the hole concentration increases with increasing fraction of Sb vacancies.

and 2.8b. Here, the Sb deficient samples all have positive Seebeck coefficients across the measured temperature interval indicating that p-type transport has survived SPS. Additionally, as the value of y is increased the electrical conductivities increase and the Seebeck coefficients decrease, suggesting that the hole concentration increases with higher number of Sb vacancies. In fact, for the samples with $y > 0.05$, the temperature dependence of both the electrical conductivities and Seebeck coefficients is characteristic of nearly degenerate semiconductors, exhibiting decreasing σ and rising S over the temperatures 300–650 K before the onset of bipolar diffusion above 650 K.

Finally, to further raise the hole carrier concentration and optimize the thermoelectric properties, we substituted Na for Pb while keeping Sb fixed at $y = 0.85$ for compounds with a range of m across the system ($\text{Na}_{1+x}\text{Pb}_{m-x}\text{Sb}_{0.85}\text{Te}_{m+2}$, $m = 6, 8, 10, 20$, $x = 0.02-0.15$). The powder X-

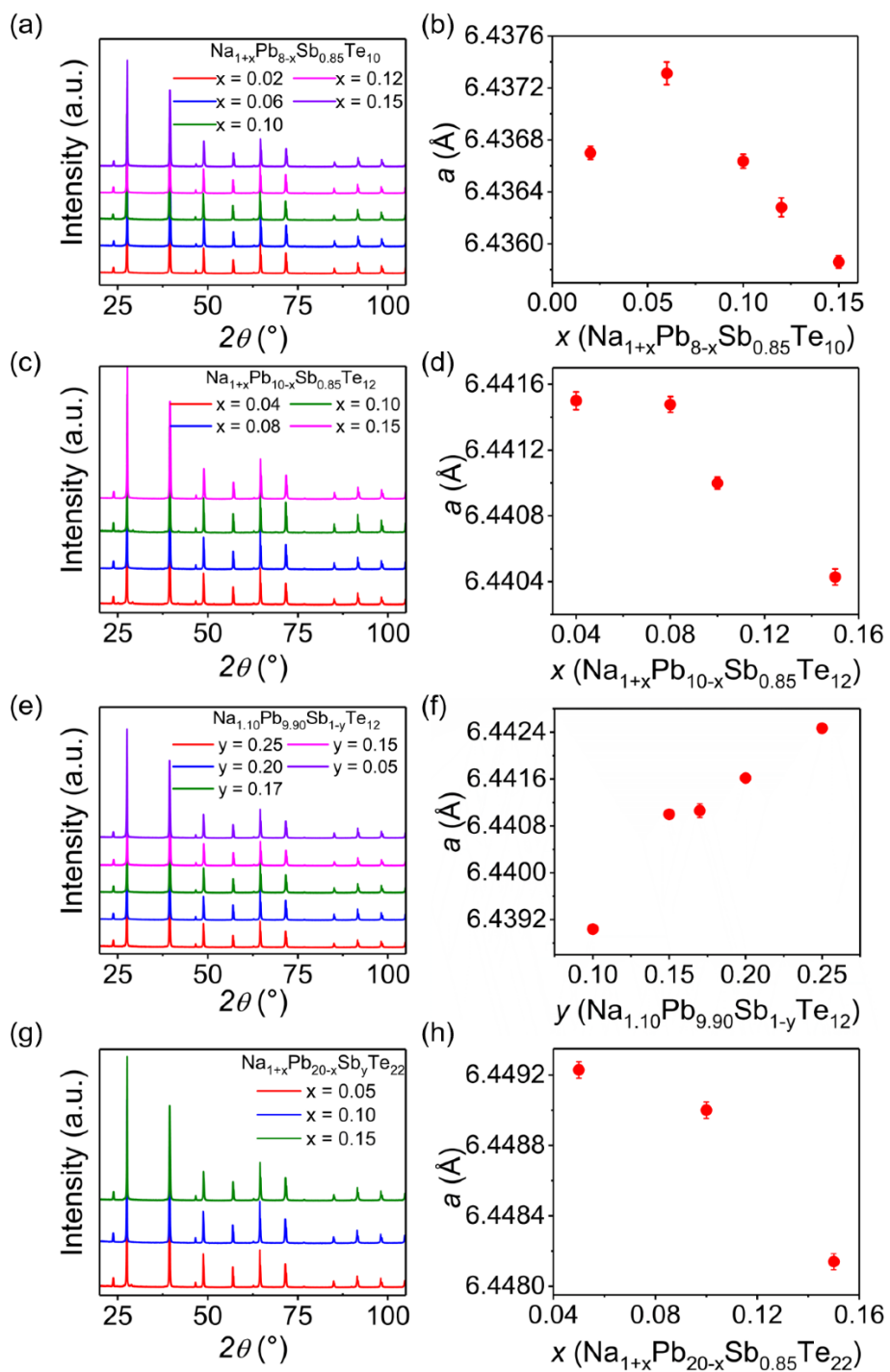


Figure 2.9 Laboratory powder X-ray diffraction patterns for doped $\text{NaPb}_m\text{SbTe}_{m+2}$. (a) $\text{Na}_{1+x}\text{Pb}_{8-x}\text{Sb}_{0.85}\text{Te}_{10}$, (c) $\text{Na}_{1+x}\text{Pb}_{10-x}\text{Sb}_{0.85}\text{Te}_{12}$, (e) $\text{Na}_{1.10}\text{Pb}_{9.90}\text{Sb}_y\text{Te}_{12}$, and (g) $\text{Na}_{1+x}\text{Pb}_{20-x}\text{Sb}_{0.85}\text{Te}_{22}$. (b), (d), (f), and (h) are the respective lattice parameters of each compound.

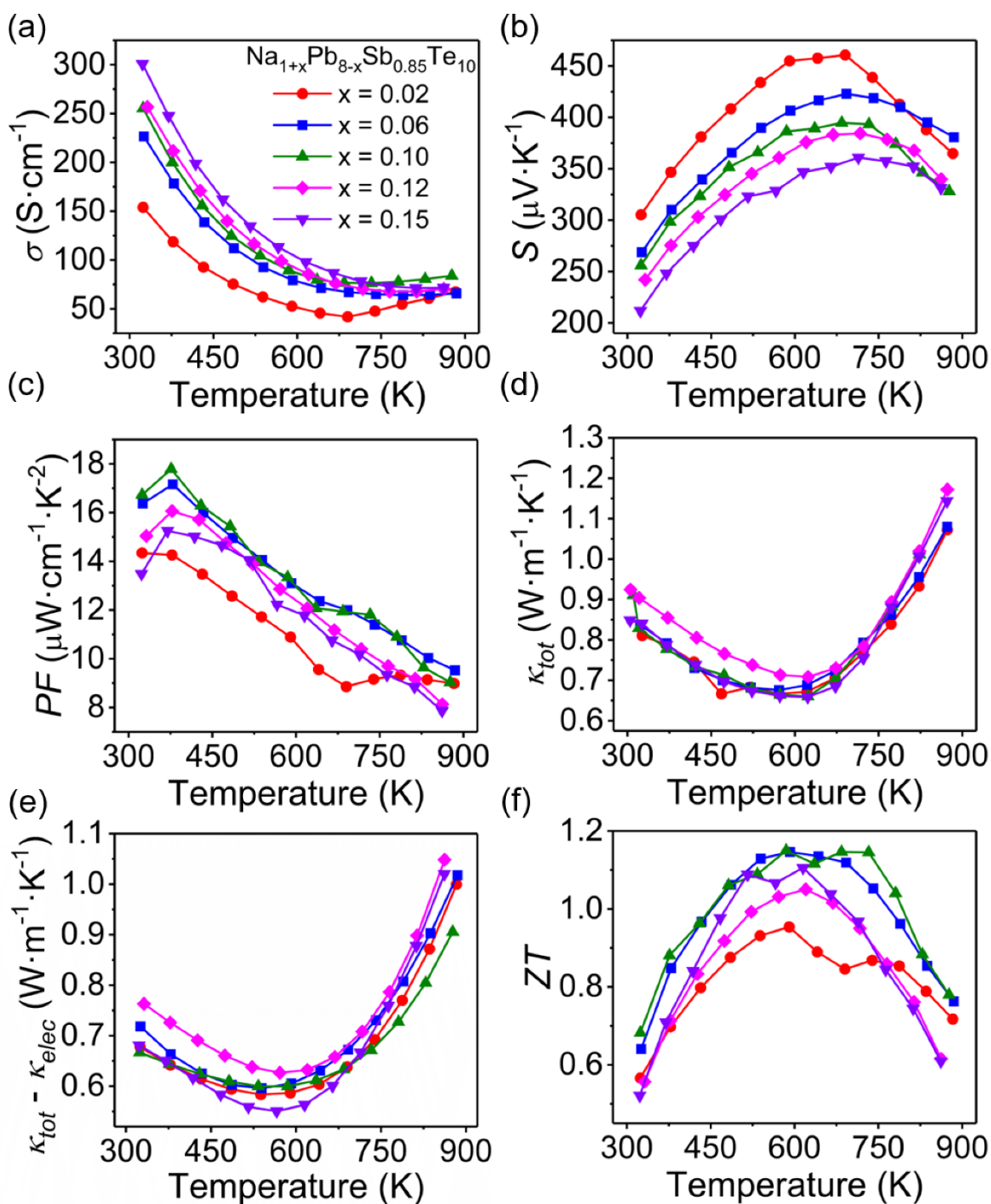


Figure 2.10 Thermoelectric properties of SPSed $\text{Na}_{1+x}\text{Pb}_{8-x}\text{Sb}_{0.85}\text{Te}_{10}$. (a) Electrical conductivities, (b) Seebeck coefficients, (c) power factors, (d) lattice thermal conductivities ($\kappa_{\text{tot}} - \kappa_{\text{elec}}$), (e) total thermal conductivities, and (f) ZT .

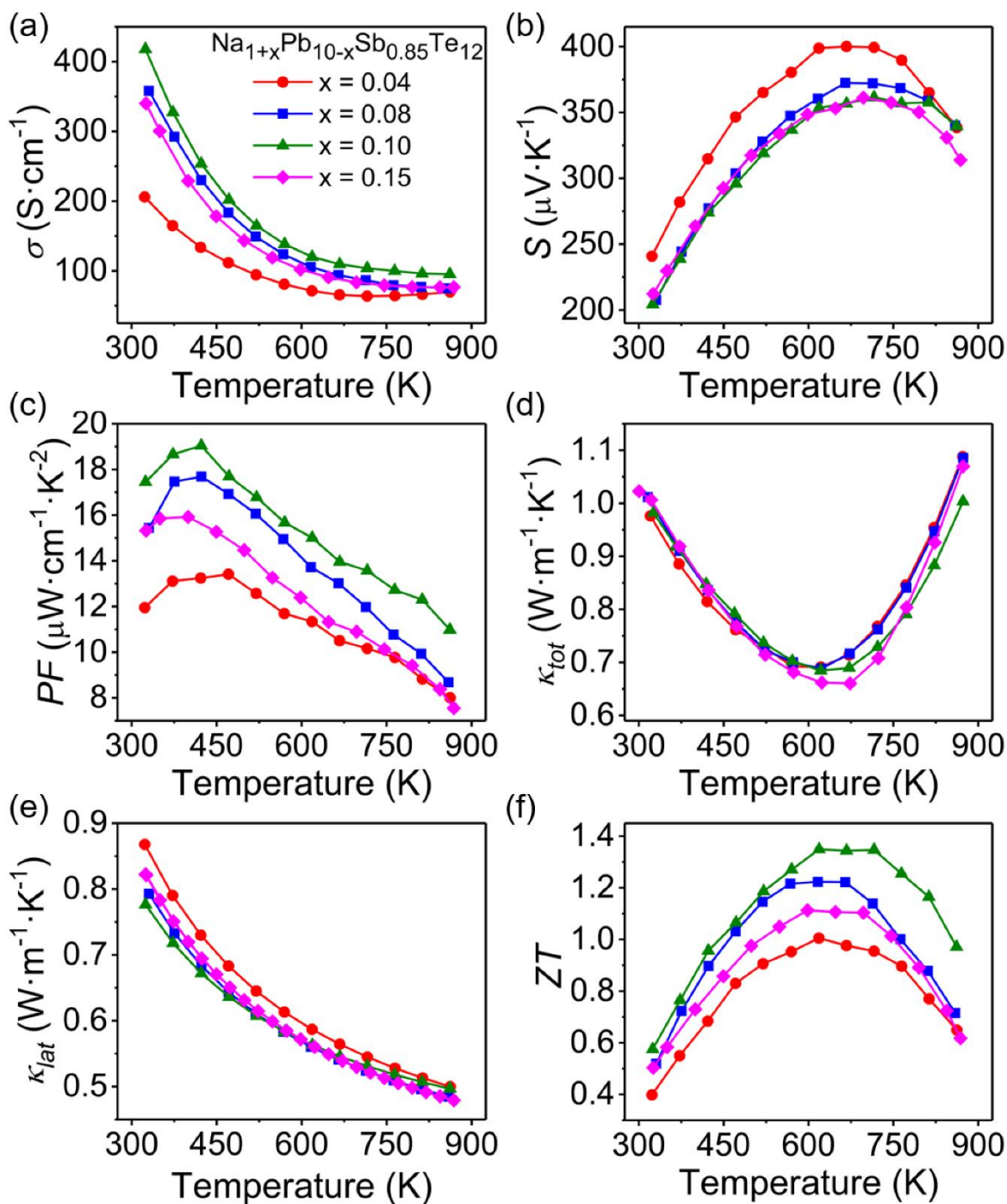


Figure 2.11 Thermoelectric properties of SPSed $\text{Na}_{1+x}\text{Pb}_{10-x}\text{Sb}_{0.85}\text{Te}_{12}$. (a) Electrical conductivities, (b) Seebeck coefficients, (c) power factors, (d) lattice thermal conductivities ($\kappa_{\text{tot}} - \kappa_{\text{elec}}$), (e) total thermal conductivities, and (f) ZT .

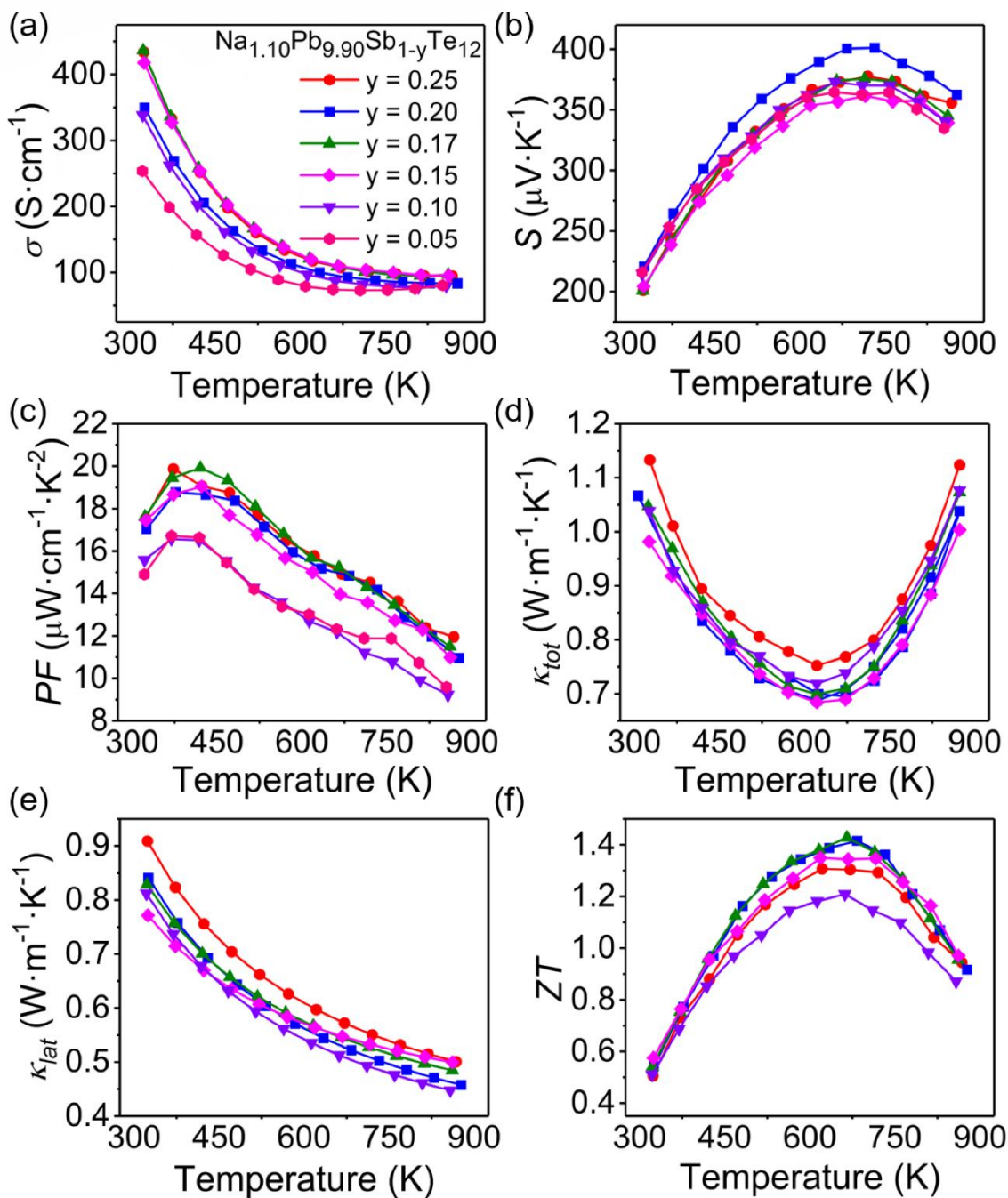


Figure 2.12 Thermoelectric properties of SPSed $\text{Na}_{1.10}\text{Pb}_{9.90}\text{Sb}_{1-y}\text{Te}_{12}$ ($y = 0.05-0.25$). (a) Electrical conductivities, (b) Seebeck coefficients, (c) power factors, (d) lattice thermal conductivities ($\kappa_{\text{tot}}-\kappa_{\text{elec}}$), (e) total thermal conductivities, and (f) ZT . The thermal conductivity of $y = 0.05$ sample was not measured due to the lower power factor.

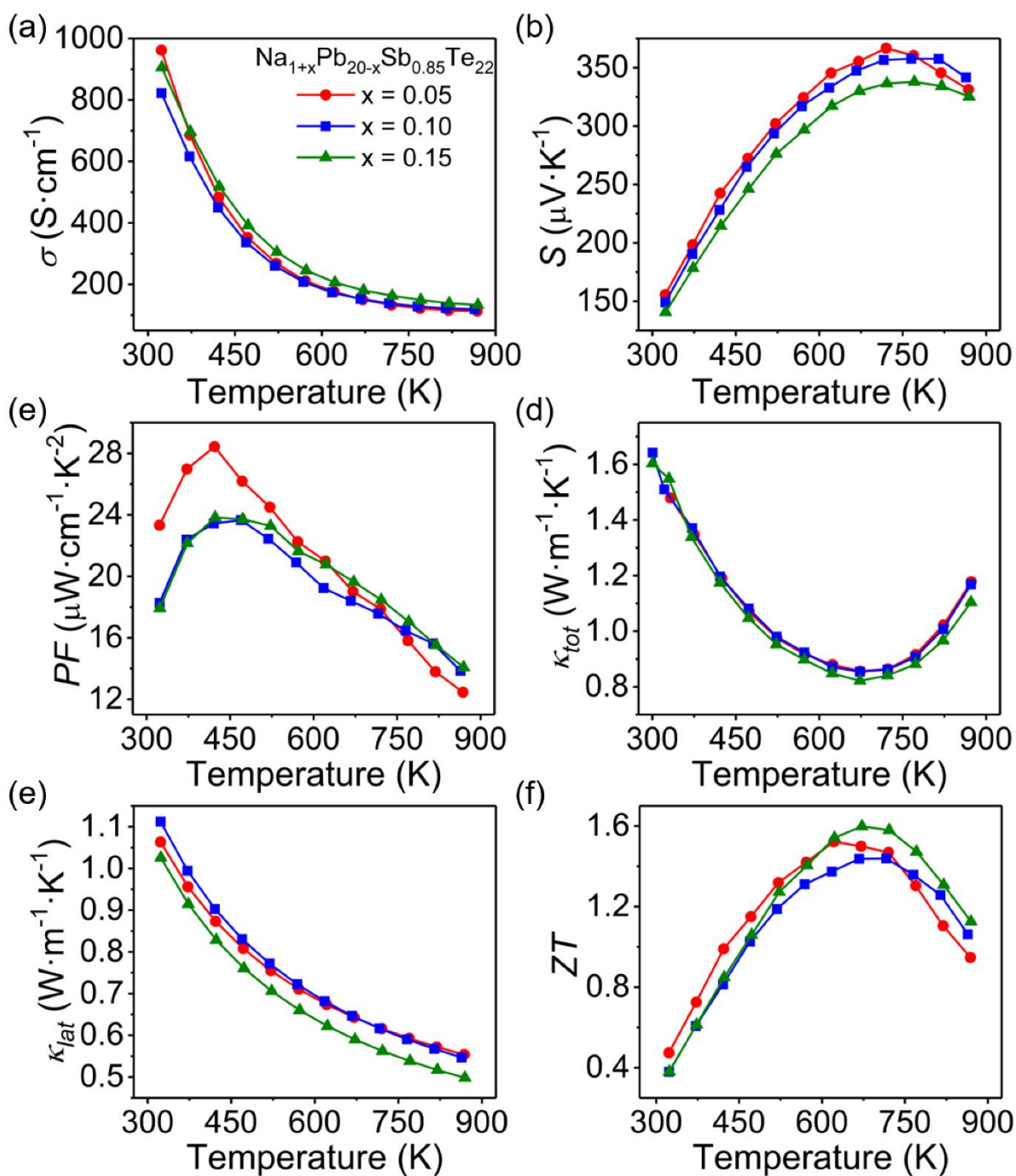


Figure 2.13 Thermoelectric properties of SPSed $\text{Na}_{1+x}\text{Pb}_{20-x}\text{Sb}_{0.85}\text{Te}_{22}$. (a) Electrical conductivities, (b) Seebeck coefficients, (c) power factors, (d) lattice thermal conductivities, (e) total thermal conductivities ($\kappa_{\text{tot}} - \kappa_{\text{elec}}$), and (f) ZT .

ray diffraction patterns for these compounds are presented in Figure 2.9 and show that despite the heavy deviations from the ideal $\text{NaPb}_m\text{SbTe}_{m+2}$ stoichiometry, the samples remain phase pure according to laboratory X-ray diffraction. The complete thermoelectric properties of each series (m) are shown below in Figures 2.10–2.13.

As m increases from 6 to 20, the electrical conductivities generally rise and the Seebeck coefficients decrease, suggesting that PbTe-rich compositions (larger m) can be more readily doped to higher hole concentrations. Indeed, the properties measured for the stoichiometric ingots (Figure 2.1d, 2.1e) show the same trend in electrical conductivities and Seebeck coefficients with changing m . Interestingly, however, the results derived from the variable temperature Hall effect measurements (Figure 2.14a) show similar hole densities of $\sim 5 \times 10^{19} \text{ cm}^{-3}$ at 300 K for each compound, indicating that the trends in electrical properties as functions of m cannot be explained on the basis of changing carrier concentration. Therefore, the decrease in the electrical conductivity and increase in the Seebeck coefficient are likely the result of larger hole effective mass (m^*) as the system becomes richer in NaSbTe_2 (lower m). This occurs because raising the fraction of NaSbTe_2 will increase the ionicity of the system, which is expected to lower the energy of the primary L valence band and yield a less dispersive band structure with increased band gap and higher effective mass.¹⁰⁰ Such a situation is supported by the calculated electronic band structures shown in Figure 2.15, which reveal a flattening of the bands, a widening band gap, and a significant increase in m^* as more NaSbTe_2 is added to the system. As depicted in Figure 2.14b, an enhanced effective mass for greater NaSbTe_2 fractions is confirmed from estimations of m^* using the measured carrier densities and Seebeck coefficients (details on the calculations in the

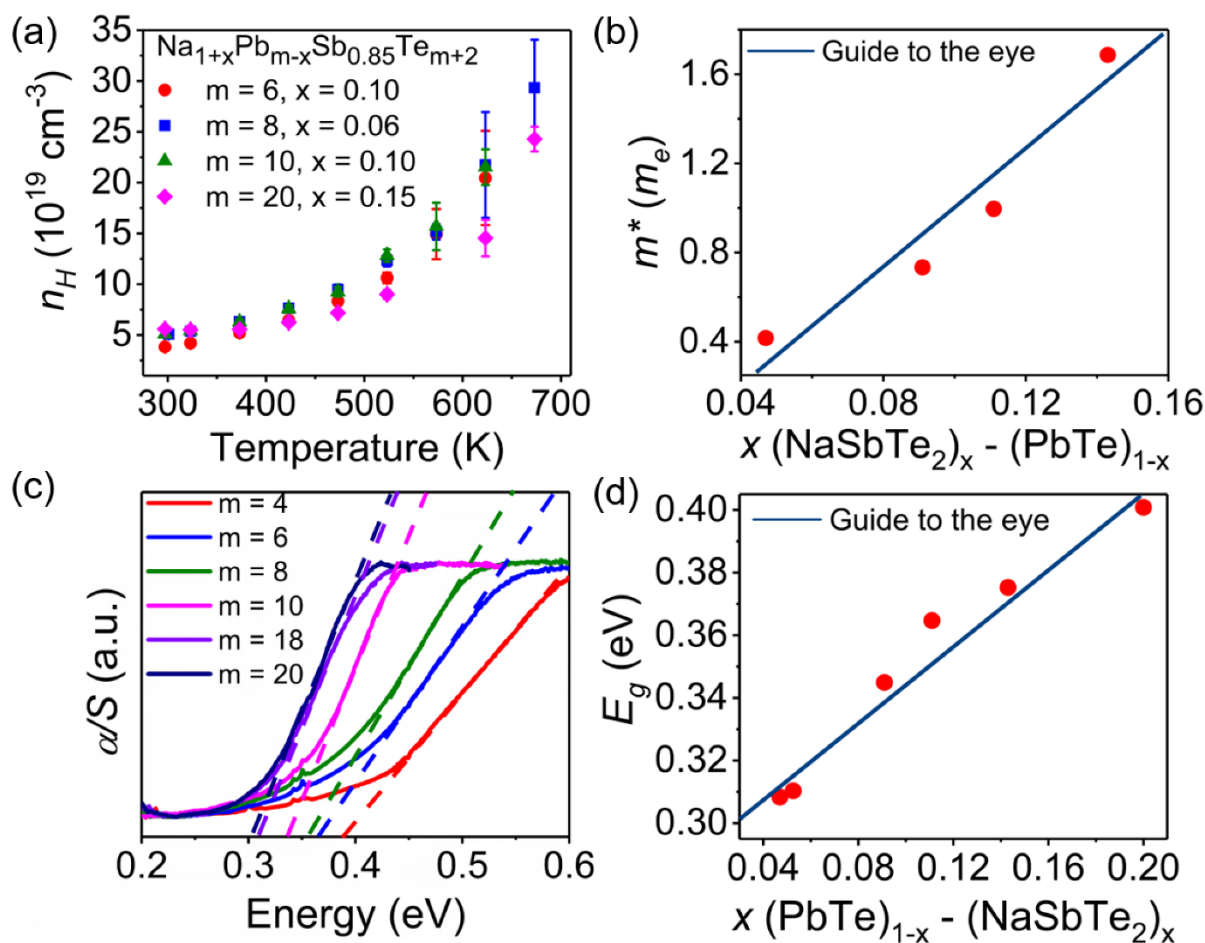


Figure 2.14 (a) Hall carrier densities for the $\text{Na}_{1+x}\text{Pb}_{m-x}\text{Sb}_{0.85}\text{Te}_{m+2}$ derived from variable temperature Hall effect measurements. (b) Room temperature effective masses estimated from the carrier densities and Seebeck coefficients. (c) Infrared absorption spectra for SPSed $\text{NaPb}_m\text{SbTe}_{m+2}$ ($m = 4-20$). Dashed lines show the tangents used to estimate the band gaps. (d) Band gaps estimated from the FTIR spectra showing an increase in E_g with increasing NaSbTe_2 fraction (larger x or smaller m).

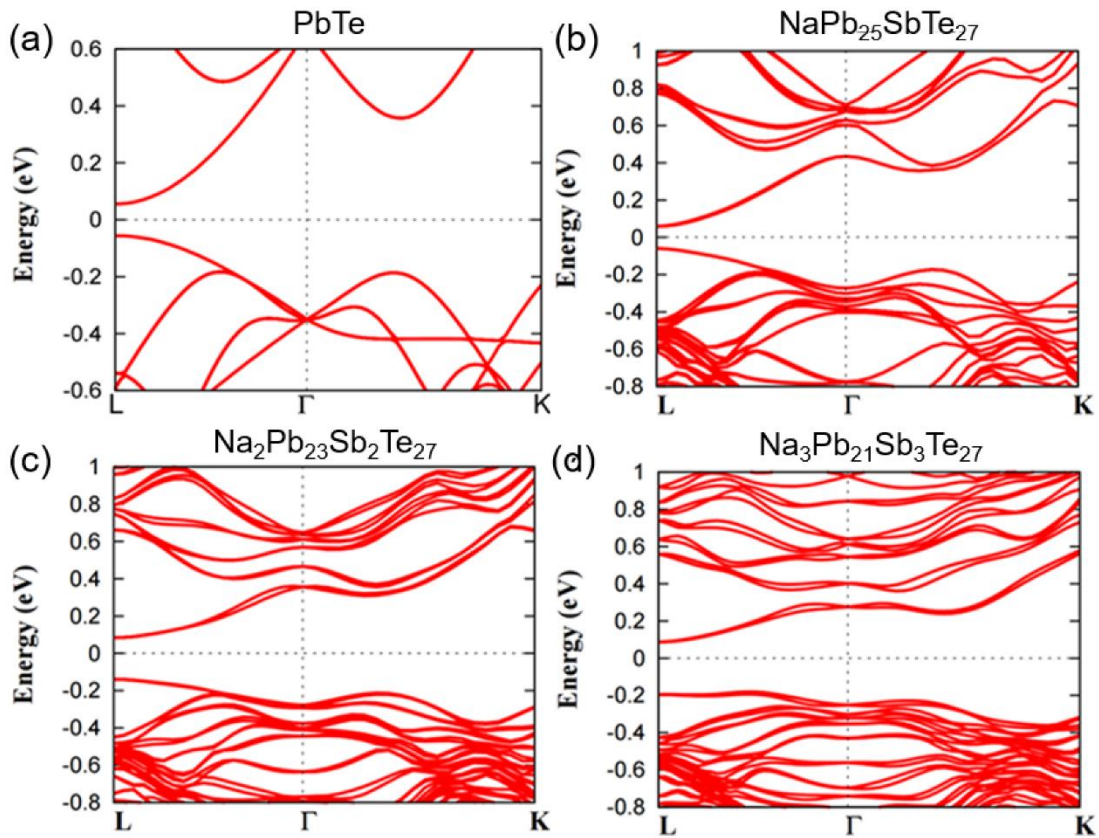


Figure 2.15 Calculated band structures for (a) $\text{Pb}_{27}\text{Te}_{27}$, (b) $\text{NaPb}_{25}\text{SbTe}_{27}$, (c) $\text{Na}_2\text{Pb}_{23}\text{Sb}_2\text{Te}_{27}$, and (d) $\text{Na}_3\text{Pb}_{21}\text{Sb}_3\text{Te}_{27}$, or equivalently $m = \infty, 25, 11.5, 7, (\sim 0, 4, 8, \text{ and } 12 \text{ percent NaSbTe}_2)$ respectively. The calculations reveal both an increase in the band gap and a significant flattening of the bands (increase in m^*) with greater NaSbTe_2 fraction.

experimental). The augmented band gap for smaller m is also verified by the infrared absorption measurements shown in Figure 2.14c and 2.14d. Confirmed by both computational work and experiment, as the NaSbTe_2 fraction increases, The effective mass is significantly raised, resulting in a large increase in the Seebeck coefficients and a decrease in the electrical conductivity due to the reduced hole mobility ($\mu \sim 1/m^*$). Inspection of all the data outlined in Figure 2.10–2.13 shows

the net effect is a shift in the maximum power factor to lower temperatures and an overall decrease in power factors for lower values of m (more NaSbTe₂-rich compositions).

As shown in Figures 2.10–2.13, both the lattice ($\kappa_{\text{tot}} - \kappa_{\text{elec}}$) and total thermal conductivities are very low, respectively ranging from 1–0.55 W·m⁻¹ K⁻¹ and 1.6–0.6 W·m⁻¹ K⁻¹ over 300–900 K. As expected from phonon scattering by point defects, the thermal conductivities decrease with a greater NaSbTe₂ fraction (smaller m). In all cases, there is a downturn in the Seebeck coefficients and an upturn in the thermal conductivities as functions of temperature beginning at 600–700 K. This is from the excitation of minority carriers across the band gap (bipolar diffusion), which adds negatively to the Seebeck coefficient while increasing the electronic component of the thermal conductivity κ_{elec} . As a consequence, the ZT s increase from 0.4–0.65 at 300 K up to the temperature at which bipolar conduction becomes significant, with peak values of 1.1–1.6 at 650 K.

To study the impact of different Sb stoichiometry on the thermoelectric properties of the doped compounds, we chose $m = 10$ as representative of the full system. Figure 2.12 shows the thermoelectric properties of Na_{1.10}Pb_{9.90}Sb _{y} Te₁₂ ($y = 0.05$ – 0.25), and we find that variations in y over the range 0.25–0.15 have relatively minor consequences on the thermoelectric properties, while the electrical conductivity quickly decreases when $y = 0.1$ and 0.05, resulting in reduced performance. For $m = 10$, the net result of changing the Sb stoichiometry is a small increase in the maximum ZT from 1.3 at 650 K for Na_{1.10}Pb_{9.90}Sb_{0.85}Te₁₂ ($y = 0.15$) to 1.4 in Na_{1.10}Pb_{9.90}Sb_{0.83}Te₁₂ ($y = 0.17$). Because of the relatively minor changes observed between these samples, the impact of different Sb stoichiometries was not explored for compounds with different m .

Compared to other state-of-the-art PbTe based thermoelectrics such as PbTe-SrTe,⁴⁹ PbTe-MgTe,⁴⁰ and PbTe-PbS,⁸¹ it is noteworthy that the ZT s found in the optimized $\text{Na}_{1+x}\text{Pb}_{m-x}\text{Sb}_{1-y}\text{Te}_{m+2}$ are unusually high at temperatures under 600 K. For example, in each of the aforementioned systems, the ZT s near room temperature are all ~ 0.2 , while the ZT s of the $\text{Na}_{1+x}\text{Pb}_{m-x}\text{Sb}_{1-y}\text{Te}_{m+2}$ compounds are up to three times higher, in the range 0.4–0.6 at 323 K. The enhancement in the lower temperature ZT s found in $\text{Na}_{1+x}\text{Pb}_{m-x}\text{Sb}_{1-y}\text{Te}_{m+2}$ derives from two primary factors: the low carrier densities and the extremely small lattice thermal conductivities. It is well known that the optimal charge carrier concentration needed for maximizing ZT is itself dependent on the temperature, with smaller carrier densities necessary to achieve the highest ZT s at lower temperatures.¹⁰¹⁻¹⁰² Here, the relatively low carrier densities of $\sim 5 \times 10^{19} \text{ cm}^{-3}$ push the maximum power factors to lower temperature as observed in Figures 2.10–2.13c while also limiting the impact of the electronic contribution to the total thermal conductivity. These factors both improve the low temperature ZT s found in $\text{Na}_{1+x}\text{Pb}_{m-x}\text{Sb}_{1-y}\text{Te}_{m+2}$.

Moreover, the lattice thermal conductivities measured for $\text{Na}_{1+x}\text{Pb}_{m-x}\text{Sb}_{1-y}\text{Te}_{m+2}$ are extremely low across the full temperature regime. As shown in Figure 2.10–2.13d, and 2.10–2.13e, depending on the value of m , the κ_{lat} (shown as $\kappa_{tot} - \kappa_{elec}$) for the best performing $\text{Na}_{1+x}\text{Pb}_{m-x}\text{Sb}_{1-y}\text{Te}_{m+2}$ samples are in the range 0.7–1 $\text{W} \cdot \text{m}^{-1} \text{K}^{-1}$ at 323 K and fall with increasing temperature until the onset of bipolar diffusion at ~ 600 – 700 K. Estimated values of κ_{lat} across the full temperature range are shown in Figures 2.10e–2.13e, and suggest the lattice thermal conductivities continue to fall with temperature reaching minimum values $\sim 0.5 \text{ W} \cdot \text{m}^{-1} \text{K}^{-1}$ at 873 K. Crucially, the low temperature values of κ_{lat} are very small compared to other PbTe based alloys. For example, at 300 K, the κ_{lat} of nanostructured PbTe–SrTe and PbTe–MgTe are each $\sim 1.7 \text{ W} \cdot \text{m}^{-1} \text{K}^{-1}$

¹, and that of nanostructured PbTe–PbS is $\sim 1.1 \text{ W}\cdot\text{m}^{-1} \text{ K}^{-1}$. Clearly, the low temperature values of κ_{lat} found in $\text{Na}_{1+x}\text{Pb}_{m-x}\text{Sb}_{1-y}\text{Te}_{m+2}$ are much smaller and provide a significant boost to the low temperature ZT s.

2.2.6 High average ZT in optimized $\text{NaPb}_m\text{SbTe}_{m+2}$

When considering the potential performance of a thermoelectric material, the figure of merit ZT gives only the efficiency at a given temperature. Because thermoelectric modules operate across a temperature gradient, high maximum ZT alone is insufficient to achieve good performance.⁷⁷ Instead, materials with high ZT_{avg} over the temperature range of interest are desired, as can be seen from the equation describing the overall thermoelectric efficiency η :¹⁰³

$$\eta = \left(\frac{T_H - T_C}{T_H} \right) \cdot \frac{\sqrt{1 + ZT_{\text{avg}}} - 1}{\sqrt{1 + ZT_{\text{avg}}} + (T_C/T_H)} \quad (2.1)$$

where T_H and T_C are, respectively, the hot and cold side temperatures of the module. As noted previously, the ZT s of $\text{Na}_{1+x}\text{Pb}_{m-x}\text{Sb}_{1-y}\text{Te}_{m+2}$ are unusually high near room temperature compared to other state-of-the-art PbTe based materials, and this results in improved ZT_{avg} over intermediate temperatures when $m = 10, 20$. In fact, the materials developed here have figures of merit equal to or above 1 over a broad range of temperatures (450–900 K). Figure 2.16a illustrates this by comparing the ZT s of $\text{Na}_{1.10}\text{Pb}_{9.90}\text{Sb}_{0.83}\text{Te}_{12}$ and $\text{Na}_{1.15}\text{Pb}_{19.85}\text{Sb}_{0.85}\text{Te}_{22}$ with the state-of-the-art low and medium temperature polycrystalline thermoelectrics $\text{Bi}_{0.4}\text{Sb}_{1.6}\text{Te}_3$ ¹⁰⁴ and PbTe-8\%SrTe ,⁴⁹ respectively. Clearly, PbTe-8\%SrTe and $\text{Bi}_{0.4}\text{Sb}_{1.6}\text{Te}_3$ have the highest maximum ZT s but not the highest ZT_{avg} . Most importantly, the $\text{Na}_{1+x}\text{Pb}_{m-x}\text{Sb}_{1-y}\text{Te}_{m+2}$ materials have a competitive ZT_{avg} across a wide range of temperatures as illustrated in Figure 2.16b. In the lower temperature range 323 K–523 K, $\text{Na}_{1+x}\text{Pb}_{m-x}\text{Sb}_{0.85}\text{Te}_{m+2}$ have much lower ZT_{avg} than $\text{Bi}_{0.4}\text{Sb}_{1.6}\text{Te}_3$ but significantly

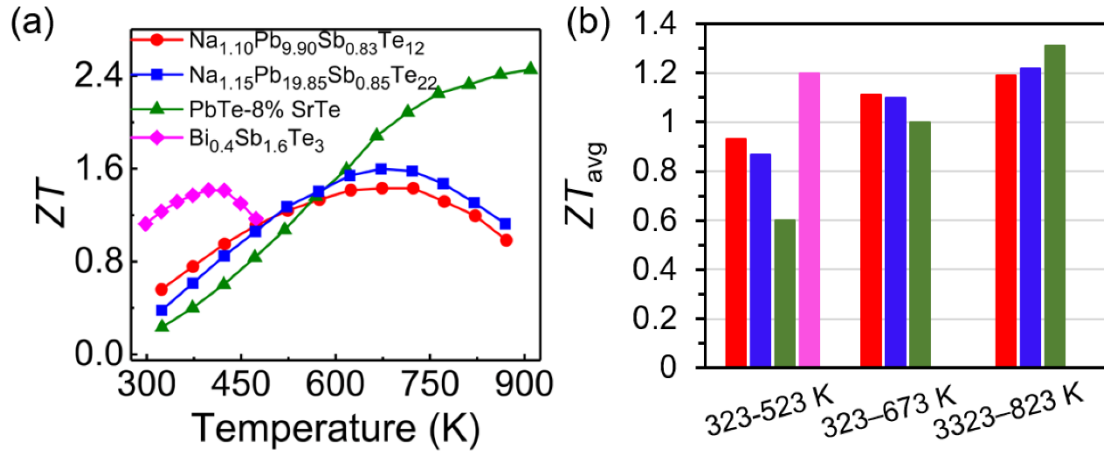


Figure 2.16 (a) Comparison of ZT s for high performing SPSed $\text{Na}_{1+x}\text{Pb}_{m-x}\text{Sb}_{1-y}\text{Te}_{m+2}$ compositions developed in this work with the state-of-the-art low and high temperature thermoelectrics $\text{Bi}_{0.4}\text{Sb}_{1.6}\text{Te}_3$ ¹⁰⁴ and PbTe-8\%SrTe ,⁴⁹ respectively. (b) The average ZT for materials shown in (a) over temperature ranges 323–523, 323–673, and 323–823 K.

outperform PbTe-8\%SrTe . Over the intermediate temperature interval 323 K–673 K, both $\text{Na}_{1+x}\text{Pb}_{m-x}\text{Sb}_{0.85}\text{Te}_{m+2}$ materials have the highest ZT_{avg} , making these materials among the best performing PbTe -based systems for temperatures under 650 K. The high ZT_{avg} values found in $\text{Na}_{1+x}\text{Pb}_{m-x}\text{Sb}_{1-y}\text{Te}_{m+2}$ ($m = 10\text{--}20$) are comparable to the recently developed n-type polycrystalline $\text{Mg}_3\text{Sb}_{1.5-0.5x}\text{Bi}_{0.5-0.5x}\text{Te}_x$.⁵⁶ In addition, although doped single-crystalline SnSe is superior in terms of both average and maximum ZT ,⁸³⁻⁸⁴ the challenge of preparing and cleaving single crystals of the brittle materials makes the polycrystalline SPSed $\text{Na}_{1+x}\text{Pb}_{m-x}\text{Sb}_{0.85}\text{Te}_{m+2}$ potentially more attractive despite its lower performance, particularly for emerging applications at low and intermediate temperatures under 700 K.

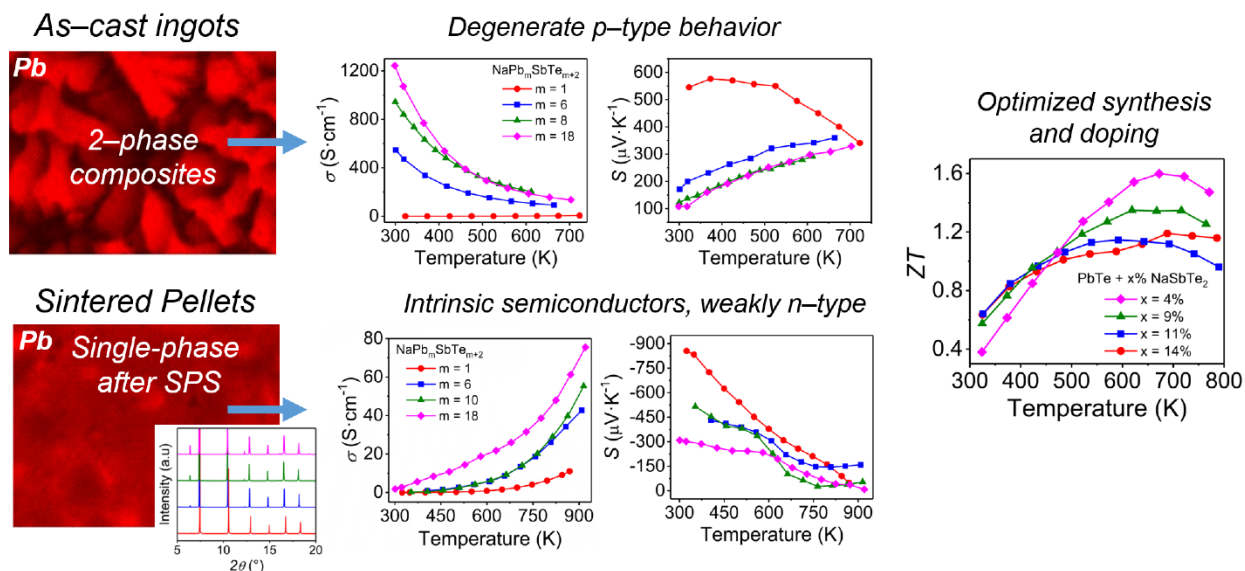


Figure 2.17 Summary of the work on $\text{NaPb}_m\text{SbTe}_{m+2}$ compounds. The as-cast ingots are inhomogeneous and behave as p-type semiconductors. Spark plasma sintering results in dissolution of the secondary phases to form more homogeneous solid solutions, which exhibit nearly intrinsic n-type behavior. Optimizing the cation stoichiometry in SPSed $\text{NaPb}_m\text{SbTe}_{m+2}$ results in p-type compounds with excellent average ZT of 1.1 over 323–673 K.

2.3 Summary and Conclusions

The thermoelectric properties of the $\text{NaPb}_m\text{SbTe}_{m+2}$ system were studied across a wide range of compositions $m = 1$ –20 and the overall findings are presented in Figure 2.17. It was found that the as-cast ingots behave as degenerate semiconductors with moderately high ZT s in the range 1.2–1.4 at 700 K when $m = 6$ –18. The ingots were extremely brittle and phase separated, while spark plasma sintering (SPS) can produce single phase pellets with increased mechanical toughness. Surprisingly, in $\text{NaPb}_m\text{SbTe}_{m+2}$, SPS processing results in a transition from the degenerate p-type behavior to weakly n-type transport as a result of the dissolution of the

secondary phases present in the ingot into the primary matrix. The thermoelectric properties of the SPSed materials can be optimized by adjusting the stoichiometry of the Na and Sb for $m = 6$ – 20 , and Na-rich and Sb-deficient compounds retain their p-type transport after the SPS process. Surprisingly, TEM results show that the SPSed compounds remain single phase at the nanoscale, in sharp contrast to the similar $\text{AgPb}_m\text{SbTe}_{m+2}$ and $\text{AgPb}_m\text{SbSe}_{m+2}$ systems which are heavily nanostructured. Even without nanostructures, the optimized $\text{Na}_{1+x}\text{Pb}_{m-x}\text{Sb}_{1-y}\text{Te}_{m+2}$ ($m = 10, 20$) exhibit very low lattice thermal conductivities of 1.1 – $0.55 \text{ W}\cdot\text{m}^{-1} \text{ K}^{-1}$ over 300 – 650 K , yielding enhanced low–medium temperature performance with ZT s up to 1.6 at 673 K . Most notably, when $m = 10$ – 20 , $\text{Na}_{1+x}\text{Pb}_{m-x}\text{Sb}_{1-y}\text{Te}_{m+2}$ have excellent ZT_{avg} of 1.1 over 323 – 673 K and are among the best performing PbTe-based thermoelectric materials at temperatures under 650 K .

2.4 Experimental Section

2.4.1 Synthesis and processing

Polycrystalline ingots with nominal compositions of $\text{Na}_{1+x}\text{Pb}_{m-x}\text{Sb}_{1-y}\text{Te}_{m+2}$ ($m = 0.25$ – 20 , $x = 0$ – 0.15 , $y = 0$ – 0.25) were synthesized by weighing stoichiometric quantities of each element into 13 mm diameter carbon coated fused silica tubes, which were then flame sealed at $\sim 2 \times 10^{-3} \text{ Torr}$. The tubes were heated in a box furnace to 1273 K over 14 h and held at this temperature for 6 h . During this time the tubes were periodically shaken to ensure good mixing and homogeneity in the melt. After 6 h , the tubes were quenched in ice water, and the polycrystalline ingots were removed and ground into powders in an N_2 -filled glovebox. The powders were sieved ($53 \mu\text{m}$),

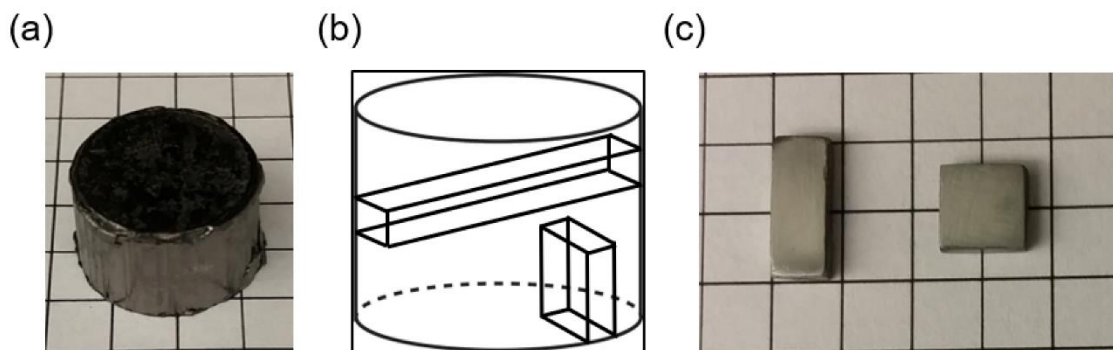


Figure 2.18 (a) A typical pellet of $\text{NaPb}_m\text{SbTe}_{m+2}$ after SPS sintering. (b) Schematic showing how the samples were cut from the SPS pellet for thermoelectric characterization. (c) Final samples for ZEM-3 (left) and LFA-457 (right).

loaded into 12.7 mm graphite dies, and sintered by SPS (SPS-211LX, Fuji Electronic Industrial Co. Ltd) at 823 K and 40 MPa for 10 min into pellets, which were then re-sealed in 18 mm diameter tubes at $\sim 2 \times 10^{-3}$ Torr and annealed at 673 K for 24 h to achieve improved thermal stability (discussed in below in Figure 2.19). The pellets were lastly cut and polished into $3 \times 3 \times 10 \text{ mm}^3$ bars and $6 \times 6 \times 2 \text{ mm}^3$ squares for thermoelectric characterization. The cuts were made such that transport measurements were done perpendicular to the pressing direction in the SPS (images shown in Figure 2.18), although minimal differences were observed between measurement directions.

The thermoelectric properties of polycrystalline ingots were also studied, bypassing the SPS step. However, water quenching from the melt resulted in samples too brittle to be cut and polished as described above. To help avoid this, the tubes were instead heated to 1273 K in a rocking furnace where they were held for 2 h. Afterwards, the rocking furnace was turned on to provide continuous mixing for an additional 2 h. The furnace was then fixed in an upright position

and cooled to 820 K over 44 h and finally turned off to allow the tubes to naturally cool to room temperature. Significantly lower electrical conductivities were observed when the rocking furnace was not utilized, indicating the importance of homogeneity in the melt in the case of the ingots. Using this technique, the resulting polycrystalline ingots were considerably less brittle than those prepared from quenching; however, great care was still needed in subsequent handling. Lastly, the ingots were carefully cut and polished into $3 \times 3 \times 10 \text{ mm}^3$ bars and $6 \times 6 \times 2 \text{ mm}^3$ squares for property measurements, as described above.

2.4.2 Electrical properties

Using the $3 \times 3 \times 10 \text{ mm}^3$ bars, the Seebeck coefficients and electrical conductivities were measured jointly between room temperature and 873 K using an Ulvac Riko ZEM-3 instrument operating under partial He backpressure. To prevent outgassing at elevated temperatures, the bars were spray-coated with boron nitride prior to measurements except at locations needed for contacts with the electrodes and thermocouples. The uncertainty in the electrical measurements is approximately 5%, which is well accepted for ZEM-3 instruments.¹⁰⁵ As shown in Figure 2.19, all samples showed hysteresis between the initial heating and cooling profile. The properties stabilized upon cooling and were reversible upon further heating/cooling cycles. Therefore, all properties reported in this work come from the cooling profile.

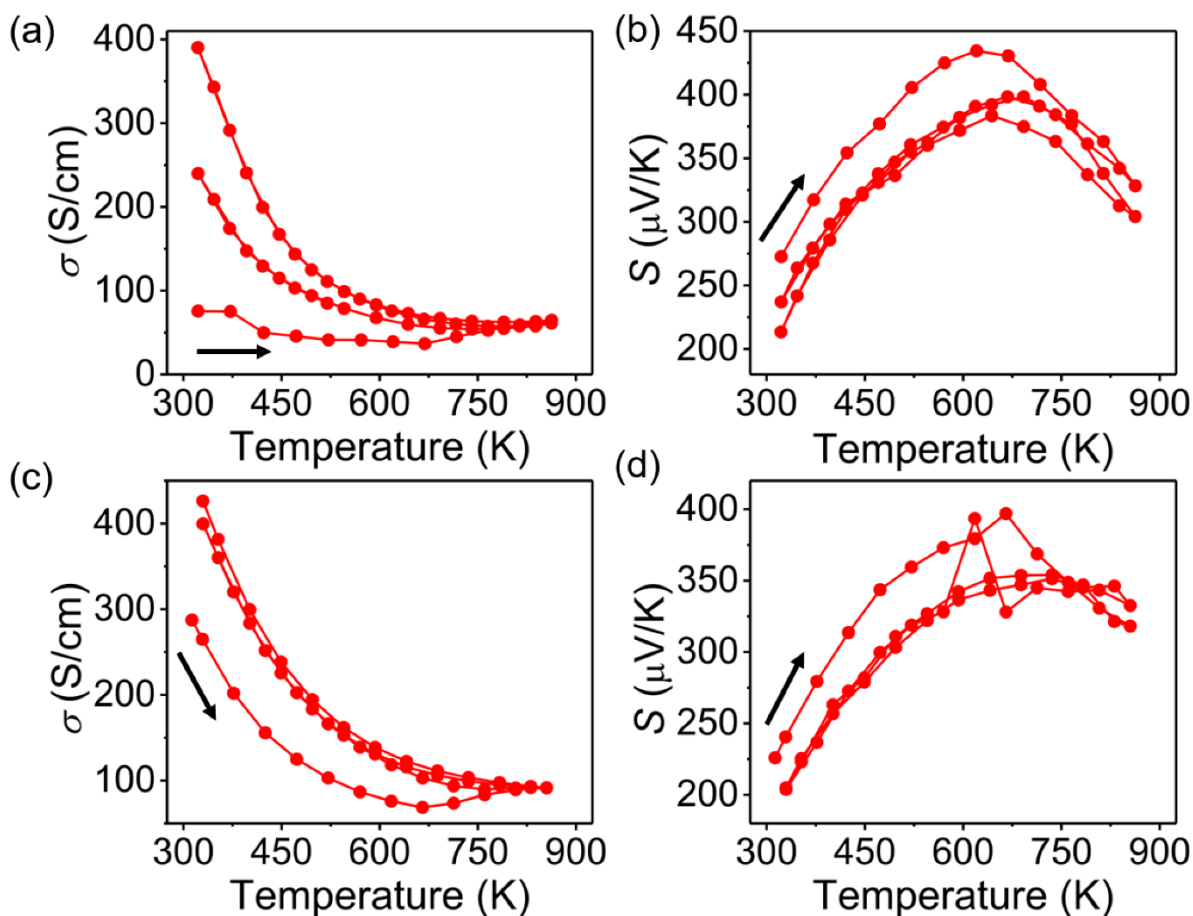


Figure 2.19 Comparison of the electrical conductivity and Seebeck coefficient for $\text{Na}_{1.10}\text{Pb}_{9.90}\text{Sb}_{0.85}\text{Te}_{12}$ with no annealing (a, b) and after annealing the SPS pellet prior to measurements for 24 h at 673 K (c, d). In each case, 3 heating/cooling cycles between 300–900 K were conducted with a 50 K step size. Large hysteresis is observed without annealing; however, after annealing, the thermoelectric properties show significantly improved thermal stability and little to no changes are observed after the initial heating profile. Black arrows denote the beginning of the first heating cycle.

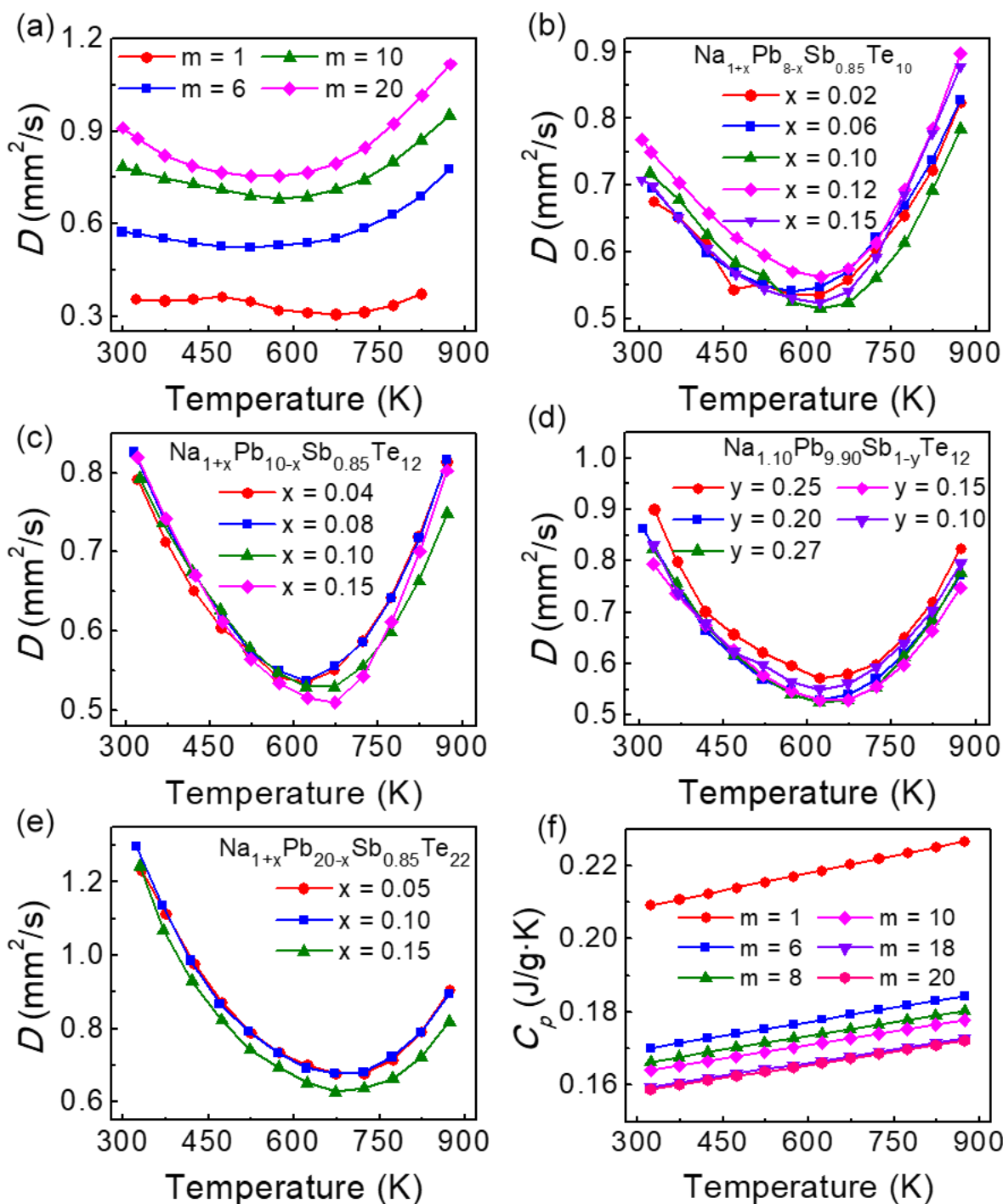


Figure 2.20 Measured thermal diffusivities for (a) $\text{NaPb}_m\text{SbTe}_{m+2}$ ($m = 1-20$), (b) $\text{Na}_{1+x}\text{Pb}_{8-x}\text{Sb}_{0.85}\text{Te}_{10}$, (c) $\text{Na}_{1+x}\text{Pb}_{10-x}\text{Sb}_{0.85}\text{Te}_{12}$, (d) $\text{Na}_{1.10}\text{Pb}_{9.90}\text{Sb}_{1-y}\text{Te}_{12}$, and (e) $\text{Na}_{1+x}\text{Pb}_{20-x}\text{Sb}_{0.85}\text{Te}_{22}$. (f) Calculated values for C_p . All samples shown above were sintered by SPS.

Table 2.4 Measured densities and corresponding fractions of the theoretical densities for the SPSed $\text{NaPb}_m\text{SbTe}_{m+2}$ and doped $\text{Na}_{1+x}\text{Pb}_{m-x}\text{Sb}_{1-y}\text{Te}_{m+2}$ (nominal compositions of $m = 6\text{--}20$, $x = 0.02\text{--}0.15$, $y = 0.10\text{--}0.25$, all SPS processed). Theoretical densities were obtained from the Rietveld refinements of the PXRD data.

Compound	Density (g/cm ³)	% Theoretical
NaPbSbTe_3	5.963	95
$\text{NaPb}_6\text{SbTe}_8$	7.148	93
$\text{NaPb}_{10}\text{SbTe}_{12}$	7.354	95
$\text{NaPb}_{18}\text{SbTe}_{20}$	7.478	94
$\text{Na}_{1.10}\text{Pb}_{5.90}\text{Sb}_{0.85}\text{Te}_8$	7.111	96
$\text{Na}_{1.02}\text{Pb}_{7.98}\text{Sb}_{0.85}\text{Te}_{10}$	7.273	95
$\text{Na}_{1.06}\text{Pb}_{7.94}\text{Sb}_{0.85}\text{Te}_{10}$	7.217	95
$\text{Na}_{1.10}\text{Pb}_{7.90}\text{Sb}_{0.85}\text{Te}_{10}$	7.246	96
$\text{Na}_{1.12}\text{Pb}_{7.88}\text{Sb}_{0.85}\text{Te}_{10}$	7.211	95
$\text{Na}_{1.15}\text{Pb}_{7.85}\text{Sb}_{0.85}\text{Te}_{10}$	7.189	95
$\text{Na}_{1.04}\text{Pb}_{9.96}\text{Sb}_{0.85}\text{Te}_{12}$	7.491	97
$\text{Na}_{1.08}\text{Pb}_{9.92}\text{Sb}_{0.85}\text{Te}_{12}$	7.448	97
$\text{Na}_{1.10}\text{Pb}_{9.90}\text{Sb}_{0.85}\text{Te}_{12}$	7.519	98
$\text{Na}_{1.15}\text{Pb}_{9.85}\text{Sb}_{0.85}\text{Te}_{12}$	7.466	97
$\text{Na}_{1.10}\text{Pb}_{9.90}\text{Sb}_{0.75}\text{Te}_{12}$	7.649	99
$\text{Na}_{1.10}\text{Pb}_{9.90}\text{Sb}_{0.80}\text{Te}_{12}$	7.540	98
$\text{Na}_{1.10}\text{Pb}_{9.90}\text{Sb}_{0.83}\text{Te}_{12}$	7.739	99
$\text{Na}_{1.10}\text{Pb}_{9.90}\text{Sb}_{0.90}\text{Te}_{12}$	7.587	99
$\text{Na}_{1.05}\text{Pb}_{19.95}\text{Sb}_{0.85}\text{Te}_{22}$	7.516	95
$\text{Na}_{1.10}\text{Pb}_{19.90}\text{Sb}_{0.85}\text{Te}_{22}$	7.545	95
$\text{Na}_{1.15}\text{Pb}_{19.85}\text{Sb}_{0.85}\text{Te}_{22}$	7.808	98

2.4.3 Total thermal conductivities

The thermal diffusivities (D) were measured by the laser flash method with the $6 \times 6 \times 2 \text{ mm}^3$ squares in a Netzsch LFA-457 instrument, and the data was analyzed using a Cowen model with pulse correction. Prior to measurement, the squares were spray coated with graphite to prevent errors from sample emissivity. The total thermal conductivities were obtained from the relation

$\kappa_{tot} = DC_p d$, where C_p is the constant pressure heat capacity and d is the density. The densities were calculated using the sample masses and geometries, and C_p was estimated from the relationship C_p/k_b (*per atom*) = $3.07 + 4.7 \times 10^{-4}(T - 300)$,^{49, 90} which was obtained by fitting experimental data for the lead chalcogenides by Blachnik.¹⁰⁶ This relationship was used to provide a comparison between the large range of compositions studied in the work and has an uncertainty of $\sim 2\%$ across the measured temperature range. To ensure consistency with the electrical properties, all thermal data reported in this work was also taken from the cooling profile. The uncertainty in the total thermal conductivity arising from the measurements and calculations of the density, heat capacity, and diffusivity is estimated to be within 8%.¹⁰⁵

2.4.4 Lattice thermal conductivity

The lattice thermal conductivities κ_{lat} were obtained by subtracting the electronic and bipolar contributions κ_{elec} and κ_{bip} from the total thermal conductivity as follows: $\kappa_{lat} = \kappa_{tot} - \kappa_{elec} - \kappa_{bip}$. The electronic contribution to the thermal conductivity was estimated from the Wiedemann–Franz law $\kappa_{elec} = \sigma LT$, where σ is the electrical conductivity and L is the Lorenz number. Details on calculating the Lorenz number are described below. Subtracting κ_{elec} from κ_{tot} gives the sum of the lattice and bipolar contributions. To separate these terms and estimate the high temperature κ_{lat} , $\kappa_{lat} + \kappa_{bip}$ was plotted against $1000/T$. Utilizing the T^{-1} dependence of κ_{lat} , the linear portion of the curve is easily identified and used to extract the lattice thermal conductivity.¹⁰⁷⁻¹⁰⁸

2.4.5 Calculation of the Lorenz number

The temperature dependence of L was obtained by fitting the reduced chemical potential η to the measured Seebeck coefficients as shown below:^{26, 109}

$$S = \frac{k}{e} \left(\frac{2F_1(\eta)}{F_0(\eta)} - \eta \right) \quad (2.2)$$

where $F_j(\eta)$ are the Fermi-Dirac integrals defined as follows:¹¹⁰

$$F_j(\eta) = \int_0^\infty \frac{\varepsilon^j d\varepsilon}{1+e^{(\varepsilon-\eta)}} \quad (2.3)$$

and ε is the reduced carrier energy. The values of η that fit the temperature-dependent Seebeck coefficients were then used to calculate L through

$$L = \left(\frac{k}{e} \right)^2 \left(\frac{3F_0(\eta)F_2(\eta) - 4F_1(\eta)^2}{F_0(\eta)^2} \right) \quad (2.4)$$

This fitting process assumes a single parabolic band dominated by acoustic phonon scattering and an energy-independent scattering time. Calculated values of L are shown in Figure 2.21 and the corresponding electronic thermal conductivities in Figure 2.23.

2.4.6 Calculation of effective masses

The room temperature band effective masses m_b^* were estimated from the measured Hall carrier densities using the following relationship for a single parabolic band:¹¹¹

$$n = \frac{\sqrt{2}(m_{DOS}^* k_B T)^{3/2}}{\pi^2 \hbar^3} F_{1/2}(\eta) \quad (2.5)$$

Where n is the carrier density, m_{DOS}^* is the density of states effective mass, \hbar is the reduced Plank constant, and $F_{1/2}$ is the Fermi-Dirac integral defined previously for $j = 1/2$. The reduced chemical potentials η were determined from the temperature-dependent Seebeck coefficients using

equations 1 and 2 as discussed previously. The band effective masses were then determined using the relationship with the density of states mass:⁴⁶

$$m_{DOS}^* = N_v^{2/3} m_b^* \quad (1.6)$$

where N_v is the valley degeneracy, assumed to be 4 for all calculations (transport only in the L valence band).

2.4.7 Powder X-ray diffraction

Laboratory powder X-ray diffraction (PXRD) was done using a Rigaku Miniflex 600 instrument operating with Cu $K\alpha$ radiation ($\lambda = 1.5406 \text{ \AA}$) at 40 kV and 15 mA and with a $K\beta$ filter. Lattice parameters were refined using the Rietveld method in GSAS-II software. Synchrotron X-ray diffraction was performed at the Advanced Photon Source 11-BM at Argonne National Laboratory. The synchrotron wavelength was $\lambda = 0.412642 \text{ \AA}$.

2.4.8 Infrared spectroscopy

To determine the optical band gaps, room temperature diffuse reflectance measurements were made on finely ground powders of the SPSed $\text{NaPb}_m\text{SbTe}_{m+2}$ using a Nicolet 6700 FT-IR spectrometer. To estimate the band gap, the reflectance data was converted to absorption with the Kubelka–Munk equation $\alpha/S = (1-R)^2/2R$ where R is the reflectance, and α and S are the absorption and scattering coefficients, respectively.

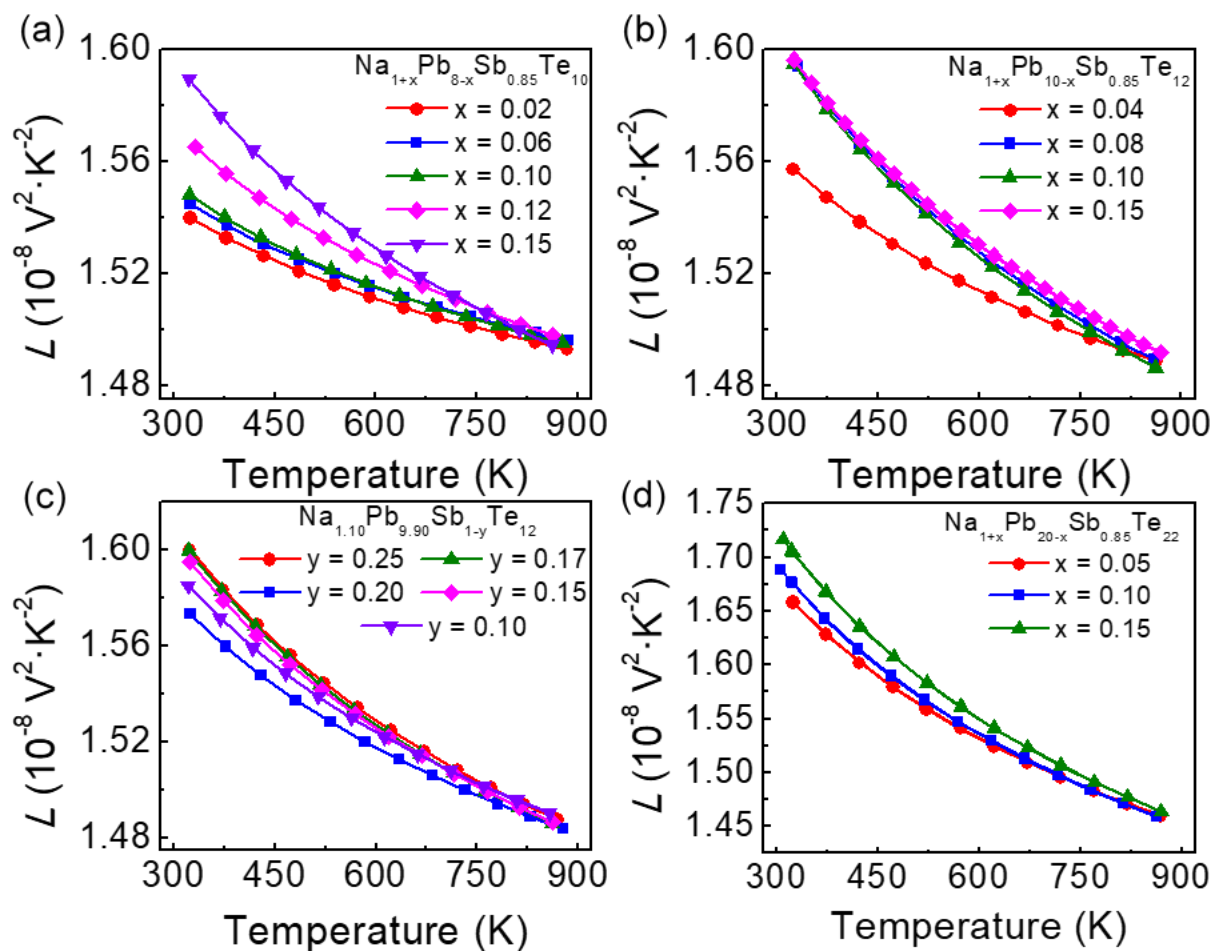


Figure 2.21 Calculated temperature-dependent Lorenz numbers for (a) $\text{Na}_{1+x}\text{Pb}_{8-x}\text{Sb}_{0.85}\text{Te}_{10}$, (b) $\text{Na}_{1+x}\text{Pb}_{10-x}\text{Sb}_{0.85}\text{Te}_{12}$, (c) $\text{Na}_{1.10}\text{Pb}_{9.90}\text{Sb}_{1-y}\text{Te}_{12}$, and (e) $\text{Na}_{1+x}\text{Pb}_{20-x}\text{Sb}_{0.85}\text{Te}_{22}$.

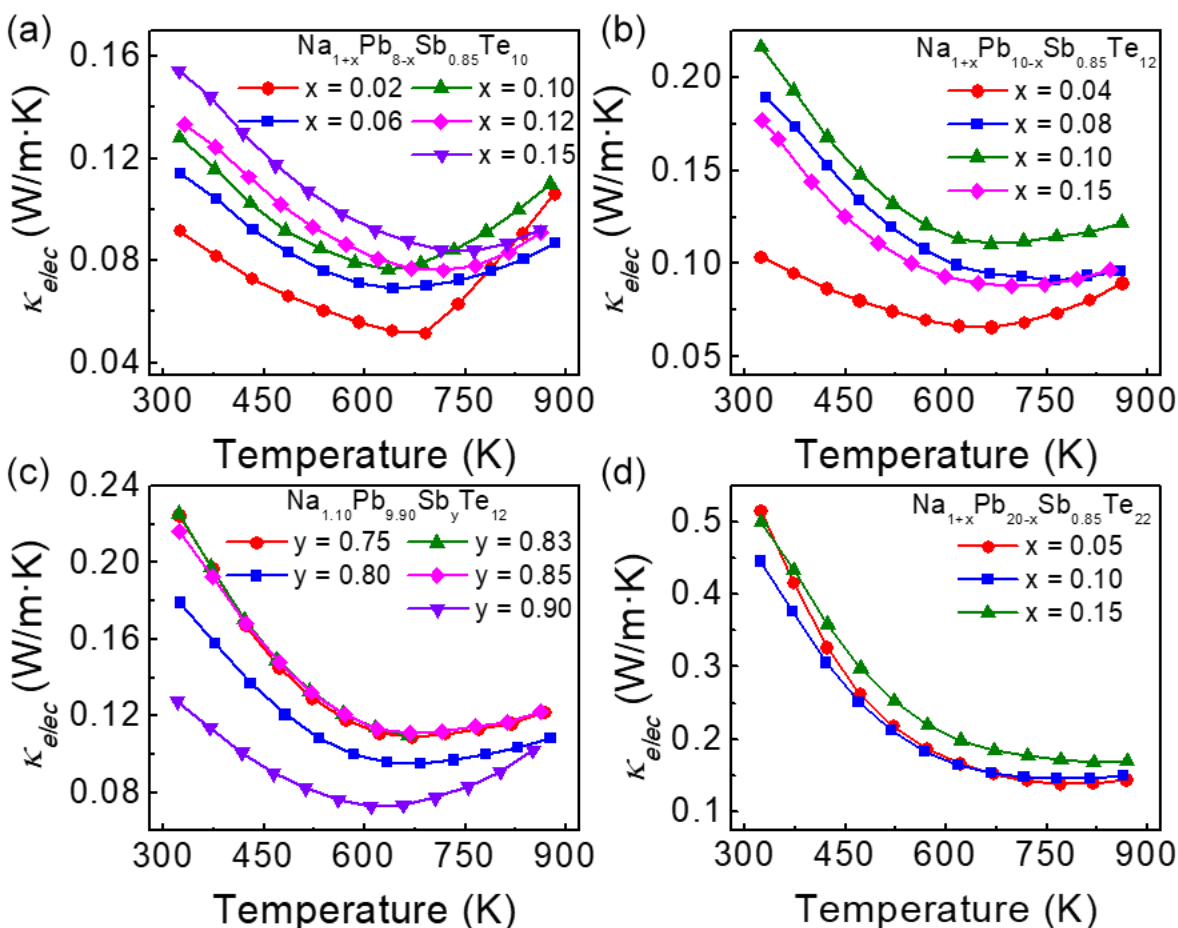


Figure 2.22 Electronic contribution to the thermal conductivity (κ_{elec}) for (a) $\text{Na}_{1+x}\text{Pb}_{8-x}\text{Sb}_{0.85}\text{Te}_{10}$, (b) $\text{Na}_{1+x}\text{Pb}_{10-x}\text{Sb}_{0.85}\text{Te}_{12}$, (c) $\text{Na}_{1.10}\text{Pb}_{9.90}\text{Sb}_y\text{Te}_{12}$, and (e) $\text{Na}_{1+x}\text{Pb}_{20-x}\text{Sb}_{0.85}\text{Te}_{22}$.

2.4.9 Scanning electron microscopy

Microscopy analysis was first performed using Scanning Electron Microscopy (SEM) to obtain information about grain size, orientation, and chemical segregation on a micro- and meso-scale. Samples were ground and polished on a grinding wheel to produce a fine surface finish in order to perform electron backscattered diffraction (EBSD). EBSD is sensitive to surface roughness and deformation, so the sample preparation was critical to attain a proper signal. The

sample was ground using 600, 800, and then 1200 grit SiC abrasive paper for approximately 5-10 min each. The polishing steps required using 1 μm and 0.1 μm diamond polish on a polishing pad for 15 and 45 minutes, respectively. Electron Backscattered Diffraction Patterns (EBSPs) were obtained simultaneously while collecting energy dispersive spectroscopy (EDS) maps using an FEI Quanta 650 ESEM. Collecting both signals from the same area allowed us to observe whether chemical segregation was occurring, and whether it was constrained to the grain boundaries or occurred within the matrix.

2.4.10 Transmission electron microscopy

TEM samples were prepared using the conventional bulk thinning method by grinding and polishing, dimpling, and ion milling in a water free environment. Samples were ground to 100 μm thickness or less before dimpling. Once dimpled, samples were milled until a hole appeared using a 5 keV ion beam, and were then cleaned using 1, 0.5, and 0.3 keV at cryogenic temperatures. Imaging and diffraction of all samples were performed using a Hitachi H-8100 TEM operating at 200 kV.

2.4.11 Hall effect measurements

The Hall effect measurements were completed using an AC 4-probe method in a homemade system with excitation fields of ± 0.5 Tesla. The system uses an air-bore, helium-cooled superconducting magnet to generate the field within a high temperature oven that surrounds the Ar-filled sample probe. The carrier density n_H was calculated from the Hall coefficient assuming

a single carrier band, i.e., $n_H = 1/eR_H$, where R_H is the Hall coefficient. The estimated error is based on the standard deviation of several data points at a single temperature.

2.4.12 Density functional theory (DFT) calculations

The total energies and relaxed geometries of the crystal structures (54 atom supercells) were calculated by DFT within the generalized gradient approximation (GGA) of the Perdew-Burke-Ernzerhof exchange correlation functional with Projector Augmented Wave potentials.¹¹² We used periodic boundary conditions and plane wave basis sets as implemented in the Vienna *ab initio* simulation package.¹¹³ The total energies were numerically converged to approximately 3meV/cation with spin-orbit coupling using a basis set energy cutoff of 500 eV and dense k -meshes corresponding to 4000 k -points per reciprocal atom in the Brillouin zone. On the basis of the band structure of the rock-salt phase, the effective masses are calculated by fitting the actual E - k diagram around the valence band maximum; for the different directions, the effective mass m^* is defined as:

$$m^* = \hbar \left(\frac{\partial^2 E}{\partial k^2} \right)^{-1} \quad (1.7)$$

where \hbar is the reduced Planck constant.

Chapter 3

High thermoelectric performance in PbSe–NaSbSe₂ alloys from valence band convergence and low thermal conductivity

Portions of this chapter were previously published in *Advanced Energy Materials*. 2019, 9 (30), 1901377, and are reproduced (adapted) with permission from © 2019 WILEY-VCH Verlag GmbH & Co. KGaA, Weinheim.

3.1 Introduction

Thermoelectric modules allow for interconversion between heat and electrical energy and are attractive for emerging applications in clean energy generation and solid-state cooling.¹¹⁴⁻¹¹⁵ Unfortunately, the high cost and relatively low conversion efficiencies of even high quality thermoelectric materials currently restricts usage to small scale and niche applications, making further advancement necessary to achieve wide spread commercialization.⁶ The key challenge in developing efficient thermoelectrics is the realization of materials that together possess high electrical conductivity, σ , large Seebeck coefficient, S , and low thermal conductivity, κ_{tot} , as parameterized in the dimensionless figure of merit $ZT = \frac{\sigma S^2}{\kappa_{tot}} T$ in which T is the absolute temperature.^{29, 57} Unfortunately, attaining substantial ZT values has proven to be an extremely difficult task, as the thermoelectric properties σ , S , and κ are intimately coupled through both the electronic structure and charge carrier density such that optimization of any one property generally degrades another and makes the development of robust strategies to enhance ZT very elusive.^{5, 78}

Lead chalcogenides are among the premier materials for intermediate temperature (cold and hot sides respectively in the range 400–900 K) heat to electrical energy conversion, as a number of powerful routes to independently engineer the electronic and thermal properties have been developed,^{28, 46-47, 65, 87, 89} culminating in outstanding maximum ZT greater than 2 at 923 K in Na-doped PbTe-SrTe.^{38, 49} In contrast, the top PbSe-based alloys significantly underperform compared to PbTe, with maximum ZT s ~ 1.6 near 923 K.^{50-51, 116} Despite possessing inferior figures of merit, PbSe remains an attractive alternative because of its lower cost, intrinsically lower lattice thermal conductivity,¹¹⁷ superior mechanical robustness, and higher maximum operating

temperature.¹¹¹ As such, PbSe continues to garner significant attention directed towards improving its thermoelectric performance.

Intriguingly, although the valence band structure of PbSe is more favorable than that of the conduction band for achieving high power factor ($S^2\sigma$), both p- and n-type alloys have been reported to exhibit comparable maximum figures of merit near 1.6. Furthermore, the ZT s of the n-type materials actually exceed those of the p-type at most temperatures,¹¹⁸⁻¹²² yielding superior average ZT s of 1 over 300–900 K compared to values of only ~ 0.5 for the p-type compounds. This is the opposite of what is observed in PbTe systems. A principal reason for this discrepancy is that while high ZT in p-type PbSe is generally achieved by means of electronic band structure engineering,⁵⁰⁻⁵¹ which primarily improves the performance only at elevated temperatures, exceptionally low lattice thermal conductivity has been achieved in the n-type materials over a broad range of temperatures, providing a wider interval of enhancement to the figure of merit.^{37, 118, 121-122} Therefore, improving the thermoelectric performance of p-type PbSe requires the integration of valence band convergence and a wide interval of ultra-low thermal conductivity.

Alloys of PbSe with NaSbSe₂ (represented here as NaPb_{*m*}SbSe_{*m+2*} or equivalently NaSbSe₂ + *m*PbSe) are a new family of materials that may be well suited to fit this need. NaPb_{*m*}SbSe_{*m+2*} compounds can be envisioned as solid solutions between NaSbSe₂ and PbSe, in which the three cations are randomly distributed across the Pb sites in the $Fm\bar{3}m$ crystal structure. Because of the heavy cation disorder, all PbQ-NaSbQ₂ (Q = Te, Se, S) compounds are intuitively expected to exhibit strong point defect phonon scattering and low thermal conductivity. Indeed, alloys of PbTe with ASbTe₂ (A = Ag, Na, K) are already well established thermoelectric materials that possess high maximum ZT s of 1.5–1.7 near 700 K as a consequence of their ultra-low lattice thermal

conductivities.^{13, 67, 123-124} Historically, while the tellurides $\text{AgPb}_m\text{SbTe}_{m+2}$ and $\text{NaPb}_m\text{SbTe}_{m+2}$ have been well studied and proven to be outstanding thermoelectrics, the selenide and sulfide analogues have not been investigated and are strong candidates for new research.

We find that alloying NaSbSe_2 into PbSe has two beneficial effects on the thermoelectric properties: (1) reduction of the energy separation between L and Σ valence band raises the density of states effective mass and boosts the power factors; (2) strong point-defect phonon scattering yields exceptionally low thermal conductivity without nanostructuring. As a result, properly doped $\text{NaPb}_m\text{SbSe}_{m+2}$ achieves maximum ZT of 1.4 near 900 K and critically, a record estimated ZT_{avg} for p-type PbSe of 0.64 over 400–873 K, marking a significant improvement on existing tellurium free p-type PbSe -based thermoelectrics. In addition, we surprisingly discovered that even when possessing degenerate carrier densities over 10^{20} cm^{-3} , the heavily doped samples of $\text{NaPb}_m\text{SbSe}_{m+2}$ compounds exhibit unusual semiconducting behavior with thermally activated electrical conductivity up to 500 K. We suggest that the unorthodox electrical transport under 500 K is the result of charge carrier scattering by the grain boundaries analogous to the behavior recently observed in Mg_3Sb_2 thermoelectrics.^{56, 68-69} Elimination of this effect may represent a future path towards further improving the thermoelectric performance of $\text{NaPb}_m\text{SbSe}_{m+2}$.

3.2 Results and Discussion

3.2.1 Structural and optical characterization

While Na and Sb individually have limited solubility (under 2%) in lead chalcogenides,^{121, 125} joint integration of both Na^+ and Sb^{3+} in equal quantities mimics the Pb^{2+} and allows for dramatically higher solubility. In fact, previous work on NaSbTe_2 – PbTe demonstrated that with proper

processing, single phase samples could be prepared with even up to 50% NaSbTe₂.¹²⁴ Such high solubility allows access to a broad compositional space over which to study and optimize the thermoelectric properties.

To explore the solubility of NaSbSe₂ in PbSe, we began by synthesizing a range of NaPb_mSbSe_{m+2} compounds with $m = 2-30$ (or equivalently ~3–33% NaSbSe₂). The powder X-ray diffraction (PXRD) patterns are shown in Figure 3.1a. The experimental diffraction patterns reveal no evidence of secondary phases and are in excellent agreement with the expected peaks for the rocksalt crystal structure, suggesting that phase pure samples can be synthesized down to at least $m = 2$ (33% NaSbSe₂). The refined lattice parameters are presented in Figure 3.1b as functions of NaSbSe₂ fraction, i.e. (PbSe)_{1-x}–(NaSbSe₂)_x and decrease linearly as x increases (m decreases) as expected for a solid solution of NaSbSe₂ and PbSe. The lattice parameters and diffraction patterns are identical before and after SPS, indicating no chemical changes occur during sintering. Similarly, Fourier transformed infrared (FTIR) spectroscopy data and the corresponding estimated band gaps presented respectively in Figures 3.1c and 3.1d show that the band gaps increase in a linear manner from 0.27 to 0.48 eV as greater fractions of NaSbSe₂ are added to PbSe. This result is consistent with the wider electronic band gap of ~1.1 eV for NaSbSe₂ compared to that of 0.27 eV for PbSe. Together, the clean diffraction patterns paired with linear trends in lattice parameters and band gaps support the notion that NaSbSe₂ and PbSe form a solid solution over the compositions of interest ($m = 2-30$).

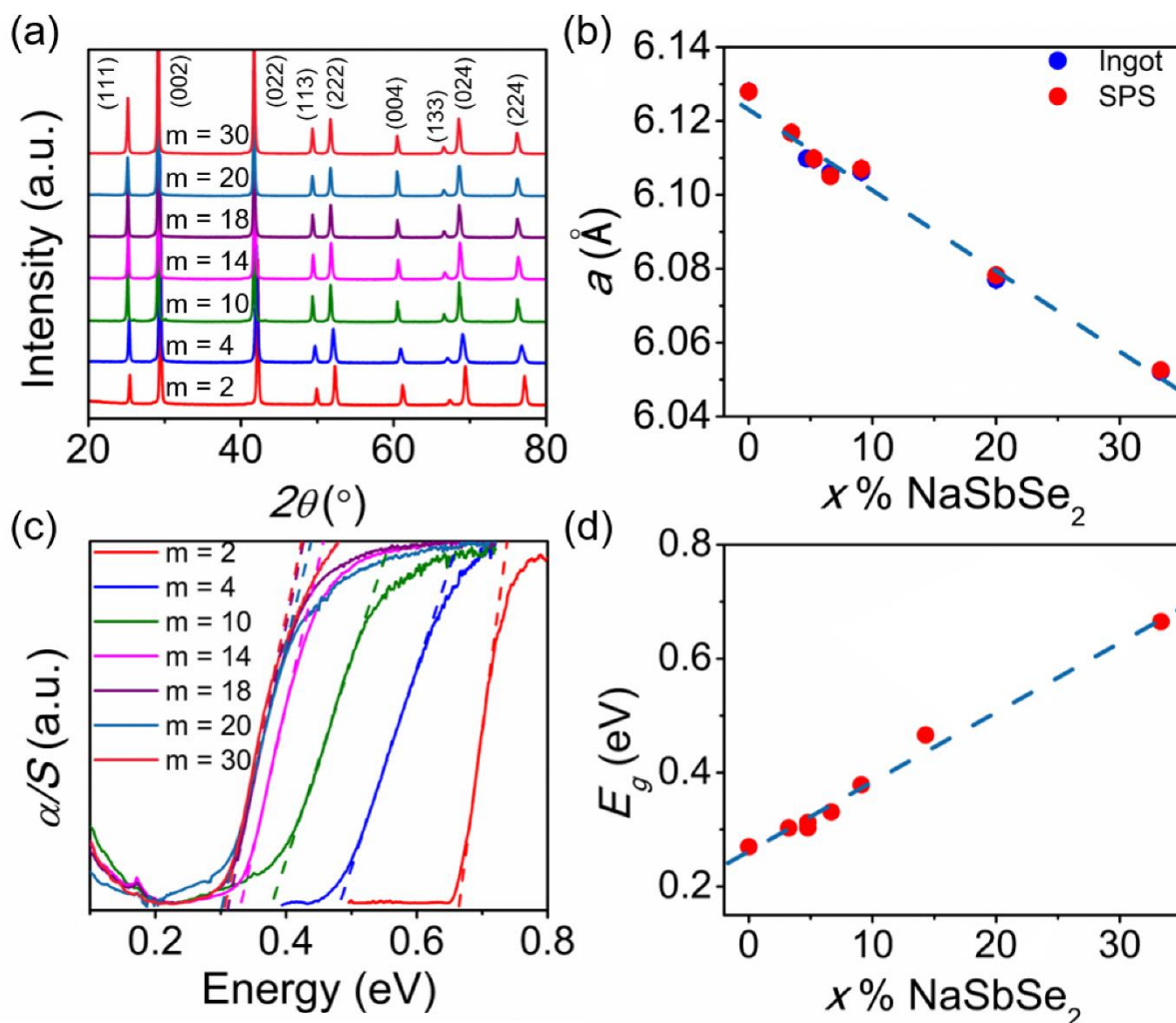


Figure 3.1 a) Powder X-ray diffraction patterns for $\text{NaPb}_m\text{SbSe}_{m+2}$ ($m = 2-30$). b) Refined lattice parameters for $\text{NaPb}_m\text{SbSe}_{m+2}$, represented as $\text{PbSe} + x\% \text{NaSbSe}_2$. c) Fourier transformed infrared spectroscopy spectra for the same $\text{NaPb}_m\text{SbSe}_{m+2}$ compounds (the dashed lines show the extrapolation used to estimate the bandgaps) and d) the estimated bandgaps. The dashed blue lines in (b) and (d) are guides to the eye showing the approximately linear trends in lattice parameter and bandgap as functions of NaSbSe_2 content. Unless noted, the data shown above was obtained from samples after SPS sintering.

3.2.2 Microstructural characterization of $\text{NaPb}_m\text{SbSe}_{m+2}$

To characterize the microscopic nature of the PbSe-NaSbSe_2 alloys, we performed a combination of transmission electron microscopy (TEM) and scanning electron microscopy (SEM). A characteristic high-resolution TEM images of a $m = 10$ sample is presented in Figure 3.2a and shows no evidence of nanoscale precipitation. The selected area electron diffraction pattern shown in Figure 3.2b is in good agreement with the expected rock-salt structure and exhibits no unexpected diffraction spots, further indicating a phase pure material. Considering that the closely related PbSe-AgSbSe_2 ($\text{AgPb}_m\text{SbSe}_{m+2}$) alloys have been reported to be heavily nanostructured,⁹⁵ these findings may initially be surprising. Despite this, the TEM results reported here are consistent with our previous work on the telluride analogues, $\text{NaPb}_m\text{SbTe}_{m+2}$, which were also found to be free of nanostructures after SPS sintering.¹²⁴ The lack of nanostructures in $\text{NaPb}_m\text{SbSe}_{m+2}$ is moreover in agreement with theoretical calculations on phase stability in these systems, which find lower mixing energies for PbQ-NaSbQ_2 alloys than for PbQ-AgSbQ_2 ,^{97, 124, 126} suggesting that mixtures of lead chalcogenides with NaSbQ_2 are less prone to the formation of nano-precipitates than those alloyed with AgSbQ_2 .

Intriguingly, while the TEM analysis shows the PbSe-NaSbSe_2 alloys to be single phase on the nanoscale, the SEM results shown in Figures 2c-g indicate elemental segregation at the micron level. Figure 3.2c displays a typical backscattered electron (BSE) image. Here, the image shows significant Z-contrast, suggesting that the sample is not perfectly homogeneous. Indeed, the energy dispersive spectroscopy (EDS) maps of each element (Figure 3.2d-g) confirm that the brighter regions in Figure 3.2c are richer in Pb, while the darker areas contain more Na and Sb. Despite this, the degree of inhomogeneity is likely small, considering that the powder diffraction

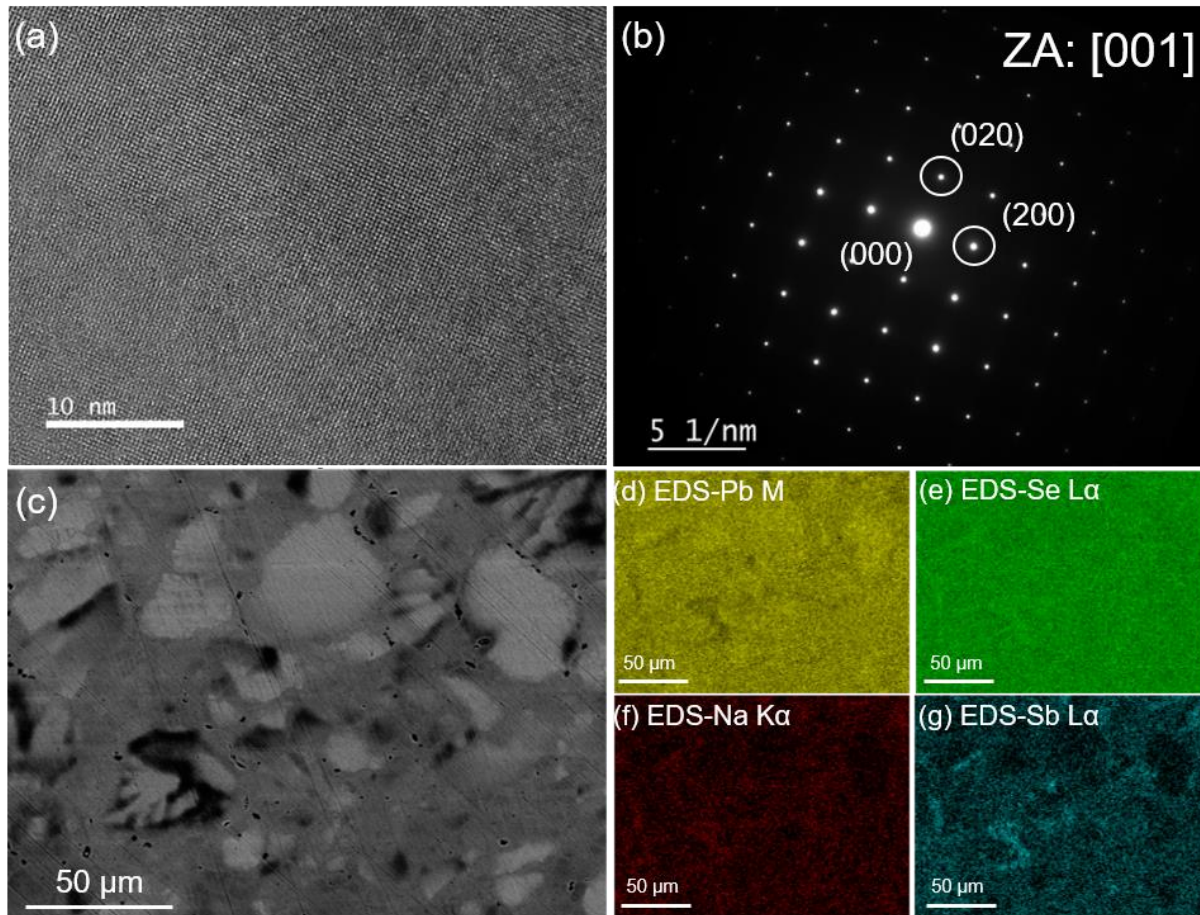


Figure 3.2 (a) A characteristic high-resolution TEM image of a sample with nominal composition $\text{Na}_{1.15}\text{Pb}_{9.85}\text{SbSe}_{12}$ and (b) a selected area electron diffraction pattern, both confirming a clean rocksalt structure with no nanoscale precipitates. (c) Backscattered electron image showing noticeable micron-level Z-contrast, and (d-g) EDS elemental maps over the region shown in (c). The EDS maps confirm minor segregation into Pb- and Na/Sb-rich regions.

patterns do not show evidence of secondary phases. Therefore, the data presented in Figures 3.2c-g likely represents minor perturbations of the nominal $\text{NaPb}_{10}\text{SbSe}_{12}$ stoichiometry, i.e. some regions of slightly lower m (richer in NaSbSe_2) and other areas of slightly higher m (richer in

PbSe). Similar micron-level inhomogeneity has also been reported in as-cast ingots of the related compounds $\text{AgPb}_m\text{SbTe}_{m+2}$ ¹²⁷ and $\text{NaPb}_m\text{SbTe}_{m+2}$.¹²⁴ Considering the thermoelectric properties of identically prepared samples are consistent, it is unlikely the above inhomogeneity has a significant impact on the thermoelectric properties.

3.2.3 Thermoelectric properties of p-type $\text{NaPb}_m\text{SbSe}_{m+2}$

Stoichiometric $\text{NaPb}_m\text{SbSe}_{m+2}$ compounds are valence-precise materials composed of Na^+ , Pb^{2+} , Sb^{3+} , and Se^{2-} ions, and therefore, are expected to be intrinsic semiconductors with low carrier densities. In principle, $\text{NaPb}_m\text{SbSe}_{m+2}$ should be tunable as n- or p-type with the proper dopants. Considering PbSe has a favorable band structure for achieving high power factor, we chose to first investigate p-type $\text{NaPb}_m\text{SbSe}_{m+2}$. In previous studies on the telluride analogues, $\text{NaPb}_m\text{SbTe}_{m+2}$, the highest ZT s were found near the PbTe-rich side of the system ($m > 8$),^{67, 124} and here we focused our work on $\text{NaPb}_{10}\text{SbSe}_{12}$ ($m = 10$). To add p-type charge carriers (holes), we first introduced additional Na^+ into the lattice in place of Pb^{2+} (i.e. $\text{Na}_{1+x}\text{Pb}_{m-x}\text{SbSe}_{m+2}$). The resulting thermoelectric properties are outlined and discussed below.

Figure 3.3a and 3.3b respectively show PXRD patterns and refined lattice constants for Na doped samples ($\text{Na}_{1+x}\text{Pb}_{m-x}\text{SbSe}_{m+2}$). The reflections are well indexed to the expected rocksalt reflections and show no secondary phases below $x = 20$. The data for most Na-rich sample ($x = 0.2$) shows minor peaks corresponding to secondary phases, indicating the dopant solubility is likely reached. The refined lattice parameters decrease nearly linearly with increasing Na fraction, as anticipated considering the smaller ionic radius of Na compared to Pb. The diffraction data therefore suggest successful dopant incorporation.

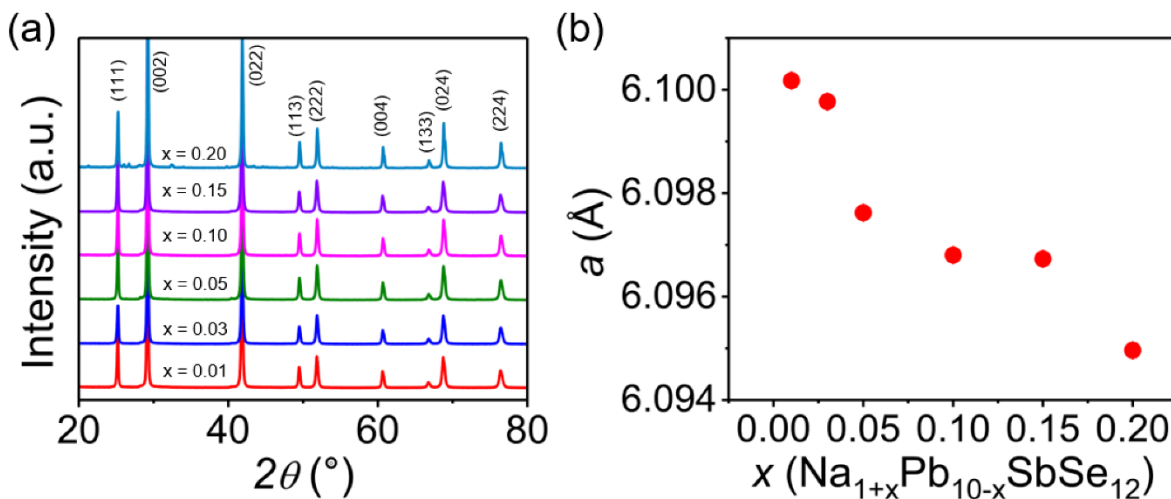


Figure 3.3 (a) PXRD patterns for $\text{Na}_{1+x}\text{Pb}_{m-x}\text{SbSe}_{m+2}$ and (b) refined lattice parameters.

Figure 3.4a and 3.4b display the electrical conductivities and Seebeck coefficients of $\text{Na}_{1+x}\text{Pb}_{10-x}\text{SbSe}_{12}$ ($x = 0.01$ – 0.20). These compounds all have a fixed fraction of $\sim 9\%$ NaSbSe_2 alloyed into PbSe , and are extrinsically doped with additional Na. The electrical conductivities rise with greater Na doping (higher x) reaching maximum values $\sim 600 \text{ S}\cdot\text{cm}^{-1}$ at $\sim 450 \text{ K}$ for $x = 0.20$. The Seebeck coefficients are all positive over the measured temperatures, suggestive of p-type charge transport and decrease as the doping level rises. The trends in both electrical conductivities and Seebeck coefficients indicate that the hole density is effectively raised by the Na doping. Successful doping of $\text{NaPb}_m\text{SbSe}_{m+2}$ is confirmed by the temperature-dependent Hall effect data shown in Figure 3.4c. Na doping significantly increases the carrier density from $1.4 \times 10^{18} \text{ cm}^{-3}$ for $x = 0.01$ to $1.5 \times 10^{20} \text{ cm}^{-3}$ for $x = 0.15$. The Hall carrier mobilities are lastly shown in Figure 3.4d and rapidly drop with greater Na content. Namely, at 300 K there is a large decrease in mobility between $x = 0.01$ and 0.05 from 100 to $20 \text{ cm}^2\cdot\text{V}^{-1}\cdot\text{s}^{-1}$ followed by a smaller decline to $10 \text{ cm}^2\cdot\text{V}^{-1}$

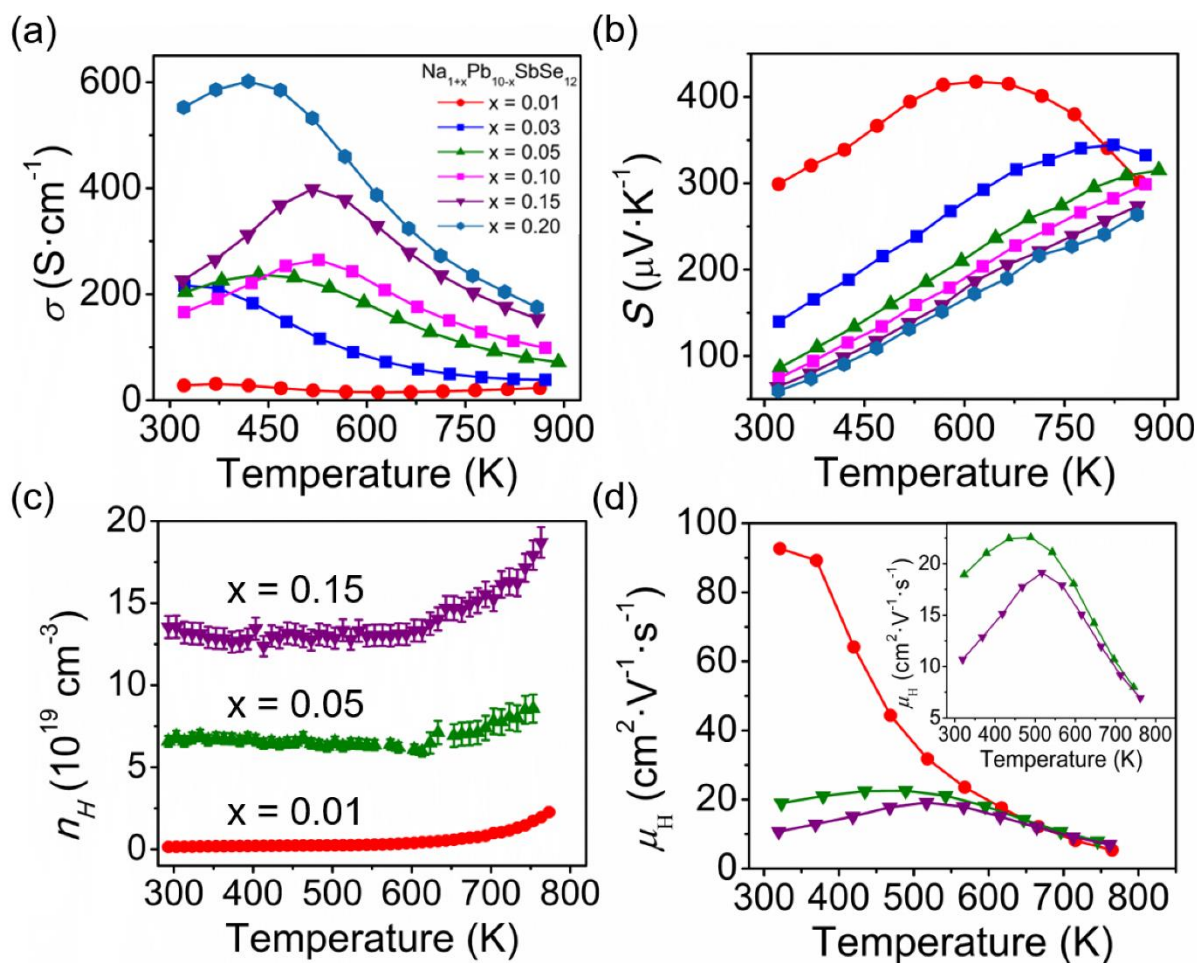


Figure 3.4 Temperature-dependent (a) electrical conductivities, (b) Seebeck coefficients, (c) Hall carrier densities, and (d) Hall carrier mobilities for $\text{Na}_{1+x}\text{Pb}_{10-x}\text{SbSe}_{12}$. The inset in (d) shows a close up of the mobilities of samples for which $x = 0.05$ and 0.15 , emphasizing the positive temperature dependence of μ below 500 K.

$\cdot\text{s}^{-1}$ for $x = 0.15$. Lastly, it should be noted that the electrical conductivities are thermally activated below $\sim 500\text{K}$ (Figure 3.4a), which is highly anomalous and will be explained in detail at the end of the discussion section.

Figure 3.5a shows the temperature-dependent total thermal conductivities of $\text{Na}_{1+x}\text{Pb}_{10-x}\text{SbSe}_{12}$. The measured thermal conductivities are very low and decrease as functions of temperature to converge at minimum values of $\sim 0.8 \text{ W}\cdot\text{m}^{-1}\cdot\text{K}^{-1}$ at 873 K. At room temperature, the total thermal conductivities increase with greater Na fraction because of the higher electronic conductivities, which increase the electronic contributions to the thermal conductivity κ_{elec} . Likewise, the estimated lattice thermal conductivities (shown as $\kappa_{\text{tot}} - \kappa_{\text{elec}}$) in Figure 3.5b are exceptionally low, with values under $1 \text{ W}\cdot\text{m}^{-1}\cdot\text{K}^{-1}$ over nearly the full temperature regime, all of which mostly converge to a minimum of $\sim 0.55 \text{ W}\cdot\text{m}^{-1}\cdot\text{K}^{-1}$ at 873 K. The *ZT*s are finally displayed in Figure 3.5c and increase with both temperature and doping level, achieving high maximum values of approximately 1.3 at 873 K for $x = 0.20$.

To explore the best route to tune the carrier density in $\text{NaPb}_m\text{SbSe}_{m+2}$, we also attempted to introduce additional Na in place of Sb (i.e. $\text{Na}_{1+x}\text{Pb}_{10}\text{Sb}_{1-x}\text{Se}_{12}$). Figure 3.6a and 3.6b respectively display the corresponding electrical conductivities and Seebeck coefficients. Here, the electrical conductivity increases dramatically between $x = 0.05$ and $x = 0.10$, accompanied by a decrease of the Seebeck coefficients, suggestive of an increased hole concentration. As the Na doping level is further increased from $x = 0.10$ to 0.15, the Seebeck coefficients remain largely unchanged, indicating little effect on the carrier density. However, the electrical conductivity of the more heavily doped compound is suppressed under $\sim 600 \text{ K}$, while at high temperatures, the electrical conductivities of both compounds converge to similar values near $200 \text{ S}\cdot\text{cm}^{-1}$. The temperature-dependent charge carrier density of the $x = 0.10$ sample (shown in Figure 3.6c) shows a nearly constant value of $\sim 2 \times 10^{20} \text{ cm}^{-3}$ between room temperature and 650 K, the highest of all measured samples.

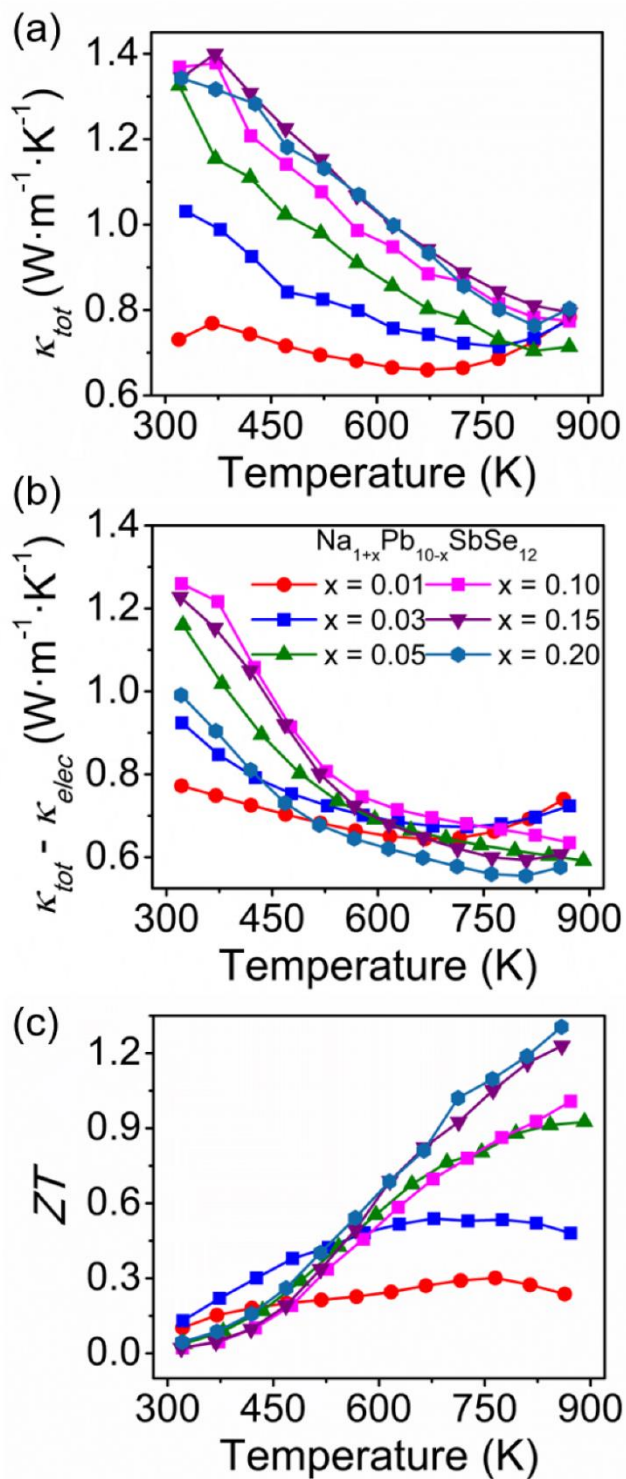


Figure 3.5 Temperature-dependent (a) total thermal conductivities, (b) estimated lattice thermal conductivities $\kappa_{tot} - \kappa_{elec}$ and (c) ZT s for $\text{Na}_{1+x}\text{Pb}_{10-x}\text{SbSe}_{12}$.

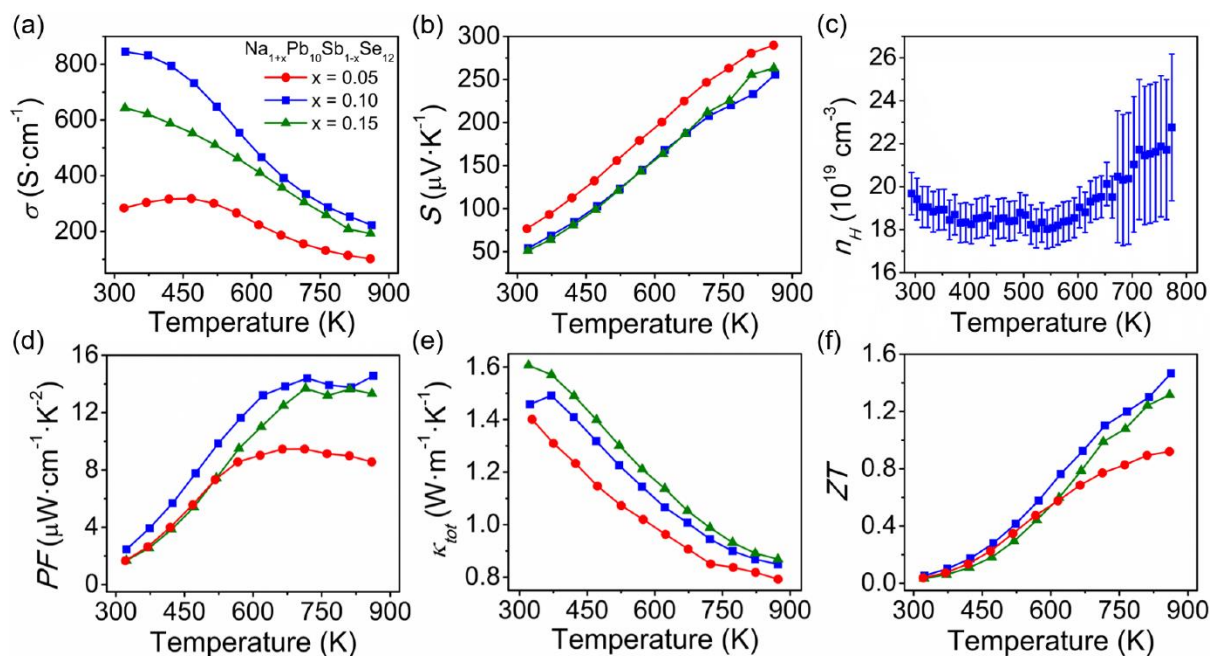


Figure 3.6 Temperature-dependent thermoelectric properties of $\text{Na}_{1+x}\text{Pb}_{10}\text{Sb}_{1-x}\text{Se}_{12}$. (a) electrical conductivity, (b) Seebeck coefficient, (c) Hall carrier concentration for $x = 0.10$, (d) power factors, (e) total thermal conductivities, and (f) ZT .

The higher carrier densities that can be achieved by substituting additional Na in place of Sb is the key difference between the data in Figure 3.6 and that presented in Figures 3.4 and 3.5. As a consequence, the power factors of $\text{Na}_{1+x}\text{Pb}_{10}\text{Sb}_{1-x}\text{Se}_{12}$ are slightly higher and achieve maximum values of 13–14 $\mu\text{W}\cdot\text{cm}^{-1}\cdot\text{K}^{-2}$ between 700–873 K (Figure 3.6d). Furthermore, the total thermal conductivities of $\text{Na}_{1+x}\text{Pb}_{10}\text{Sb}_{1-x}\text{Se}_{12}$ shown in Figure 3.6e are again very low over the measured temperature regime with small differences between doping level. In general, the total thermal conductivities decrease with temperature from 1.6 to 0.8 $\text{W}\cdot\text{m}^{-1}\cdot\text{K}^{-1}$ over 323–873 K. The ZT s are shown in Figure 3.6f and are slightly improved compared to those shown in Figure 3.5c

for $\text{Na}_{1+x}\text{Pb}_{10-x}\text{SbSe}_{12}$, increasing with temperature over the full measurement range and approaching a maximum of 1.4 at 873 K for $x = 0.10$.

3.2.4 Low lattice thermal conductivity in $\text{NaPb}_m\text{SbSe}_{m+2}$

Figures of merit approaching 1.4 near 900 K make $\text{NaPb}_m\text{SbSe}_{m+2}$ competitive with state-of-the-art p-type PbSe-based thermoelectrics such as PbSe-SrSe,⁵¹ PbSe-CaS,¹¹⁶ and PbSe-HgSe.⁵⁰ To understand the origin of the outstanding thermoelectric performance, we note that the lattice thermal conductivities displayed in Figure 3.5b and 3.6e are among the lowest measured in a PbSe-based alloy, particularly at intermediate temperatures under 700 K. Unfortunately, investigating the details and origin of the low thermal conductivity is challenging, primarily complicated by the fact that anomalous electrical conductivity described previously limits our ability to reliably estimate κ_{elec} . This issue is outlined in greater detail in Chapter 4.

Yet, we can still glean several insights on the low thermal conductivities from other perspectives. From our TEM study, no nanostructures nor precipitates were observed in any of the $\text{NaPb}_m\text{SbSe}_{m+2}$ samples, suggesting that the bulk of the reduction in thermal conductivity stems from strong point defect phonon scattering, the result of the random occupation of Na^+ , Pb^{2+} , and Sb^{3+} on the cation sites. To provide evidence for this, we estimated the lattice thermal conductivities of undoped $\text{NaPb}_m\text{SbSe}_{m+2}$ ($m = 2-30$) and pure PbSe and compared the experimental values with calculations from a simplified Debye-Callaway model that considered only phonon-phonon and point defect scattering.^{21, 125} Here, the low carrier densities of the undoped samples yield small κ_{elec} , making any errors in the estimated κ_{lat} stemming from the unusual electrical conductivity negligible. Details concerning the model are found in the

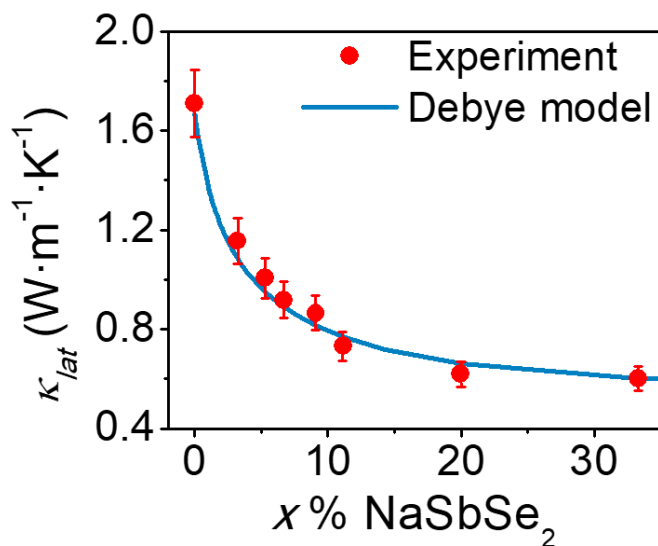


Figure 3.7 Experimentally determined lattice thermal conductivity for $\text{NaPb}_m\text{SbSe}_{m+2}$ for $m = 2\text{--}30$ and PbSe , plotted as % NaSbSe_2 in PbSe , compared with the theoretical curve generated from the simplified Debye-Callaway model. The error bars are 8%.

experimental section. The data is presented in Figure 3.7 and shows that the κ_{lat} of the undoped samples decrease monotonically with NaSbSe_2 fraction, agreeing reasonably well with the projected values from the alloy model. While the strong bipolar diffusion in the undoped samples limits analysis of the temperature dependence, the results provide support that the primary origin of the extremely low lattice thermal conductivities in $\text{NaPb}_m\text{SbSe}_{m+2}$ is point defect scattering, although other mechanisms may also be at play.

3.2.5 Role of NaSbSe_2 in modifying the electronic structure of PbSe

In addition to the low lattice thermal conductivities, the thermoelectric performance in $\text{NaPb}_m\text{SbSe}_{m+2}$ is moreover augmented by the electronic properties. Namely, the Seebeck

coefficients shown in Figure 3.4 and 3.6 are comparable to those found in band engineered PbSe,⁵⁰⁻⁵¹ indicating NaSbSe₂ may have a favorable impact on the electronic structure of PbSe. To probe this, we used density functional theory (DFT) to calculate the band structures of several PbSe-NaSbSe₂ compounds. The results are presented in Figure 3.8a and demonstrate that NaPb_mSbSe_{m+2} retains the same general features as that of pure PbSe. In particular, the NaPb_mSbSe_{m+2} compounds are direct gap semiconductors with a primary band gap at the *L*-point of the Brillouin zone and secondary valence- and conduction-bands deeper in energy at the Σ -point. The calculations further demonstrate that the band gap widens as a function of the NaSbSe₂ fraction, consistent with the experimental trends observed in Figure 3.1d.

Importantly, Figure 3.8b reveals that the energy offset between the *L* and Σ valence bands ($\Delta E_{L-\Sigma}$) significantly decreases with greater NaSbSe₂ content, from ~0.3 to 0.14 eV between $n = 0$ and 2. This supports the suggestion that high Seebeck coefficients may result from the converging bands. Care must be taken in this interpretation, as the calculations also show that as more NaSbSe₂ is added to PbSe, both valence and conduction bands flatten, i.e. the band effective mass m_b^* increases. This is understandable, as introduction of Na⁺ and Sb³⁺ into PbSe is expected to increase the ionicity of the compound and in turn widen the band gap and flatten the bands.¹⁰⁰ Considering the large fraction of NaSbSe₂ found in NaPb₁₀SbSe₁₂ (~9%), it is reasonable to expect a significantly higher m_b^* for this material compared to PbSe. Unfortunately, because band flattening (increasing m_b^*) and band convergence (increasing m_{DOS}^*) will both enlarge the Seebeck coefficient ($S \propto m_{DOS}^*$ and $m_{DOS}^* = N_V^{2/3} m_b^*$, where N_V is the degeneracy of the bands), these two processes must be separated to understand both the origin of the high Seebeck coefficients and the full role of NaSbSe₂ in PbSe.

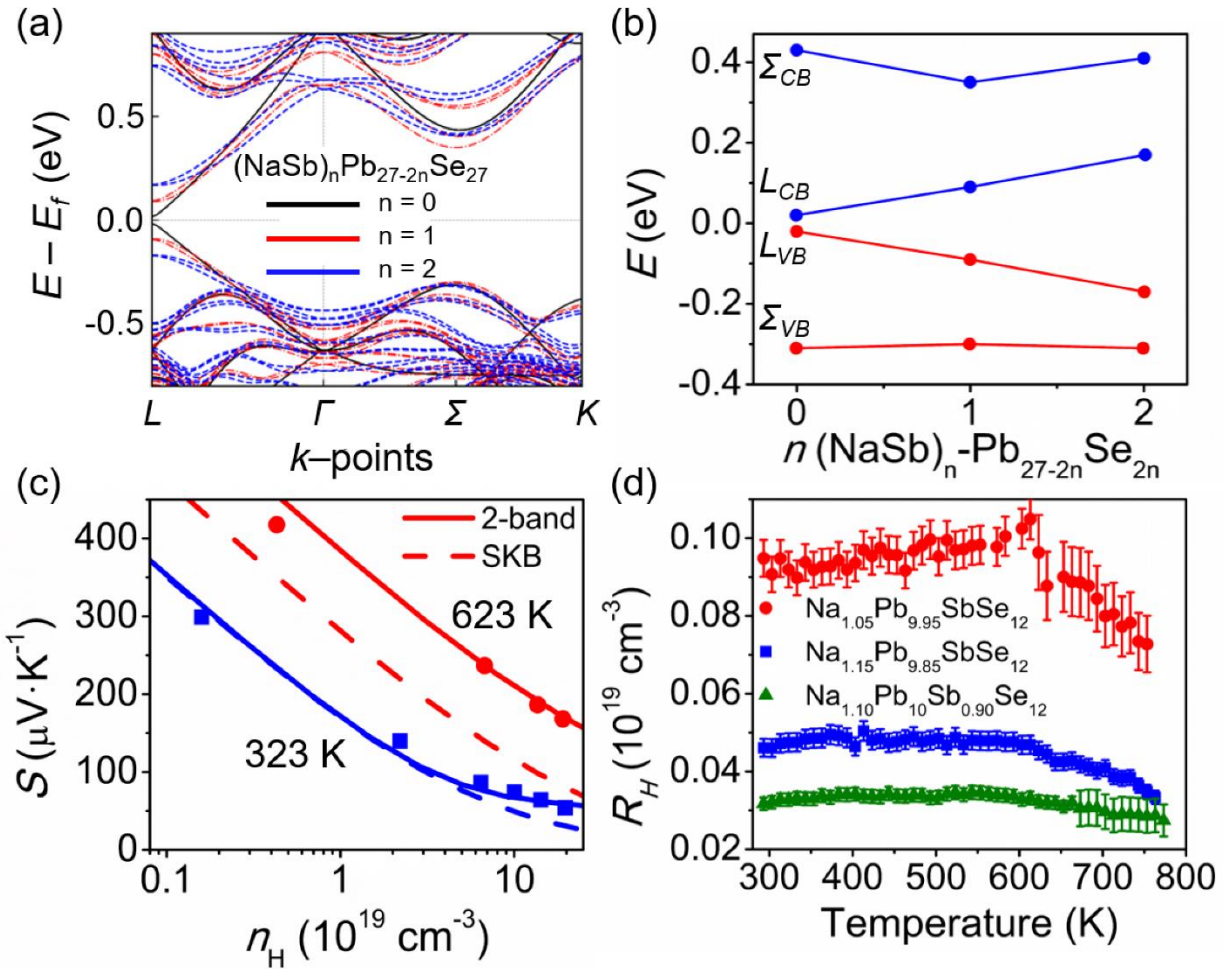


Figure 3.8 (a) DFT calculated band structures for $\text{NaPb}_m\text{SbSe}_{m+2}$ (shown as $\text{Na}_n\text{Sb}_n\text{Pb}_{27-2n}\text{Se}_{27}$ and representing 0, 4, and 8 percent NaSbSe_2 respectively). (b) DFT calculated energy differences between L and Σ bands for the band structures shown in (a). (c) Pisarenko plots for $\text{NaPb}_{10}\text{SbSe}_{12}$ at 323 K and 623 K. The theoretical lines were calculated with both a single band (SKB) and two-band model, shown as dashed and solid lines respectively. (d) Temperature-dependent Hall coefficients for p-type doped $\text{NaPb}_{10}\text{SbSe}_{12}$.

To decouple the potential impacts of valence band flattening and band convergence in $\text{NaPb}_m\text{SbSe}_{m+2}$, we generated theoretical graphs of the carrier density vs. Seebeck coefficient

(Pisarenko plots) using both a single Kane band (SKB)^{45, 111, 128-129} and a two-band model¹²⁹ and compared the results with the experimental data. The details of our Pisarenko calculations are shown in the experimental section and the results are presented in Figure 3.8. The Pisarenko curves confirm the increase in effective mass predicted by the DTF calculations, as we find that an L -band density of states mass of $m_L^* = 0.37m_e$ is required to fit the experimental data at 323 K, a considerable increase over that of pure PbSe ($m_L^* = 0.27m_e^*$). We moreover find that while both the single-band and 2-band curves can be fit reasonably well with the experimental data at 323 K, the SKB model severely underestimates the measured points at 623 K, implying that the effective mass of NaPb₁₀SbSe₁₂ increases with heating faster than anticipated from a SKB model and thus suggesting the single band model is incorrect. On the other hand, the two-band model provides a much better prediction of the experimental data at 623 K while also giving a more satisfactory fit to the high n_H data at 323 K. The good agreement between the two-band Pisarenko curves and experimental data therefore supports the results observed in the calculated electronic band structures, that the energy separation between the L and Σ valence bands decreases upon alloying with NaSbSe₂ and that both bands contribute to the charge transport.

To provide further experimental support for two band charge transport, we measured the temperature-dependent Hall coefficients, R_H , the results of which are shown in Figure 3.8d. In p-type lead chalcogenides, a peak in R_H plotted as a function of temperature is often interpreted as evidence of multi-band behavior, characteristic of the carriers redistributing between converging bands.^{40, 101, 129-130} The measured Hall coefficients displayed in Figure 3.8d are approximately constant functions of temperature until 600 K, at which point they decrease with further heating. Close inspection of the individual curves of Figure 3.8d does reveal that the Hall coefficients

increase weakly with temperature before ~ 600 K; however, the peaks in the R_H vs. T plots are clearly much weaker than what is typically observed in p-type PbSe.¹²⁹ Although at first glance the Hall data appears characteristic of single band transport, in disagreement with the DFT calculations and Pisarenko plots, this interpretation requires closer inspection.

First, the decrease in the experimental R_H values as functions of temperature beginning at 600 K cannot, as one may initially suspect, be from the onset of intrinsic conduction, as the Seebeck coefficients (shown in Figure 3.4b) do not exhibit a corresponding downturn. Furthermore, no evidence for bipolar diffusion is found in the estimated electronic and lattice thermal conductivities (Figures 3.4b and 3.X respectively). Therefore, despite the relatively flat temperature dependence, the Hall data is likely not characteristic of single-band transport. As discussed by Allgaier, a maximum in a plot of R_H vs. T occurs in two band systems not when the energies of each band are equal, as is commonly suggested, but instead when the respective contributions to the total electrical conductivity from each band are equal.¹³¹ As a result, signs of band convergence in the electronic transport may be suppressed even in true multi-band systems depending on the specific parameters of each band.

Interestingly, work by Wang *et al.* on p-type PbSe–SrSe shows very similar Hall data for high fractions of Sr (8–12%), in which the Hall coefficients are nearly independent of temperature until ~ 600 – 700 K,⁵¹ providing an example of a well-established two-band system lacking a strong R_H peak. This may be understood by considering Allgaier's general two-band model and the impact of NaSbSe₂ (and Sr) on the electronic structure. As discussed previously, introducing NaSbSe₂ (or Sr) into PbSe will flatten the bands, increasing m_b^* and therefore lowering the mobility ratio between L - and Σ - bands. In this interpretation, the relatively flat temperature dependence of

R_H between 300 and 600 K suggests that both L - and Σ -bands have comparable partial electrical conductivities over this temperature range (i.e. both contribute significantly to the charge transport), and the decrease in R_H beginning at 600 K marks the temperature at which the majority of the conduction occurs in the second band.¹³¹⁻¹³²

As a final means of experimentally probing the electronic band edge positions, we utilized photoemission yield spectroscopy in air (PESA)¹³³⁻¹³⁵ to determine the work functions of several nominally undoped samples of $\text{NaPb}_m\text{SbSe}_{m+2}$ for $m = 10\text{--}30$ and pure PbSe. The photoemission spectra are shown in Figure 3.9. Extrapolating the linear region of each spectrum to the baseline determines the work function. Because these samples are only weakly p-type (see Figure 3.13), the carrier densities are small, and the work functions give the energies of the valence band edge (L -point) vs. vacuum. Adding the experimentally determined band gaps to the work functions will therefore determine the energy of the conduction band edge. The results are displayed in Figure 3.9b and show that between 0–9% NaSbSe_2 the valence band edge (work function) moves deeper in energy from ~ 4.97 to 5.06 eV, while the conduction band edge remains approximately unchanged.

Since the room temperature energy difference between L - and Σ -bands in pure PbSe is known to be ~ 0.25 eV^{51, 129}, we can use the observed energy shifts in the measured work functions to estimate the energy difference between L - and Σ - valence bands. To do this, we must assume that the position of the Σ -band does not change appreciably with NaSbSe_2 alloying. This assumption is supported by the DFT calculated band structures shown in Figure 3.7a and is further justified considering the significant cation (Pb s-orbital) character of valence band at the L -point, whereas the Σ -band is expected to be mostly anion (Se p-orbital) in character and therefore weakly

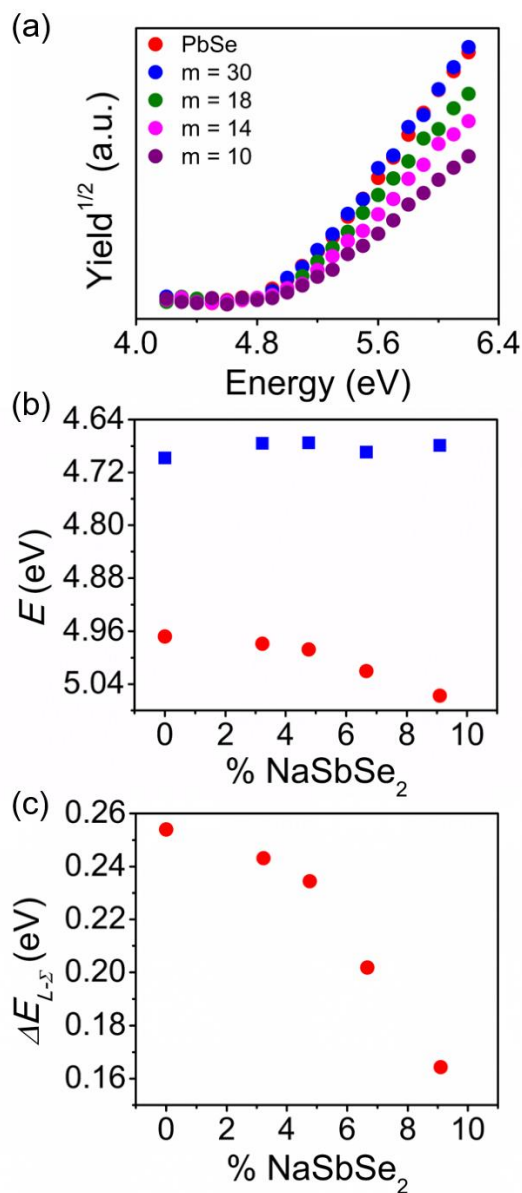


Figure 3.9 (a) Photoemission yield spectroscopy in air (PYSA) spectra for nominally undoped samples of $\text{NaPb}_m\text{SbSe}_{m+2}$ ($m = 10\text{--}30$, and pure PbSe). (b) Energies of the valence band edges (work functions) and conduction band edges for each sample extracted from the linear regions of the photoemission spectra, shown as red and blue points respectively. 9% NaSbSe_2 corresponds to the $m = 10$ sample discussed most thoroughly in the text. (c) Experimentally estimated energy differences between L - and Σ - valence band for each sample.

impacted by alloying onto the cation site.^{100, 136} The energy differences between L and Σ -valence bands estimated from the work functions of each compound are presented in Figure 3.9c and show that the $\Delta E_{L-\Sigma}$ decreases with NaSbSe₂ fraction down to ~ 0.16 eV for 9% NaSbSe₂. These results are in general agreement with the DFT calculations shown in Figure 3.7a (which are calculated for 0, 4, and 8% NaSbSe₂), albeit the experimental values are somewhat higher than the calculated energy differences. The experimentally estimated values of $\Delta E_{L-\Sigma}$ are moreover in excellent agreement with the theoretical 2-band Pisarenko calculations found in Figure 3.7c. To generate the Pisarenko curve, we used an energy difference ($\Delta E_{L-\Sigma}$) of 0.15 eV at room temperature (see the experimental section for more details) to fit the experimental Seebeck coefficients, clearly in strong agreement with the experimental value of 0.16 eV.

The combined results from the DFT calculations, the 2-band Pisarenko curves, experimental Hall effect data, and photoemission experiments all indicate that introducing NaSbSe₂ into PbSe both raises the band effective mass and reduces the energy separation of the L and Σ valence bands, allowing both bands to contribute similarly to charge transport even at relatively low temperatures near 300 K. The net effect of the two-band transport is significantly increased valley degeneracy ($N_v = 4$ and 12 for the L and Σ bands respectively), which boosts the density of states effective mass and enhances the Seebeck coefficients as is well known in many high quality thermoelectrics.⁴⁶ Indeed, as displayed in Figure 3.10, at temperatures under ~ 700 K our optimally doped NaPb₁₀SbSe₁₂ has superior power factors to both Na-doped PbSe and band engineered PbSe-HgSe.⁵⁰ Considering that our NaPb₁₀SbSe₁₂ samples have comparable carrier concentrations and lower charge carrier mobilities than the aforementioned materials, we attribute the improved power factors (under 700 K) to the fact that in NaPb₁₀SbSe₁₂, both valence bands

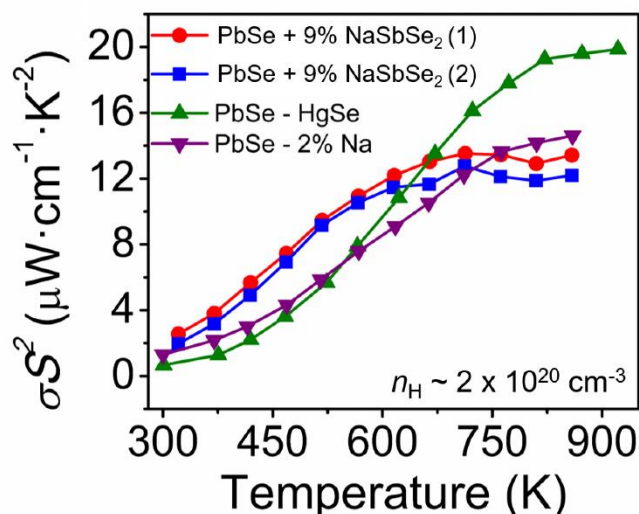


Figure 3.10 Temperature-dependent power factors of two differently doped $\text{NaPb}_{10}\text{SbSe}_{12}$ samples compared with those of $\text{PbSe}-2\%\text{Na}$ and band engineered $\text{PbSe}-2\%\text{HgSe}$ (2% Na doped). The $\text{PbSe}-\text{HgSe}$ exhibits a record high power factor $\sim 20 \mu\text{W}\cdot\text{cm}^{-1}\cdot\text{K}^{-2}$ above 900 K; however, the $\text{NaPb}_{10}\text{SbSe}_{12}$ have superior power factors below ~ 700 K that contribute to outstanding average ZT s. Considering each of the compounds shown above has comparable carrier densities $\sim 2 \times 10^{20} \text{cm}^{-3}$, we attribute the high power factors below 700 K in $\text{NaPb}_{10}\text{SbSe}_{12}$ to the greater contribution of the Σ -band. Namely, in $\text{NaPb}_{10}\text{SbSe}_{12}$ both L - and Σ -bands participate in the charge transport even near room temperature, which should improve the power factors at low and moderate temperatures due to the high valley degeneracy.

contribute more significantly to the charge transport even near room temperature.

3.2.6 Thermoelectric figure of merit

In $\text{NaPb}_m\text{SbSe}_{m+2}$, the high solubility of NaSbSe_2 in PbSe discussed in Figure 3.1 allows for a significant fraction ($\sim 9\%$ for $m = 10$) of NaSbSe_2 to be incorporated into the PbSe matrix. As

a consequence, both extremely low lattice thermal conductivity and two-band charge transport are accessed over a wide temperature interval, substantially augmenting the thermoelectric performance. As an illustration, the temperature dependent ZT s for optimally doped $\text{NaPb}_{10}\text{SbSe}_{12}$ with several of the highest performing p-type PbSe alloys found in the literature is presented in Figure 3.11a. While the maximum ZT s at high temperature are somewhat lower in $\text{NaPb}_{10}\text{SbSe}_{12}$ compared to the other materials, the ZT s found here are superior over nearly the full range of temperatures. The broad span of improved ZT has a direct impact on the performance $\text{NaPb}_{10}\text{SbSe}_{12}$ may reach when integrated into a thermoelectric module. This is parameterized by the device figure of merit ZT_{avg} (also often referred to as ZT_{dev} , $ZT_{\text{effective}}$, or ZT_{eng} in other publications) and related to the energy conversion efficiency η as follows.^{77, 137-138}

$$\eta = \left(\frac{T_H - T_C}{T_H} \right) \cdot \frac{\sqrt{1 + ZT_{\text{avg}}} - 1}{\sqrt{1 + ZT_{\text{avg}}} + (T_C/T_H)} \quad (3.1)$$

Here, T_H and T_C are the hot and cold side temperatures respectively. We utilized the method presented by Snyder *et al.* to estimate the device ZT directly from the thermoelectric properties for our $\text{NaPb}_{10}\text{SbSe}_{12}$ and for the other PbSe-alloys shown in Figure 3.11a.¹³⁹ This method is considered an accurate means of estimating the device figure of merit and provides for a reliable means of comparing our $\text{NaPb}_{10}\text{SbSe}_{12}$ compounds with the state-of-the-art PbSe-alloys found in the literature. Considering a cold side temperature of 400 K and hot side of 873 K, Figure 3.11b demonstrates that the $ZT_{\text{avg}} \sim 0.64$ of the best $\text{NaPb}_{10}\text{SbSe}_{12}$ is markedly improved compared to the competing materials and is to our knowledge the highest value yet reported in p-type PbSe. It should be pointed out that superior performance was very recently achieved in p-type Cd-alloyed $\text{PbSe}_{1-x}\text{Te}_x$,³⁹ however, these compounds are not tellurium free, so this is not a direct comparison

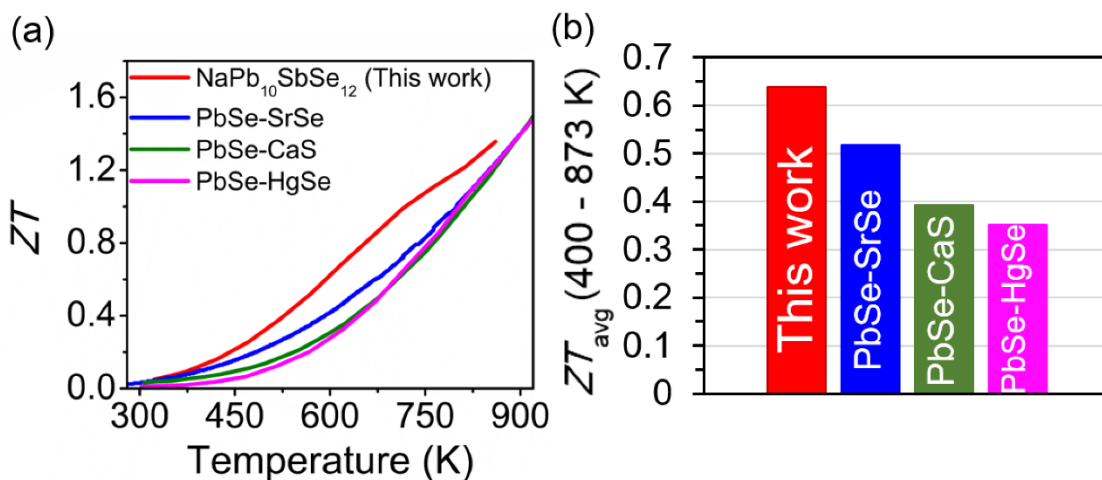


Figure 3.11 (a) Traces of the temperature-dependent ZT values for $\text{Na}_{1.10}\text{Pb}_{10}\text{Sb}_{0.90}\text{Se}_{12}$ (this work, denoted as $\text{NaPb}_{10}\text{SbSe}_{12}$), PbSe-SrSe , and PbSe-CaS , PbSe-HgSe . The line for $\text{Na}_{1.10}\text{Pb}_{10}\text{Sb}_{0.90}\text{Se}_{12}$ was obtained from the averages of 5 separate samples. (b) Comparison of the average (device) ZT s estimated for the same materials.

and the higher ZT is expected. Evidently, $\text{NaPb}_m\text{SbSe}_{m+2}$ should have strong potential as a PbSe -based thermoelectric material for modules with intermediate operating temperature.

3.2.7 Unorthodox charge transport below 500 K and future directions

As noted earlier, the electrical properties displayed in Figure 3.4a and to a lesser extent Figure 3.6a are highly anomalous and warrant an explanation. Namely, the Seebeck coefficients are characteristic of degenerate semiconductors and increase nearly linearly as functions of temperature between 300 and 900 K. Given the 10^{19} – 10^{20} cm^{-3} charge carrier concentration for the heavily doped samples, one should anticipate electrical conductivities that follow a negative temperature dependence characteristic of acoustic phonon scattering. Clearly, however, the

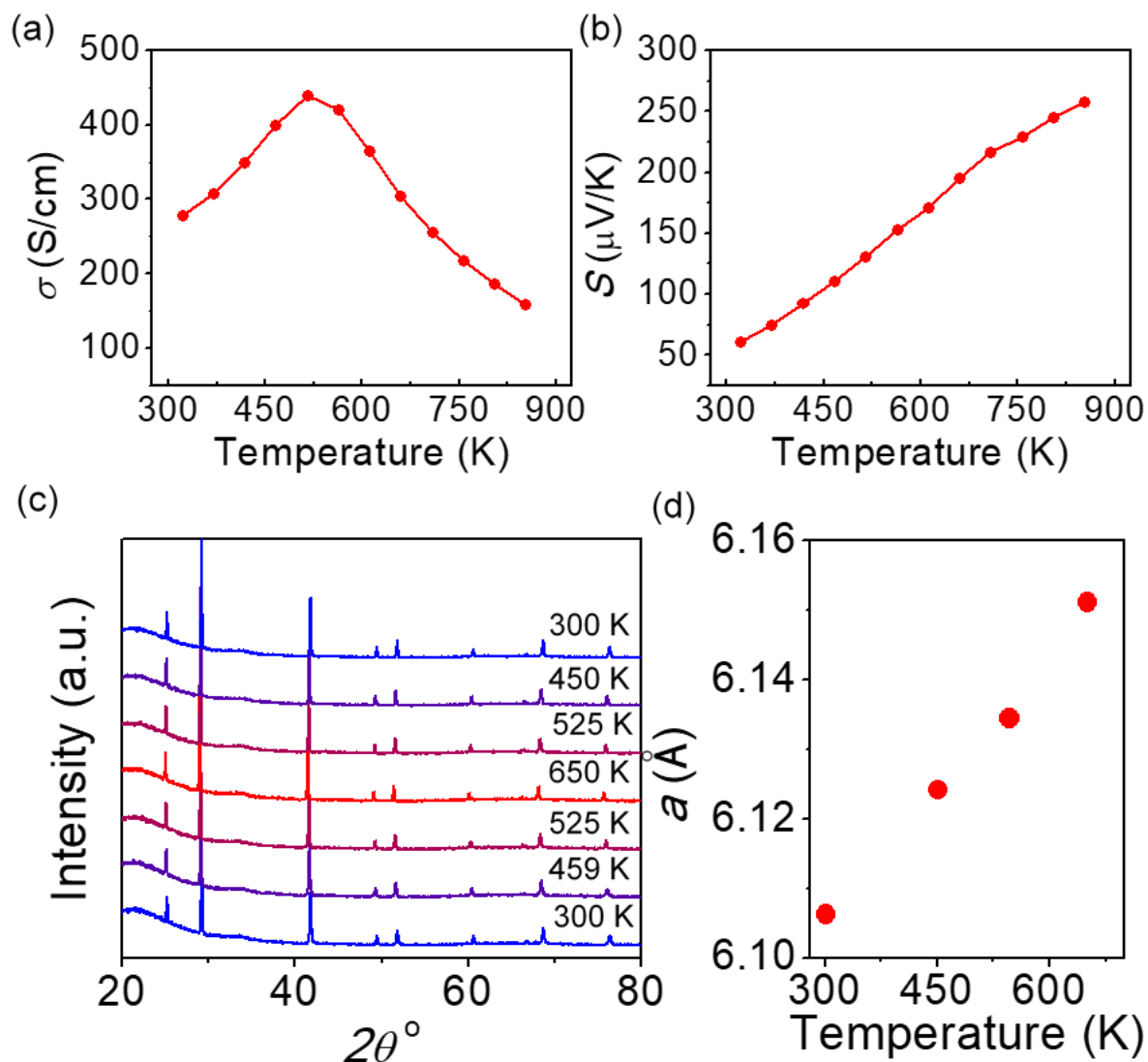


Figure 3.12 Temperature-dependent (a) electrical conductivity, (b) Seebeck coefficient, (c) variable-temperature powder X-ray diffraction patterns of a p-type $\text{NaPb}_m\text{SbSe}_{m+2}$ sample with nominal composition $\text{Na}_{1.10}\text{Pb}_{9.90}\text{Sb}_{0.90}\text{Se}_{12}$, and (d) refined lattice parameters from first four patterns shown in (c). The PXRD patterns show no clear changes upon heating and cooling, and the lattice parameters increase nearly linearly with heating as expected. These results suggest the unorthodox semiconducting-like electrical conductivity and turnover to metallic charge transport above in (a) is not from a change in phase or change in dopant solubility.

experimental electrical conductivities shown in Figure 3.4a deviate dramatically from this expectation, with semiconducting-like thermally activated conduction up to ~500 K. The Hall effect data adds to the puzzle, showing that the carrier concentrations are nearly constant over the temperatures of interest, implying the charge carrier mobilities increases with temperature under 500 K as shown in the inset of Figure 3.4d. This type of charge transport behavior is rarely observed in PbTe or PbSe and is therefore a highly unorthodox finding for a degenerately doped lead chalcogenide. To investigate if the unusual electrical behavior is from a phase change or temperature dependent increase in dopant solubility, we performed in-situ PXRD over 300–650 K. The variable temperature PXRD patterns shown in Figure 3.12 are unchanged with heating, and the corresponding lattice parameters increase linearly, indicating a different origin for the strange charge transport.

Similar results have been reported in the analogous systems $\text{AgPb}_m\text{SbSe}_{m+2}$ ¹⁴⁰ and $\text{AgPb}_m\text{SnSe}_{m+2}$,¹⁴¹ and also in SnSe ¹⁴² and Mg_3Sb_2 -based thermoelectrics,^{56, 69} all of which show thermally activated charge carrier mobilities well above room temperature. In $\text{AgPb}_m\text{SnSe}_{m+2}$ and Mg_3Sb_2 , the atypical charge transport mechanism was first suggested to be ionized impurity scattering, which generally gives carrier mobilities with positive $T^{1.5}$ temperature dependence and was shown to be in good agreement with the experimental data for these respective compounds. Here, however, we believe that ionized impurity scattering is insufficient to explain the experimental data, namely the Seebeck coefficients. This is best illustrated by inspecting the general equation for the Seebeck coefficient, assuming a single parabolic band, as shown below:

$$S = \frac{k_B}{e} \left(\frac{(r+5/2)F_{r+3/2}(\eta)}{(r+3/2)F_{r+1/2}(\eta)} - \eta \right) \quad (3.2)$$

where k_B is the Boltzmann constant, η is the reduced chemical potential, $F_r(n)$ are the Fermi-Dirac integrals, and r is a constant that is reflective of the energy dependence of the carrier relaxation time. Because the temperature dependence of S is contained in the $F_r(n)$ terms, Equation 2 clearly demonstrates that the Seebeck coefficient is a strong function of r . In the cases of acoustic phonon and ionized impurity carrier scattering, r is equal to $-1/2$ and $3/2$ respectively. Therefore, if the positive temperature dependence of the carrier mobilities measured in $\text{NaPb}_m\text{SbSe}_{m+2}$ is indeed due to ionized impurity scattering, r would switch from $3/2$ to $-1/2$ between 400–500 K when acoustic phonon scattering begins to dominate the transport. According to Equation 1, such a change in r would dramatically alter the temperature dependence of the Seebeck coefficients, which is clearly not observed in Figure 3b; as such, we conclude that ionized impurity scattering is insignificant in our samples.

Recently, Kuo *et al.* have pointed out the same issue in their analysis of Mg_3Sb_2 .⁶⁸ In the place of ionized impurity scattering, they proposed a model of grain boundary (GB) dominated electrical transport which provides a good theoretical prediction of both the electrical conductivities and Seebeck coefficients. In short, their model expanded on previous works, highlighting that electrostatic potential barriers can form at the grain boundaries of some polycrystalline materials, possibly originating from inhomogeneity, phase separation, lattice mismatch, defects, or impurities.¹⁴²⁻¹⁴⁴ If the barrier height is sufficiently high, the charge carriers would require considerable thermal energy to pass the grain boundaries and participate in electrical conduction. Therefore, as temperature is increased an increasing number of electrons or holes will overcome the grain boundary potentials, thereby augmenting the carrier mobility as the material is heated. At high enough temperatures, a sufficient number of charge carriers can cross the grain

boundary barriers and acoustic phonon scattering becomes the dominant mechanism, giving the classical negative temperature dependence of the carrier mobility and electrical conductivity.

The GB model is in excellent qualitative agreement with the electrical properties measured here in $\text{NaPb}_m\text{SbSe}_{m+2}$, and we believe it is the origin of the unanticipated charge transport. Because the GB scattering significantly degrades the charge carrier mobility, while providing no competing beneficial effects, it is an undesirable feature in thermoelectric materials and should be eliminated if possible. Therefore, this indicates that $\text{NaPb}_m\text{SbSe}_{m+2}$ likely has room for further improvement, as the GB scattering is severely detrimental to the power factor at lower temperatures.⁶⁸

3.3 Summary and Conclusions

$\text{NaPb}_m\text{SbSe}_{m+2}$ (PbSe-NaSbSe_2) compounds were synthesized over the range $m = 2-30$ (3–33% NaSbSe_2), and the thermoelectric properties were investigated with a focus on $m = 10$ (~9% NaSbSe_2). We show that the high solubility of NaSbSe_2 in PbSe facilitates two beneficial effects on the thermoelectric properties. The NaSbSe_2 both flattens the bands and lowers the energy separation between L and Σ valence bands, allowing both bands to contribute to the transport even near room temperature and resulting in high power factors of $\sim 2-13 \mu\text{W}\cdot\text{cm}^{-1}\cdot\text{K}^{-2}$ in the intermediate temperature interval of 323 and 700 K. Additionally, strong point defect phonon scattering from the crystallographic disorder of Na^+ , Pb^{2+} , and Sb^{3+} results in exceptionally low lattice thermal conductivities of $\sim 1-0.55 \text{ W}\cdot\text{m}^{-1}\cdot\text{K}^{-1}$ over 400–873 K without nanostructuring. Together, the high Seebeck coefficients and broad interval of low lattice thermal conductivity produces maximum ZT s approaching 1.4 at 873 K and outstanding ZT_{avg} of 0.64 between 400–873

K, marking nearly a 20% improvement over existing tellurium free PbSe based thermoelectric materials. We moreover find that $\text{NaPb}_m\text{SbSe}_{m+2}$ exhibits highly unusual semiconducting charge transport below ~ 500 K, which we ascribe to charge carrier scattering at the grain boundaries. Because the GB scattering degrades the power factor at low temperatures under 500 K, future enhancement to the thermoelectric performance can likely be expected through engineering the grains in order to eliminate the undesired scattering.

3.4 Experimental Section

3.4.1 Synthesis and processing

The starting materials were as follows: Pb wire (99.99%, American Elements, USA), Se shot (99.99%, American Elements, USA), Sb shot (99.999%, American Elements, USA), and Na cubes (99.95%, Sigma Aldrich). Prior to synthesis, a razor blade was used to scrape the surface oxidation off the lead and sodium pieces. All sodium was handled in a N_2 filled glovebox.

Polycrystalline ingots with nominal compositions of $\text{NaPb}_m\text{SbSe}_{m+2}$, $\text{Na}_{1+x}\text{Pb}_{10-x}\text{SbSe}_{12}$, and $\text{Na}_{1+x}\text{Pb}_{10}\text{Sb}_{1-x}\text{Se}_{12}$ were synthesized by weighing stoichiometric quantities of each element (15 g total for each sample) into 13 mm diameter carbon coated fused silica tubes that were then flame sealed at $\sim 2 \times 10^{-3}$ Torr. The tubes were heated in a box furnace to 773 K over 12 h, held for 2 h, then heated to 1473 K over 7 h where they were held for 5 h. The tubes were next quenched in ice water followed by annealing at 773 K for 12 h. After annealing, the tubes were again quenched in water, and the ingots were removed and ground to a fine powder with a mortar and pestle. To provide a homogeneous powder, the powders were passed through a 53 μm mesh sieve, then loaded into 12.7 mm graphite dies, and sintered into dense pellets by spark plasma sintering

(SPS-211LX, Fuji Electronic Industrial Co. Ltd) at 823 K and 40 MPa for 10 min. The pellets were finally cut and polished into bars and squares of approximate dimensions $3 \times 3 \times 10 \text{ mm}^3$ and $6 \times 6 \times 2 \text{ mm}^3$ for electrical and thermal characterization respectively. The cuts were made such that transport measurements were conducted perpendicular to the pressing direction in the SPS.

3.4.2 Thermoelectric Measurement

Using the $3 \times 3 \times 10 \text{ mm}^3$ bars, the Seebeck coefficients and electrical conductivities were measured jointly between room temperature and 873 K using an Ulvac Riko ZEM-3 instrument operating with partial He backpressure. To limit outgassing at elevated temperatures, the bars were spray-coated with boron nitride aerosol prior to measurements except at the points needed for contacts with the electrodes and thermocouples. The uncertainty in the electrical measurements is approximately 5%, which is well accepted for ZEM-3 instruments.¹⁰⁵ All samples showed hysteresis between the initial heating and cooling profile; however, because the properties generally stabilized upon cooling and become reversible upon further heating/cooling cycles, the data reported in this work is from the cooling profile.

The thermal diffusivities (D) were measured with the laser flash method using the $6 \times 6 \times 2 \text{ mm}^3$ squares in a Netzsch LFA-457 instrument, and the data was analyzed using a Cowen model with pulse correction. Before each measurement, the samples were spray coated with a thin graphite layer to prevent errors from emissivity. The total thermal conductivities were obtained from the relation $\kappa_{tot} = DC_p d$, in which C_p is the constant pressure heat capacity and d is the density. The densities were calculated using the sample masses and geometries, and C_p was estimated from the relationship C_p/k_b (*per atom*) = $3.07 + 4.7 \times 10^{-4}(T - 300)$.¹⁰⁶ This

equation has an estimated uncertainty of ~2% across the measured temperature range. To ensure consistency with the electrical properties, the thermal data reported in this work was also obtained from the cooling cycle. The uncertainty in the total thermal conductivity arising from the measurements and calculations of the density, heat capacity, and diffusivity is estimated to be approximately 8%.¹⁰⁵

Table 3.1 Measured densities and fraction of the theoretical density (obtained by refinement of the powder XRD patterns) of $\text{NaPb}_m\text{SbSe}_{m+2}$, $\text{Na}_{1+x}\text{Pb}_{10-x}\text{SbSe}_{12}$, and $\text{Na}_{1+x}\text{Pb}_{10}\text{Sb}_{1-x}\text{Se}_{12}$. The densities were measured from the masses and volumes of the ~6x6x2 mm² squares.

Compound	Density (g·cm ⁻³)	% of theoretical
$\text{NaPb}_{30}\text{SbSe}_{32}$	7.831	97
$\text{NaPb}_{18}\text{SbSe}_{20}$	7.675	97
$\text{NaPb}_{14}\text{SbSe}_{16}$	7.715	98
$\text{NaPb}_{10}\text{SbSe}_{12}$	7.525	98
$\text{NaPb}_8\text{SbSe}_{10}$	7.33	96
$\text{NaPb}_4\text{SbSe}_6$	7.056	98
$\text{NaPb}_2\text{SbSe}_4$	6.321	96
$\text{Na}_{1.01}\text{Pb}_{9.99}\text{SbSe}_{12}$	7.292	95
$\text{Na}_{1.03}\text{Pb}_{9.97}\text{SbSe}_{12}$	7.32	95
$\text{Na}_{1.05}\text{Pb}_{9.95}\text{SbSe}_{12}$	7.35	95
$\text{Na}_{1.10}\text{Pb}_{9.90}\text{SbSe}_{12}$	7.446	97
$\text{Na}_{1.15}\text{Pb}_{9.85}\text{SbSe}_{12}$	7.469	97
$\text{Na}_{1.20}\text{Pb}_{9.80}\text{SbSe}_{12}$	7.291	95
$\text{Na}_{1.05}\text{Pb}_{10}\text{Sb}_{0.95}\text{Se}_{12}$	7.502	97
$\text{Na}_{1.10}\text{Pb}_{10}\text{Sb}_{0.90}\text{Se}_{12}$	7.348	95
$\text{Na}_{1.15}\text{Pb}_{10}\text{Sb}_{0.85}\text{Se}_{12}$	7.254	94

3.4.3 Calculation of the Lorenz number and estimation of the lattice thermal conductivity

For the nominally undoped $\text{NaPb}_m\text{SbSe}_{m+2}$ compounds, we calculated the Lorenz number using the following equation for nondegenerate semiconductors:^[1]

$$L = \left(r + \frac{5}{2}\right) \left(\frac{k_B}{e}\right)^2 \quad (3.3)$$

Where k_B is the Boltzmann constant, e is the electron charge, and r gives the energy dependence of the relaxation time. Here, we used $r = -1/2$ characteristic of acoustic phonon scattering, which yields $L = 1.485 \times 10^{-8} \text{ V}^2 \cdot \text{K}^{-2}$. While the acoustic phonon scattering assumption is not valid in our compounds under 500 K where grain boundary scattering dominates the transport, we expect this to ultimately contribute negligible errors to the estimation of the lattice thermal conductivities in the undoped samples because the electrical conductivities are all very low (under $80 \text{ S} \cdot \text{cm}^{-3}$).

In the case of the doped samples: $\text{Na}_{1+x}\text{Pb}_{10-x}\text{SbSe}_{m+2}$ and $\text{Na}_{1+x}\text{Pb}_{10}\text{Sb}_{1-x}\text{Se}_{m+2}$, we estimated the temperature dependence of L by fitting the reduced chemical potential η to the measured Seebeck coefficients as shown below:^[2]

$$S = \frac{k_B}{e} \left(\frac{2F_1(\eta)}{F_0(\eta)} - \eta \right) \quad (3.4)$$

where $F_j(\eta)$ are the Fermi-Dirac integrals defined as follows:

$$F_j(\eta) = \int_0^\infty \frac{\varepsilon^j d\varepsilon}{1 + e^{(\varepsilon - \eta)}} \quad (3.5)$$

and ε is the reduced carrier energy. The values of η that fit the temperature-dependent Seebeck coefficients were then used to calculate L through

$$L = \left(\frac{k}{e}\right)^2 \left(\frac{3F_0(\eta)F_2(\eta) - 4F_1(\eta)^2}{F_0(\eta)^2} \right) \quad (3.6)$$

This fitting process assumes a single parabolic band dominated by acoustic phonon scattering and an energy-independent scattering time. Calculated values of L and the corresponding electronic thermal conductivities in Figures 3.13–3.16,

Once we determined the temperature depend values of L , the electronic (κ_{elec}) and lattice (κ_{lat}) thermal conductivities were calculated using the following:

$$\kappa_{elec} = \sigma LT \quad (3.7)$$

$$\kappa_{lat} = \kappa_{tot} - \kappa_{elec} \quad (3.8)$$

Where σ is the electrical conductivity, T is the absolute temperature and κ_{tot} is the total thermal conductivity.

3.4.4 Hall Effect

The Hall effect measurements were completed using an AC 4-probe method in a homemade system with excitation fields of ± 0.5 Tesla. The system uses an air-bore, helium-cooled superconducting magnet to generate the field within a high temperature oven that surrounds the Ar-filled sample probe. The carrier density n_H was calculated from the Hall coefficient assuming a single carrier band, i.e., $n_H = 1/eR_H$, where R_H is the Hall coefficient. The estimated error is based on the standard deviation of several data points at a single temperature. The measured Hall coefficients are given in Table 3.3.

Table 3.2 Room temperature Hall coefficients and Hall carrier densities for $\text{Na}_{1+x}\text{Pb}_{10-x}\text{SbSe}_{12}$ and $\text{Na}_{1.10}\text{Pb}_{10}\text{Sb}_{0.90}\text{Se}_{12}$.

Compound	R_H ($\text{cm}^3 \cdot \text{C}^{-1}$)	n_H (10^{19}cm^{-3})
$\text{Na}_{1.01}\text{Pb}_{9.99}\text{SbSe}_{12}$	14.494	0.043
$\text{Na}_{1.03}\text{Pb}_{9.97}\text{SbSe}_{12}$	0.284	2.198
$\text{Na}_{1.05}\text{Pb}_{9.95}\text{SbSe}_{12}$	0.097	6.433
$\text{Na}_{1.10}\text{Pb}_{9.90}\text{SbSe}_{12}$	0.062	10.028
$\text{Na}_{1.15}\text{Pb}_{9.85}\text{SbSe}_{12}$	0.044	14.239
$\text{Na}_{1.10}\text{Pb}_{10}\text{Sb}_{0.90}\text{Se}_{12}$	0.032	19.681

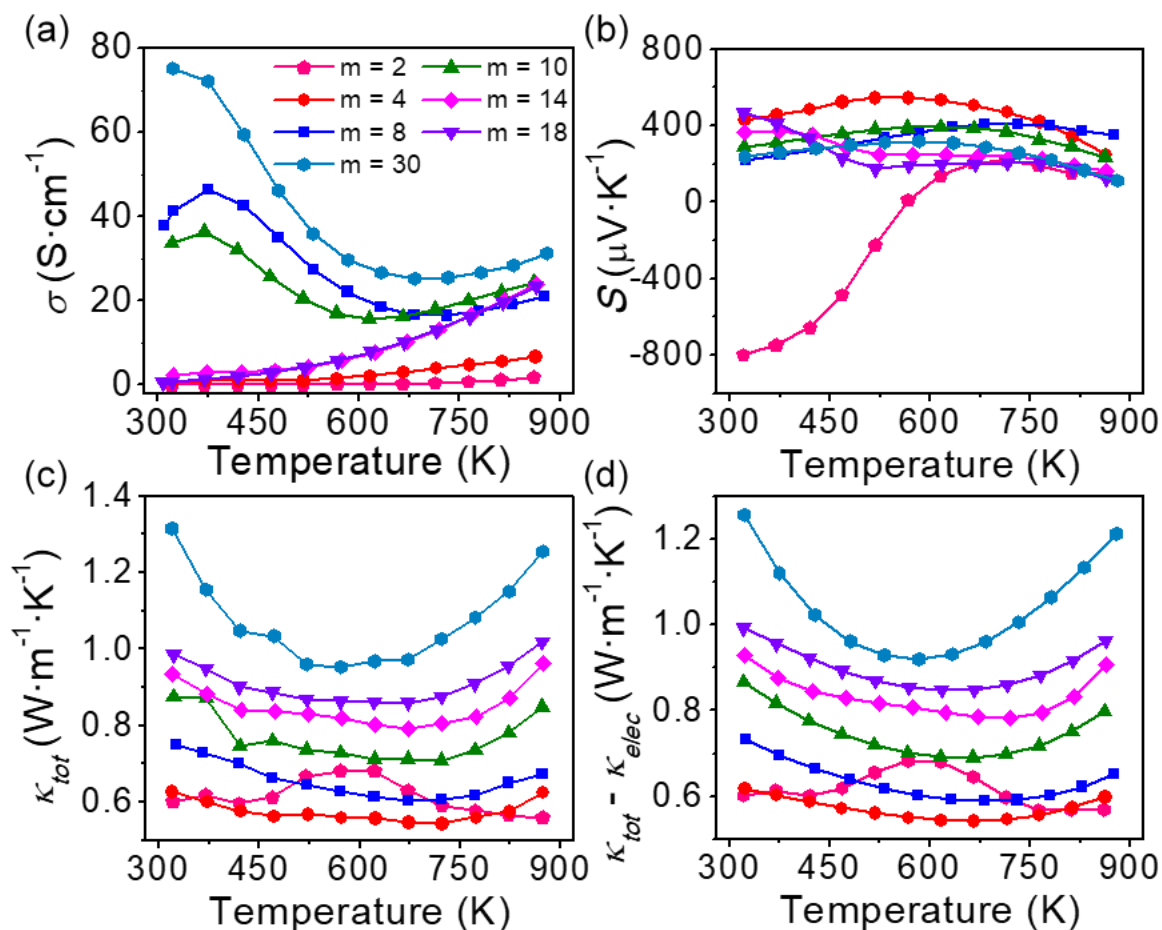


Figure 3.13 Temperature-dependent thermoelectric properties of nominally undoped of $\text{NaPb}_m\text{SbSe}_{m+2}$ ($m = 2-30$). (a) electrical conductivity, (b) Seebeck coefficients, (c) total thermal conductivity, and (d) estimated lattice thermal conductivity ($\kappa_{tot} - \kappa_{elec}$). The $m = 8, 10$, and 30 samples have slightly higher p-type electrical conductivities, potentially arising from cation vacancies or slight off-stoichiometry during the synthesis; the other compounds behave as undoped semiconductors as expected. All compounds show strong bipolar diffusion above 600 K, consistent with low charge carrier densities.

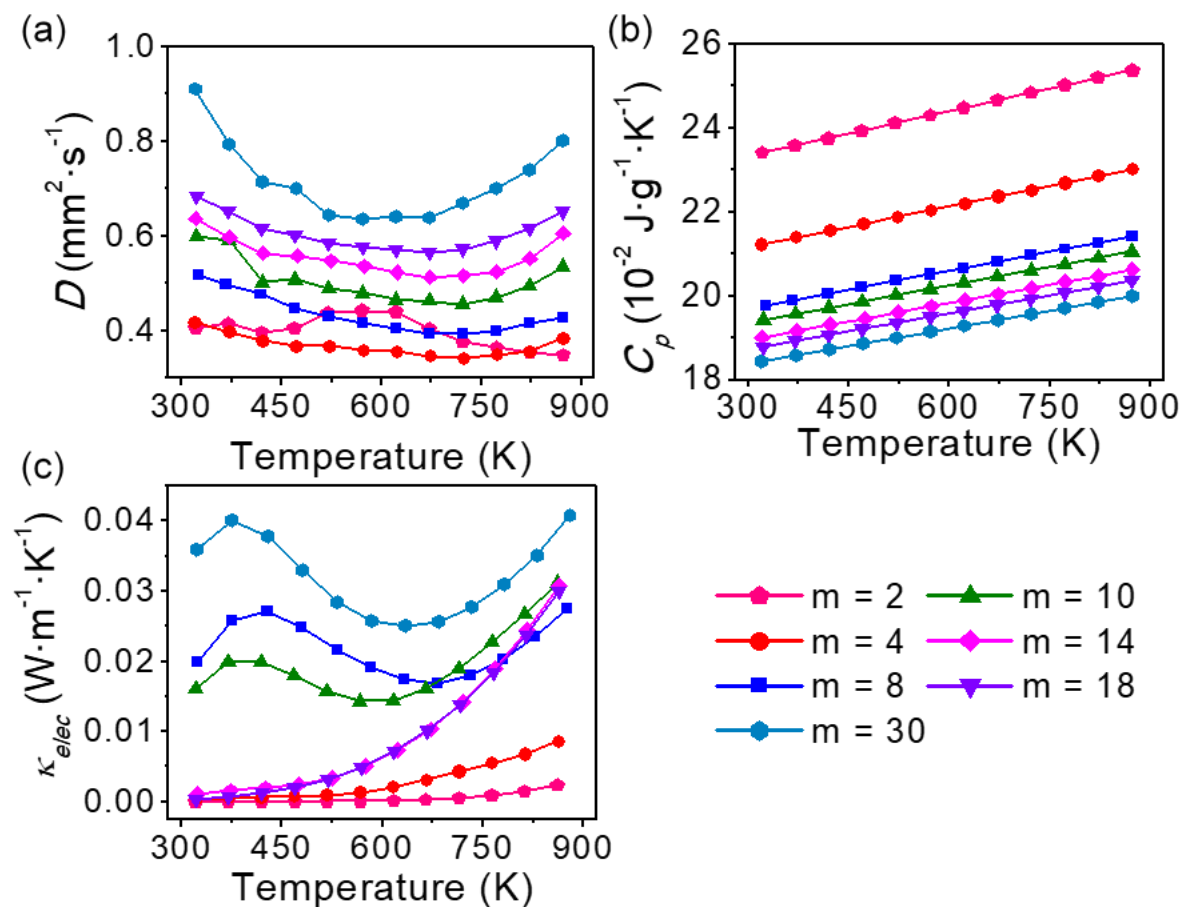


Figure 3.14 Temperature-dependent (a) thermal diffusivities, (b) estimated specific heats, (c) and calculated electronic thermal conductivities of nominally undoped $\text{Na}_{1+x}\text{Pb}_{10-x}\text{SbSe}_{12}$ ($m = 2-30$). For all samples shown above we used $L = 1.485 \times 10^{-8} \text{ V}^2 \cdot \text{K}^{-2}$.

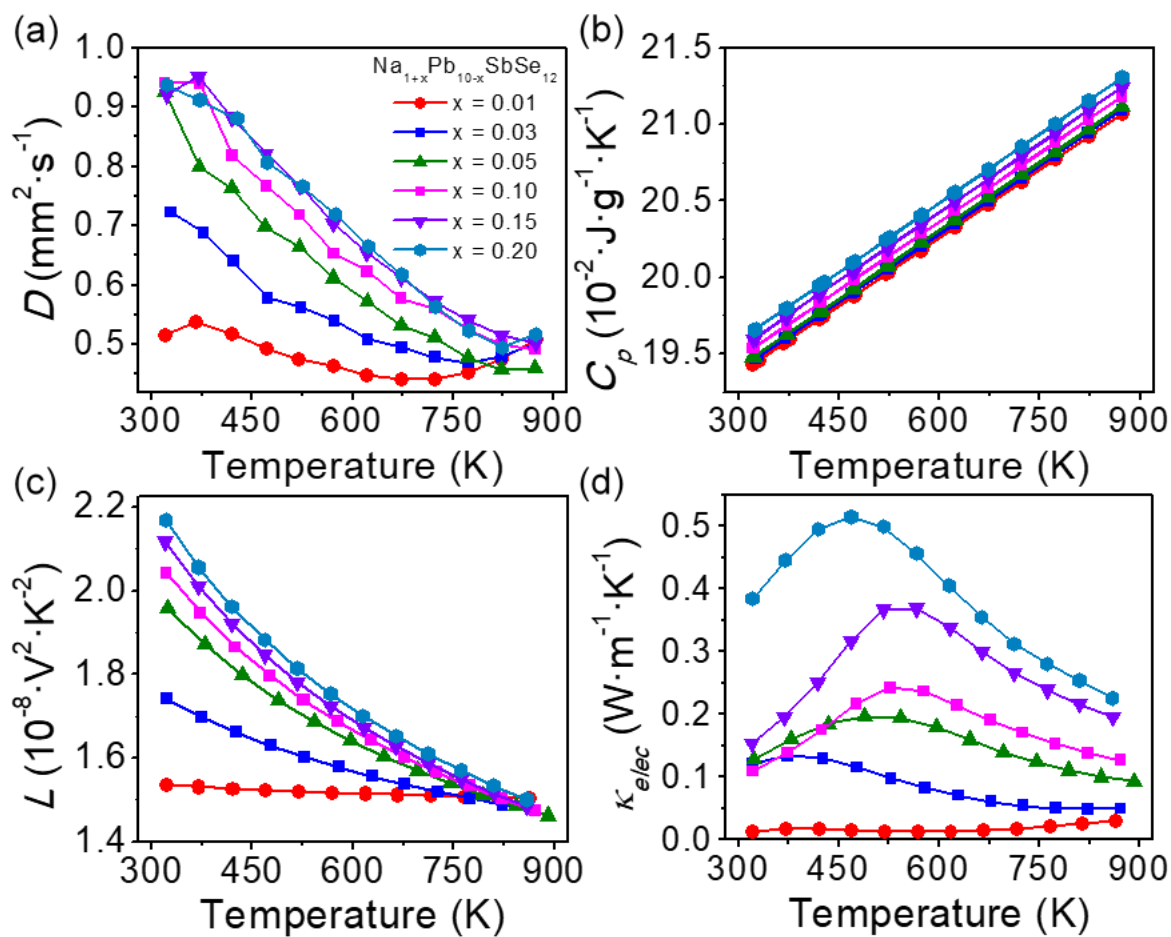


Figure 3.15 Temperature-dependent (a) thermal diffusivities, (b) estimated specific heats, (c) Lorentz numbers, and (d) calculated electronic thermal conductivities of $\text{Na}_{1+x}\text{Pb}_{10-x}\text{SbSe}_{12}$.

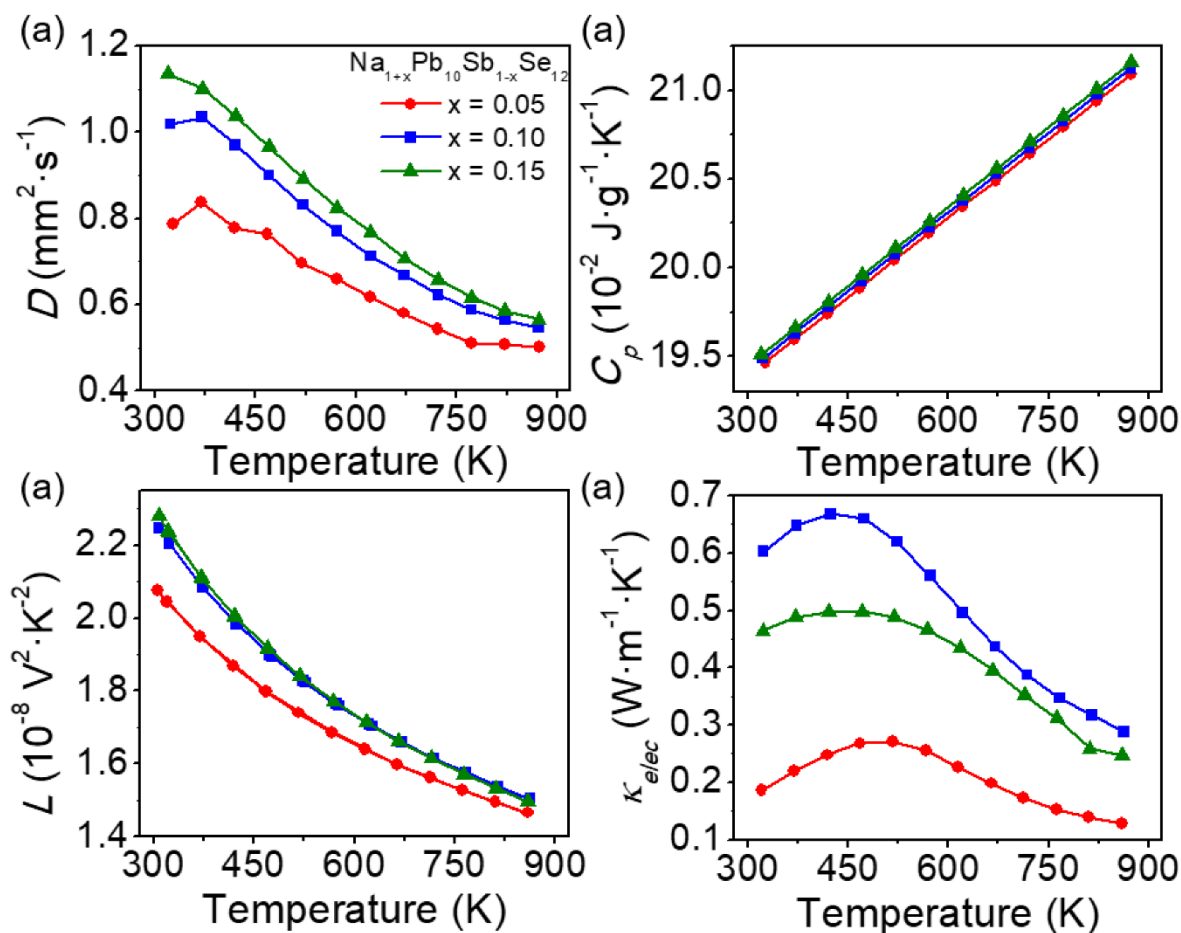


Figure 3.16 Temperature-dependent (a) thermal diffusivities, (b) estimated specific heats, (c) Lorentz numbers, and (d) calculated electronic thermal conductivities of $\text{Na}_{1+x}\text{Pb}_{10}\text{Sb}_{1-x}\text{Se}_{12}$.

3.4.5 Microscopy characterization

To prepare for analysis with scanning electron microscopy-energy dispersive spectroscopy (SEM-EDS), bulk samples were ground and polished to remove maximum surface deformation and reveal the true pristine sample structure. The samples were first ground using SiC grinding paper of grit size 600, 800, and 1200 for 5 min each to produce an even surface with minimal roughness. Ethanol was used as the water-free lubricant, as the samples contain Na. Next, the

samples were polished using a polishing pad and water-free diamond slurry of particle size 1 μm , and 0.1 μm for 15 min and 30 min respectively. Finally, the sample was placed in a vibratory polisher with 0.05 μm alumina for 3 hours to achieve the final surface finish. SEM analysis was performed at 30 kV using a Hitachi S-3400N-II SEM.

S/TEM samples were polished on one surface in the same manner as the SEM samples, with the exception of the vibratory polishing step. Once the top surface was polished, a TEM grid was fastened to the polished surface using M-Bond. The sample was then thinned using 600 and 800 grit SiC grinding paper until it was less than 80 μm thick (again using ethanol as the water-free lubricant). Next, the sample was dimpled, and subsequently thinned with an argon ion mill at cryogenic temperatures. Milling took place at 2.8 kV and 8° until a hole was formed in the sample, forming an electron transparent wedge at the edge of the hole. Final milling took place at 1.5 kV and 6° , and 0.3 kV at 4° for 90 min each to properly clean the sample surface and remove any sample defects potentially introduced by higher energy ion milling. STEM was performed at 200kV using a JEOL JEM-2100 FasTEM, and high resolution TEM was performed at 300 kV using a JEOL ARM300F GrandARM TEM.

3.4.6 Photoemission spectroscopy

The work functions (Valance band maxima), were measured by photoemission yield spectroscopy in air (PESA, AC-2, Riken-Keiki). In PYSA, the sample is scanned by tunable monochromatic ultraviolet light (UV, 4.2-6.2 eV) under ambient conditions, and the number of generated photoelectrons are measured at each excitation energy. Photoelectrons are only

generated when the photon energy is higher than the work function. The work function is determined by finding the onset of the PESA spectra.

3.4.7 Electronic structure calculations

Density Functional Theory (DFT)¹⁴⁵⁻¹⁴⁶ calculations were performed using the Vienna ab initio Simulation Package (VASP)^{113, 147-149} with projector augmented (PAW)¹⁵⁰ pseudopotentials utilizing Perdew- Burke-Ernzerhof (PBE) generalized gradient approximation (GGA) exchange correlation¹⁵¹. NaSb-doped PbSe calculations were performed on 54-atom supercells created by Pb atoms with Na and Sb. We calculated the energies of Na and Sb placed far from or near each other in the PbSe lattice and selected those with lower energies. For Pb and Na atoms, the semicore d and p electrons were treated as valence states, respectively. Both relaxation calculations and band structure calculations were performed with a plane-wave basis cutoff energy of 520 eV. The total energies were converged within 10^{-6} eV with a Monkhorst–Pack k-mesh¹⁵² with 8000 k-points per reciprocal atom in the Brillouin zone. Spin-orbit coupling (SOC) is taken into account only in our band structure calculations.

3.4.8 Powder X-ray diffraction

Powder X-ray diffraction (PXRD) patterns were measured on a Rigaku Miniflex 600 instrument with Cu K α radiation ($\lambda = 1.5406 \text{ \AA}$) at 40 kV and 15 mA and with a K β filter. Lattice parameters were refined using the Rietveld method in GSAS-II software.

3.4.9 Fourier transformed infrared spectroscopy (FT-IR)

Optical band gaps were determined by diffuse reflectance measurements performed with a Nicolet 6700 FT-IR spectrometer. Samples consisted of powders prepared by finely grinding the SPSe_d NaPb_{*m*}SbSe_{*m*+2} in a mortar and pestle. The reflectance data was converted to absorption with the Kubelka–Munk equation $\alpha/S = (1-R)^2/2R$ where R is the reflectance, and α and S are the absorption and scattering coefficients, respectively. The band gaps were estimated by extrapolating the absorption edges of each spectra.

3.4.10 Impact of the grain boundary charge carrier scattering on the estimated lattice thermal conductivity

As discussed above, the process described above will impede reliable estimation of the lattice thermal conductivity. This occurs because most of the heat transported by charge carriers will come from the electrical conduction in the bulk grains, where σ is presumably much higher than our measured values. Our measured σ are lower than the true bulk values because the electrical conductivities are dominated by the GBs below 500 K. As a consequence, the values of σ measured below 500 K reflect only the electrical conduction at the GBs, leaving the bulk electrical conductivity unknown. Therefore, our estimations of κ_{elec} also are reflective only of the GBs and are severely underestimated when the GB charge carrier scattering is strong, leading to potentially severe overestimation of κ_{lat} . Indeed, comparing the κ_{lat} presented in Figure 3.5b with the corresponding electrical conductivities plotted in Figure 3.4a, we indeed see that the compounds with strongest GB scattering ($x = 0.05$ – 0.15) appear to have the highest estimated lattice thermal conductivities under 500 K, exactly as anticipated from the above analysis.

3.4.11 Pisarenko plots

To compliment the predictions of band convergence indicated by the DFT calculated band structures, we compared theoretical plots of carrier density (n) vs. Seebeck coefficient generated using a single Kane band (SKB) model and a two-band model. The SKB Pisarenko plots utilized following equations,

$$n = \frac{(m_{DOS}^* k_B T)^{3/2}}{2\pi^2 \hbar^3} {}_0F_0^{3/2} \quad (3.9)$$

where m_{DOS}^* is the density of states effective mass and \hbar is the Planck constant. The Hall coefficient R_H and carrier density are related by:

$$R_H = A/en \quad (3.10)$$

and A is the Hall factor given as:

$$A = \frac{3K(K+2)}{(2K+1)^2} \frac{{}_0F_{-4}^{1/2} \cdot {}_0F_0^{3/2}}{({}_0F_{-2}^1)^2} \quad (3.11)$$

Where K parameterizes the anisotropy of the band structure and is equal to 1.75 for PbSe. The Seebeck coefficients are calculated as follows:

$$S = \frac{k_B}{e} \left(\frac{{}_1F_{-2}^1}{{}_0F_{-2}^1} - \eta \right) \quad (3.12)$$

Where η is the reduced chemical potential. The functions ${}_nF_k^m$ are of the following form,

$${}_nF_k^m = \int_0^\infty \left(\frac{-df}{d\varepsilon} \right) \varepsilon^n (\varepsilon + \alpha \varepsilon^2)^m [(1 + \alpha \varepsilon)^2 + 2]^{k/2} d\varepsilon \quad (3.13)$$

with $\alpha = \frac{k_b T}{E_g}$ and E_g is the band gap. For the SKB Pisarenko plot calculations, we kept all of the above variables constant and varied the band effective mass to achieve the best fit to the experimental data. The band effective mass is related to the density of states mass through the band degeneracy N_v :

$$m_{DOS}^* = N_v^{2/3} m_b^* \quad (3.14)$$

For the two-band model we utilized the relationships presented by Chasapis *et al.* in their work on Na doped PbSe. Here, the thermoelectric properties of the L -band were calculated using the equations shown above for a single Kane type band. The Σ -band uses the same equations but is considered parabolic by setting $\alpha = 0$ and $K = 1$. The parameters considered for the temperature dependent bands are shown below.

$$E_g = 0.25 + 0.0004 \cdot T \quad (3.15)$$

$$\Delta E_{L-\Sigma} = 0.22 - 0.00022 \cdot T \quad (3.16)$$

$$m_L^* = 0.14m_e \quad (3.17)$$

$$m_\Sigma^* = 0.475m_e \quad (3.18)$$

$$\eta_\Sigma = \eta_L - \Delta E_{L-\Sigma}/k_B T \quad (3.19)$$

Where $\Delta E_{L-\Sigma}$ is the energy difference between the two bands and m_L^* and m_Σ^* are respectively the band effective mass of the L - and Σ -bands, and η_Σ is the chemical potential of the Σ -band. The valley degeneracy of each band is 4 (L -band) and 12 (Σ -band). The temperature dependence of the L -band was assumed to follow the relationship $d\ln(m_b^*)/d\ln(T) = 0.5$ found by Wang *et al.*¹⁵³ Using the above parameters for each band, the carrier densities and Seebeck coefficients were calculated in the two-band model as follows:

$$n_H = n_L + n_\Sigma \quad (3.20)$$

$$S = \frac{S_L \sigma_L + S_\Sigma \sigma_\Sigma}{\sigma_L + \sigma_\Sigma} \quad (3.21)$$

3.4.11 Debye-Callaway model for theoretical lattice thermal conductivity

To gain insight into the origins of the low thermal conductivity measured in $\text{NaPb}_m\text{SbSe}_{m+2}$, we calculated theoretical values of κ_{lat} based on a simplified Debye-Callaway model.^{20, 125, 154} Here, we only considered phonon-phonon scattering (Umklapp and Normal processes) and point defect phonon scattering processes. The lattice thermal conductivity is given as follows:

$$\kappa_{lat} = \frac{k_B}{2\pi^2v} \left(\frac{k_B T}{\hbar}\right)^3 \int_0^{\theta_D/T} \tau_c(x) \frac{x^4 e^x}{(e^x - 1)^2} dx \quad (3.22)$$

Where $x = \hbar\omega/k_B T$ is the phonon frequency, θ_D is the Debye temperature, τ_c is the combined phonon relaxation time, and v is the phonon group velocity (equal to the average speed of sound in our polycrystalline samples). The combined relaxation time was found by summing the contributions from the various phonon scattering processes considered in our model.

$$\tau_c^{-1} = \tau_U^{-1} + \tau_N^{-1} + \tau_{PD}^{-1} \quad (3.23)$$

The above correspond to the relaxation times for Umklapp, normal, and point defect phonon scattering respectively. In principle, many more mechanisms may contribute to phonon scattering such as grain boundaries, precipitates, phase boundaries, electron phonon interaction, etc.; however, we found that our simplified model matches experimental the data well near room temperature, suggesting that point defect phonon scattering is the primary origin of the low thermal conductivity.

The relaxation times for Umklapp and Normal processes are given in the following equations:

$$\tau_U^{-1} = \frac{\hbar\gamma^2}{Mv^2\theta_D} \omega^2 T \exp\left(\frac{-\theta_D}{3T}\right) \quad (3.24)$$

$$\tau_N^{-1} = \beta\tau_U^{-1} \quad (3.25)$$

Where γ is the Gruneisen parameter, M is the average mass of an atom in the crystal, and β is a fitting constant used to determine the ratio of Umklapp to normal processes. β was determined by fitting the calculated values of κ_{lat} for experimental data to that of pure PbSe.

Lastly the relations for the point defect phonon scattering in a solid solution are shown below:

$$\tau_{PD}^{-1} = \frac{\omega^4 V}{4\pi v^3} \Gamma \quad (3.27)$$

$$\Gamma = \Gamma_M + \Gamma_S \quad (3.28)$$

where V is the average volume of an atom in the crystal, and Γ is the disorder scaling parameter which characterizes the phonon scattering from mass and strain field fluctuations between the host lattice and alloying atoms.

$$\Gamma_M = \frac{\sum_{i=1}^n c_i \left(\frac{\langle M_i \rangle}{M^*}\right)^2 f_i^1 f_i^2 \left(\frac{M_i^1 - M_i^2}{\langle M_i \rangle}\right)^2}{\sum_{i=1}^n c_i} \quad (3.29)$$

$$\Gamma_S = \frac{\sum_{i=1}^n c_i \left(\frac{\langle M_i \rangle}{M^*}\right)^2 f_i^1 f_i^2 \varepsilon \left(\frac{r_i^1 - r_i^2}{\langle r_i \rangle}\right)^2}{\sum_{i=1}^n c_i} \quad (3.30)$$

Where c_i is the degeneracy (here $c_i = 2$), f_i^k is the fractional occupation of atom k (Pb, Sb, Na), $\langle M_i \rangle$ and $\langle r_i \rangle$ are the average mass and radius of the i th sublattice ($\langle M_i \rangle = \sum_k f_i^k M_i^k$ and $\langle r_i \rangle = \sum_k f_i^k r_i^k$), and M^* is the average atomic mass of the compound ($M^* = \frac{1}{2} \sum_i \langle M_i \rangle$). ε is a phenomenological parameter related to the lattice anharmonicity which was found by fitting the experimental data. Here, we found $\varepsilon = 90$ to give a satisfactory fit, which is in reasonable agreement with previous studies on PbTe, which reported $\varepsilon = 110$.¹⁵⁴ The parameters used in the Debye-Callaway calculations are outlined below in Table 3.3.

Table 3.3 Constants and parameters used in the Debye-Callaway lattice thermal conductivity calculations for $\text{NaPb}_m\text{SbSe}_{m+2}$.

Parameters	Value
ν	1926.3 $\text{m}\cdot\text{s}^{-1}$
θ_D	125 K
γ	1.65
M_{Pb}	207.2 $\text{g}\cdot\text{mol}^{-1}$
M_{Se}	78.96 $\text{g}\cdot\text{mol}^{-1}$
M_{Na}	22.989 $\text{g}\cdot\text{mol}^{-1}$
M_{Sb}	121.76 $\text{g}\cdot\text{mol}^{-1}$
r_{Pb}	175 pm
r_{Se}	115 pm
r_{Na}	186 pm
r_{Sb}	136 pm
β (fit)	3.8
ε (fit)	90

Chapter Four

Understanding the thermally activated charge transport in $\text{NaPb}_m\text{SbQ}_{m+2}$ ($\text{Q} = \text{S, Se, Te}$)

thermoelectrics: weak dielectric screening leads to grain boundary dominated charge carrier scattering

Portions of this chapter were previously published in (*Energy & Environmental Science*, 2020, DOI: 10.1039/d0ee00491j) and are reprinted (adapted) with permission from Royal Society of Chemistry.

4.1 Introduction

Thermoelectric modules are quiet, reliable, and emission free systems capable of both converting heat into electrical energy and solid-state cooling. As such, thermoelectric technology is attractive for potential applications in waste heat recovery, remote electricity generation, space exploration, and environmentally friendly refrigeration.¹¹⁴⁻¹¹⁵ Indeed, over the past two decades, researchers directed intense efforts toward thermoelectrics, making significant progress in both the improvement of traditional thermoelectric materials^{38, 47, 49, 104, 155} and the discovery of new and promising candidates.^{56, 82, 156-157} Despite the steady advancement, the high cost and/or low efficiencies of most thermoelectric materials are impediments for thermoelectric technology to achieve widespread utilization, and improving material performance remains a key challenge facing the field. The maximum energy conversion efficiency of a thermoelectric material is parameterized by the dimensionless figure of merit $ZT = \sigma S^2 T / \kappa$ where σ is the electrical conductivity, S is the Seebeck coefficient, κ is the thermal conductivity, and T is the absolute temperature. In many of the most common thermoelectric materials ZT is maximized at temperatures greater than 600 K. However, because modules operate across a temperature gradient, maximizing the figure of merit at both hot and cold sides is critical to achieving the best performance.⁵⁵

The demand for large ZT values between low and high temperatures is particularly relevant in many emerging thermoelectric materials that exhibit seemingly anomalous thermally activated electrical conductivity below ~600 K. Examples include $\text{NaPb}_m\text{SbSe}_{m+2}$,¹⁵⁸ SnSe ,¹⁵⁹ Mg_3Sb_2 ,⁶⁹ KAlSb_4 ,⁷⁰ CoSb ,⁷¹ NbFeSb ,⁷³ and Ge-alloyed PbSe .¹¹⁸ An illustration of the temperature-dependent electrical conductivity observed in these materials is shown in Figure 4.1a. Considering

these are typically degenerately doped (e.g. charge carrier concentrations greater than $10^{19-20} \text{ cm}^{-3}$), such semiconducting-like behavior is highly irregular, as phonon scattering is expected to dominate the electrical transport and yield a negative temperature dependence at these doping concentrations.¹¹¹ From the standpoint of engineering high quality thermoelectrics, the unusual charge transport behavior is undesirable, as it suppresses the power factor (σS^2) at low temperatures and ultimately degrades the device figure of merit. Establishing a detailed understanding of the mechanism behind the low temperature carrier scattering and developing routes to mitigate its effect are therefore crucial application issues and are furthermore of fundamental interest.

In recent work on Mg_3Sb_2 , Kuo *et al.* explained the irregular electrical behavior by proposing that the charge carriers are strongly scattered by energy barriers present at the grain boundaries (GBs).⁶⁸ In polycrystalline forms of many traditional semiconductors such as Si, CdSe, and GaAs, energy barriers are known to form at the GBs and restrict electronic conduction.^{142-144, 160-163} Despite this, the impact of the GBs is rarely discussed in the context of charge transport in thermoelectric materials. Drawing on the previous work, Kuo *et al.* proposed that in Mg_3Sb_2 , otherwise mobile charge carriers are impeded when encountering the GBs, limiting the electrical conductivity at low temperatures; however, with heating, an increasing number of electrons or holes are thermally excited across the potential barriers, and the electrical conductivity rises. Eventually, when the temperature is sufficiently high, the expected phonon scattering becomes the dominant scattering mechanism, giving rise to the classic negative temperature dependence of the conductivity. This model shows that the combination of GB dominated transport at low

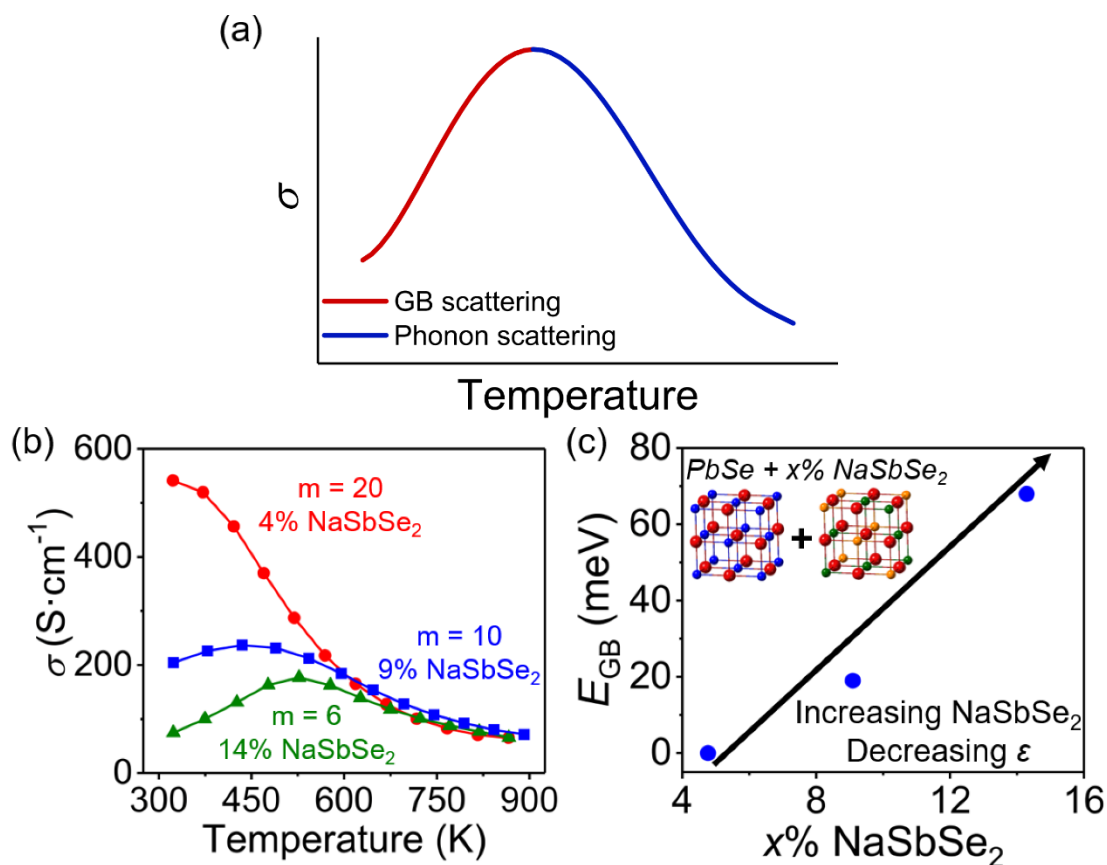


Figure 4.1 (a) Illustration of the unusual temperature dependence of the electrical conductivity observed in thermoelectric materials such as PbSe-NaSbSe₂ ($\text{NaPb}_m\text{SbSe}_{m+2}$), Mg₃Sb₂, SnSe, and Zintl antimonides. At low temperatures, charge carriers are scattered at the grain boundaries, leading to thermally activated conduction. Above a threshold temperature, the expected phonon scattering dominates the electronic transport. (b) Variable-temperature electrical conductivities for PbSe alloyed with ~4, 9, and 14 percent NaSbSe₂. The electrical conductivities are increasingly suppressed under ~600 K for greater NaSbSe₂ fraction. (c) Estimated energy barriers at the GBs for the samples in (b). As the more ionic NaSbSe₂ is added to PbSe, the charge carrier screening is weakened (decreased ϵ) and the barrier heights increase. The inset in (c) is a cartoon illustration of alloying NaSbSe₂ into PbSe to form $\text{NaPb}_m\text{SbSe}_{m+2}$.

temperatures and phonon scattering at high temperatures can produce the distinctive σ vs. T curve illustrated in Figure 4.1a.

While the GB model provides an accurate theoretical account of the otherwise mysterious electrical behavior, it also raises several important questions. Foremost, other models such as ionized impurity scattering can give qualitatively similar temperature dependent behavior and have also been invoked to explain the irregular transport properties.^{69, 141} Currently, debate remains on the proper microscopic description of the low-temperature scattering. Furthermore, there is little work addressing why some materials are seemingly more prone to this deleterious behavior than others. For example, both $\text{NaPb}_m\text{SbSe}_{m+2}$ and $\text{AgPb}_m\text{SbSe}_{m+2}$ families are reported to exhibit strong charge carrier scattering under ~ 500 K;^{140, 158} however, the closely related tellurides $\text{NaPb}_m\text{SbTe}_{m+2}$ and $\text{AgPb}_m\text{SbTe}_{m+2}$ behave as typical degenerate semiconductors.^{67, 85, 124}

Here, we address these issues by studying the unusual charge carrier scattering in alloys of PbSe with NaSbSe₂ ($\text{NaPb}_m\text{SbSe}_{m+2}$) and the chalcogenide analogues $\text{NaPb}_m\text{SbS}_{m+2}$ and $\text{NaPb}_m\text{SbTe}_{m+2}$. We first provide unambiguous evidence directly linking the thermally activated conductivity to the grain boundaries. By preparing $\text{NaPb}_m\text{SbSe}_{m+2}$ samples with identical chemical compositions and varying grain sizes, we show that the low-temperature scattering is suppressed, and the expected metallic behavior is recovered as the density of boundaries is reduced. We next propose simple chemical guidelines for addressing what compounds will be most susceptible to GB limited electrical conductivity. We suggest that GB scattering will be strongest in materials composed of ionic and weakly polarizable atoms where charge carriers are poorly screened from electric fields. We support this argument by studying the electrical properties of $\text{NaPb}_m\text{SbSe}_{m+2}$ as a function of NaSbSe₂ fraction. As shown in Figure 4.1b and 4.1c, we observe stronger GB

scattering and estimate higher GB energy barriers as increasing amount of the ionic NaSbSe₂ is alloyed into PbSe. We furthermore demonstrate that the GB scattering is strongest in the sulfides (NaPb_mSbS_{m+2}) but is completely absent in the tellurides (NaPb_mSbTe_{m+2}). Lastly, we discuss how this framework elegantly explains the presence of GB limited electrical conductivity in numerous ionic thermoelectric materials. We suggest how the insight provided by this work gives valuable intuition on engineering the proper microstructure for many emerging thermoelectric materials.

4.2 Results and Discussion

4.2.1 Experimental evidence for grain boundary charge carrier scattering in NaPb_mSbSe_{m+2}

Our previous work in chapter two established that NaPb_mSbSe_{m+2} has atypical electrical transport properties consisting of semiconducting electrical conductivity below 500 K despite being degenerately doped to charge carrier densities over 10²⁰ cm⁻³.¹⁵⁸ At the time, we suggested this behavior to be from GB charge carrier scattering, but without providing direct evidence. Indeed, other models such as ionized impurity scattering can in principle give a similar temperature dependence and have been invoked to explain comparable transport properties in Mg₃Sb₂.^{69, 141} Considering this, we sought to obtain conclusive experimental evidence regarding the source of the unusual charge transport properties measured in NaPb_mSbSe_{m+2}. To test if the thermally activated scattering is rooted at the GBs, we prepared large grained samples of NaPb_mSbSe_{m+2} with fewer GBs and compared the electrical properties with the data from our previously reported small grained SPS processed materials.¹⁵⁸

To prepare samples with a reduced number of GBs, we heated vacuum sealed tubes containing the starting reagents to 1473 K and held them at temperature for 5 h. The samples were

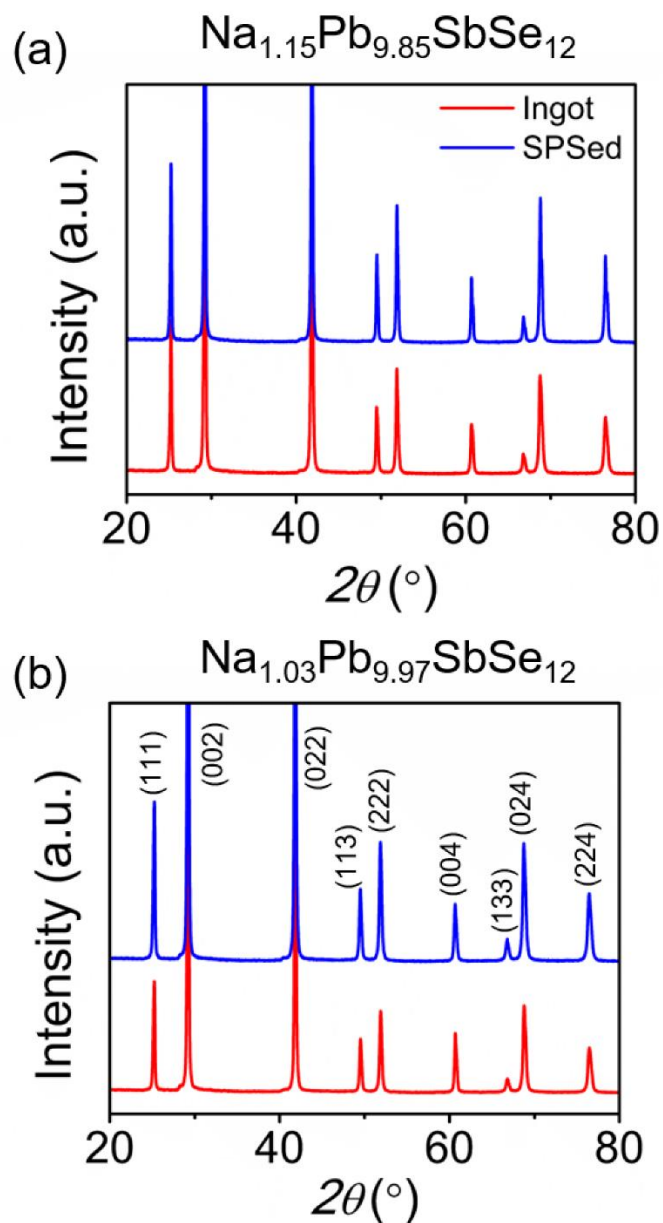


Figure 4.2 Comparison of the powder X-ray diffraction patterns of SPS-processed and as-cast ingots of p-type doped $\text{Na}_{1+x}\text{Pb}_{10-x}\text{SbSe}_{12}$. (a) is for $x = 0.15$ and (b) for $x = 0.03$. In both cases, the PXRD patterns show the expected peaks characteristic of the rocksalt structure with no evidence for secondary phases. These patterns suggest negligible chemical changes between SPS-processed and ingot forms.

next slowly cooled from 1473 K to 823 K over 48 h and then brought to room temperature in 12 h. This slow cooling procedure gave time for large grains (mm scale) to nucleate and yielded dense ingots with a relatively low number of GBs. More information on the grain size will be provided by the microscopy data discussed below. Because subsequent pulverization and SPS sintering gives samples with small grains and many boundaries, the as-cast ingots were directly cut and polished into $\sim 3 \times 3 \times 10 \text{ mm}^3$ bars to characterize the electrical properties. The synthesis is presented in greater detail in the experimental section. Powder X-ray diffraction patterns for both the as-cast ingots and SPS processed samples are presented in Figure 4.2. The diffraction patterns show negligible differences between samples, confirming the expected rocksalt crystal structure with no detectable secondary phases in any of the samples we analyzed.

The primary results are outlined in Figure 4.3, which shows a comparison of the grain structures and electrical properties of two differently doped samples of $\text{Na}_{1+x}\text{Pb}_{10-x}\text{SbSe}_{12}$ (nominally $\sim 9\%$ NaSbSe_2 in PbSe , with additional Na dopant fractions of $x = 0.03, 0.15$) prepared by slowly cooling the ingots and through rapid quenching and subsequent SPS processing. These compositions were chosen to compare the electrical properties of both lightly and heavily doped samples in small- and large-grained forms. We used electron backscatter diffraction (EBSD) to analyze the grain morphologies of the different samples. Figures 4.2a and 4.2b show characteristic EBSD images, demonstrating that while the SPS processed material contains relatively small grains on the order of $\sim 50 \text{ }\mu\text{m}$ or less in size, the slow cooled ingot has much larger grains on the millimeter scale. This implies a dramatically lower density of GBs in the slow cooled ingot. As anticipated from the GB scattering model, the lower GB density has direct consequences on the electrical conductivity. Most importantly, for both sample pairs ($x = 0.03$ and 0.15), Figure 4.2c

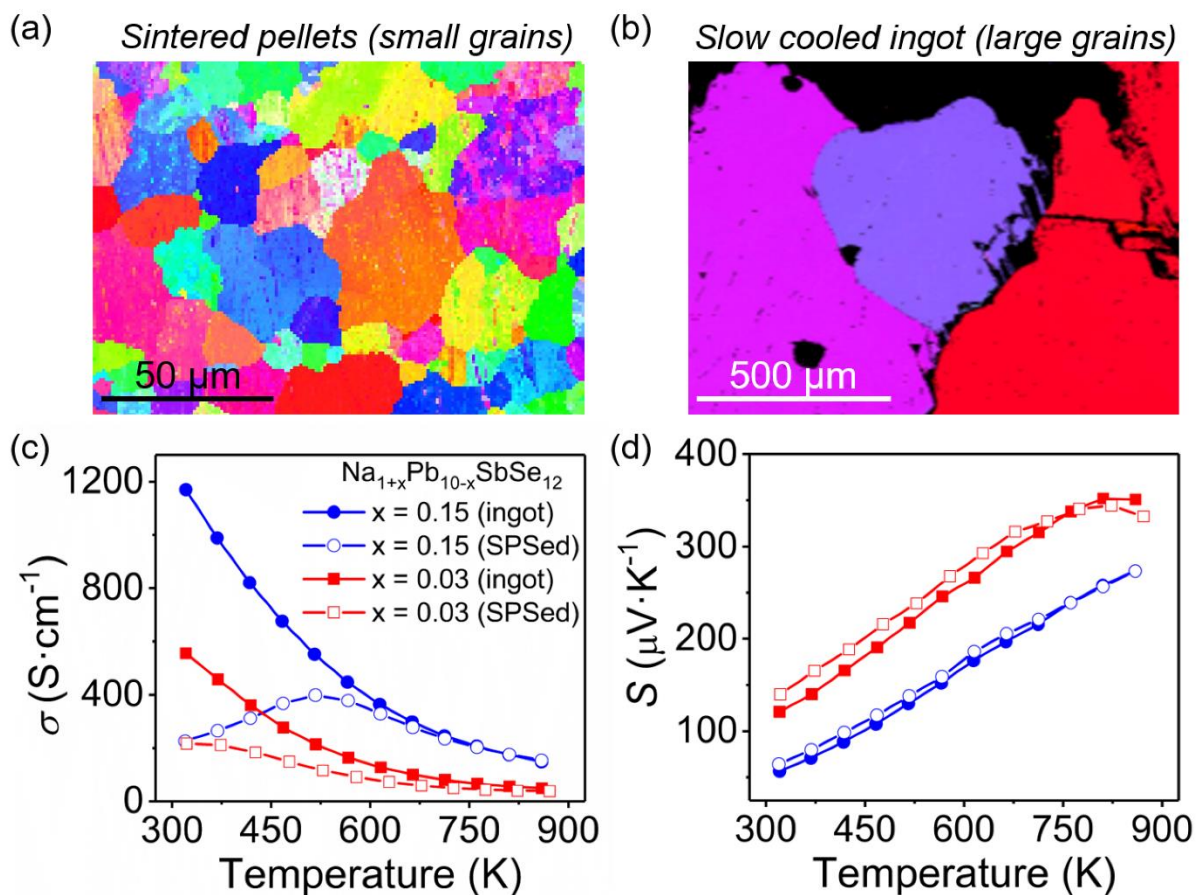


Figure 4.3 Electron backscatter diffraction (EBSD) images showing the grain structure of $\text{Na}_{1.15}\text{Pb}_{9.85}\text{SbSe}_{12}$ samples prepared by (a) water quenching followed by powdering and SPS sintering and (b) slow cooling of ingots. Each individually colored region represents a single grain. Comparison of the (c) electrical conductivities and (d) Seebeck coefficients for large grained (slow cooled ingots), and small grained (SPS sintered pellets) Na-doped $\text{Na}_{1+x}\text{Pb}_{10-x}\text{SbSe}_{12}$. The closed and open points represent data for the large and small grained samples respectively.

shows that the semiconducting charge transport observed in the SPS processed samples vanishes in the slow cooled ingots, and the expected metallic behavior is recovered. Furthermore, Figure

4.2d demonstrates that the Seebeck coefficients of each pair are nearly identical over the full temperature window, indicating the charge carrier densities are approximately equal between ingot and SPS processed samples. Moreover, because the Seebeck coefficients and PXRD data indicate that each pair of compounds has nominally identical doping and chemical composition, impurity scattering in each should be comparable. As such, the results presented in Figure 4.2 unambiguously links the thermally activated charge transport to the GBs, providing strong evidence in favor of the GB carrier scattering model.

To further strengthen the case for GB scattering, we also prepared samples with different densities of GBs by passing sample powders through sieves with different mesh sizes prior to SPS

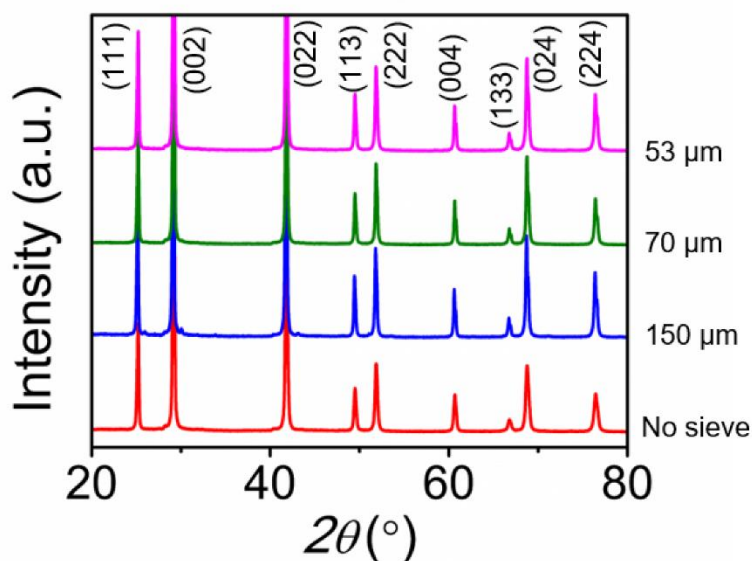


Figure 4.4 Powder X-ray diffraction patterns of SPS-processed samples prepared with different mesh sieves. All samples have the same nominal composition $\text{Na}_{1.10}\text{Pb}_{9.90}\text{Sb}_{0.90}\text{Se}_{12}$. The diffraction patterns all suggest each is phase pure with negligible chemical differences.

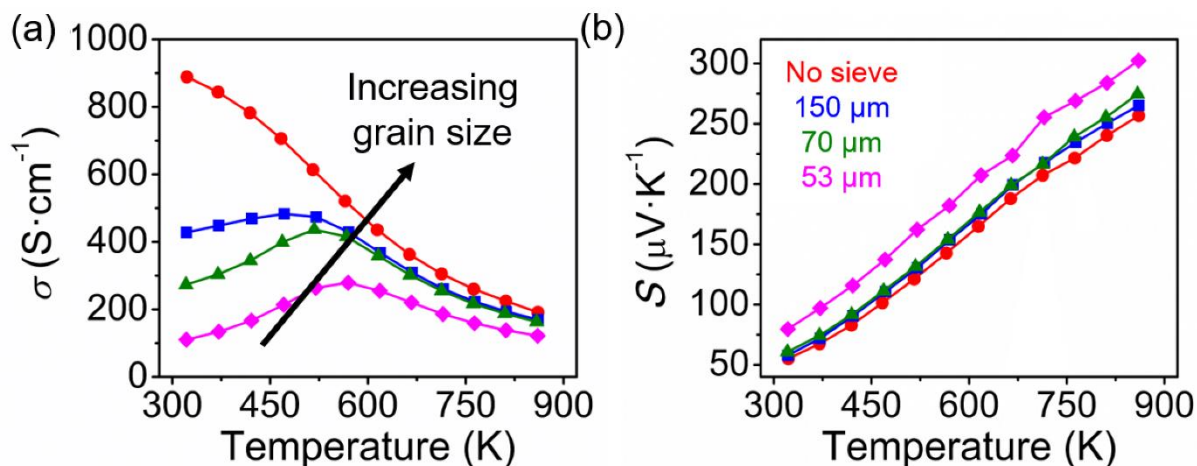


Figure 4.5 Electrical transport properties of samples with nominal composition of $\text{Na}_{1.10}\text{Pb}_{9.90}\text{Sb}_{0.90}\text{Se}_{12}$ prepared to have different sized grains by passing powdered ingots through different mesh sieves. (a) Electrical conductivities, (b) Seebeck coefficients. The sample passed through a 53 μm sieve likely has a somewhat smaller charge carrier concentration than the other samples, as evidenced by the greater Seebeck coefficient over the full temperature range.

sintering. More details on this procedure are given in the experiment section, and PXRD patterns obtained for each sample are shown in Figure 4.4. Like the slow cooled ingots, the powder patterns confirm the rocksalt structure with negligible secondary phases for each sample. In principle, samples passed through smaller mesh sieves should have on average smaller grains and therefore a greater density of boundaries. Here, we utilized meshes of 53, 70, and 150 μm , as well as one sample that was not sieved. The thermoelectric data for the resulting samples is shown in Figure 4.5 and again demonstrates a direct link between GBs and low temperature carrier scattering. As the mesh (and the grain) size is decreased, the electrical conductivity is increasingly suppressed under ~ 500 K, while the values all approximately converge above this temperature. The Seebeck

coefficients of these samples are likewise extremely similar, indicating comparable carrier concentrations. Together, the electrical data of the slow-cooled ingots and samples prepared with varying GB density provide substantial experimental support that the low temperature carrier scattering found in $\text{NaPb}_m\text{SbSe}_{m+2}$ originates from the GBs.

4.2.2 Microscopic characterization of the grain boundaries in $\text{NaPb}_m\text{SbQ}_{m+2}$

Having directly linked the low temperature charge carrier scattering in $\text{NaPb}_m\text{SbSe}_{m+2}$ to the GBs, we found it surprising that the chemically similar telluride analogues ($\text{NaPb}_m\text{SbTe}_{m+2}$) do not show GB charge carrier scattering, and instead exhibit the typical degenerate semiconducting electrical behavior.^{67, 124} Moreover, because lead chalcogenide thermoelectrics do not normally feature GB scattering, the apparent uniqueness of the $\text{NaPb}_m\text{SbSe}_{m+2}$ family warrants an explanation. Our initial hypothesis was that the GBs in $\text{NaPb}_m\text{SbSe}_{m+2}$ act as sinks for phase or dopant separation, thereby leading to thin resistive barriers along the boundaries that impede the flow of charge carriers. Indeed, small quantities of SnO_2 are known to form along the GBs and dramatically restrict charge transport in polycrystalline SnSe .^{142, 164} To investigate if similar phase segregation is occurring in our materials, we performed scanning transmission electron microscopy (STEM) and transmission electron microscopy (TEM) on several samples of SPS-processed $\text{NaPb}_m\text{SbSe}_{m+2}$ and $\text{NaPb}_m\text{SbTe}_{m+2}$ to elucidate any structural and chemical differences along the grain boundaries.

Several representative high angle annular dark field-scanning transmission electron microscopy (HAADF-STEM) and high resolution TEM (HRTEM) images of a sample with nominal composition $\text{Na}_{1.15}\text{Pb}_{9.85}\text{SbSe}_{12}$ are presented in Figure 4.6. Both the HRTEM and STEM

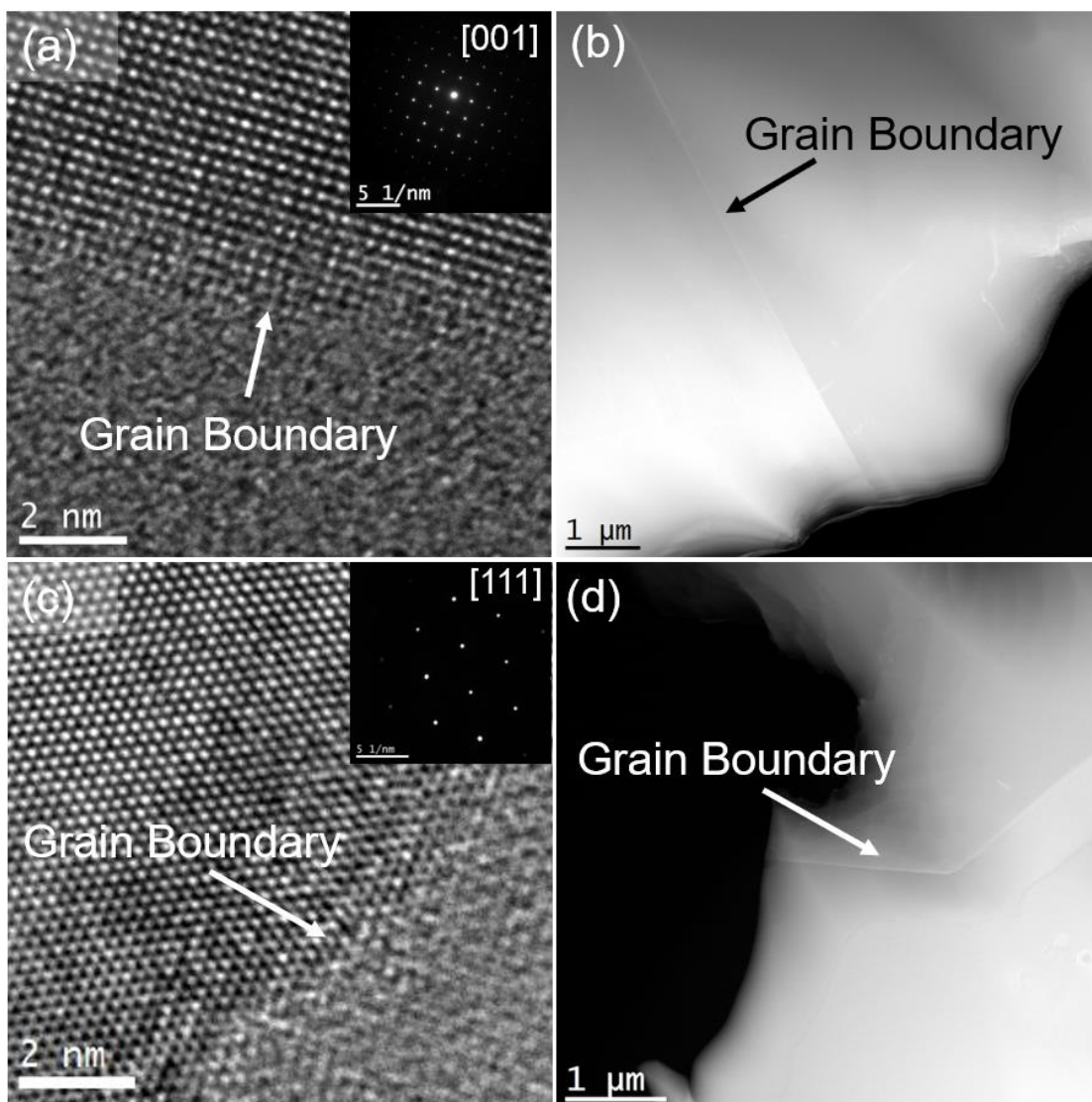


Figure 4.6 (a) A characteristic high resolution TEM image of a grain boundary in a $m = 10$ selenide sample with nominal composition $\text{Na}_{1.15}\text{Pb}_{9.85}\text{SbSe}_{12}$. The image shows a clean boundary with no evidence for secondary phase segregation. The inset displays a selected area electron diffraction pattern showing only the expected rocksalt spots. (b) A HAADF-STEM image of another GB in the same sample also showing a clean boundary. (c) and (d) are the same for telluride samples with nominal composition $\text{Na}_{1.10}\text{Pb}_{9.90}\text{Sb}_{0.85}\text{Te}_{12}$.

images shown in Figures 4.6a and 4.6b reveal a clean boundary free of obvious signs of phase segregation. In addition, we conducted energy dispersive X-ray spectroscopy (EDS) elemental maps over the GB regions and display the results in Figure 4.7. The EDS maps lack evidence for any significant phase or impurity segregation along the boundary, supporting the interpretation of Figures 4.6a and 4.6b. Taken together, the microscopy data suggests the GBs in $\text{NaPb}_m\text{SbSe}_{m+2}$ to be reasonably free of any secondary phase segregation within the limits of our analysis. Additional STEM-EDS maps of the GBs are provided in Figures 4.7 and further support the above conclusion.

Since the $\text{NaPb}_m\text{SbTe}_{m+2}$ compounds do not exhibit GB limited electrical conductivity,^{67,}¹⁵⁸ we also characterized these materials to compare the GBs with those of the selenides. Samples were prepared following the synthetic protocol outlined in our prior work,¹²⁴ and TEM and STEM images of a GB in a telluride sample with nominal composition $\text{Na}_{1.10}\text{Pb}_{9.90}\text{Sb}_{0.85}\text{Te}_{12}$ are presented in Figure 4.6c and 4.6d. Again, both the high and low magnification STEM images and EDS maps indicate clean GBs without observable phase segregation. EDS maps over the GB region shown in Figure 4.8 support this interpretation. Therefore, our electron microscopy analysis indicates there is negligible secondary phase segregation at the GBs in either $\text{NaPb}_m\text{SbSe}_{m+2}$ or $\text{NaPb}_m\text{SbTe}_{m+2}$. Other techniques, such as atom probe tomography (APT), indicate that some Na often segregates to the GBs in heavily sodium-doped lead chalcogenides,^{38, 86, 165-167} yet this does not typically lead to thermally activated conduction in these materials. A different explanation is needed to account for the presence of strong GB scattering in $\text{NaPb}_m\text{SbSe}_{m+2}$.

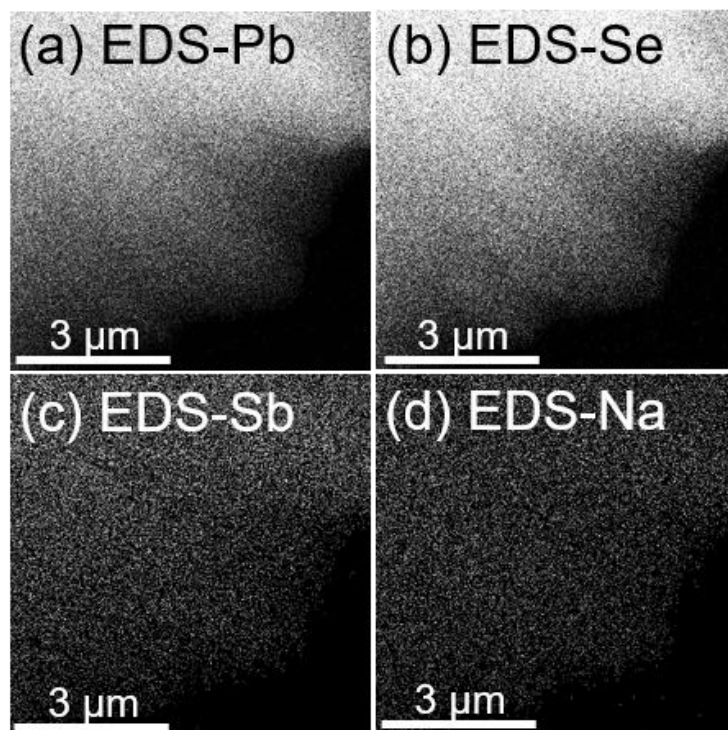


Figure 4.7 EDS maps over the GB region of the $\text{Na}_{1.15}\text{Pb}_{9.85}\text{SbSe}_{12}$ sample whose TEM and STEM images are discussed in Figure 4.6. The EDS maps also show a homogeneous distribution of elements supporting that there is negligible phase or dopant segregation at the GBs.

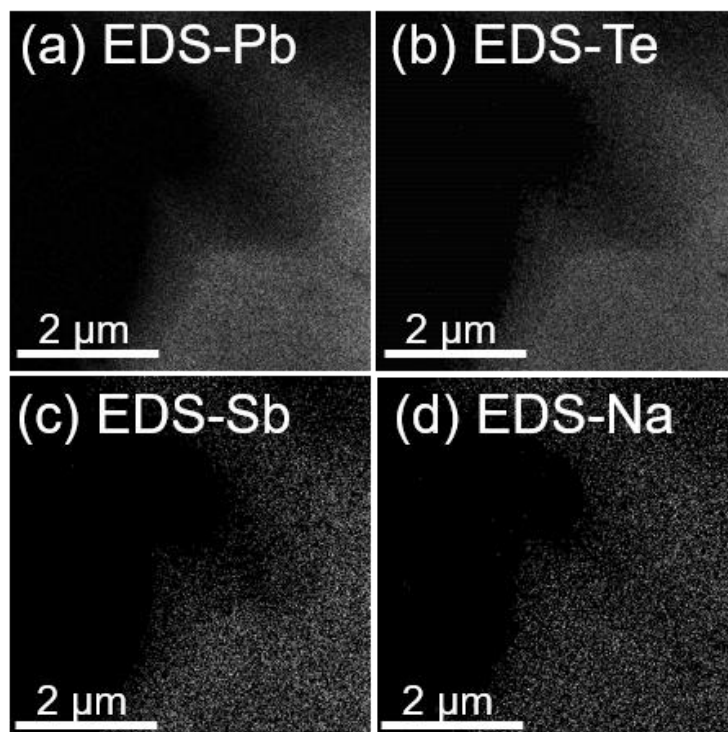


Figure 4.8 EDS maps over the GB region of a telluride sample with nominal composition $\text{Na}_{1.15}\text{Pb}_{9.85}\text{Sb}_{0.85}\text{Te}_{12}$ whose TEM and STEM images are discussed in Figure 4. The EDS maps also show a homogeneous distribution of elements supporting that there is negligible phase or dopant segregation at the GBs.

4.2.3 Charge carrier trapping at the grain boundaries

Many polycrystalline semiconductors are known to intrinsically host energy barriers localized at the grain boundaries that manifest in thermally activated charge carrier mobility.¹⁶⁰⁻¹⁶² Such a situation is well summarized by Seto, who argues the energy barriers form because the atoms at the GB are more likely to have incomplete atomic bonding, or in other words that the GB region is rich with under coordinated atoms and dangling bonds compared to the bulk. The GB defects can act as trap states that immobilize charge carriers.¹⁴³ After trapping electrons or holes,

the GBs become electrically charged, creating potential barriers physically analogous to a double Schottky barrier centered on the boundary. The barriers then strongly impede the flow of charge carriers through the material. Analysis of such a theoretical situation shows that in one dimension, the barrier height at the GBs takes the following form:¹⁴³

$$E_b = \frac{e^2 Q_t^2}{8N\varepsilon} \quad (4.1)$$

where e is the electron charge, Q_t is the density of trapping states at the GB, N is the concentration of dopant atoms, and ε is the static dielectric permittivity. This equation is derived under the assumption that the doping density is greater than the concentration of GB trap states, which seems reasonable considering that the bulk electrical conductivities and Seebeck coefficients indicate degenerate carrier concentrations. While Equation 4.1 was derived for a single dimension, we propose that it provides the necessary intuition to understand the GB scattering in our materials. Within the grains, the charge transport is dominated by phonon (deformation potential) scattering as normal; however, the carriers are impeded by the energy barriers at the GBs, and here the conduction is modeled as thermionic emission over the boundary to give electrical conductivity as follows:¹⁴³

$$\sigma_{GB} = e^2 L n \left(\frac{1}{2\pi m^* k_B T} \right)^{1/2} \exp \left(\frac{-E_b}{k_B T} \right) \quad (4.2)$$

where L is the grain size, n is the charge carrier density, m^* is the carrier effective mass and k_B is the Boltzmann constant. Using the model developed by Kuo *et al.*, the overall electrical conductivity is calculated by treating the material as a two-phase system consisting of the bulk grain phase and the GB phase. The total electrical conductivity is then modeled by considering the two phases as forming a series circuit to yield⁶⁸:

$$\sigma^{-1} = (1 - t)\sigma_G^{-1} + t\sigma_{GB}^{-1} \quad (4.3)$$

where t is a constant representing the fraction of the GB phase. Our analysis using Equations 4.1–4.3 reveals several important results relevant to $\text{NaPb}_m\text{SbQ}_{m+2}$ materials that are detailed in the following sections.

4.2.4 Relationship between polarizability and GB charge carrier scattering

If two samples have comparably sized grains, equations 4.1 and 4.2 show that the height of the GB potential barriers, and therefore the degree of GB resistance, is proportional to the square of the density of GB trapping states and inversely proportional to the doping level and the dielectric constant. Considering that lead chalcogenides have been extensively studied across a wide range of carrier concentration and with numerous dopants, yet do not normally exhibit strong GB scattering, we propose $\text{NaPb}_m\text{SbSe}_{m+2}$ is more susceptible to GB scattering because of its relatively low dielectric constant compared to that of pure PbSe. This is intuitive, as smaller values of ϵ indicate weaker screening of the charge carriers from any electric fields. Moreover, the lower dielectric constant of $\text{NaPb}_m\text{SbSe}_{m+2}$ can be rationalized with simple chemical principles. Namely, the dielectric constant (and strength of charge carrier screening) is expected to be smaller (weaker) in more ionic and less polarizable crystals than in highly covalent and polarizable compounds. With this in mind, alloying the significantly more ionic NaSbSe_2 into PbSe is expected to yield a less polarizable crystal with weaker carrier screening and lower ϵ than pure PbSe. Furthermore, the argument also explains the lack of GB scattering in the otherwise similar $\text{NaPb}_m\text{SbTe}_{m+2}$ materials. Because PbTe has a much larger dielectric constant than PbSe, respectively 414 vs. 210 at 300 K,¹⁶⁸⁻¹⁶⁹ it is reasonable to expect the charge carrier screening in $\text{NaPb}_m\text{SbTe}_{m+2}$ to be

considerably stronger than in $\text{NaPb}_m\text{SbSe}_{m+2}$, leading to weaker GB scattering in the tellurides as we indeed observe.

To support the qualitative picture outlined above, we used density functional theory to calculate the relative static dielectric constants of each lead chalcogenide and NaSbQ_2 compound, and the results are presented in Table 4.1. While the calculated values for the pure lead chalcogenides are somewhat higher than the experimental numbers,¹⁶⁸⁻¹⁷⁰ our results are in general agreement with other DFT calculated dielectric constants for these materials. Crucially, the calculated dielectric constants trend as anticipated, with three to five times higher values for the pure lead chalcogenides, which are all greater than 328, compared to their respective NaSbQ_2 analogues which are all under 113. Moreover, the calculated values of ϵ decrease moving down the periodic table from PbTe (501) to PbS (328), as anticipated by the polarizability of each compound. Somewhat surprisingly, NaSbTe_2 has the smallest calculated dielectric constant of the NaSbQ_2 materials; however, because the values of ϵ are all much larger for the pure lead chalcogenides, we do not anticipate this to finding to alter our analysis.

In light of the above calculations and discussion, we sought to provide direct experimental evidence linking the GB scattering to the charge carrier screening in $\text{NaPb}_m\text{SbSe}_{m+2}$. We prepared and investigated the electrical transport properties of p-type doped $\text{NaPb}_{20}\text{SbSe}_{22}$ ($m = 20$, ~4% NaSbSe_2) and $\text{NaPb}_6\text{SbSe}_8$ ($m = 6$, ~14% NaSbSe_2) and compared the data with our previously reported $\text{NaPb}_{10}\text{SbSe}_{12}$ ($m = 10$, ~9% NaSbSe_2) materials.¹⁵⁸ We anticipated that the charge carriers in more PbSe-rich (higher m) compositions would be more strongly screened than in NaSbSe_2 -rich (lower m) phases, and therefore have the weakest GB scattering. In order to make a meaningful comparison between samples, it is imperative for the materials to have similarly sized

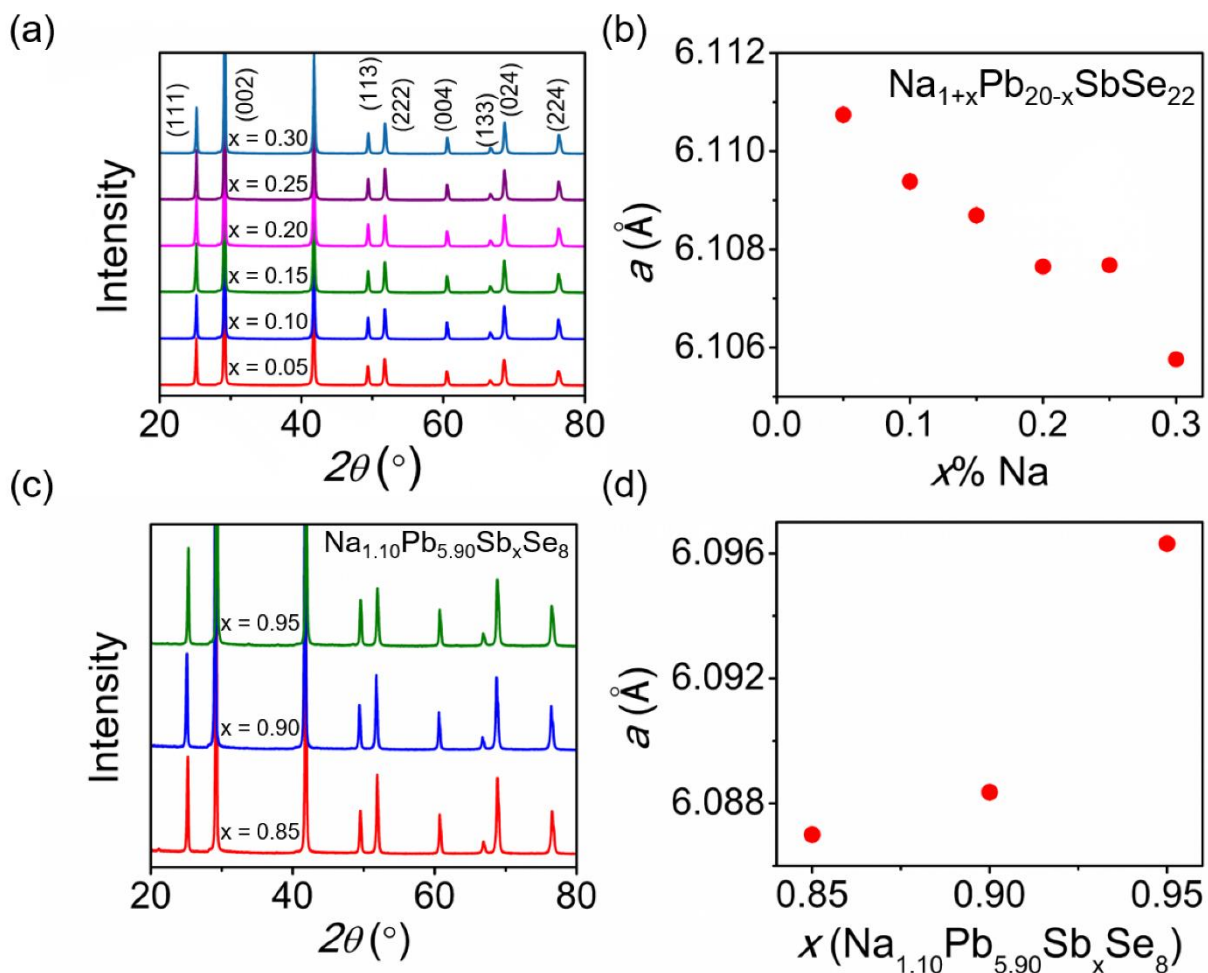


Figure 4.9 Powder X-ray diffraction patterns for p-type doped NaPb_mSbSe_{m+2} for $m = 20$ and $m = 6$ (equivalently $\sim 4\%$ and 14% NaSbSe₂ in PbSe respectively). Nominal compositions are Na_{1+x}Pb_{20-x}SbSe₂₂ and Na_{1.10}Pb_{5.90}Sb_xSe₈. (a) and (c) are the PXRD patterns, and (b) and (d) are the respective lattice parameters. In general, all patterns show the expected peaks characteristic of the rocksalt structure and the lattice parameters change (approximately) linearly with doping, indicating successful Na incorporation. A very small amount of secondary phase is found for the pattern for $m = 6$, $x = 0.95$ in (c).

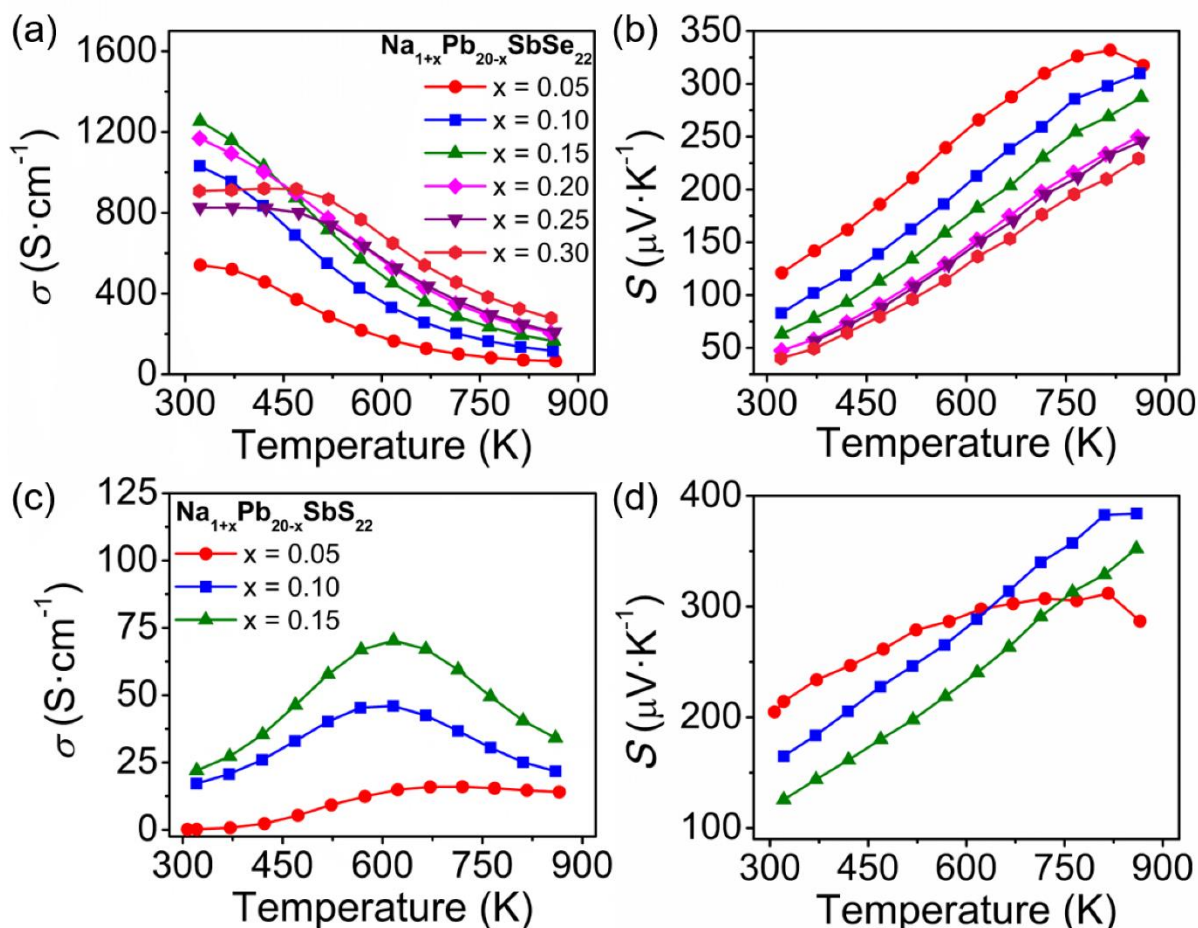


Figure 4.10 Comparison of the electrical properties for p-type doped $\text{NaPb}_m\text{SbSe}_{m+2}$ for $m = 20$ and $m = 6$ (equivalently $\sim 4\%$ and 14% NaSbSe_2 in PbSe respectively). Nominal compositions are $\text{Na}_{1+x}\text{Pb}_{20-x}\text{SbSe}_{22}$ and $\text{Na}_{1.10}\text{Pb}_{5.90}\text{Sb}_x\text{Se}_8$. (a) Electrical conductivities and (b) Seebeck coefficients for the $m = 20$ compounds. (c) Electrical conductivities and (d) Seebeck coefficients for the $m = 6$ phases. Clearly, comparing (a) and (c) shows that the $m = 6$ compounds have qualitatively stronger GB scattering, manifesting in a greater degree of suppression of σ under ~ 600 K.

grains. Because the synthesis, grinding, sieving, and sintering procedures for each compound were identical (see experimental section), we believe the assumption of comparable grain sizes is reasonable. The measured PXRD and electrical data for all $m = 20$ and $m = 6$ samples of $\text{NaPb}_m\text{SbSe}_{m+2}$ is shown in Figures 4.9 and 4.10 respectively. Inspection of the data clearly shows that the temperature dependence of the electrical conductivities of every $m = 20$ sample is much closer to the expected metallic behavior than that of the $m = 6$ samples, which feature strongly suppressed and thermally activated electrical conductivity below ~ 550 K. These factors provide qualitative evidence in support of the carrier screening hypothesis.

To provide a more quantitative argument, we used Equations 4.2 and 4.3 to estimate the height of the GB energy barriers in our samples. If the resistance from the GBs is sufficiently strong such that $\sigma_G \gg \sigma_{GB}$, then the bulk contribution to the electrical conductivity is masked by the GBs and Equation 4.3 can be approximated as $\sigma \approx \sigma_{GB}$. Therefore, over the temperature range dominated by GB scattering, Equation 4.2 approximates the electrical conductivity and gives thermally activated conduction. Importantly, Equation 4.2 indicates that plotting $\ln\sigma$ vs. $1/k_B T$ should yield a straight line with a slope of $-E_b$ if the carrier concentration remains constant with temperature.¹⁴³ Here, we selected representative samples from one of each of our $m = 6, 10, 20$ sets of compounds and display their electrical conductivities in Figure 4.11a. Because Equation 4.1 shows that the energy barriers will also be sensitive to the doping density, these samples were chosen to have similar values of n_H to provide as close a comparison as possible. The variable-temperature Hall effect data is found in Figure 4.11c and confirms that the samples have comparable hole densities of $\sim 1-1.5 \times 10^{20} \text{ cm}^{-3}$ that remain relatively constant with heating below ~ 600 K.

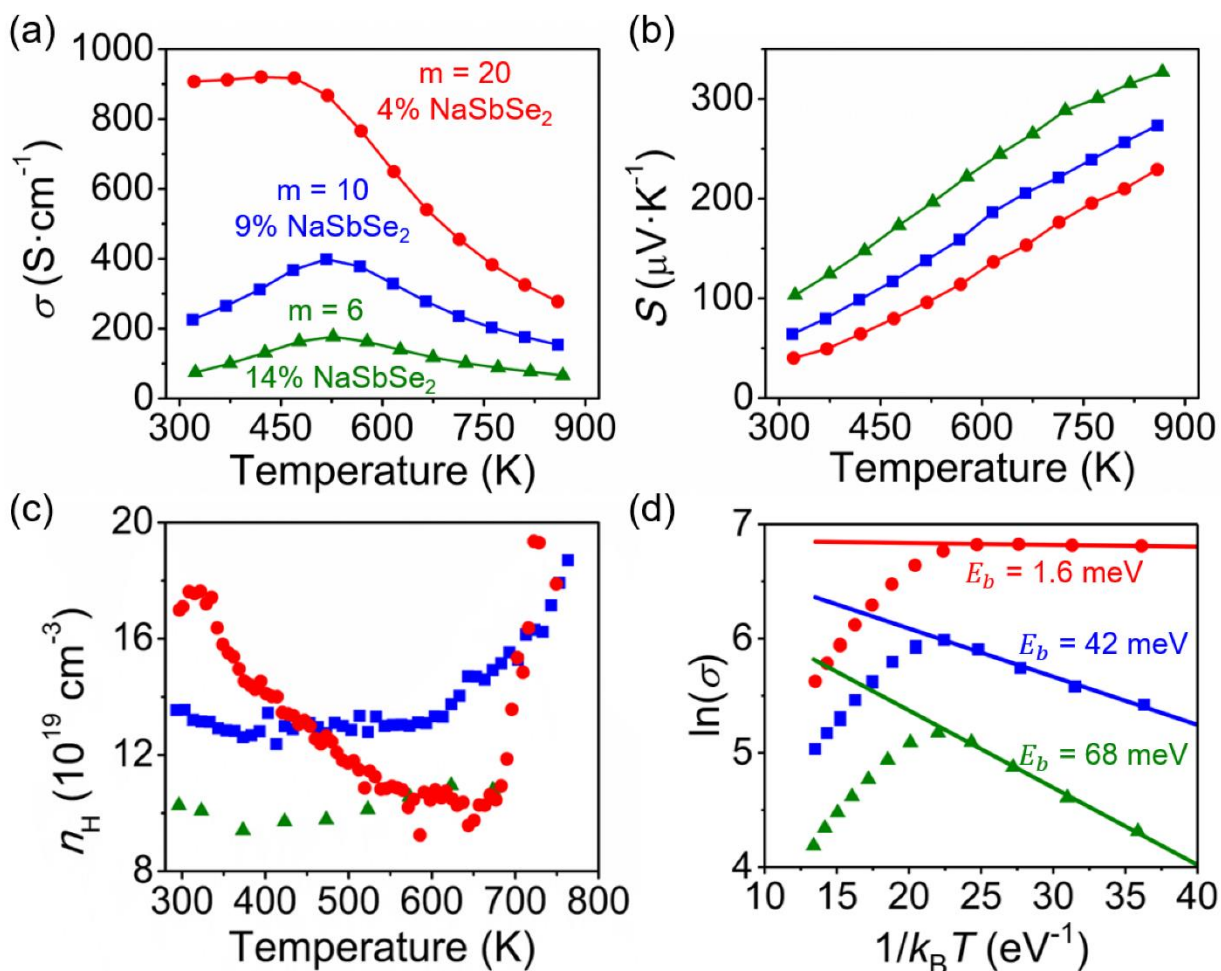


Figure 4.11 Comparison of the electrical transport properties of comparably doped samples of $\text{NaPb}_m\text{SbSe}_{m+2}$ for $m = 20, 10,$ and 6 (equivalently $\sim 4, 9,$ and 14 percent NaSbSe_2 in PbSe). (a) Electrical conductivities and (b) Seebeck coefficients, (c) variable temperature Hall charge carrier concentrations, and (d) plots of $\ln\sigma$ vs. $1/k_B T$ showing linear temperature dependence over the low temperature GB dominated regime. The solid lines in (d) are the fits used to extract E_b .

Figure 4.11c shows the plots of $\ln\sigma$ vs. $1/k_B T$, and as anticipated, each gives a reasonably linear slope over the low temperature GB dominated regime. The activation barriers extracted from the slopes increase with NaSbSe₂ fraction, from 1.6 meV for $m = 20$ to 68 meV for the $m = 6$ sample. To best eliminate any contribution from the small temperature dependence of the charge carrier densities, we moreover used the charge carrier mobilities μ_H estimated from Figures 4.11a and 4.11c to plot $\ln\mu_H$ vs. $1/k_B T$ for the same samples. The data is given below in Figure 4.12, and we estimate similar barrier heights of 7.6, 44, and 69 meV for $m = 20, 10,$ and 6 respectively. The above analysis therefore provides direct evidence that at comparable charge carrier concentrations, and for samples with similar bulk conductivity, more NaSbSe₂-rich members of the NaPb_{*m*}SbSe_{*m*+2} family have larger GB energy barriers than the PbSe-rich phases, as predicted considering the chemical arguments discussed above.

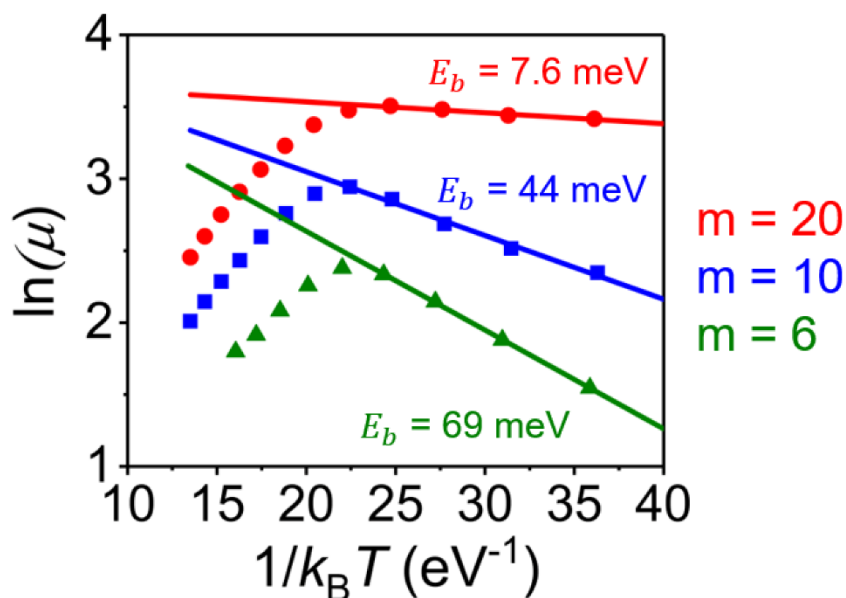


Figure 4.12 Plots of $\ln\mu$ against $1/k_B T$ for the $m = 20, 10,$ and 6 NaPb_{*m*}SbSe_{*m*+2} discussed in Figure 4.11. The extracted energy barriers from the slopes agree well with the values estimated from the plots of $\ln\sigma$ vs $1/k_B T$.

Figures 4.11 and 4.12 provide evidence that the GB charge carrier scattering is strongest in more ionic NaSbSe₂-rich phases of the PbSe-NaSbSe₂ system. Figure 4.11 demonstrates that at high temperatures, the electrical conductivities are lowest for the NaSbSe₂ rich phases, indicating that the bulk conductivities (σ_G) decrease with greater NaSbSe₂ fraction. This is reasonable, because our earlier work in chapter 3 demonstrated that addition of NaSbSe₂ to PbSe increases the charge carrier effective mass and thus lowers the carrier mobilities.¹⁵⁸ The different bulk electrical conductivities are however potentially important, as Equation 3 indicates that reliably analyzing the GB contribution to the electrical conductivity requires $\sigma_G \gg \sigma_{GB}$, which occurs when σ_G is very high and/or when E_b is also large. The different bulk conductivities of the samples discussed above thus could in principle obscure our analysis. Therefore, to supplement the data found in Figure 4.11 and provide another measure of the GB contribution at different NaSbSe₂ fractions, we compared three additional samples (again $m = 20, 10, 6$) that have similar bulk electrical conductivities. The data is presented in Figure 4.13. The electrical conductivities of each sample converge above ~600 K, suggesting similar values of σ_G . The energy barriers again increase with NaSbSe₂ fraction, with estimated values of 19 and 68 meV for $m = 10$ and 6 samples respectively. The GB scattering in the $m = 20$ sample was too weak to extract a barrier height, suggesting a very small E_b , consistent with our findings in Figure 4.11d. These findings provide greater support for our hypothesis, indicating substantially larger values of E_b for ionic NaSbQ₂ rich phases.

Lastly, we also investigated the electrical properties of PbS–NaSbS₂ alloys (NaPb_{*m*}SbS_{*m+2*}). Because the dielectric constant of PbS is measured to be ~169 at 300 K,¹⁷⁰ lower than that of PbSe and PbTe, we predicted NaPb_{*m*}SbS_{*m+2*} to have the strongest GB scattering of the NaPb_{*m*}SbQ_{*m+2*} (Q = S, Se, Te) materials for the same value of m . The electrical conductivities of the p-type doped

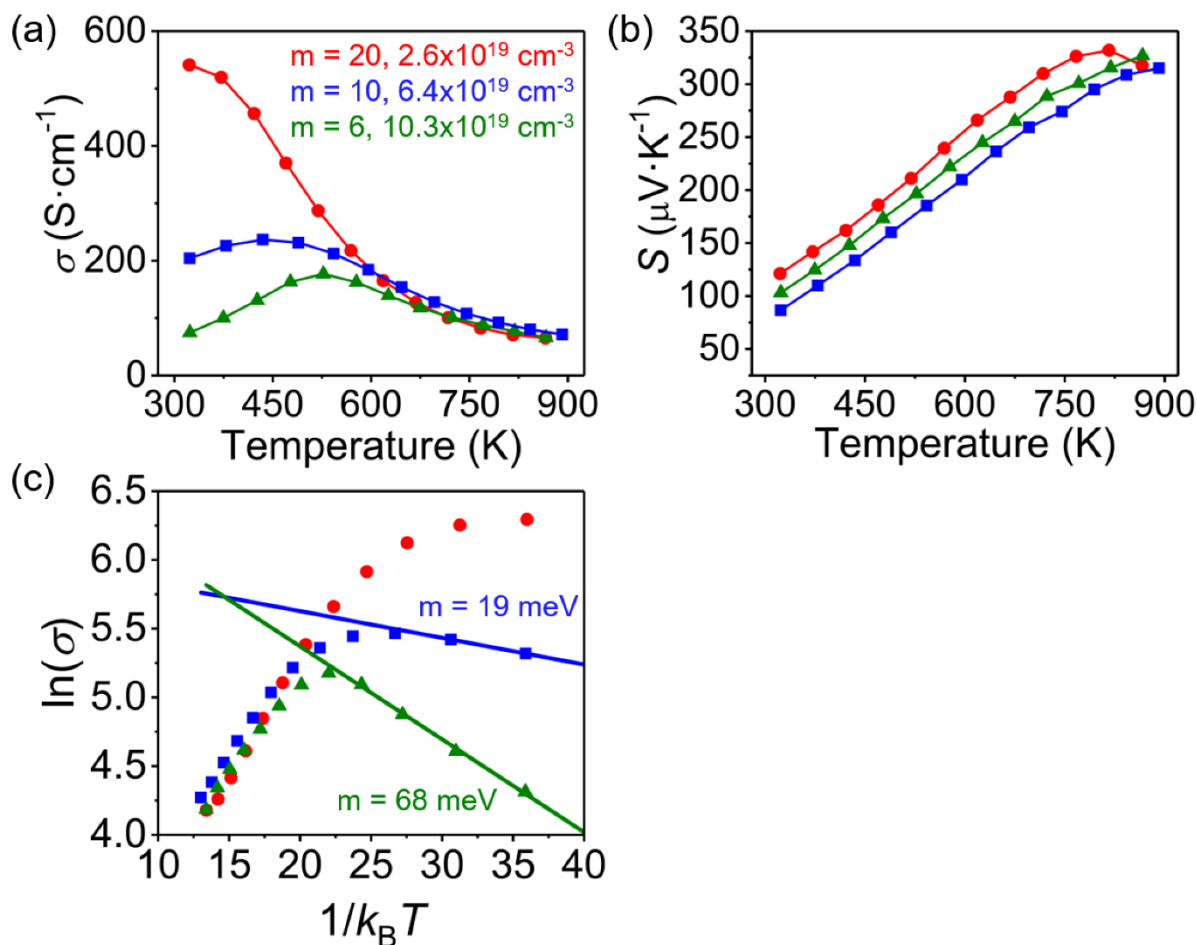


Figure 4.13 (a) Temperature-dependent electrical conductivities for three $\text{NaPb}_m\text{SbSe}_{m+2}$ ($m = 20, 10, 6$) samples that have similar bulk electrical conductivities σ_G . The room-temperature charge carrier concentrations measured for each are given in the legend. (b) Temperature-dependent Seebeck coefficients for the same samples. (c) Plots of $\ln\sigma$ vs. $1/k_B T$ for each sample, showing that the barrier height increases with NaSbSe_2 amount, consistent with the data discussed in Figure 4.11 and 4.12 above. Nominal compositions for each sample are as follows: $\text{Na}_{1.05}\text{Pb}_{19.95}\text{SbSe}_{22}$ ($m = 20$), $\text{Na}_{1.05}\text{Pb}_{9.95}\text{SbSe}_{12}$ ($m = 10$), and $\text{Na}_{1.10}\text{Pb}_{5.90}\text{Sb}_{0.90}\text{Se}_8$ ($m = 6$).

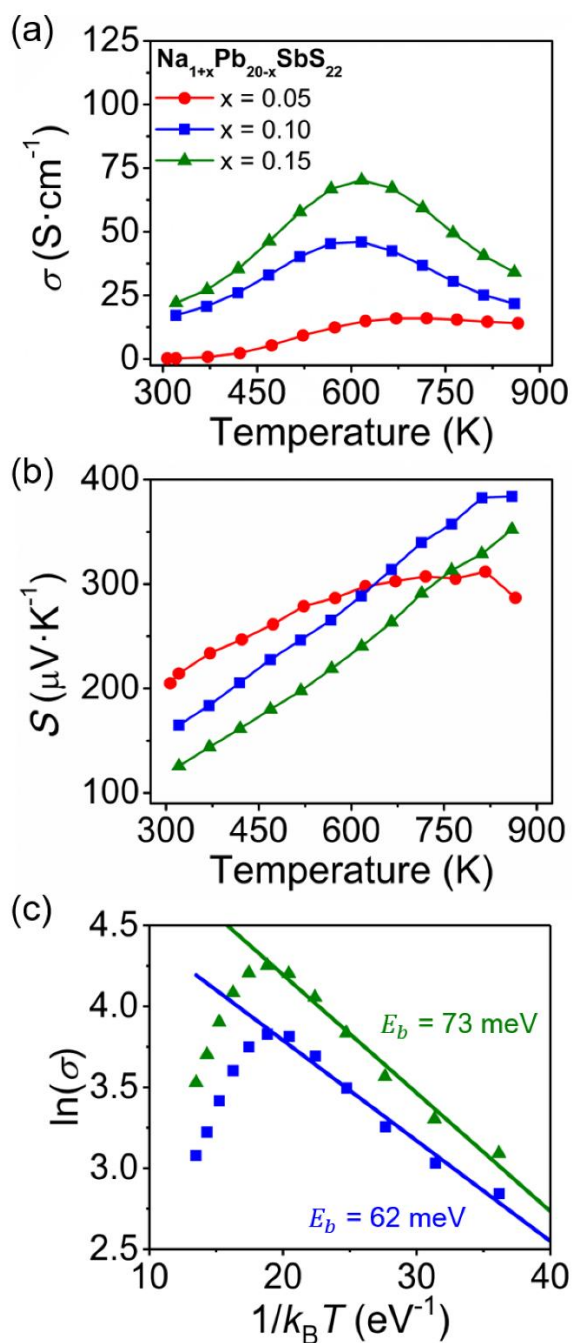


Figure 4.14 Electrical transport properties of p-type doped $m = 20$ $\text{NaPb}_m\text{SbS}_{m+2}$ (nominally $\text{Na}_{1+x}\text{Pb}_{20-x}\text{SbS}_{22}$). (a) Electrical conductivities, (b) Seebeck coefficients, and (c) plots of $\ln\sigma$ vs. $1/k_{\text{B}}T$ showing linear temperature dependence over the low temperature GB dominated regime. The solid lines in (c) show the linear fits used to extract E_b .

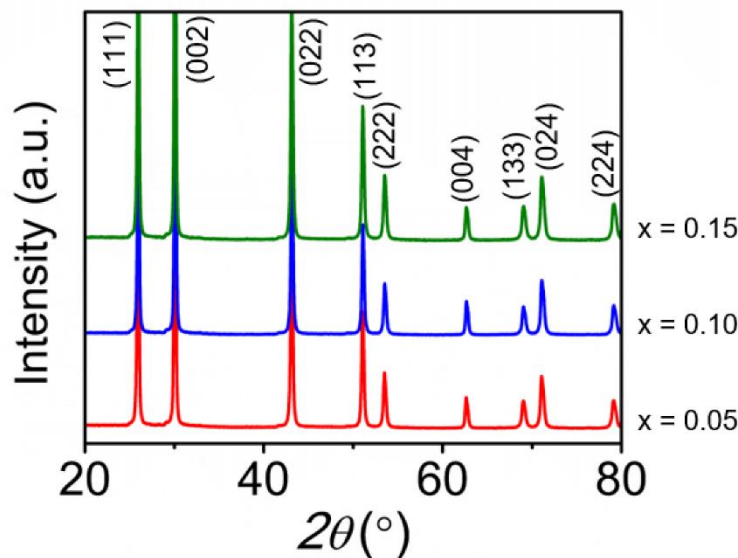


Figure 4.15 Powder X-ray diffraction patterns for p-type doped $\text{Na}_{1+x}\text{Pb}_{20-x}\text{SbS}_{22}$ ($m = 20$, equivalently $\sim 4\%$ NaSbS_2). The powder patterns show only peaks corresponding to the expected rocksalt reflections. No reflections corresponding to secondary phases are observed.

$\text{Na}_{1+x}\text{Pb}_{20-x}\text{SbS}_{22}$ ($\sim 4\%$ NaSbS_2 in PbS) samples are displayed in Figure 4.14 and PXRD patterns are shown in Figure 4.15. The electrical conductivities (Figure 4.14a) clearly indicates strong GB scattering, with semiconducting behavior up to 600 K and metallic temperature dependence above. Likewise, the Seebeck coefficients shown in Figure 4.14b increase with heating over the full range of temperatures, typical of degenerate semiconductors. While we did not conduct variable temperature Hall effect measurements on these samples, degenerate charge carrier densities of $5\text{--}15 \times 10^{19} \text{ cm}^{-3}$ are confirmed by room-temperature measurements and shown in in Table 4.2. Qualitatively, comparing the data discussed here with the transport properties of the $m = 20$ selenides shown in Figures 4.11–4.13, the sulfides clearly exhibit both lower electrical conductivity and semiconducting-like behavior that persists over a greater range of temperatures,

both suggesting stronger GB scattering. The plots of $\ln\sigma$ vs. $1/k_B T$ for the $x = 0.10$ and 0.15 samples are presented in Figure 4.14c and confirm this suspicion, with estimated energy barriers of 62 and 73 meV respectively. We excluded the $x = 0.05$ sample from this analysis, as it was too lightly doped and showed influence of intrinsic conduction, leading to an unphysical barrier height of ~ 220 meV. Clearly, the energy barriers estimated for the $m = 20$ sulfides are significantly greater than those of the $m = 20$ selenides.

In summary, we observe stronger GB scattering in the more ionic $\text{NaPb}_m\text{SbS}_{m+2}$ family than in $\text{NaPb}_m\text{SbSe}_{m+2}$, which in turn displays stronger scattering than the most polarizable $\text{NaPb}_m\text{SbTe}_{m+2}$ materials. Likewise, NaSbSe_2 -rich phases in the $\text{NaPb}_m\text{SbSe}_{m+2}$ family generally have stronger GB scattering than the PbSe -rich compositions. The energy barriers extracted from the temperature-dependent electrical conductivities support these conclusions. Overall, the above analysis of the GB scattering in the $\text{NaPb}_m\text{SbQ}_{m+2}$ families provides strong evidence that their respective susceptibilities to GB limited electrical conductivity is driven in large part by their different dielectric permittivities and that this can be rationalized with intuitive chemical principles that consider the polarizability of the atoms in each material.

4.2.5 Broader Scope: relevance of dielectric screening to GB scattering in emerging thermoelectric materials

The analysis and insight presented above can be expanded to other reported thermoelectric materials that have GB limited charge transport. As discussed above, one expects stronger GB scattering in more ionic and less polarizable crystals. Indeed, an examination of the literature supports this intuition, as GB limited behavior is regularly reported in Zintl antimonide compounds

such as Mg_3Sb_2 ,⁶⁸⁻⁶⁹ KAlSb_4 ,⁷⁰ $(\text{Hf,Zr})\text{CoSb}$,⁷¹ Sr_3GaSb_3 ,⁷² NbFeSb ,⁷³ $\text{Ca}_5\text{Al}_2\text{Sb}_6$,⁷⁴ and Ca_3AlSb ,⁷⁵ as well as other emerging thermoelectric materials like Mg_2Si .⁷⁶ Considering that these compounds are all composed of relatively small and less polarizable ions than the classic thermoelectric lead and bismuth chalcogenides, the observed GB scattering is not surprising in light of the above discussion. Indeed, we also calculated dielectric constants for Mg_3Sb_2 , NbFeSb , TiCoSb , and Mg_2Si and show the results in Table 4.1. Our calculated values are among the smallest of all materials considered in this study, suggesting these compounds to be highly prone to GB carrier scattering. Our work therefore provides an elegant explanation of the GB scattering in a host of different thermoelectric materials and gives an intuitive chemical guideline for anticipating what materials will be most prone to GB limited electronic conduction.

A generally accepted paradigm in thermoelectric research is that small grains are advantageous to maximize phonon scattering, and indeed, an enormous amount of work has

Table 4.1 DFT calculated relative isotropic dielectric constants for each PbQ and NaSbQ_2 ($\text{Q} = \text{S}, \text{Se}, \text{Te}$), as well as Mg_3Sb_2 , NbFeSb , TiCoSb , Mg_2Si .

Compound	Calculated ϵ_r
PbTe	501
PbSe	338
PbS	328
NaSbTe ₂	58
NaSbSe ₂	71.8
NaSbS ₂	113
Mg_3Sb_2	32
NbFeSb	44.7
TiCoSb	32
Mg_2Si	23

focused on both preparing materials with minimal grain size and engineering the grain boundaries to be rich with defects and dislocations in order to maximize GB phonon scattering and achieve extremely low lattice thermal conductivity.^{38, 104, 171-172} In this context, our work provides important insight into the proper engineering of high-performance thermoelectric materials. While such strategies are proven to be effective in highly polarizable materials like lead and bismuth chalcogenides, the results discussed here indicate that small grains are undesirable in more ionic thermoelectric materials such as $\text{NaPb}_m\text{SbQ}_{m+2}$ ($\text{Q} = \text{Se}, \text{S}$) and Zintl antimonides. In these cases, it may be more advantageous to prepare samples with large grains to mitigate the charge carrier scattering at the GBs and ensure high electrical mobility.

To support this proposal, we note that large grained Mg_3Sb_2 is reported to have superior thermoelectric performance to small grained samples owing to the improved charge carrier mobility and power factor at lower temperatures.^{68, 173-174} Furthermore, the figures of merit of single crystalline SnSe are markedly superior to polycrystalline forms, and recent work to overcome the severe GB resistance and poor electrical conductivity in polycrystalline SnSe achieved performance comparable to the single crystals.¹⁶⁴ We moreover show the figures of merit for large- and small-grained forms of $\text{NaPb}_m\text{SbSe}_{m+2}$ in Figures 4.16 and 4.17. The ZT s are significantly enhanced in large grained forms of the more lightly doped samples, and more modestly improved at low temperature in the heavily doped samples. Therefore, we see varying degrees of enhancement in all large grained samples. In general, we anticipate the degree of enhancement to the ZT will vary from material to material. In compounds with intrinsically short phonon mean free path, larger grains would be more strongly

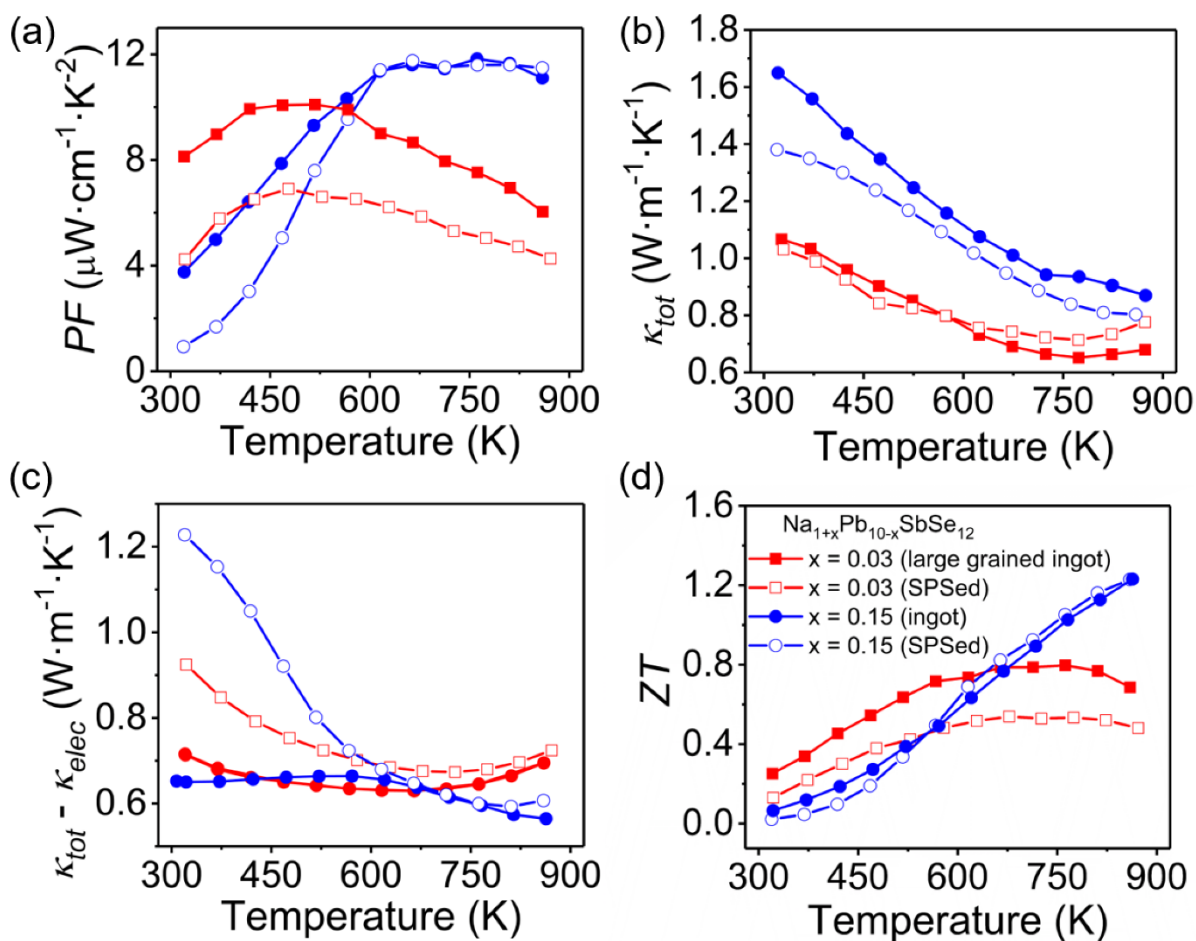


Figure 4.16 (a) Power factors, (b) total thermal conductivities, (c) estimated lattice thermal conductivity, and (d) ZT for as-cast ingots (large grained samples) and SPS-processed (small grains) $\text{Na}_{1+x}\text{Pb}_{10-x}\text{SbSe}_{12}$. Because of the improved charge carrier mobility, the power factors are enhanced in the large grained samples. The figures of merit for the $x = 0.03$ (lightly doped) sample is significantly improved for the larger grained sample. The enhancement is more modest in the large-grained forms of the more heavily doped $x = 0.15$ samples.

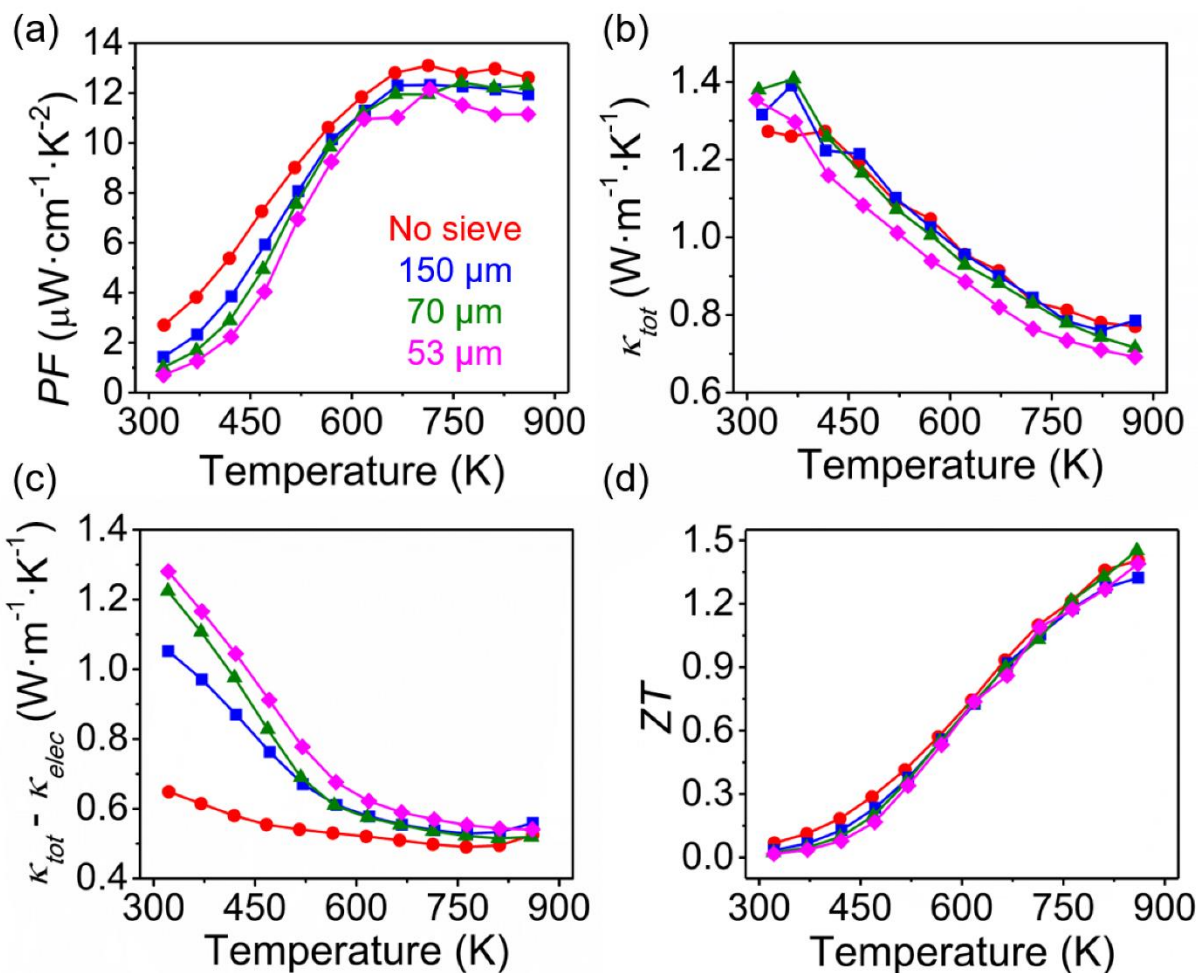


Figure 4.17 (a) Power factors, (b) total thermal conductivities, (c) estimated lattice thermal conductivity, and (d) ZT for samples with nominal composition of $\text{Na}_{1.10}\text{Pb}_{9.90}\text{Sb}_{0.90}\text{Se}_{12}$. The samples were prepared by SPS-sintering powders that were first passed through sieves with different mesh sizes. The electronic properties for these samples are discussed in Figure 4.5. Because of the improved charge carrier mobility, the power factors are increasingly enhanced as the grain size increases. The figures of merit are likewise modestly enhanced at low temperature as the grain size is raised.

avored, as the GBs would already have negligible contribution to the lattice thermal conductivity. However, in compounds where the intrinsic phonon mean free path is sufficiently long, the gains achieved by increasing the grain size to improve the electrical mobility may be more modest. Furthermore, because the charge carriers are less screened in lightly doped compounds,¹⁴³ enhancement from eliminating GB scattering may be more significant, as we observe here. While the paradigm of minimizing the grain size is deeply entrenched in the thermoelectric literature, this work shows that GB scattering is an often overlooked impediment to engineering high performance thermoelectrics, and researchers working with more ionic and less polarizable semiconductors should be wary of the potential need to suppress its effects.

4.3 Summary and conclusions

We investigated the electrical transport properties of polycrystalline $\text{NaPb}_m\text{SbQ}_{m+2}$ ($Q = \text{S}, \text{Se}, \text{Te}$) thermoelectric materials. Despite the high charge carrier densities, both the selenide and sulfide materials show irregular semiconducting electrical conductivities under 400-600 K, while the tellurides behave normally. We directly show the thermally activated transport comes from carrier scattering at the GBs and demonstrate that the expected metallic conduction can be recovered by preparing large grained samples with a reduced density of grain boundaries. Because our microscopy investigations did not find any unusual phase or dopant segregation at the GBs in the $\text{NaPb}_m\text{SbQ}_{m+2}$ materials, we attribute the differing transport properties to the relative dielectric permittivity of each respective $\text{NaPb}_m\text{SbQ}_{m+2}$ family. In particular, the tellurides feature relatively strong charge carrier screening and negligible GB scattering, while the much less polarizable sulfides exhibit the greatest degree of GB scattering. We moreover show that DFT calculated

dielectric constants and experimental estimates of the GB energy barriers support this picture. We finally suggest that weak dielectric screening explains why other emerging thermoelectrics, such as Zintl antimonides, are also reported to have strong GB scattering. This work therefore provides an intuitive chemical argument for anticipating what materials will be prone to GB scattering. Based on this analysis, we anticipate that the traditional paradigm of minimizing grain size to be inadvisable for these materials and suggest that rationally preparing larger (meso-scale) grained samples may be beneficial to eliminate the GB scattering and improve the low temperature power factors.

4.4 Experimental details

4.4.1 Synthesis and processing

The starting materials were Pb wire (99.99%, American Elements, USA), Se shot (99.99%, American Elements, USA), S pieces (99.99%, American Elements), Sb shot (99.999%, American Elements, USA), and Na cubes (99.95%, Sigma Aldrich). Before synthesis, a razor blade was used to scrape the surface oxidation off the lead and sodium. All sodium was handled in a N₂ filled glovebox.

SPS processed samples: Polycrystalline ingots were first synthesized by weighing stoichiometric quantities of each element according to the desired nominal compositions into 13 mm diameter carbon coated fused silica tubes that were then flame sealed at $\sim 2 \times 10^{-3}$ Torr. Typical samples used 15 grams of total starting material for the selenides and 10 grams for the sulfides. The tubes were heated in a box furnace to 773 K over 12 h, held for 2 h, then heated to 1473 K over 7 h where they dwelled at temperature for 5 h. The tubes were next quenched in ice water followed by

annealing at 773 K for 12 h. After annealing, the tubes were again quenched in water, and the ingots were removed and ground to a fine powder with a mortar and pestle. We attempted to ensure homogeneous powder and grain size by passing the powdered samples through a 53 μm mesh sieve. The samples were then each loaded into 12.7 mm graphite dies and sintered into dense pellets by spark plasma sintering (SPS-211LX, Fuji Electronic Industrial Co. Ltd). The sintering process was conducted under dynamic vacuum at 823 K for the selenides and at 873 K for the sulfides. In both cases the samples were held at the desired temperature for 10 min under 40 MPa of uniaxial pressure before being cooled to room temperature. To characterize the electrical properties, the pellets were finally cut and polished into bars and squares of approximate dimensions $3 \times 3 \times 10 \text{ mm}^3$ and $6 \times 6 \times 2 \text{ mm}^3$. The cuts were made such that transport measurements were conducted perpendicular to the pressing direction in the SPS.

To study the effect of GB density on the electrical properties of the $\text{NaPb}_m\text{SbSe}_{m+2}$ family, we also prepared samples with differing grain sizes. This was accomplished by following the same synthetic procedure outlined above, but after crushing and grinding the ingots, the resulting powders were passes through sieves with different mesh sizes. We utilized mesh sizes of 53, 70, and 150 μm , and one sample was only briefly crushed and left un-sieved to (in principle) give the largest grains. These samples were then sintered and prepared for measurements under the conditions discussed in the preceding paragraph.

Large grained as-cast ingots: To prepare samples with the largest possible grains and lowest number of GBs, elements were first weighed at sealed in 13 mm diameter carbon-coated tubes as discussed above. We used the same heating profile to bring the tubes to 1473 K, and then held the samples at temperature for 5 hours. Instead of rapidly quenching, the tubes were next slowly cooled

to 823 K over 48 h before finally being brought to room temperature in 12 h. The slow cooling process gave enough time for large grains to nucleate. To characterize the thermoelectric properties, the as-cast ingots were carefully removed from the tubes and directly cut/polished into $3 \times 3 \times 10 \text{ mm}^3$ bars like the SPS sintered pellets discussed above.

4.4.2 Electrical conductivity and Seebeck Coefficient

With the $3 \times 3 \times 10 \text{ mm}^3$ bars, the electrical conductivities and Seebeck coefficients were measured between room temperature and 873 K using an Ulvac Riko ZEM-3 instrument. To limit outgassing at elevated temperatures, the bars were spray-coated with boron nitride aerosol prior to measurements except at the locations needed for contacts with the electrodes and thermocouples. The measurements were conducted under partial He backpressure. The uncertainty in the electrical measurements from a ZEM-3 instrument is approximately 5%. We measured the properties upon both heating and cooling. For the samples with strong GB scattering, hysteresis was often observed between first heating and cooling profile; however, the data was consistent with additional thermal cycling, see Chapter 3 for a more detailed discussion.¹⁵⁸ As such, all data in this manuscript was taken from the cooling profile.

4.4.3 Hall effect

The Hall effect measurements were completed using two different homebuilt systems. One used an AC 4-probe method with excitation fields of ± 0.5 Tesla. The system uses an air-bore, helium-cooled superconducting magnet to generate the field within a high temperature oven that surrounds the Ar-filled sample probe. The second setup utilizes Van der Pauw geometry with

magnetic fields of $\sim 2T$. The carrier densities were calculated from the Hall coefficient assuming a single carrier band, i.e., $n_H = 1/eR_H$, where R_H is the Hall coefficient. Measured Hall coefficients and charge carrier densities are given below in Table 4.2.

Table 4.2 Room temperature Hall coefficients and Hall charge carrier densities for $\text{NaPb}_m\text{SbSe}_{m+2}$ $m = 6, 20$ and $\text{NaPb}_m\text{SbSe}_{m+2}$ $m = 20$. Nominal compositions are $\text{Na}_{1.10}\text{Pb}_{5.90}\text{Sb}_x\text{Se}_8$ and $\text{Na}_{1+x}\text{Pb}_{20-x}\text{SbSe}_{22}$, and $\text{Na}_{1+x}\text{Pb}_{20-x}\text{SbS}_{22}$.

Nominal Composition	R_H ($10^{-2} \text{ cm}^3\text{C}^{-1}$)	n_H (10^{19} cm^{-3})
$\text{Na}_{1.10}\text{Pb}_{5.90}\text{Sb}_{0.90}\text{Se}_8$	6.08	10.27
$\text{Na}_{1.05}\text{Pb}_{19.95}\text{SbSe}_{22}$	24.22	2.58
$\text{Na}_{1.10}\text{Pb}_{19.90}\text{SbSe}_{22}$	6.43	9.70
$\text{Na}_{1.15}\text{Pb}_{19.85}\text{SbSe}_{22}$	8.70	7.17
$\text{Na}_{1.20}\text{Pb}_{19.80}\text{SbSe}_{22}$	4.40	14.2
$\text{Na}_{1.25}\text{Pb}_{19.75}\text{SbSe}_{22}$	4.05	15.4
$\text{Na}_{1.30}\text{Pb}_{19.70}\text{SbSe}_{22}$	3.61	17.3
$\text{Na}_{1.10}\text{Pb}_{19.90}\text{SbS}_{22}$	11.9	5.25
$\text{Na}_{1.15}\text{Pb}_{19.85}\text{SbS}_{22}$	4.21	14.8

4.4.4 Microscopy characterization

Grain size was illustrated with Electron Backscattered Diffraction (EBSD). EBSD samples were prepared by first cold mounting samples in an epoxy to improve the quality of polishing and to reduced sample cracking and breaking during subsequent preparation steps. Samples were then ground using 600, 800, and 1200 grit SiC paper for 10 min each, while using ethanol as a water free lubricant. Next samples were polished using 1 μm and 0.1 μm glycol-based (water free) diamond slurry for 30 and 45 min respectively. EBSD was performed using a FEI Quanta 650 ESEM at 30 kV.

To investigate the grain boundaries of $\text{NaPb}_m\text{SbTe}_{m+2}$ and $\text{NaPb}_m\text{SbSe}_{m+2}$ compounds, we performed a combination of High-Resolution Transmission Electron Microscopy (HREM) and Scanning Transmission Electron Microscopy-Energy Dispersive Spectroscopy (STEM-EDS). Samples were prepared for S/TEM analysis by conventional bulk TEM sample preparation method which includes grinding and polishing, dimpling, and finally argon ion milling. Like the first steps in EBSD sample preparation, the samples were ground on the top side using 600, 800, and 1200 grit SiC paper for 10 min each using a grinding wheel. Samples were then polished for 30 min using 1- μm glycol-based diamond slurry. A TEM grid was then attached to this polished surface using M-bond. The sample was then flipped over and the backside was ground to approximately 50 μm in thickness, again using 600, 800, and 1200 grit SiC paper. The sample was then dimpled and placed in a Fischione 1050 TEM Mill. The samples were milled at 4 kV at an angle of 6° until a hole was formed, then milled at 2 kV at 4° until the hole was widened slightly (denoted by the edge features of the hole changing shape). The sample was then polished at 1 kV and 0.3 kV for 30 minutes each at 4° . HREM and STEM were then performed at 200 kV using a JEOL JEM-2100 FasTem.

4.4.5 Calculations of the dielectric constants

The dielectric constant calculations in this study were performed using density functional perturbation theory (DFPT)¹⁷⁵ as implemented in Vienna ab initio simulation package (VASP).¹⁴⁹ We used Perdew–Burke–Ernzerhof (PBE) formulation of the exchange-correlation energy functional derived under a gradient-generalized approximation (GGA).¹⁵¹ Plane-wave basis sets were truncated at an energy cutoff of 450 eV, and a G-centered k-point mesh with a density of

~16,000 k-points per reciprocal atom (KPPRA) was used. All structures were relaxed with respect to cell vectors and their internal degrees of freedom until forces on all atoms were less than 0.1 eV nm⁻¹.

Chapter Five

NaSn_mSbTe_{m+2} and NaSn_mBiTe_{m+2} thermoelectric alloys: high performance facilitated by cation vacancies and lattice softening

5.1 Introduction

Thermoelectric generators enable reliable and emission-free conversion of thermal to electrical energy and are attractive for emerging applications in waste heat recovery and remote power generation.¹¹⁴⁻¹¹⁵ For thermoelectric technology to achieve wide-spread societal utilization, it is critical to develop materials that possess both low cost and high energy conversion efficiency, the latter of which is parameterized by the dimensionless figure of merit $ZT = \sigma S^2 T / \kappa_{\text{tot}}$. Here, σ is the electrical conductivity, S is the Seebeck coefficient, T is the absolute temperature, and κ_{tot} is the total thermal conductivity which consists of contributions from the lattice vibrations (κ_{lat}) and electrical conduction (κ_{elec}). Because these material properties are interconnected through both the carrier concentration and electronic structure, optimization of any one property generally comes at the cost of another and makes achieving high ZT exceedingly challenging.⁵ Traditional routes to improving ZT include electronic structure modifications such as electronic band structure engineering and the introduction of resonance states to improve the power factor (σS^2), or the addition of extrinsic defects through alloying and nanostructuring to lower the lattice thermal conductivity.^{29, 57}

A less investigated but potentially powerful strategy to raise ZT entails the manipulation of a material's native defects. This concept was recently utilized by Tan *et al.* in alloys of SnTe with AgSbTe₂ (AgSn_{*m*}SbTe_{*m+2*}).¹⁷⁶ SnTe has been extensively studied^{54, 177-183} as a less toxic alternative to its state-of-the-art sister compound PbTe but is limited by its intrinsically high concentration of Sn vacancies, which give SnTe a nearly metallic hole density on the order of 10^{20} – 10^{21} cm⁻³ at room temperature and correspondingly poor Seebeck coefficient and high thermal conductivity. Surprisingly, the addition of AgSbTe₂ to SnTe markedly softens the lattice, lowering the sound

velocity by over 10% while simultaneously raising the concentration of intrinsic Sn vacancies, which act as strong phonon scattering centers.¹⁷⁶ Because the acoustic phonon group velocity is directly related to the speed of sound, the lattice softening and strong vacancy phonon scattering manifest in a very low lattice thermal conductivity $\sim 0.7 \text{ W}\cdot\text{m}^{-1}\cdot\text{K}^{-1}$ at 300 K for $\text{AgSn}_5\text{SbTe}_7$ ($\sim 16\%$ AgSbTe_2 in SnTe) and high $ZT \sim 1$ at 800 K. It is notable that such low values of κ_{lat} are obtained without nanostructures or significant alloy phonon scattering, as Ag and Sb have approximately the same mass as Sn.

Motivated by these findings, we now report the analogous alloys of SnTe with NaSbTe_2 and NaBiTe_2 ($\text{NaSn}_m\text{SbTe}_{m+2}$ and $\text{NaSn}_m\text{BiTe}_{m+2}$). While superficially similar, these two materials have unique thermoelectric properties. In particular, the Sb-containing $\text{NaSn}_m\text{SbTe}_{m+2}$ compounds have notably higher power factors and lower thermal conductivities than the $\text{NaSn}_m\text{BiTe}_{m+2}$ analogues. To explain the differences, we compared the effects of NaSbTe_2 and NaBiTe_2 on the electronic structure and thermal properties of SnTe . Density functional theory (DFT) calculations indicate that the addition of either ternary compound into SnTe 1) promotes convergence of the L - and Σ -valence bands and 2) sharply decreases the band gap. While the former effect improves the Seebeck coefficients and power factors, the reduced band gaps make each compound increasingly prone to detrimental bipolar diffusion. Indeed, while the room temperature Seebeck coefficients of both materials are enhanced upon alloying, the thermoelectric properties in the Bi-containing compounds are strongly limited by bipolar charge transport above 600 K. Surprisingly however, this effect is less pronounced in the SnTe - NaSbTe_2 family. Hall effect measurements explain the difference, showing that the introduction of NaSbTe_2 , but not NaBiTe_2 , to SnTe nearly doubles the charge carrier concentration, which we attribute to an increased number of intrinsic

cation vacancies. Therefore, in $\text{NaSn}_m\text{SbTe}_{m+2}$, the higher hole carrier concentration offsets the decreased band gap and suppresses bipolar diffusion, allowing the Sb-containing samples to maintain high power factor at elevated temperature. The vacancies moreover enhance the phonon scattering in $\text{NaSn}_m\text{SbTe}_{m+2}$. Lastly, we find that NaSbTe_2 reduces the sound velocity of SnTe by nearly six percent, helping to achieve glasslike thermal conductivity under $0.7 \text{ W}\cdot\text{m}^{-1}\cdot\text{K}^{-1}$ at room temperature. The synergistic effects of the vacancies and the lattice softening in $\text{NaSn}_m\text{SbTe}_{m+2}$ result in superior maximum $ZT \sim 1.2$ at 800 K and excellent $ZT_{\text{avg}} \sim 0.7$ between 323 and 873 K, while the $\text{NaSn}_m\text{BiTe}_{m+2}$ family has significantly poorer performance with maximum ZT s near 0.85. Considering the chemical similarity of $\text{NaSn}_m\text{SbTe}_{m+2}$ and $\text{NaSn}_m\text{BiTe}_{m+2}$, this work demonstrates the importance of the intrinsic defects in determining a material's thermoelectric performance.

5.2 Results and Discussion

5.2.1 Structural characterization

To determine if mixtures of NaSbTe_2 and NaBiTe_2 with SnTe form single-phase solid solutions or nanostructured/multiphase systems we initially prepared alloys across a range of $\text{NaSn}_m\text{PnTe}_{m+2}$ (Pn = Sb, Bi) compositions as follows: SnTe + 0–33 mol percent NaSbTe_2 ($m = 50\text{--}3$) and SnTe + 0–20 mol percent NaBiTe_2 ($m = 50\text{--}5$). Samples were synthesized by cooling stoichiometric mixtures of each element from the molten state followed by spark plasma sintering (SPS) sintering to obtain dense pellets ($\sim 95\%$ theoretical density). Detailed information on the synthetic procedure is outlined in the experimental section.

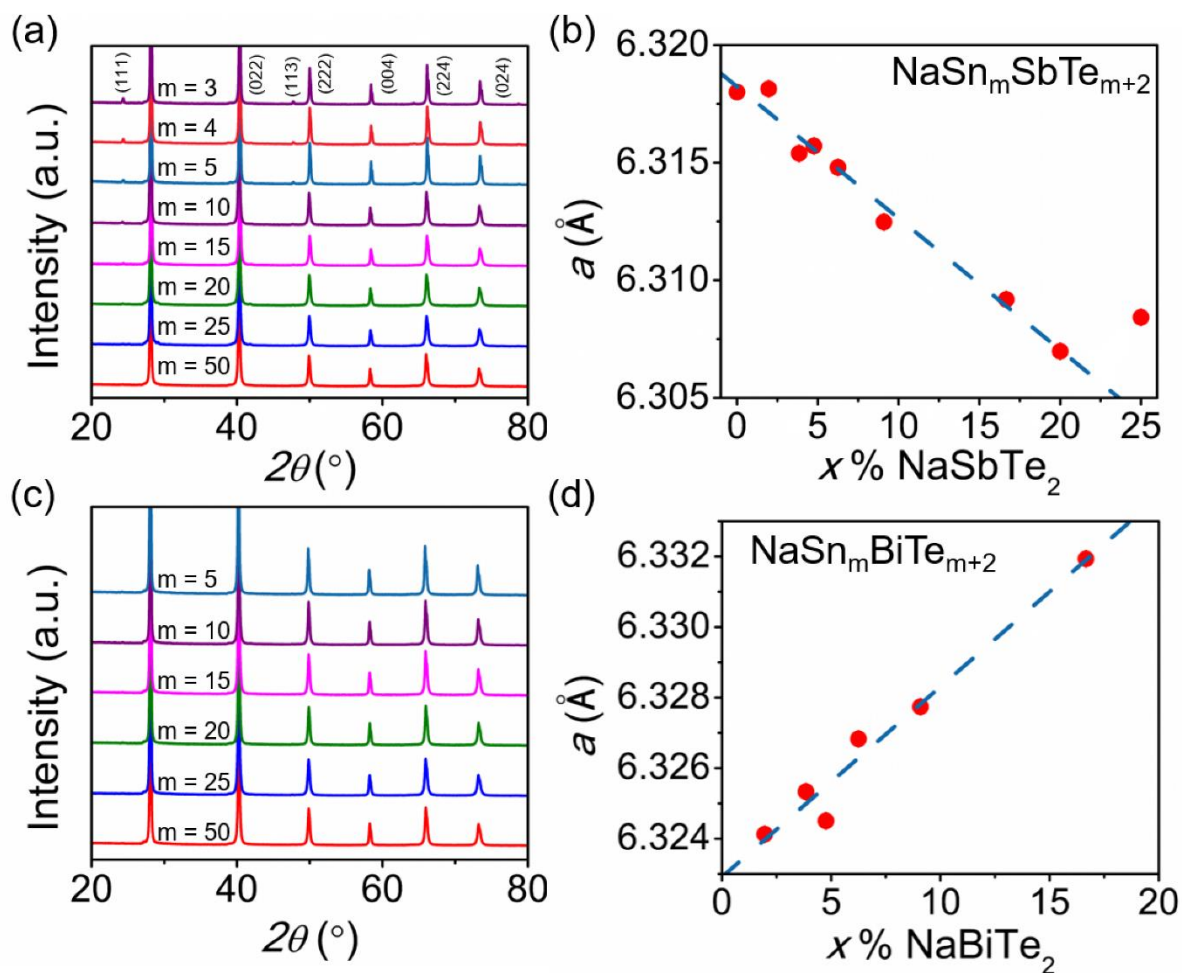


Figure 5.1 (a) Powder X-ray diffraction patterns for SnTe–NaSbTe₂ ($\text{NaSn}_m\text{SbTe}_{m+2}$) alloys for $m = 50-3$ (or equivalently up to 25% NaSbTe₂ in SnTe). (b) Rietveld refined lattice parameters obtained from diffraction patterns in (a). (c) and (d) are respectively the same for SnTe–NaBiTe₂ ($\text{NaSn}_m\text{BiTe}_{m+2}$) over $m = 50-5$ (0–16% NaBiTe₂). The dashed blue lines in (c) and (d) are guides to the eye showing the linear trends of a as function of alloy fraction. In the $\text{NaSn}_m\text{PnTe}_{m+2}$ notation, high m corresponds to SnTe-rich compositions.

Figures 5.1a and 5.1c outline the obtained power X-ray diffraction (PXRD) patterns for SPS processed $\text{NaSn}_m\text{PnTe}_{m+2}$ samples. In both cases, the diffraction patterns are consistent with the rocksalt crystal structure of SnTe, and no peaks from secondary phases are observed, indicating SnTe forms a solid solution with both NaSbTe_2 and NaBiTe_2 over the range of compositions we explored. The refined lattice parameters displayed in Figure 5.1b and 5.1d complement the diffraction patterns. In both cases, the lattice parameters decrease (increase) approximately linearly with greater alloying fraction, consistent with the smaller (larger) unit cell dimensions of NaSbTe_2 and NaBiTe_2 compared to SnTe. In Figure 5.1b, the 25% NaSbTe_2 sample deviates from the linear trend, likely indicating that the solubility limit of NaSbTe_2 in SnTe has been reached. Taken together, the diffraction data suggests both ternary compounds have high solubility (~15–20 %) in SnTe; this conclusion will be further explored below.

To confirm the single-phase nature of the SnTe– NaPnTe_2 alloys, we investigated the microstructures of our alloys with scanning electron microscopy (SEM) and transmission electron microscopy (TEM). The results for a sample with nominal composition $\text{NaSn}_5\text{SbTe}_7$ are outlined in Figure 5.2 and those for $\text{NaSn}_5\text{BiTe}_7$ are discussed in Figure 5.3. A characteristic high-resolution TEM image is found in Figure 5.2a. The TEM image shows no evidence for nanoscale precipitation, and the selected area electron diffraction (SAED) pattern displayed in the inset confirms the expected rocksalt structure without evidence of secondary peaks. Likewise, a SEM image of the same sample is shown in Figure 5.2b and again indicates a negligible phase segregation at the micron scale. Corresponding energy dispersive spectroscopy (EDS) elemental maps are presented in Figure 5.2c-f and show a homogeneous distribution of elements. Taken together, the microscopy analysis paired with the powder X-ray diffraction data

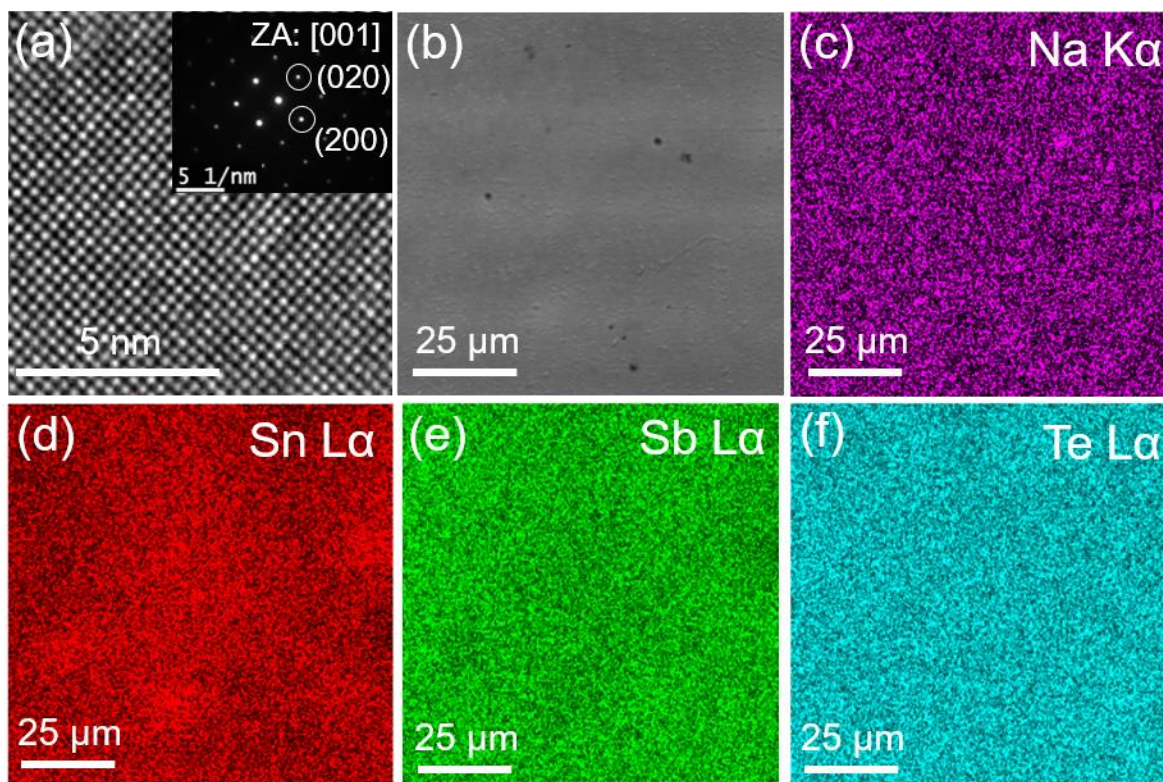


Figure 5.2 (a) High resolution TEM image of a sample with nominal composition $\text{NaSn}_5\text{SbTe}_7$) showing a clean matrix and no evidence of nanoscale precipitation. (b) SEM image of the same sample. (c-f) display EDS spectra obtained over the SEM image shown in (b). The EDS spectra for each element are uniform over the full images, indicating the sample is single phase on the micron scale.

discussed above provide strong evidence that phase-pure samples of $\text{NaSn}_m\text{SbTe}_{m+2}$ were successfully synthesized down to at least $m = 5$ (~16 % NaSbTe_2 in SnTe).

The results for the SnTe-NaBiTe_2 alloys discussed in Figure 5.3 are analogous and suggest successful synthesis of single-phase materials with homogeneous microstructures. It is noteworthy to point out that earlier studies of PbTe-NaSbTe_2 and PbSe-NaSbSe_2 report minor micron-scale

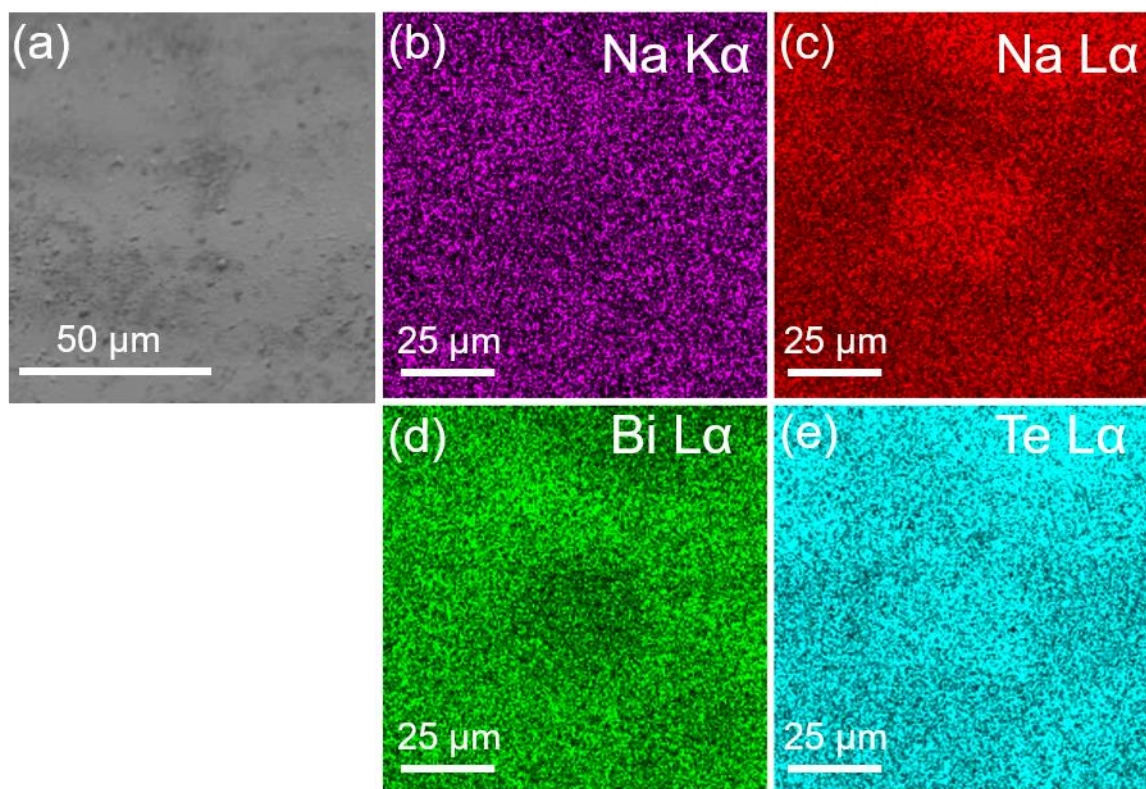


Figure 5.3 (a) A characteristic SEM image of a $\text{NaSn}_m\text{BiTe}_{m+2}$ sample with nominal composition $\text{NaSn}_5\text{BiTe}_7$ ($m = 5$). (b-e) are the corresponding energy dispersive spectroscopy (EDS) elemental maps of each element. The data shows a nearly uniform distribution of elements indicating a single-phase microstructure.

heterogeneity,^{124, 158} and PbTe-AgSbTe_2 samples are reported to have more significant segregation as well as nanostructured microstructures.^{94, 127} DFT calculations yield lower mixing energies for SnTe-APnTe_2 ($A = \text{Na, Ag}$) than the alloys with PbTe and PbSe , in agreement with the above observations;¹²⁶ however, the fundamental reasons for these differences are not well understood and may be worthy of more direct attention.

5.2.2 Comparing the thermoelectric properties of $\text{NaSn}_m\text{SbTe}_{m+2}$ and $\text{NaSn}_m\text{BiTe}_{m+2}$

After establishing the single-phase nature of $\text{NaSn}_m\text{SbTe}_{m+2}$ and $\text{NaSn}_m\text{BiTe}_{m+2}$ compounds, we next investigated their thermoelectric properties. The data for $\text{NaSn}_m\text{SbTe}_{m+2}$ and $\text{NaSn}_m\text{BiTe}_{m+2}$ are displayed in Figures 5.4 and 5.5 respectively. The electrical properties of both families are qualitatively similar, as the electrical conductivities decrease and the Seebeck coefficients increase as functions of temperature, behavior characteristic of degenerately doped semiconductors. Because SnTe is known to crystallize with an intrinsically high fraction of Sn vacancies that produce hole densities over 10^{20} cm^{-3} , the degenerate charge transport observed here indicates that the cation vacancies are retained after alloying with $\text{NaSbTe}_2/\text{NaBiTe}_2$. Furthermore, the electrical conductivities generally decrease with greater $\text{NaSbTe}_2/\text{NaBiTe}_2$

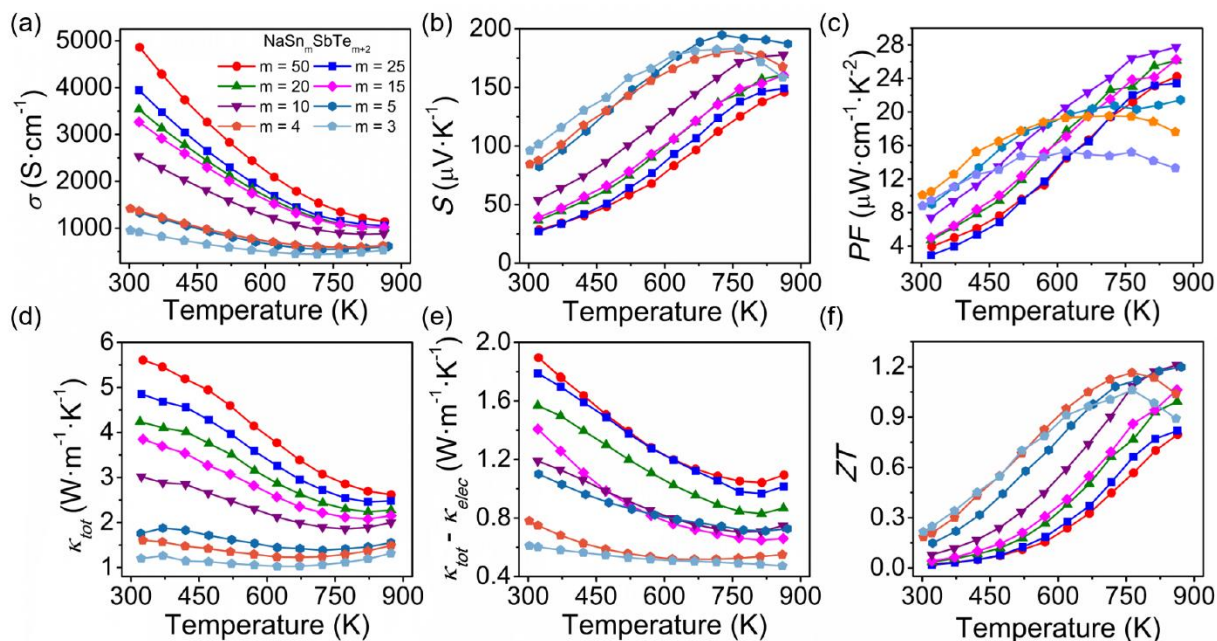


Figure 5.4 Thermoelectric properties for SnTe–NaSbTe₂ ($\text{NaPb}_m\text{SbTe}_{m+2}$) alloys over $m = 50$ – 3 (2–25 % NaSbTe₂). (a) Electrical conductivities, (b) Seebeck coefficients, (c) power factors, (d) total thermal conductivities, (e) lattice thermal conductivities, and (f) figure of merit ZT .

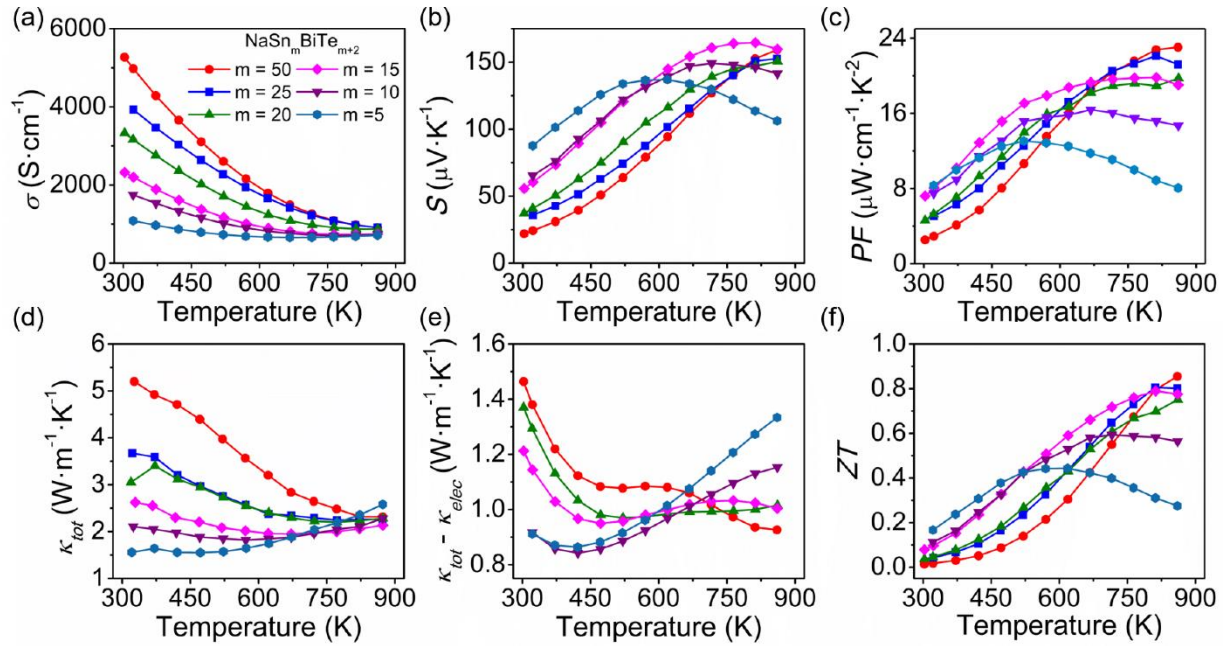


Figure 5.5 Thermoelectric properties for SnTe–NaBiTe₂ (NaPb_mBiTe_{m+2}) alloys over $m = 50$ – 5 (2–16 % NaBiTe₂). (a) Electrical conductivities, (b) Seebeck coefficients, (c) power factors, (d) total thermal conductivities, (e) lattice thermal conductivities, and (f) figure of merit ZT .

fraction, while the Seebeck coefficients are enhanced. The above trends indicate that either the charge carrier concentration falls with NaSbTe₂/NaBiTe₂ alloying, or the effective mass rises.

Comparison of the electrical properties shows that the Sb-containing NaSn_mSbTe_{m+2} materials have superior Seebeck coefficients. While the room temperature values of S are similar in both families, the Seebeck coefficients in NaSn_mBiTe_{m+2} are limited by intrinsic conduction (bipolar diffusion) and reach maximum values $\sim 160 \mu\text{V}\cdot\text{K}^{-1}$ at ~ 600 – 750 K and decrease with further heating. Bipolar diffusion is weaker in NaSn_mSbTe_{m+2} materials, and the Seebeck coefficients achieve high values approaching $200 \mu\text{V}\cdot\text{K}^{-1}$ at ~ 750 – 800 K for NaSbTe₂–rich compositions. As shown in Figures 5.4c and 5.5c, the power factors reflect the trends in Seebeck

coefficients, reaching superior maximum values $\sim 28 \mu\text{W}\cdot\text{cm}^{-1}\cdot\text{K}^{-2}$ in $\text{NaSn}_m\text{SbTe}_{m+2}$ compared to $\sim 24 \mu\text{W}\cdot\text{cm}^{-1}\cdot\text{K}^{-2}$ in $\text{NaSn}_m\text{BiTe}_{m+2}$. Likewise, the power factors are increasingly suppressed above 600 K in $\text{NaSn}_m\text{BiTe}_{m+2}$ compared to those in the Sb-containing analogues.

The total and lattice thermal conductivities for $\text{NaSn}_m\text{SbTe}_{m+2}$ are respectively outlined in Figure 5.4d and 5.5e, and those for $\text{NaSn}_m\text{BiTe}_{m+2}$ are given in Figures 5.4d and 5.5e. In both families, the values of κ_{tot} and κ_{lat} decrease with greater $\text{NaSbTe}_2/\text{NaBiTe}_2$ alloying as anticipated from strengthened point-defect phonon scattering from the Na and Sb/Bi ions. The lattice thermal conductivities estimated in $\text{NaSn}_m\text{BiTe}_{m+2}$ plateau as functions of temperature near 450 K for $m = 5\text{--}20$ (2–5% NaBiTe_2), and increase with heating over most of the measured temperature range for $m = 10$ and 5 (9 and 16 percent NaBiTe_2 respectively). The apparent thermal activation of κ_{lat} in $\text{NaSn}_m\text{BiTe}_{m+2}$ is typical of bipolar diffusion, in agreement with the electrical data discussed above. On the other hand, the estimated lattice thermal conductivities in $\text{NaSn}_m\text{SbTe}_{m+2}$ decrease over the full range of temperatures, reaching glasslike values of $\sim 0.5 \text{ W}\cdot\text{m}^{-1}\cdot\text{K}^{-1}$ that have weak temperature dependences for $m = 4$ and 3 (20 and 25 percent NaSbTe_2).

As presented in Figures 5.4f and 5.5f, the $\text{NaSn}_m\text{SbTe}_{m+2}$ family of materials achieves high $ZTs \sim 1.2$ at 800–900 K for high fractions of NaSbTe_2 ($m = 5, 4$; equivalently, 16–20% NaSbTe_2), while the poorer Seebeck coefficients and higher thermal conductivities of $\text{NaSn}_m\text{BiTe}_{m+2}$ manifest in significantly lower $ZTs \sim 0.8$. Because figures of merit near 1.2 are promising, we compare the variable-temperature ZTs of $\text{NaSn}_m\text{SbTe}_{m+2}$ with several recent examples of high performance SnTe-based thermoelectric systems in Figure 5.6a.^{178, 180, 184–185} Our $\text{NaSn}_m\text{SbTe}_{m+2}$ samples are clearly competitive with the state-of-the-art SnTe materials, particularly at low and moderate temperatures under ~ 750 K. Indeed, because the efficiency of a thermoelectric generator is

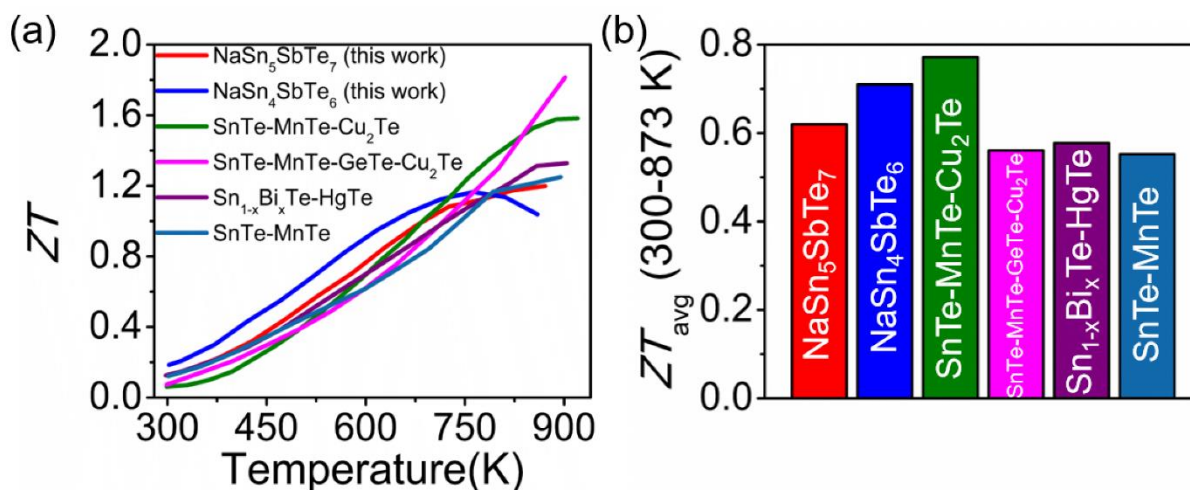


Figure 5.6 (a) Traces of the ZT vs. temperature curves for NaSn_{*m*}SbTe_{*m*+2} ($m = 4, 5$) presented in this work with several examples of high-performance thermoelectric systems recently reported in the literature.^{178, 180, 184-185} (b) Average ZT s calculated over 300–873 K corresponding to the materials in (a).

ultimately determined by the average ZT of the semiconductor legs over the operating temperature range (also denoted as device ZT , engineering ZT , etc. in other publications),¹³⁹ the high values of ZT measured here at lower temperature are noteworthy. To demonstrate the promise of our NaSn_{*m*}SbTe_{*m*+2} materials, we used the process outlined by Snyder *et al.* to estimate the average ZT (ZT_{avg}) of the materials discussed in Figure 5a.¹³⁹ As displayed in Figure 5.6b, our NaSbTe₂-rich NaSn_{*m*}SbTe_{*m*+2} samples ($m = 4, 5$) have competitive average figures of merit ~ 0.6 – 0.7 over 300 to 873 K, indicating these materials are attractive candidates for medium temperature thermoelectric applications.

5.2.3 Impact of NaSbTe₂ and NaBiTe₂ on the electronic structure of SnTe

While the NaSn_mSbTe_{m+2} materials are promising thermoelectric materials, the NaSn_mBiTe_{m+2} family has significantly poorer properties. As discussed above, the superior *ZT*s of NaSn_mSbTe_{m+2} come from higher Seebeck coefficients and lower lattice thermal conductivities. To understand the origin of the differences, we used density functional theory (DFT) and Hall effect measurements to compare the effect of NaSbTe₂ and NaBiTe₂ on the electronic structure and native defects of SnTe. Details concerning the DFT calculations and Hall measurements are given in the experimental section.

The electronic energy band structures calculated for pure SnTe and several NaSn_mSbTe_{m+2} compositions are presented in Figure 5.7 and those for NaSn_mBiTe_{m+2} are given in Figure 5.8. The notation Na_xS_{27-2x}Pn_xTe₂₇ (Pn = Sb, Bi) was used to be consistent with the supercells used for the calculations, and the compositions refer to approximately 4, 7.5, and 11 percent NaPnTe₂ in SnTe or respectively $m = 25$, 11.5, and 7. The calculated electronic structures show qualitative similarities and important differences after NaPnTe₂ incorporation. At low alloying, both NaSn_mSbTe_{m+2} and NaSn_mBiTe_{m+2} retain the key features of the SnTe band structure, with a primary band gap at the *L*-point of the Brillouin zone and a second valence band deeper in energy the Γ -*K* line (Σ point). As greater fractions of the ternary compounds are added to SnTe, our calculations suggest the energy separation between the *L*- and Σ -valence bands ($\Delta E_{L-\Sigma}$) decreases, from 0.26 eV in pure SnTe to approximately 0.11 eV for 11 % NaPnTe₂. Enhancing the density of states effective mass through valence band convergence is a well-established means of improving the power factor and electronic component of the thermoelectric quality factor in lead and tin chalcogenides.^{46-47, 89} As shown in Figures 5.5b and 5.6b, the room temperature values of

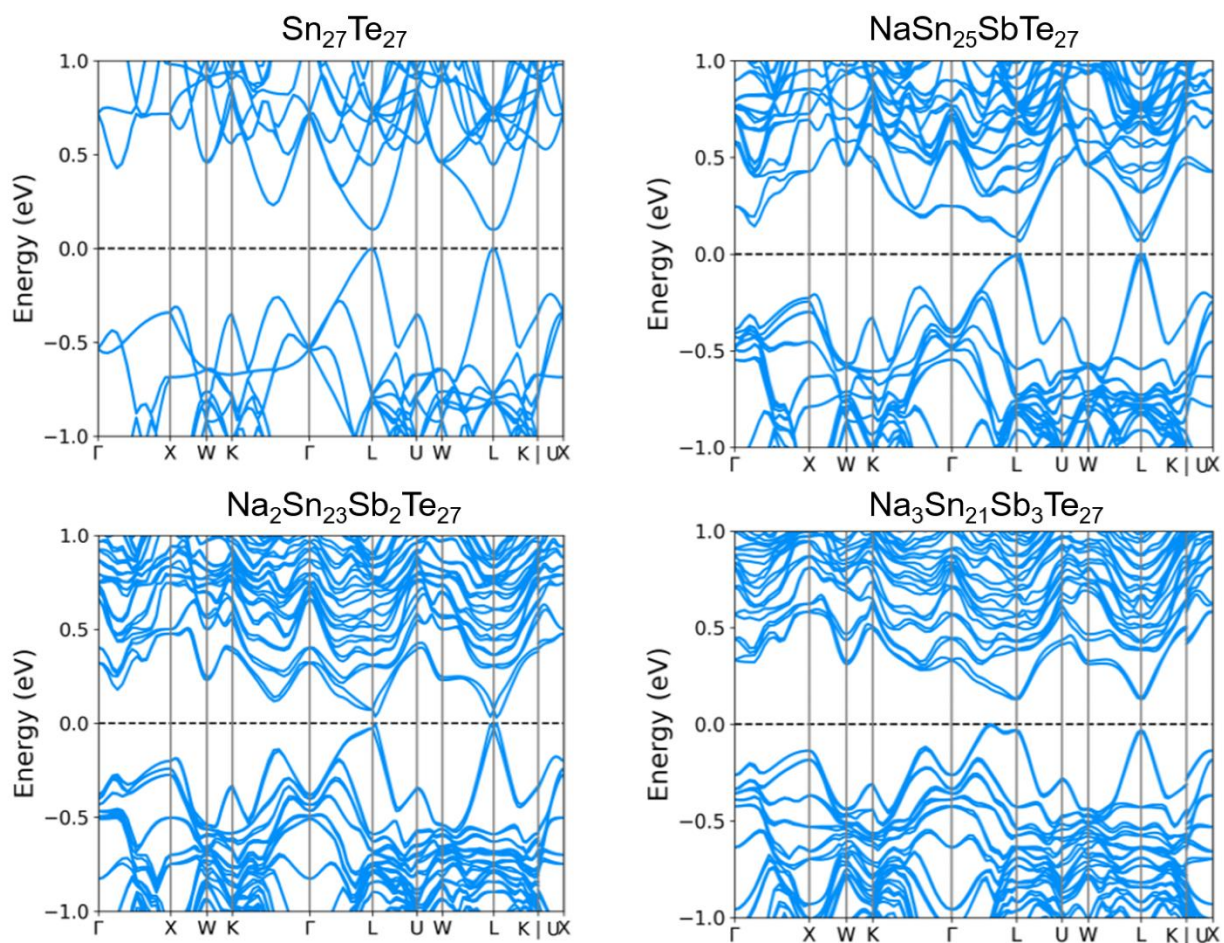


Figure 5.7 DFT calculated electronic energy band structures of SnTe–NaSbTe₂ (NaSn_{*m*}SbTe_{*m+2*}) for pure SnTe and approximately 4, 7.5, and 11 percent NaSbTe₂ or respectively *m* = 25, 11.5, and 7. The compositions are denoted Na_{*x*}Sn_{27-2*x*}Sb_{*x*}Te₂₇ to reflect the supercells used in the calculations. The band along the Γ –*K* line is the Σ -band.

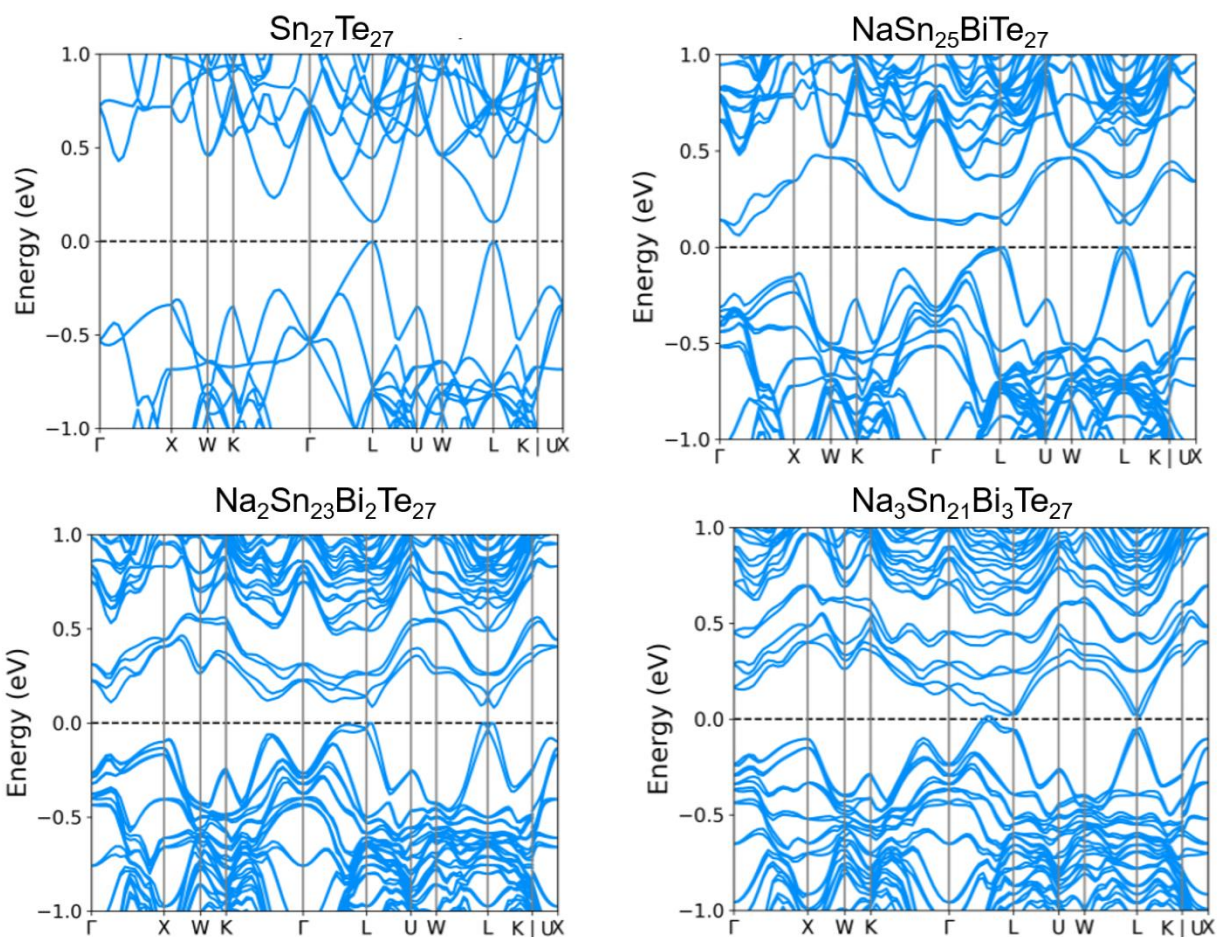


Figure 5.8 DFT calculated electronic energy band structures for SnTe–NaBiTe₂ (NaSn_{*m*}BiTe_{*m*+2}) for pure SnTe and approximately 4, 7.5, and 11 percent NaBiTe₂ or respectively $m = 25, 11.5,$ and 7 . The compositions are denoted Na_{*x*}Sn _{$27-2x$} Bi_{*x*}Te₂₇ to reflect the supercells used in the calculations. The band along the Γ – K line is the Σ -band.

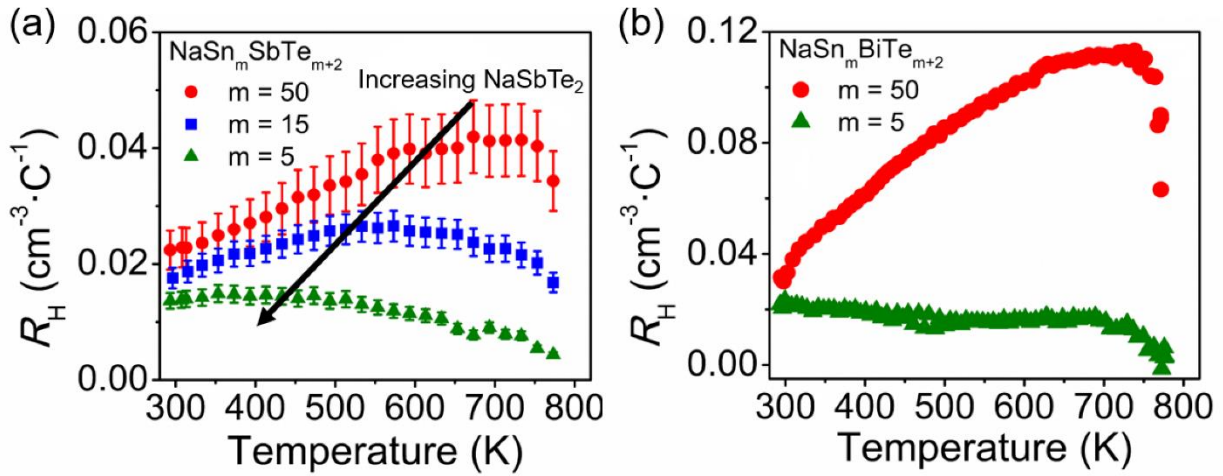


Figure 5.9 Variable temperature Hall coefficients measured for (a) $\text{NaSn}_m\text{SbTe}_{m+2}$ ($m = 50, 15, 5$) and (b) $\text{NaSn}_m\text{BiTe}_{m+2}$ ($m = 50, 5$).

S for are monotonically enhanced at room temperature with increasing $\text{NaSbTe}_2/\text{NaBiTe}_2$ incorporation, in agreement with the DFT predicted band convergence. Moreover, the calculations indicate the electronic bands flatten at higher concentration of NaSbTe_2 , i.e. that the band effective mass increases. This is anticipated considering the more ionic nature of the Na and Sb ions compared to the host Sn^{100} and is reflected in the large reduction of electrical conductivity with greater NaSbTe_2 alloying observed in Figure 5.4a.

To supplement the DFT calculations, we measured the variable-temperature Hall coefficients R_H . The data for three $\text{NaSn}_m\text{SbTe}_{m+2}$ samples is shown in Figure 5.9a. For the $m = 50$ sample, the Hall coefficients increase with heating to ~ 650 K after which they plateau and begin to slightly decrease at the highest temperatures. As the NaSbTe_2 fraction is increased, the peak value of R_H shifts to lower temperatures, and the temperature dependence of the curves becomes weaker. A peak in the R_H vs temperature plot occurs in multi-band systems when charge

carries redistribute between bands upon heating. In lead and tin chalcogenides, this is generally accepted as a rough indication of band convergence,¹³² and the clear shift in the R_H peak to lower temperatures upon greater NaSbTe₂ alloying fraction suggests a decreased energy separation between valence bands, in agreement with the DFT calculations. The weakened temperature dependence of R_H noted above is also important. Because the temperature dependence of the Hall coefficient is ultimately a function of the ratio of partial electrical conductivities of each band participating in the transport,¹³¹ the flattened temperature dependence of the Hall data in low- m samples indicates that the charge carrier effective mass m_L^* of the L -band increases with NaSbTe₂, again in agreement with the results predicted by the DFT calculated band structures.

The Hall coefficients measured for two samples of NaSn _{m} BiTe _{$m+2$} are likewise presented in Figure 5.9b and are qualitatively similar. In both cases, the absolute values of R_H are larger than the respective Sb-containing samples, indicative of their smaller charge carrier concentrations. For $m = 50$, the Hall coefficients rise with heating up to ~ 650 K where they plateau. At the highest temperatures near 800 K, the Hall coefficients begin to decrease rapidly, likely from the onset of bipolar diffusion and/or the influence of the second heavy valence band. The Hall coefficients for the $m = 50$ sample are nearly temperature independent. Again, these results are in good agreement with the DFT calculations, which show flattening of the electronic bands and decreased separation between the L - and Σ -bands for more NaBiTe₂-rich compositions.

To assess the impact of the band convergence and increased effective mass, we plot the room temperature Seebeck coefficients against charge carrier density (Pisarenko plots) in Figure 5.10. The experimental data is compared with theoretical values for pure SnTe, and clearly shows that the measured Seebeck coefficients of NaSn _{m} SbTe _{$m+2$} and NaSn _{m} BiTe _{$m+2$} are significantly

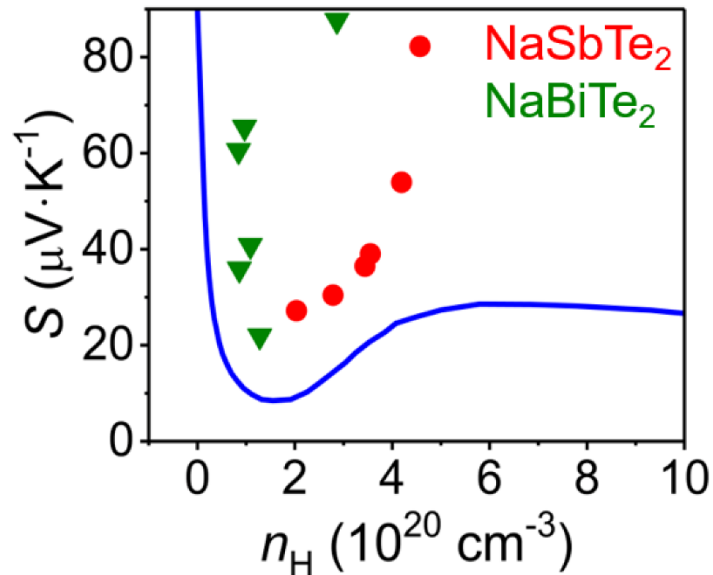


Figure 5.10 Pisarenko plot showing the Seebeck coefficients plotted against charge carrier concentration for $\text{NaSn}_m\text{SbTe}_{m+2}$ (red) and $\text{NaSn}_m\text{BiTe}_{m+2}$ (green). The solid blue line is the theoretical curve calculated for pure SnTe.¹⁸³

enhanced, therefore indicating the density of states effective mass m_{DOS}^* is enhanced upon alloying with NaSbTe₂ and NaBiTe₂. Unfortunately, because band convergence (enhanced N_v) and band flattening (increased m_b^*) will both raise m_{DOS}^* , it is very challenging to decouple the individual effects of each in our samples. Despite this, the Pisarenko curve and Hall effect data both support that the enhanced Seebeck coefficients in $\text{NaSn}_m\text{SbTe}_{m+2}$ and $\text{NaSn}_m\text{BiTe}_{m+2}$ come from the changes each ternary compound imparts on the electronic structure of SnTe.

Surprisingly, the DFT calculations furthermore indicate that the band gap of SnTe decreases with greater NaPnTe₂ fraction, narrowing from ~0.1 eV for SnTe to ~0.03 eV for ~7.5% NaSbTe₂, after which the gap widens and becomes indirect. The predicted band gaps for $\text{NaSn}_m\text{BiTe}_{m+2}$ (SnTe – NaBiTe₂) shrink with increasing alloying and completely close at ~12%

NaBiTe₂, indicating NaSn_mBiTe_{m+2} becomes a semimetal at high NaBiTe₂ fraction. Upon first consideration, these results are unexpected, as NaSbQ₂ (Q = Te and Se) are reported to widen the energy gaps in the isostructural compounds PbTe and PbSe.^{124, 158} Despite this, band structures calculated for the related SnTe–AgSbTe₂ alloys also predict a decreased band gap for greater AgSbTe₂ content,¹⁷⁶ indicating our calculations are not unprecedented. Compared to the lead chalcogenides, the opposite band gap trends as functions of APnTe₂ (A = Na, Ag) alloying may feasibly be due to the inverted order of bands at the Brillouin zone *L*-point in SnTe.¹⁸⁶ Unfortunately, experimentally probing the DFT predictions is challenging, as the intrinsically high charge carrier density of SnTe materials severely complicates accurately measuring the band gap using electronic absorption spectroscopy.

In summary, the electronic band structure calculations and variable temperature Hall effect measurements indicate that the introduction of either NaSbTe₂ or NaBiTe₂ in SnTe lowers the energy separation between the *L*- and Σ -valence bands while also raising the effective mass of the *L*-band. Moreover, the DFT calculations surprisingly suggest that alloying either ternary compound reduces the band gap of SnTe. Critically however, the calculations predict that high fractions of NaBiTe₂ will close the band gap to form a semimetal, while the gap remains finite and even widens at high alloying fraction in the SnTe–NaSbTe₂ system. These results provide some theoretical rationalization for the different thermoelectric performance of each family. Namely, while band convergence improves the Seebeck coefficients (and power factors) of NaSbTe₂-rich compositions of NaSn_mSbTe_{m+2}, the favorable effects of NaBiTe₂ are largely suppressed by bipolar diffusion in NaSn_mBiTe_{m+2} owing to its closed band gap.

5.2.4 The role of cation vacancies in $\text{NaSn}_m\text{SbTe}_{m+2}$

The measured room temperature charge carrier densities are outlined in Figure 5.11a. As anticipated from the electrical transport properties, the Hall data confirms the degenerate nature of both families of compounds, with measured hole densities all over 10^{20} cm^{-3} . Surprisingly, the charge carrier densities for $\text{NaSn}_m\text{SbTe}_{m+2}$ increase with NaSbTe_2 fraction, nearly doubling from $\sim 2.5 \times 10^{20} \text{ cm}^{-3}$ for SnTe to $\sim 4.6 \times 10^{20} \text{ cm}^{-3}$ after 16% NaSbTe_2 alloying ($m = 5$). On the other hand, the measured Hall carrier concentrations for $\text{NaSn}_m\text{BiTe}_{m+2}$ are somewhat lower $\sim 1 \times 10^{20} \text{ cm}^{-3}$ and stay approximately constant with increasing NaBiTe_2 , except for the highest alloying fraction, which has a greater carrier density comparable to pure SnTe and the low m $\text{NaSn}_m\text{SbTe}_{m+2}$ samples. These results are unusual; because both NaSbTe_2 and NaBiTe_2 are charge balanced semiconductors, neither compound is anticipated to alter the charge carrier concentration of SnTe. Yet, n_H nearly doubles between $m = 50$ and 5 ($\sim 2\text{--}16\%$ NaSbTe_2) in $\text{NaSn}_m\text{SbTe}_{m+2}$. In principle, Na is a p-type dopant in SnTe, so if greater quantities of Na than Sb were incorporated into the SnTe matrix after alloying with NaSbTe_2 , we would expect to observe an increasing hole concentration with greater alloy fraction. However, if this were the case, we would also expect to observe Sb-rich secondary phases or precipitates in the microstructure. Since our X-ray diffraction and microscopy data discussed earlier does not contain evidence for precipitation at nano- or micron length scales, we can likely rule out unintentional Na doping from the ternary compounds. Instead, we believe that incorporation of NaSbTe_2 into SnTe increases the density of cation vacancies in the $\text{NaSn}_m\text{SbTe}_{m+2}$ compounds.

As already noted, SnTe always crystallizes with an intrinsically high fraction of cation vacancies, yielding metallic hole densities. Here, the room temperature Hall effect data suggests

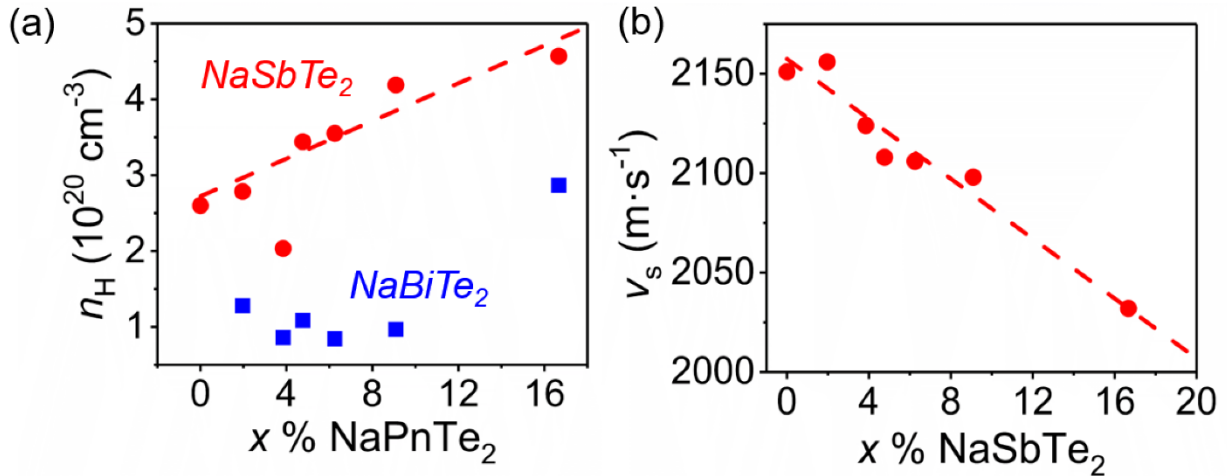


Figure 5.11 (a) Room temperature hall charge carrier concentrations for SnTe-NaSbTe_2 ($\text{NaSn}_m\text{SbTe}_{m+2}$) and SnTe-NaBiTe_2 ($\text{NaSn}_m\text{BiTe}_{m+2}$). (b) Room temperature (average) sound velocities for SnTe-NaSbTe_2 ($\text{NaSn}_m\text{SbTe}_{m+2}$). The dashed line in (b) shows the linear fit.

that incorporation of NaSbTe_2 , but not NaBiTe_2 , into SnTe further raises the number of vacancies and correspondingly increases n_H . This result is not unprecedented, as the analogous alloys of SnTe with AgSbTe_2 ($\text{AgSn}_m\text{SbTe}_{m+2}$) are reported to show the same behavior.¹⁷⁶ Notably however, the SnTe-NaBiTe_2 alloys do not appear to exhibit this effect. Furthermore, the carrier densities reported for SnTe-AgBiTe_2 also do not change significantly with AgBiTe_2 fraction.¹⁸⁷ Therefore, only NaSbTe_2 and AgSbTe_2 , but not the Bi-containing analogues, increase the concentration of Sn vacancies in SnTe .

Unlike in most SnTe -based thermoelectric materials where high vacancy concentrations degrade the performance, the enhanced number of cation vacancies in $\text{NaSn}_m\text{SbTe}_{m+2}$ is critical to obtaining high ZT . This is because both NaSbTe_2 and NaBiTe_2 decrease the band gap of SnTe , as shown by the DFT calculations, making the $\text{NaSn}_m\text{PnTe}_{m+2}$ more prone to detrimental bipolar

diffusion than pure SnTe. In $\text{NaSn}_m\text{SbTe}_{m+2}$, the elevated hole concentration acts against this and helps suppresses bipolar diffusion.¹⁸⁸⁻¹⁸⁹ On the other hand, NaBiTe_2 alloying does not substantially alter the carrier concentration, leaving the $\text{NaSn}_m\text{BiTe}_{m+2}$ materials increasingly vulnerable to bipolar diffusion at high NaBiTe_2 fraction (low m). As seen in Figure 5.5, the Seebeck coefficients, power factors, and thermal conductivities of the NaBiTe_2 -rich (low m) $\text{NaSn}_m\text{BiTe}_{m+2}$ samples are all limited by bipolar diffusion above ~ 500 K, while the detrimental effect is significantly less pronounced in the Sb-containing analogues.

In addition to favorably augmenting the electrical properties of $\text{NaSn}_m\text{SbTe}_{m+2}$, the cation vacancies also facilitate low lattice thermal conductivity. In SnTe-AgSbTe_2 , Tan *et al.* discovered that AgSbTe_2 precipitously reduces the sound velocity v_s of pure SnTe by over 10%, which they attribute to the increased concentration of Sn vacancies. Because the speed of sound is approximately equal to the phonon velocity v_g at low wavevector, and κ_{lat} scales as v_g^3 at relevant temperatures,¹⁷ the reduced sound velocity manifests in exceptionally low lattice thermal conductivities in $\text{AgSn}_m\text{SbTe}_{m+2}$.¹⁷⁶ Motivated by these results, we used a pulse-echo technique to measure the sound velocities of our SnTe-NaSbTe_2 alloys. The data is outlined in Figure 5.11b and reveals an almost linear reduction of v_s with increasing fraction of NaSbTe_2 , falling $\sim 6\%$ from ~ 2150 to 2030 $\text{m}\cdot\text{s}^{-1}$. To confirm the lattice softening, we also measured the low temperature specific heats of several of our samples and show the data in Figures 5.12a–c. We use the low temperature specific heat data to estimate the Debye temperatures θ_D of each sample (Figures 5.12d–f. The Debye temperature serves as an additional measure of the softness of the lattice, and Figure 5.13 show a linear decrease in θ_D as a function of NaSbTe_2 percent, supplementing the sound velocity measurements and providing firm evidence for significant lattice softening in the

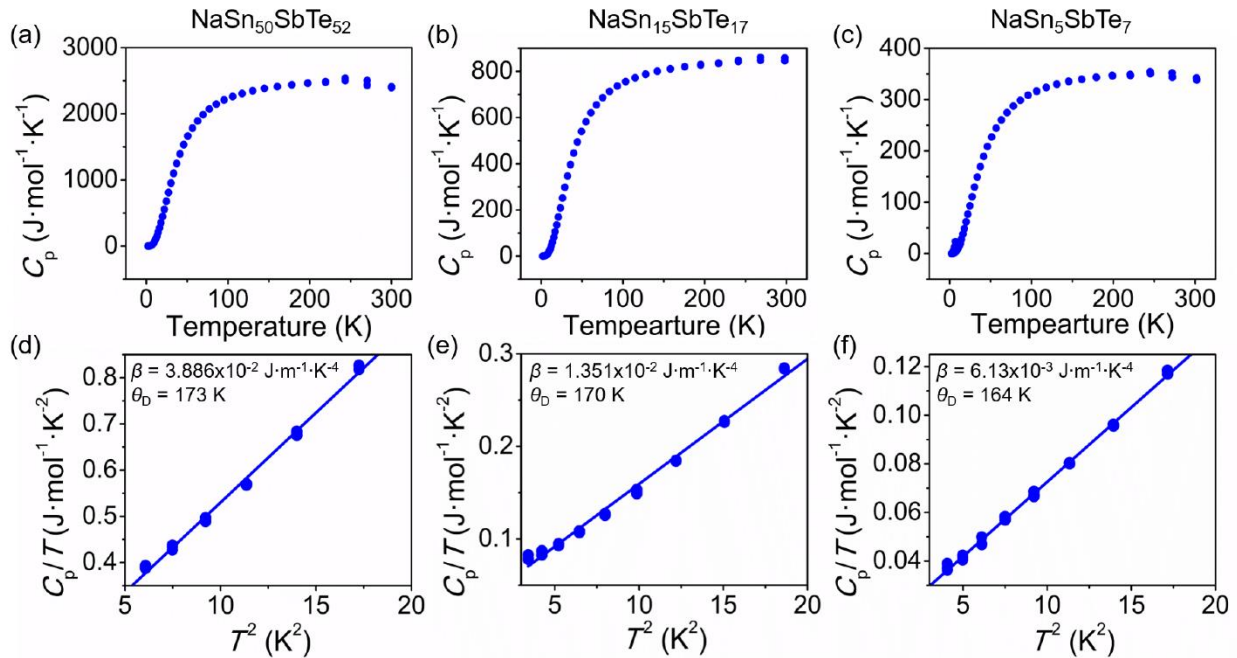


Figure 5.12 (a-c) Temperature-dependent specific heats measured for $\text{NaSn}_m\text{SbTe}_{m+2}$ for $m = 50, 15, 5$ (equivalently $\sim 2, 6, 16.6$ percent NaSbTe_2 in SnTe respectively). (d-f) Low-temperature plots of C_p/T vs. T^2 corresponding to C_p data displayed in (a-f). The slopes (β) and estimated Debye temperatures (θ_D) are also shown for each.

SnTe – NaSbTe_2 alloys. Comparing figures 5.11a and 5.11b, the trends in V_{Sn} and v_s indicate that the reduction in sound velocity/Debye temperatures may be related to the enhanced number of Sn vacancies. This will be the topic of an upcoming manuscript.

Because vacancies represent a strong local perturbation of the lattice, vacancy-phonon scattering is a particularly strong form of point defect scattering.^{19, 190-191} Since our $\text{NaSn}_m\text{SbTe}_{m+2}$ materials host enhanced concentrations of vacancies compared to $\text{NaSn}_m\text{BiTe}_{m+2}$, we anticipate the NaSbTe_2 alloyed family to also host stronger phonon scattering. The joint effects of decreased sound velocity and enhanced phonon-vacancy scattering should reduce the lattice thermal

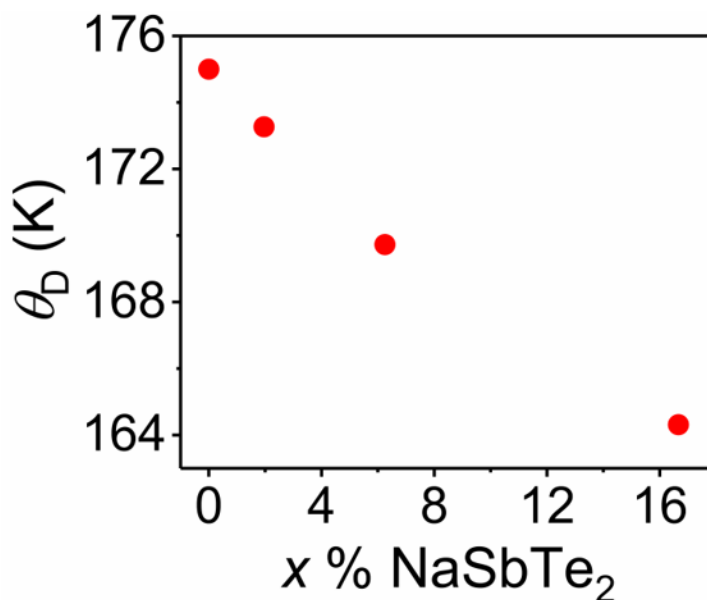


Figure 5.13 Debye temperatures SnTe–NaSbTe₂ (NaSn_mSbTe_{m+2}) estimated from the specific heat data and plotted vs. NaSbTe₂ fraction.

conductivities of NaSn_mSbTe_{m+2} beyond what would be anticipated by only point defect phonon scattering. To illustrate this, Figure 5.14 shows the measured values of κ_{lat} along with those calculated using two Debye-Callaway type models.¹⁷⁶ The details concerning the calculations are outlined in the experimental section.

The room temperature data is presented in Figure 5.14a. The theoretical curve shown in blue assumes a constant Sn vacancy concentration (V_{Sn}) and sound velocity and considers intrinsic phonon–phonon scattering, phonon–vacancy scattering, phonon–grain boundary scattering, and point-defect phonon scattering resulting from the NaSbTe₂.¹⁷⁶ While the blue curve matches the experimental data reasonably well at low alloying fraction, it clearly overestimates the measured points at high x . On the other hand, the second theoretical projection (red curve) utilizes the

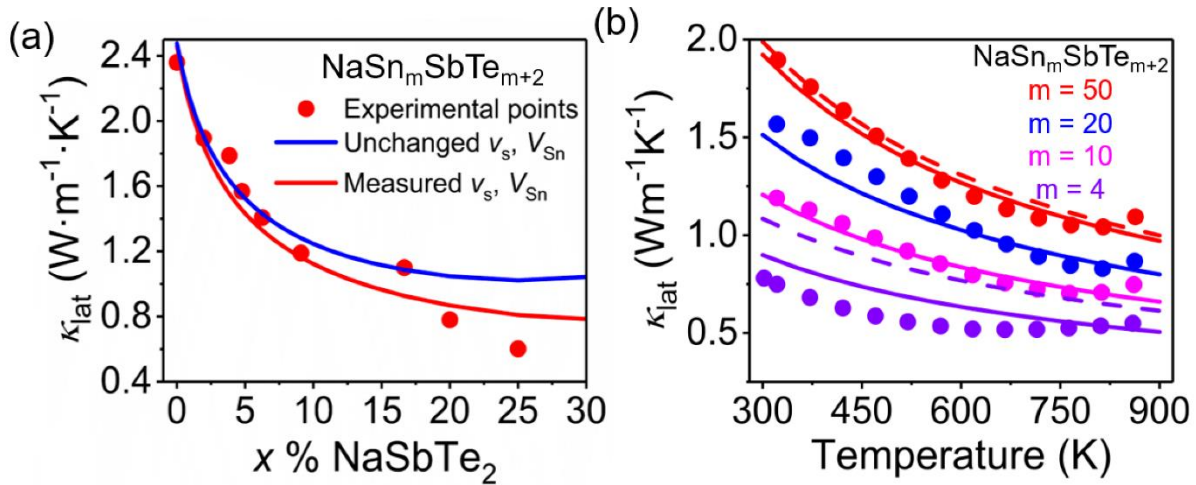


Figure 5.14 (a) Comparison of the experimental and theoretical lattice thermal conductivities of SnTe–NaSbTe₂ measured at 323 K. The solid lines are the thermal conductivities predicted by the Debye-Callaway model using the sound velocity and Sn vacancies concentration found in pure SnTe (blue) and the measured values (red). (b) Lattice thermal conductivities of SnTe–NaSbTe₂ over the full temperature range of the study. The points are the measured values and the lines are calculated from our model. The dashed lines exclude the softening and phonon–vacancy scattering and the solid lines include each.

measured Sn vacancy concentrations (estimated from the Hall data as $2V_{\text{Sn}} = n_{\text{H}}$) and sound velocities of our SnTe–NaSbTe₂ compounds. Including the experimental values of V_{Sn} and v_s in the calculation provides a much better prediction of the experimental κ_{lat} over nearly the full composition range. The same analysis for NaSn_mBiTe_{m+2} is provided in Figure 5.15, and discussed below, we find the reduction of the lattice thermal conductivity upon NaBiTe₂ incorporation is well described without changing v_s or V_{Sn} . Lastly, figure 5.14b shows the experimental temperature-dependent lattice thermal conductivities paired with the values calculated from our

model. While the model somewhat overestimates the κ_{lat} of the most heavily alloyed samples, the calculations clearly provide a sound prediction of the temperature dependence of the lattice thermal conductivities for $\text{NaSn}_m\text{SbTe}_{m+2}$. The dashed lines in Figure 5.12b are theoretical curves calculated without the vacancy–phonon scattering and lattice softening. The projected values severely overestimate the experimental values of κ_{lat} at high NaSbTe_2 fraction. Figures 5.12a and 5.12b directly demonstrate the importance of the cation vacancies in facilitating low lattice thermal conductivity in SnTe–NaSbTe_2 alloys.

5.2.5 Analysis of the sound velocities of $\text{NaSn}_m\text{BiTe}_{m+2}$ (SnTe–NaBiTe_2)

In addition to the data discussed above for the SnTe–NaSbTe_2 alloys, we also measured sound velocities for the bismuth analogues (SnTe–NaBiTe_2). The data is shown in Figure 5.15a. While the sound velocities are effectively unchanged for low NaBiTe_2 fraction, the samples begin to soften rapidly above $\sim 10\%$ NaBiTe_2 . Unlike with NaSbTe_2 alloying, some degree of softening is expected after addition of NaBiTe_2 to SnTe , owing to the considerably higher mass of bismuth (~ 209 g/mol) compared Sb (~ 122 g/mol) and Sn (~ 119 g/mol), as it is well known that greater mass generally leads to lower phonon velocities. Furthermore, Table 5.1 shows that the measured densities for SnTe–NaBiTe_2 samples increasingly deviates from the theoretical values as the NaBiTe_2 fraction is raised. Reliable pulse–echo measurements of v_s require samples $\geq \sim 95\%$ dense. While our SnTe–NaSbTe_2 materials are all sufficiently dense, the heavily alloyed ($m = 10$ and 5) Bi analogues are not, indicating the degree of softening shown in Figure 5.15a may be overestimated in SnTe–NaBiTe_2 . Figure 5.15b supports this conclusion, showing that the lattice thermal conductivities of SnTe–NaBiTe_2 are well described without considering any changes to

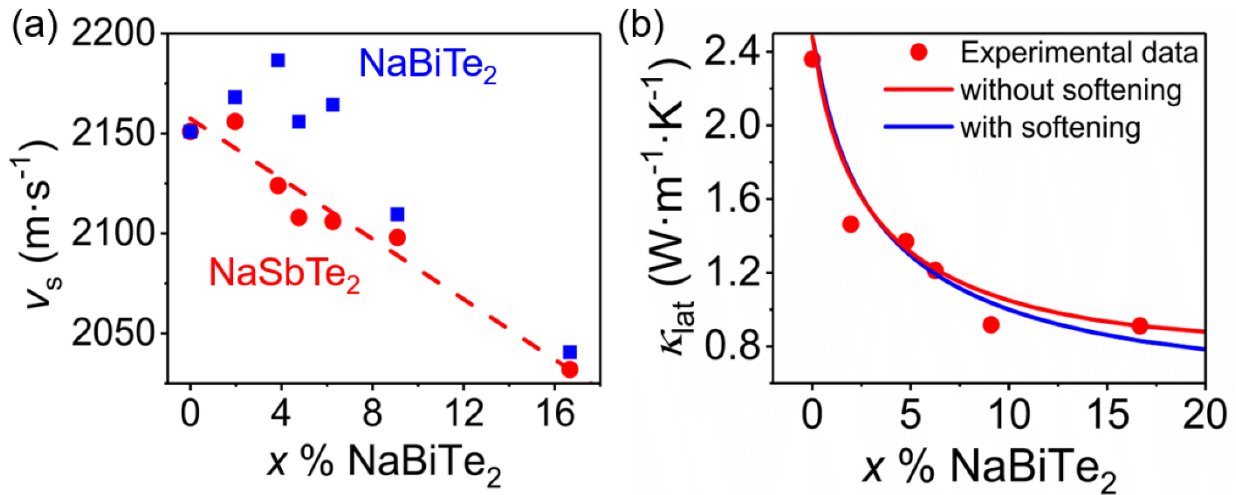


Figure 5.15 (a) Measured sound velocities for SnTe alloys with NaBiTe_2 and NaSbTe_2 . While the SnTe– NaSbTe_2 soften monotonically and approximately linearly with NaSbTe_2 fraction, the SnTe– NaBiTe_2 samples show little dependence on the alloy fraction under $\sim 10\%$ NaBiTe_2 and then soften at higher concentrations. (b) Room temperature lattice thermal conductivities for SnTe– NaBiTe_2 and model calculations with and without the reduced v_s shown in (a). Both curves provide reasonably satisfactory fits to the experimental data.

the sound velocity, unlike in the SnTe– NaSbTe_2 family where the reduced v_s and phonon–vacancy scattering are essential to properly model κ_{lat} .

5.2.6 Potential mechanism of vacancy formation in $\text{NaSn}_m\text{SbTe}_{m+2}$

As discussed above, the enhanced vacancy concentration in SnTe– NaSbTe_2 ($\text{NaSn}_m\text{SbTe}_{m+2}$) helps suppress bipolar diffusion while also reducing the sound velocity and enhancing phonon scattering. Likewise, SnTe– AgSbTe_2 ($\text{AgSn}_m\text{SbTe}_{m+2}$) are reported to show very similar behavior. It is surprising that the bismuth containing analogues, SnTe– NaBiTe_2 and

SnTe–AgBiTe₂ (NaSn_mBiTe_{m+2} and AgSn_mBiTe_{m+2}) to not show significant changes to the Sn vacancy concentration upon alloying.¹⁸⁷ Due to the critical role played by the cation vacancies in SnTe–NaSbTe₂ and SnTe–AgSbTe₂, it is worth speculating on possible reasons why the Sb-containing systems show enhanced vacancy concentration while the Bi-based materials do not. We believe this can be understood using a simple chemical argument by considering the bonding or antibonding character of the band edges in SnTe and the subsequent effect of each NaPnTe₂ compound on the band extrema.

Figure 5.15a shows a very simple molecular orbital (MO) schematic for a SnTe₆ octahedron that captures the key features of the bonding situation in pure SnTe. While most insulators and semiconductors have bonding-valence and antibonding-conduction bands respectively dominated by anion and cation p-states,¹⁹² the occupied 5s orbitals in Sn²⁺ give a valence band edge that is generated by an antibonding interaction between tin-5s and tellurium-5p orbitals. Figure 5.16c shows the DFT calculated partial density of states (pDOS) for SnTe and shows the largest contributions to the DOS at the VB edge are from tin-5s and tellurium-5p interaction. Likewise, Figure 5.16d shows a DFT calculated crystal orbital Hamilton population (COHP) plot for SnTe. COHP plots show the bonding and antibonding contributions to the total density of states at each energy, where positive values indicate bonding interactions and negative values indicate antibonding character. Our COHP calculation clearly demonstrates that both valence and conduction band edges are predominantly antibonding in character. The DFT calculations thus show the simple MO approach qualitatively captures the bonding at the electronic band edges in SnTe.

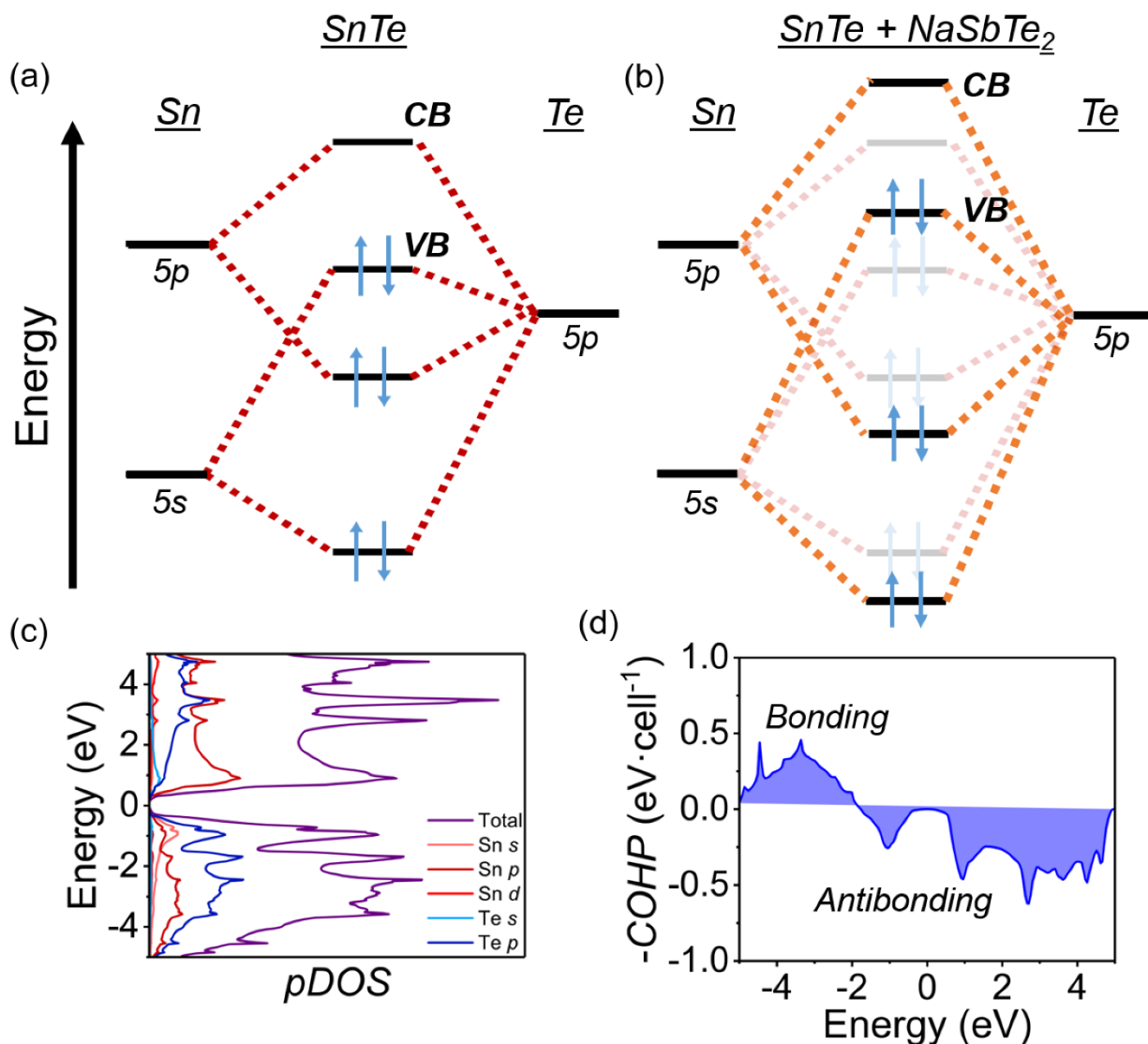


Figure 5.16 (a) Simplified molecular orbital (MO) diagram for a SnTe₆ octahedron. (b) The same MO diagram considering the lattice contraction induced by NaSbTe₂. The contraction increases orbital overlap and destabilizes the VB edge. The diagram in (b) overlays the original (for pure SnTe) in faded color to emphasize the change after NaSbTe₂ addition. (c) DFT calculated partial density of states for pure SnTe. (d) DFT calculated COHP plot for pure SnTe.

Here, we propose the antibonding nature of the valence band in SnTe explains the tendency to form additional Sn vacancies upon alloying with NaSbTe₂ (or AgSbTe₂). As shown in Figure 5.1b, because Na⁺ and Sb³⁺ are smaller cations than Sn²⁺, introduction of NaSbTe₂ to SnTe contracts the lattice and exerts chemical pressure. The shrinking lattice should increase the orbital overlap and therefore amplify bonding and antibonding interactions, thus increasing the energy of the valence band edge. We illustrate this effect in Figure 5.16d, emphasizing the changes in the electronic states resulting from the Sn-5s and Te-5p interaction. Figures 5.17 show the DFT calculated pDOS after alloying, for NaSn_mSbTe_{m+2} and NaSn_mBiTe_{m+2}. Likewise Figure 5.18 shows the COHP plots for the same compositions. These DFT confirm that the VB edge remains antibonding in character and arises from Sn-5s and Te-5p interactions after NaSbTe₂ and NaBiTe₂ alloying, again justifying our use of the MO framework. This simplified picture therefore predicts that lattice contraction will destabilize the electrons in at valence band edge.

According to simple charge balance considerations, each Sn vacancy removes two electrons from the valence band (i.e. creates two holes). Therefore, because the valence band is antibonding in character, raising its energy destabilizes electrons at the band edge and creates a driving force to form Sn vacancies to reduce its electronic occupation. This simple argument also explains why alloying NaBiTe₂ into SnTe does not appreciably change the charge carrier concentration. As shown in Figure 5.1d, NaBiTe₂ expands the SnTe lattice. Expansion would have the opposite effect of NaSbTe₂, weakening bonding and antibonding interactions and therefore should provide no additional driving force to form Sn vacancies. To illustrate the power of this simple analysis, we plot the measured charge carrier concentrations against the lattice constants of our SnTe–NaSbTe₂ and SnTe–NaBiTe₂ alloys with the previously reported SnTe–

AgSbTe₂ compounds in Figure 5.19.¹⁷⁶ We find the hole concentrations generally increase with rising lattice constant, in agreement with the qualitative bonding picture sketched above. This argument could be further supported by investigating the impact of other 2+ cations with different ionic radii on the charge carrier concentration of SnTe.

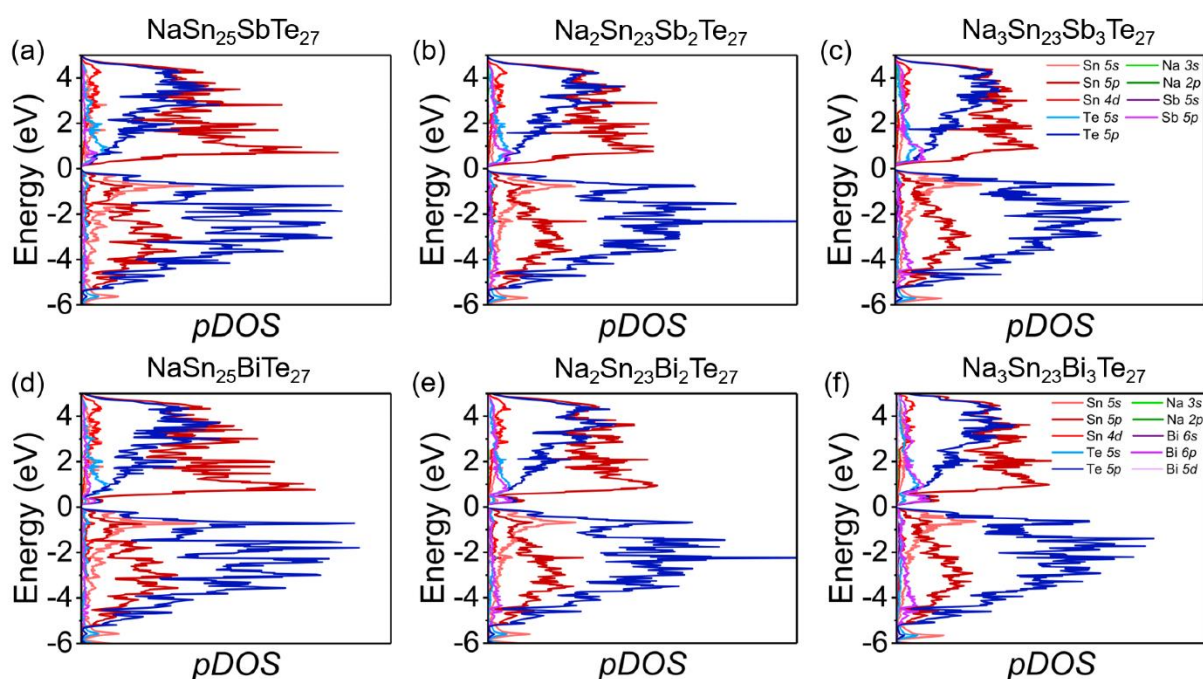


Figure 5.17 Partial density of states (pDOS) for (a–c) NaSn_mSbTe_{m+2} (SnTe–NaSbTe₂) and (d–f) NaSn_mBiTe_{m+2} (SnTe–NaBiTe₂) materials. The compositions reflect the supercells used for the DFT calculations. The calculations show the valence band edge primarily originates from interactions between Sn–5s and Te–5p orbitals, agreeing with the MO framework.

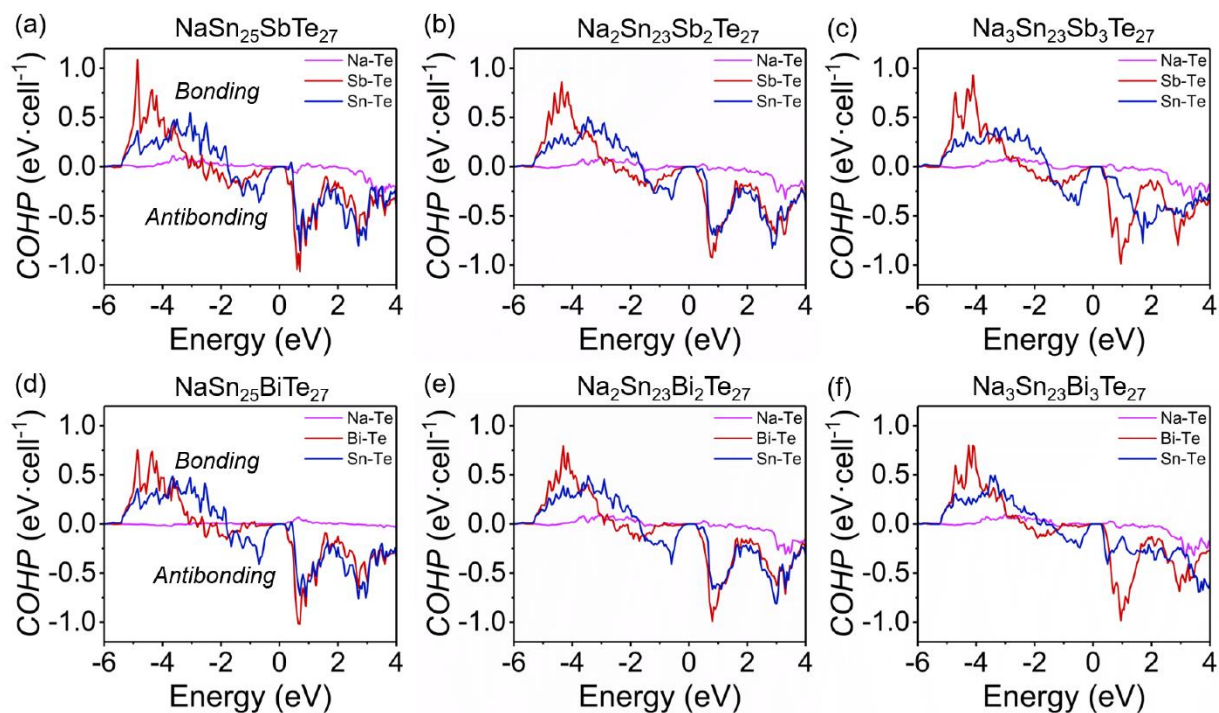


Figure 5.18 Crystal orbital Hamilton population plots for (a–c) $\text{NaSn}_m\text{SbTe}_{m+2}$ (SnTe – NaSbTe_2) and (d–f) $\text{NaSn}_m\text{SbTe}_{m+2}$ (SnTe – NaBiTe_2) materials showing bonding/antibonding interactions for the Na–Te, Sb–Te, and Sn–Te interactions. The compositions reflect the supercells used for the DFT calculations. The calculations show the valence band edge remains antibonding in character after alloying with NaSbTe_2 or NaBiTe_2 .

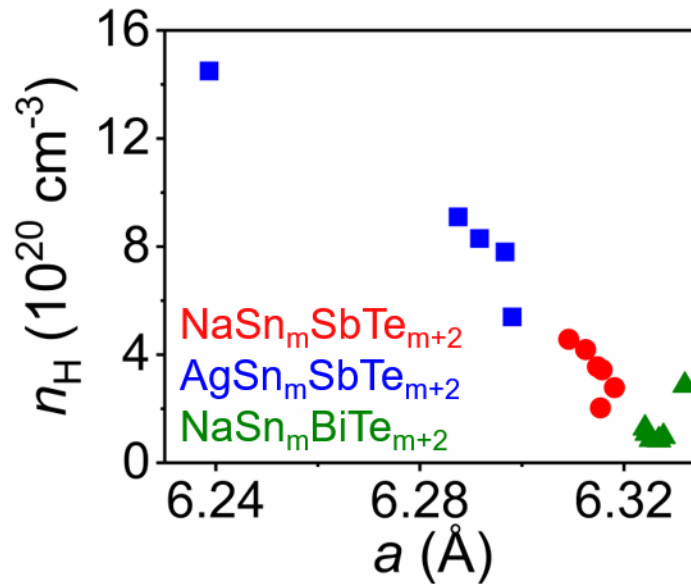


Figure 5.19 The room temperature Hall hole densities plotted against the lattice constants for our $\text{NaSn}_m\text{SbTe}_{m+2}$ and $\text{NaSn}_m\text{BiTe}_{m+2}$ samples as well as for the $\text{AgSn}_m\text{SbTe}_{m+2}$ previously reported by Tan et al.¹⁷⁶ The graph shows a nearly linear dependence of n_H on a .

5.3 Summary and Conclusions

We report the new alloys of SnTe with NaSbTe₂ and NaBiTe₂ ($\text{NaSn}_m\text{PnTe}_{m+2}$; Pn = Sb, Bi respectively) and find that while superficially similar, the two material families have unique thermoelectric properties. In particular, the Sb-containing $\text{NaSn}_m\text{SbTe}_{m+2}$ have superior Seebeck coefficients and lower lattice thermal conductivities, which result in high ZT s ~ 1.2 at 800-900 K and competitive $ZT_{\text{avg}} \sim 0.7$ over 300–873 K, indicating that $\text{NaSn}_m\text{SbTe}_{m+2}$ are promising candidates for intermediate temperature thermoelectric applications. Our DFT calculations and Hall effect measurements suggest the addition of either NaSbTe₂ or NaBiTe₂ into SnTe promotes convergence of the L - and Σ -bands and facilitates high Seebeck coefficients. However, the DFT calculations also indicate that both ternary compounds narrow the band gap of SnTe, making each

family increasingly prone to detrimental bipolar diffusion. We find that bipolar charge transport is partially suppressed in $\text{NaSn}_m\text{SbTe}_{m+2}$, owing to enhanced Sn vacancy and charge carrier concentrations. On the contrary, NaBiTe_2 does not significantly alter the vacancy concentration, and the Seebeck coefficients and thermal conductivities of the Bi containing samples are severely limited by bipolar diffusion. Lastly, we find that alloying NaSbTe_2 into SnTe markedly reduces the sound velocity and Debye temperature, indicating a softer lattice with lower phonon velocities. Facilitated by lattice softening and enhanced phonon-vacancy scattering, the $\text{NaSn}_m\text{SbTe}_{m+2}$ materials reach glasslike thermal conductivity unobtainable in $\text{NaSn}_m\text{BiTe}_{m+2}$. Therefore, the cation vacancies induced by NaSbTe_2 favorably modulate both the electronic and thermal properties of SnTe to yield high thermoelectric performance. The contrast between the seemingly similar $\text{NaSn}_m\text{SbTe}_{m+2}$ and $\text{NaSn}_m\text{BiTe}_{m+2}$ highlights the important role played by the native defects in engineering high performance thermoelectric materials.

5.4 Experimental details

5.4.1 Synthesis and SPS processing

The starting materials were Sn shot (99.99%, American Elements, USA), Te pieces (99.99%, American Elements, USA), Sb pieces (99.999%, American Elements, USA), Bi pieces (99.99%, American Elements, USA), and Na cubes (99.95%, Sigma Aldrich, USA). All sodium was handled in a N_2 filled glovebox, and the surface oxidation was scrapped off the sodium pieces before weighing.

Polycrystalline ingots of nominal compositions $\text{NaSn}_m\text{SbTe}_{m+2}$ and $\text{NaSn}_m\text{BiTe}_{m+2}$, were first synthesized by weighing stoichiometric quantities of each element into 13 mm diameter fused

silica tubes. All tubes were carbon coated 3 times prior to usage to limit glass attach from the Na. The tubes were flame sealed at $\sim 3 \times 10^{-3}$ torr and heated in a box furnace to 1273 K over 12 hours, where they were held at temperature for 5 hours. After dwelling, the tubes were cooled to room temperature in the furnace over another 12 hours. The ingots were next removed and hand ground in an agate mortar and pestle to fine powders. To ensure a relatively uniform particulate size, we passed the powdered samples through a 53 μm mesh sieve. The samples were then loaded into 12.7 mm diameter graphite dies and consolidated into dense pellets by spark plasma sintering (SPS) using a SPS-211LX, Fuji Electronic Industrial Co. Ltd. Instrument. During SPS processing, samples were held under dynamic vacuum at 773 K for 10 minutes and under 40 MPa of uniaxial pressure before being cooled to room temperature. Resulting pellets had greater than 96 % the theoretical density, as outlined in the experimental section in Table 5.1. After sintering, the pellets were cut and polished into $\sim 3 \times 3 \times 10 \text{ mm}^3$ bars for electrical measurements and $\sim 6 \times 6 \times 2 \text{ mm}^3$ square prisms for thermal and Hall effect measurements. Cuts were made such that the measurements were made perpendicular to the pressing direction.

5.4.2 Electrical conductivity and Seebeck coefficient

Using the $\sim 3 \times 3 \times 10 \text{ mm}^3$ bars, the electrical conductivities and Seebeck coefficients were measured simultaneously on an Ulvac ZEM-3 instrument. The measurements were conducted in 50 K intervals between 300–873 K under partial He backpressure. Prior to each measurement, to limit sample outgassing at elevated temperatures, the samples were spray coated with boron nitride except where needed for contact with electrodes. Full heating and cooling profiles were measured for each sample, and data found in this work comes from the cooling cycle.

5.4.3 Hall effect

Hall effect measurements were conducted using two different homebuilt systems. One setup used an AC 4-probe method with excitation fields of ± 0.5 Tesla. The system used an air-bore, helium-cooled superconducting magnet to generate the field within a high temperature oven that surrounds the Ar-filled sample probe. For these measurements, samples were cut and polished into thin bars of approximate dimensions $2 \times 1 \times 8$ mm³. The second setup utilizes Van der Pauw geometry with magnetic fields of ~ 2 T. The carrier densities were calculated from the Hall coefficient assuming a single carrier band, i.e., $n_H = 1/eR_H$, where R_H is the Hall coefficient.

5.3.4 Thermal Conductivity

Using the $6 \times 6 \times 2$ mm³ squares, the thermal diffusivity (D) of each sample was measured over 300–873 K on a Netzsch LFA-457 instrument. The experimental data is found in Figures 5.20 and 5.21. To limit errors from emissivity, the samples were spray coated with a thin layer of graphite prior to measurement. The total thermal conductivities were obtained from the relation $\kappa_{tot} = DC_p d$, in which C_p is the constant pressure heat capacity and d is the density. The densities were calculated using the sample masses and geometries, and C_p was estimated from the relationship C_p/k_b (*per atom*) = $3.07 + 4.7 \times 10^{-4}(T - 300)$,¹⁰⁶ which has an estimated uncertainty of $\sim 2\%$ over the measured temperatures. Heating and cooling cycles of 50 K increments were also measured here, and to ensure consistency with the electrical properties, the thermal data reported in this work was also taken from the cooling cycle. As outlined in the experimental section, the lattice thermal conductivities were estimated with the Wiedemann–Franz law using the measured Seebeck coefficients and a single band model to determine the Lorenz

number. The estimated values of L , C_p , and κ_{elec} are presented in Figures 5.20 and 5.21, and the measured densities in Table 5.1.

Table 5.1 Measured densities and fraction of the theoretical density (obtained by refinement of the powder XRD patterns) of $\text{NaSn}_m\text{SbTe}_{m+2}$ and $\text{NaSn}_m\text{BiTe}_{m+2}$. The densities were measured from the masses and volumes of the $\sim 6 \times 6 \times 2 \text{ mm}^2$ squares used for the LFA measurements.

Compound	Density ($\text{g}\cdot\text{cm}^{-3}$)	% of theoretical
$\text{NaSn}_{50}\text{SbTe}_{52}$	6.198	96
$\text{NaSn}_{25}\text{SbTe}_{27}$	6.234	97
$\text{NaSn}_{20}\text{SbTe}_{22}$	6.187	97
$\text{NaSn}_{15}\text{SbTe}_{17}$	6.161	97
$\text{NaSn}_{10}\text{SbTe}_{12}$	6.091	97
$\text{NaSn}_5\text{SbTe}_7$	5.996	97
$\text{NaSn}_4\text{SbTe}_6$	5.876	96
$\text{NaSn}_3\text{SbTe}_5$	5.642	94
$\text{NaSn}_{50}\text{BiTe}_{52}$	6.291	97
$\text{NaSn}_{25}\text{BiTe}_{27}$	6.112	95
$\text{NaSn}_{20}\text{BiTe}_{22}$	6.009	93
$\text{NaSn}_{15}\text{BiTe}_{17}$	6.09	94
$\text{NaSn}_{10}\text{BiTe}_{12}$	5.989	93
$\text{NaSn}_5\text{BiTe}_7$	6.141	92

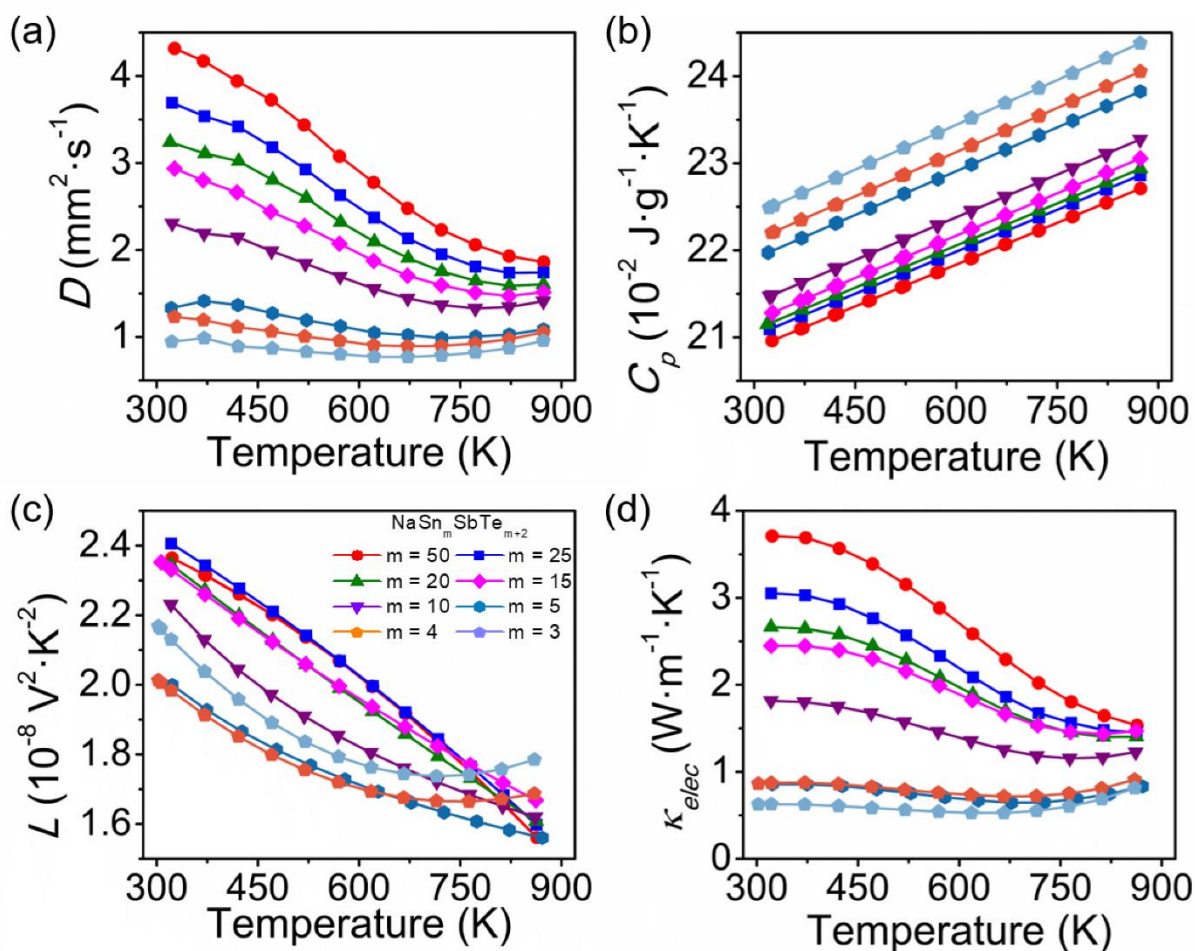


Figure 5.20 (a) Measured thermal diffusivities, (b) estimated heat capacities used to calculate κ_{tot} , (c) estimated temperature-dependent Lorenz numbers, and (d) estimated electronic contribution to the thermal conductivities for $\text{NaSn}_m\text{SbTe}_{m+2}$ ($m = 50-3$), equivalently $\sim 2-25$ percent NaSbTe_2 .

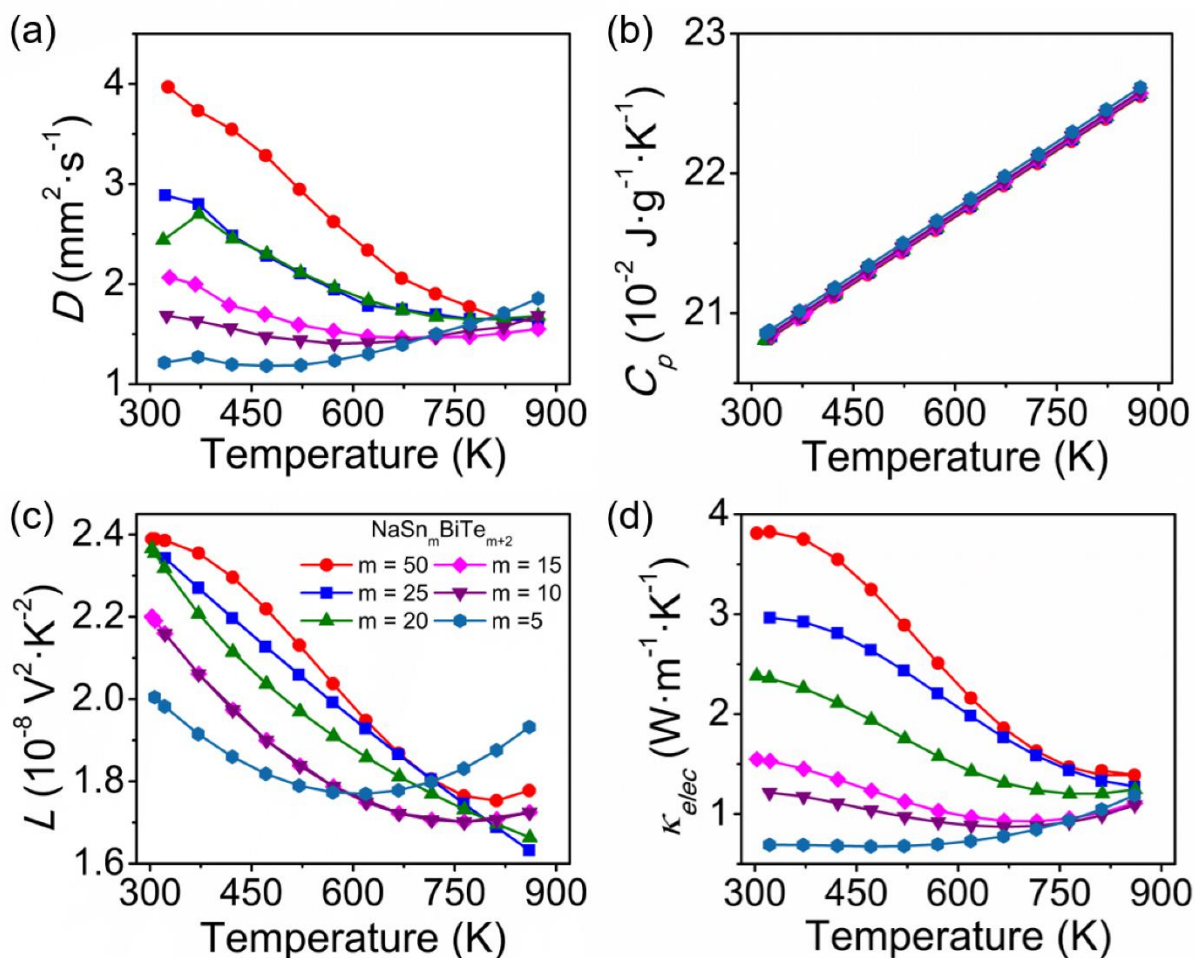


Figure 5.21 (a) Measured thermal diffusivities, (b) estimated heat capacities used to calculate κ_{tot} , (c) estimated temperature-dependent Lorenz numbers, and (d) estimated electronic contribution to the thermal conductivities for $\text{NaSn}_m\text{BiTe}_{m+2}$ ($m = 50-5$), equivalently 2–16 percent NaBiTe_2 .

5.4.5 Model for theoretical lattice thermal conductivity

To assess the impact of the vacancies and lattice softening on the thermal conductivities of $\text{NaSn}_m\text{SbTe}_{m+2}$ and $\text{NaSn}_m\text{BiTe}_{m+2}$, we calculated theoretical values of κ_{lat} based on a simplified Debye–Callway type model.¹⁷⁶ Here, we considered phonon-phonon, phonon-vacancy, and point

defect phonon scattering processes, and compared calculations carried out with an unchanged concentration of Sn vacancies and speed of sound with a second calculation that used the experimental values that are sample dependent. The lattice thermal conductivity is given by:

$$\kappa_{lat} = \frac{1}{2\pi^2} \int_0^{k_{max}} C_{v,ph}(k, T) \tau_c(k, T) v_g^2 k^2 dk \quad (5.1)$$

where, k_{max} is the maximum phonon wavevector given by $(6\pi^2/V_{atom})^{1/3}$ and V_{atom} is the volume per atom. $C_{v,ph}$ is the phonon specific heat, equal to $C_{v,ph} = k_B \frac{x^2 e^x}{(e^x - 1)^2}$ and $x = \hbar\omega/k_B T$ where ω is the phonon frequency. τ_c is the combined phonon relaxation time, and v_g is the phonon group velocity (equal to the average speed of sound in our polycrystalline samples). The combined relaxation time was found by summing the contributions from each phonon scattering process considered in our model.

$$\tau_c^{-1} = \tau_{ph}^{-1} + \tau_{vac}^{-1} + \tau_{PD}^{-1} \quad (5.2)$$

These correspond to the relaxation times for intrinsic phonon-phonon (Umklapp and normal) scattering, phonon-vacancy scattering, and point defect phonon scattering respectively. More mechanisms may in principle contribute to phonon scattering; however, we found that our simplified model matches the experimental data reasonably well to show the importance of the lattice softening in our materials. The group velocity is given by $v_g = d\omega/dk$. Our model used Born-von Karmon boundary conditions to give phonon frequencies of $\omega = \omega_0 \sin \frac{\pi k}{2k_{max}}$ where $\omega_0 = \frac{2}{\pi} v_s k_{max}$.

The relaxation times for each phonon scattering process are given by the following equations:

$$\tau_{ph}^{-1} = A \frac{k^2 T}{v_g} \quad (5.3)$$

$$\tau_{vac}^{-1} = f \frac{3V\omega^2 k^2}{\pi v_g} s^2 \quad (5.4)$$

$$\tau_{PD}^{-1} = \frac{3V\omega^2 k^2}{\pi v_g} \Gamma \quad (5.5)$$

where A is a fitting constant, s is the phonon-vacancy scattering strength,¹⁹¹ f is the fraction of Sn vacancies and is equal to $2V_{Sn}V_{atom}$ and V_{Sn} is the concentration of Sn vacancies determined by the Hall effect measurements. Lastly, Γ is the disorder scaling parameter that characterizes the phonon scattering from mass and strain field fluctuations between the host lattice and alloying atoms as $\Gamma = \Gamma_M + \Gamma_S$.

$$\Gamma_M = \frac{\sum_{i=1}^n c_i \left(\frac{\langle M_i \rangle}{M^*}\right)^2 f_i^1 f_i^2 \left(\frac{M_i^1 - M_i^2}{\langle M_i \rangle}\right)^2}{\sum_{i=1}^n c_i} \quad (5.6)$$

$$\Gamma_S = \frac{\sum_{i=1}^n c_i \left(\frac{\langle M_i \rangle}{M^*}\right)^2 f_i^1 f_i^2 \varepsilon \left(\frac{r_i^1 - r_i^2}{\langle r_i \rangle}\right)^2}{\sum_{i=1}^n c_i} \quad (5.7)$$

where c_i is the degeneracy (in SnTe $c_i = 2$), f_i^k is the fractional occupation of atom k (Sn, Sb, Na), $\langle M_i \rangle$ and $\langle r_i \rangle$ are the average mass and radius of the i th sublattice ($\langle M_i \rangle = \sum_k f_i^k M_i^k$ and $\langle r_i \rangle = \sum_k f_i^k r_i^k$), and M^* is the average atomic mass of the compound ($M^* = \frac{1}{2} \sum_i \langle M_i \rangle$). ε is a phenomenological parameter related to the lattice anharmonicity that is fit to the experimental data.

To determine the impact of the lattice softening on the thermal conductivities, we calculated two theoretical curves with our Debye-Callaway model. The first used a constant concentration of Sn vacancies of $1.3 \times 10^{20} \text{ cm}^{-3}$ and speed of sound of $2151 \text{ m} \cdot \text{s}^{-1}$ (that of pure SnTe)¹⁷⁶ over the full SnTe–NaSbTe₂ compositional range. For the second, we attempt to account for the enhanced vacancy density and lattice softening as a function of the NaSbTe₂ content. To do so, we used

linear fits to the experimental sound velocities and vacancy concentrations to estimate v_g and V_{Sn} at each composition. In the case of our SnTe–NaBiTe₂ alloys, our calculations considered the same sources of phonon scattering and used a constant sound velocity of 2151 m·s⁻¹ and vacancy concentration of 1.3x10²⁰ cm⁻³ (the values found in pure SnTe). We found the reduction of thermal conductivity in NaSn_mBiTe_{m+2} can be reasonably well accounted for without changing the sound velocity or Sn vacancy concentration. The raw data and fits are shown in Figure 5.15, and the fit parameters are listed in Table 5.2.

Table 5.2 Constants and fitted parameters used in our model lattice thermal conductivity calculations for NaSn_mSbTe_{m+2} and NaSn_mBiTe_{m+2}.

Parameters	NaSn _m SbTe _{m+2}	NaSn _m BiTe _{m+2}
v_s	753x + 2157 m·s ⁻¹	2151 m·s ⁻¹
V_{Sn}	6.21x + 1.36 cm ⁻³	1.3x10 ²⁰ cm ⁻³
A	2.3x10 ⁻⁸	2.3x10 ⁻⁸
s	0.89	0.89
M_{Sn}	118.71 g·mol ⁻¹	118.71 g·mol ⁻¹
M_{Te}	78.96 g·mol ⁻¹	78.96 g·mol ⁻¹
M_{Na}	22.989 g·mol ⁻¹	22.989 g·mol ⁻¹
M_{Sb}	121.76 g·mol ⁻¹	-
M_{Bi}	-	208.98 g·mol ⁻¹
r_{Sn}	158 pm	158 pm
r_{Te}	135 pm	135 pm
r_{Na}	186 pm	186 pm
r_{Sb}	136 pm	-
r_{Bi}	-	143 pm
ε (fit)	5	5

5.4.6 Powder X-ray diffraction

Powder X-ray diffraction (PXRD) patterns were measured with a Rigaku Miniflex 600 instrument using Cu K α radiation with wavelength $\lambda = 1.5406 \text{ \AA}$ and operating at 40 kV and 15

mA and with a $K\beta$ filter. Using the obtained diffraction patterns, we refined the lattice parameters using the Rietveld method in GSAS-II software.

5.4.7 Sound velocity

The sound velocities of the SnTe–NaSbTe₂ samples were measured using a pulse-echo technique. Typical samples were polished squares similar to the geometry used for the LFA. The samples were coupled to a piezoelectric transducer with a small amount of honey. The transducer sends an initial stress-wave pulse into the sample, and then acts as a detector by receiving and measuring the echoed ultrasound reflections. The time delay t_d between reflections was determined by maximizing the cross-correlation of the two reflections,¹⁷⁶ and the sound velocity calculated as $v = 2d/t_d$ where d is the sample thickness. We measured both longitudinal and transverse components of the sound velocity using 5 MHz longitudinal and transverse transducers (Olympus V1091 and Olympus V157-RM respectively). The crystallographic average sound velocity was then calculated as follows:

$$v_{avg} = \left[\frac{1}{3} \left(\frac{1}{v_L^3} + \frac{2}{v_T^3} \right) \right]^{-1/3} \quad (5.8)$$

where v_L and v_T are the measured longitudinal and transverse velocities respectively.

5.4.8 Measurement of heat capacity and Debye temperature

The heat capacities C_p of selected samples of NaSn_mSbTe_{m+2} ($m = 50, 15, 5$) were measured on a Dynacool Physical Property Measurement System (PPMS, Quantum Design) between 1.8 and 300 K. Apiezon N grease was used to fix polycrystalline samples prepared by SPS to the sample stage. The variable temperature heat capacities are presented in Figure 5.12a-c. The Debye

temperatures of each sample were estimated from the heat capacity data as follows. At low temperatures, the heat capacity is expressed by the equation:¹⁹³

$$C_p = \alpha T + \beta T^3 \quad (5.9)$$

where α parameterizes the electronic contribution to the specific heat, and β determines the lattice contribution. Plotting C_p/T vs. T^2 gives a straight line with a slope of β , from which the Debye temperature is calculated using the following relationship:¹⁹⁴

$$\theta_D = \left(\frac{12\pi^4 NR}{5\beta} \right)^{1/3} \quad (5.10)$$

The experimental plots of C_p/T vs. T^2 and extracted values of β and θ_D for our $\text{NaSn}_m\text{SbTe}_{m+2}$ samples are displayed along with the C_p data in Figures 5.12e-f.

5.4.9 Electron microscopy

In order to identify the microscale and nanoscale structures of $\text{NaSn}_5\text{SbTe}_7$ and $\text{NaSn}_5\text{BiTe}_7$, we performed both Scanning Electron Microscopy (SEM) and Transmission Electron Microscopy (TEM). We first analyzed the samples with SEM imaging, Energy Dispersive Spectroscopy (EDS), and Electron Backscattered Diffraction (EBSD). Of these techniques, EBSD is the most sensitive to surface quality and therefore samples were prepared to minimize surface deformation and scratching. Samples were ground using SiC paper of grit size 600, 800, and 1200 for 10 min each on a rotating grinding wheel. Ethanol was used as a water free lubricant. Next, samples were polished using 1 μm and 0.1 μm glycol-based diamond polishing slurry for 30 min and 45 min respectively. Finally, samples were placed into a vibratory polisher and polished for 3 hours in 0.1 μm glycol-based diamond slurry with conditions of 150 V and 62.7 Hz. All SEM techniques were then performed at 30 kV using a FEI Quanta 650 ESEM.

After performing SEM, the polished samples were cut into smaller pieces using a wire saw. A TEM grid was then attached to the polished surface of one of the smaller pieces using M-bond. Once the TEM grid had been attached, the sample was turned over and polished down to 50 μm thick using 600, and 800 grit SiC paper. We then performed dimpling to reduce the thickness of the sample at the center of the grid area, followed by ion milling in a Fischione 1050 TEM Mill. To thin the sample, the ion mill was set to a voltage of 4 kV and top and bottom guns were placed at an angle of 6° and -6° respectively ($\pm 6^\circ$). Milling at these conditions was performed until a hole was formed. The angle was then reduced, and milling was performed at 2 kV and $\pm 4^\circ$ until the hole visibly changed shape. For the final cleaning steps, the angles remained at $\pm 4^\circ$ and voltage was reduced to 1 kV for 1 hour and 0.3 kV for 30 minutes. High Resolution TEM was then performed at 200 kV using a JEOL JEM-2100F TEM.

5.4.10 Electronic structure calculations

We performed first-principles calculations based on density functional theory (DFT) using the Vienna Ab-initio Simulation Package (VASP)^{113, 195} employing the projector-augmented wave (PAW)^{150, 196} method with the Perdew-Burke-Ernzerhof (PBE) generalized gradient approximation (GGA)¹⁵¹ to the exchange-correlation functional. We used a kinetic energy cut-off of 350 eV to truncate the expansion of the electronic wave functions in a plane wave basis. We used 3x3x3 supercells (27 Sn and 27 Te atoms) of the primitive unit cell of SnTe to model the substitutions of the parent compound with NaSbTe₂ and NaBiTe₂. We generated multiple supercell configurations with different concentrations of NaSbTe₂ and NaBiTe₂, namely Na₁Sb₁Sn₂₅Te₂₇ (Na₁Bi₁Sn₂₅Te₂₇), Na₂Sb₂Sn₂₃Te₂₇ (Na₂Bi₂Sn₂₃Te₂₇), and Na₃Sb₃Sn₂₁Te₂₇

($\text{Na}_3\text{Bi}_3\text{Sn}_{21}\text{Te}_{27}$) in which the mole concentrations of the guest atoms (Na, Sb, Bi) correspond to 3.7%, 7.4% and 11.1%, respectively. To select the energetically most favorable supercell configuration at each concentration, we used the Supercell program¹⁹⁷ to generate only symmetrically inequivalent structures for which we calculated the electro-static energies. We picked the ten lowest energy (electrostatic) structures at each concentration of Na-Sb(Bi) among several hundreds of thousands of possibilities and performed static DFT calculations. The DFT calculated lowest energy structure at each concentration was then taken and atomic positions were fully relaxed before performing the electronic band structure calculations. The spin-orbit coupling (SOC) was taken into account while doing relaxation and band calculations for all structures. We used a uniform k-point mesh of 4x4x4 for the calculations involving the 3x3x3 supercells.

Chapter Six**Electron count mediated lattice softening in semiconductors**

6.1 Introduction

Lattice vibrations, or phonons, give rise to many of the most important physical properties of solids, and understanding and controlling the microscopic processes that impact phonon transport is essential both at a fundamental level and for numerous technologies. A common experimental means of assessing the acoustic phonon modes is measuring the sound velocity, v_s , which is approximately equal to the acoustic phonon group velocity at low wavevector. The sound velocity is linearly related to the Debye temperature,¹⁹⁸ and thus gives a measure of the relative “stiffness” of a material. Because reliable measurements of v_s are straightforward, the speed of sound serves as a useful metric in many phenomenological models for expressing thermodynamic and transport properties. For example, the sound velocity is central to the Debye-Callaway model of lattice thermal conductivity κ_{lat} ,^{18, 199-200} which shows that above the Debye temperature, κ_{lat} scales with the cube of v_s .¹⁷ Likewise, the temperature dependence the electrical conductivity of metals and doped semiconductors is determined by phonon scattering and described by deformation potential theory.²⁰¹⁻²⁰² In the deformation potential model, the electron–phonon scattering rate is inversely proportional to v_s .²⁰²⁻²⁰³ At a macroscopic level, the elastic properties of materials are fundamentally determined by the phonon dispersion and related to the speed of sound by

$$v_s = \sqrt{C/d} \quad (1)$$

Where C is an elastic constant and d is the density.

Because the sound velocity is intimately coupled to the electronic, thermal, and mechanical properties of solids, v_s should ideally be properly chosen and/or engineered to match the needs of a specific application. For example, high performance thermoelectric materials require minimal

thermal conductivity, and many of the premier materials such as PbTe and Bi₂Te₃ are composed of large, heavy atoms to give high density and low v_s . Similarly, increasing the internal strain was recently shown to suppress the speed of sound and provide a new means of achieving low lattice thermal conductivity and enhanced thermoelectric performance.¹⁷ Furthermore, the sound velocity has emerged as an important parameter for the design of battery materials, where low average vibrational frequencies are associated with low ion migration barriers in solid state electrolytes.²⁰⁴⁻

205

While the sound velocity is broadly relevant to a variety of physical properties and technologies, engineering v_s is challenging. The typical picture of elasticity links the speed of sound to the crystal structure, where materials with short, stiff atomic bonds and lower coordination number typically feature higher sound velocities.²⁰⁶⁻²⁰⁷ Similarly, Equation 1 shows the sound velocity is inversely related to the density. Unfortunately, these parameters can hardly be modified within a single material system. Because the sound velocity is generally associated exclusively with structural features, other possible means of changing v_s have historically been overlooked. As a case in point, doped semiconductors have been widely used for half a century in applications ranging from microelectronics to solar cells and battery materials, yet there is little work addressing the charge carrier or Fermi level dependence of the elastic properties. Nevertheless, the strength of chemical bonding is directly linked to the electron count, indicating that changing the charge carrier concentration n_H (Fermi level) in semiconductors could feasibly alter the lattice vibrations and impact the speed of sound. Furthermore, unlike structure and density, n_H can be easily manipulated by several orders of magnitude in both p- and n-type directions. Importantly, because doped semiconductors form the bedrock of all electronic

technologies, a relationship between sound velocity and charge carrier concentration would likely have wide reaching implications.

6.2 Results and Discussion

Thermoelectric materials require both minimal lattice thermal conductivity and high charge carrier concentration n_H above 10^{19} cm^{-3} ,⁹³ making them ideal systems with which to investigate the doping dependence of the speed of sound. Motivated by the above considerations, we prepared variably doped forms of eight common thermoelectric semiconductors, SnTe, PbTe, NbCoSb, La_3Te_4 , Pr_3Te_4 , CoSb_3 , Mg_3Sb_2 , and Mo_3Sb_7 , and used Hall effect measurements to measure their charge carrier densities and an ultrasonic pulse–echo technique to characterize the sound velocities. The primary results of our work are summarized in Figure 1, which shows the measured values v_s plotted against n_H for each material. Details concerning the measurements for each individual material are given in the following discussion and the experimental section.

The results displayed in Figure 1 are striking. The measured sound velocities of each compound decrease markedly upon raising the charge carrier concentration. Of all materials, SnTe and La_3Te_4 soften by the greatest magnitude, with the respective sound velocities suppressed by approximately 16 and 20 percent. Both p- and n-type doping directions are represented, and similar degrees of softening found in each case. Furthermore, we introduce a range of different extrinsic impurity types to modify n_H , i.e. point defects (PbTe, SnTe, Mg_3Sb_2 , Mo_3Sb_7), atomic vacancies (SnTe, Nb_xCoSb , La_3Te_4 , Pr_3Te_4), and filler/rattler atoms (CoSb_3). These various impurities are anticipated to impart different effects on the host lattice, yet we still observe a strong dependency between v_s and n_H . The combined results found in Figure 1 strongly point to a direct

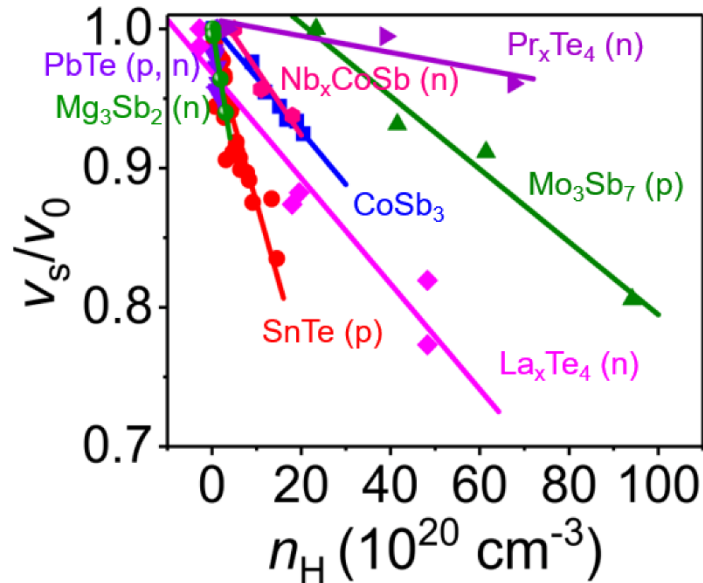


Figure 6.1 Sound velocities plotted against Hall charge carrier concentration for SnTe, PbTe, Nb_xCoSb , CoSb_3 , La_3Te_4 , Pr_3Te_4 , Mg_3Sb_2 , and Mo_3Sb_7 . All materials show a negative linear dependence of v_s on n_H . The sound velocities are all normalized the by the highest measured value (v_0) for each respective compound.

relationship between the charge carrier density and the sound velocity.

To address the potential alternative mechanisms of lattice softening, we first focus specifically on SnTe. Figure 2a displays average sound velocities plotted against charge carrier density for SnTe prepared with nine different dopants/alloys. We find the sound velocities decrease nearly linearly with increasing charge carrier density, with v_s falling approximately 16 percent, from ~ 2230 to $1860 \text{ m}\cdot\text{s}^{-1}$, as n_H is raised from $\sim 4 \times 10^{19}$ to $1.5 \times 10^{21} \text{ cm}^{-3}$. The choice of dopant has little impact on the sound velocities, and the relatively tight dependence of v_s on n_H indicates the electron count underpins the softening.

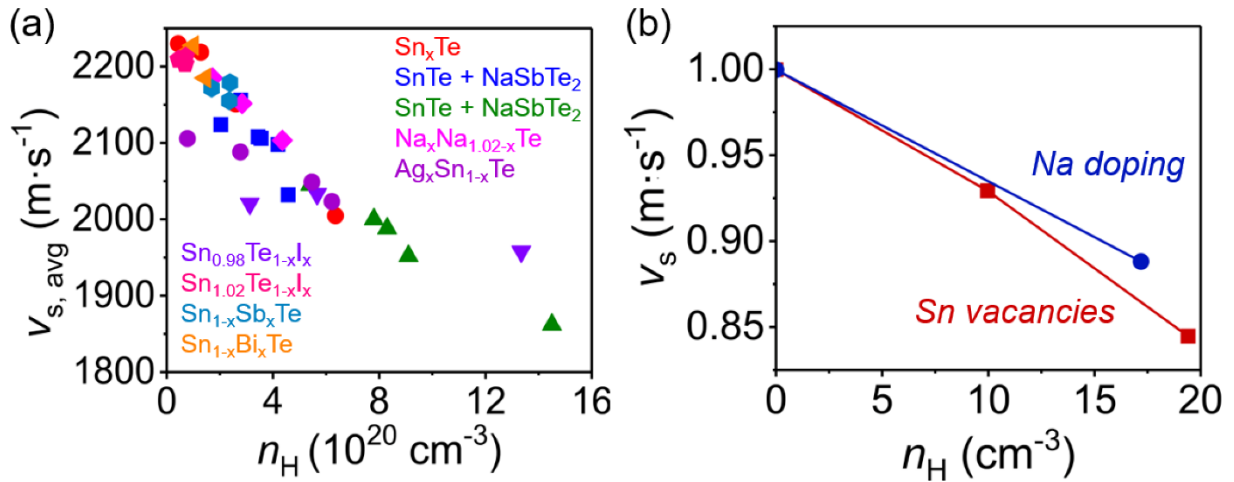


Figure 6.2 Measured average sound velocities plotted against Hall charge carrier concentration for p-type SnTe based samples. The legend shows the different dopants and alloys (b) DFT calculated sound velocities as a function of charge carrier concentration. The values of v_s are normalized to the calculated results for zero charge carriers (v_0). The blue line shows the calculated results using Na as a dopant, and the grey line the calculated results using Sn vacancies to modulate n_H .

Changes to the lattice constant a or sample density d that result from doping could also impact the speed of sound, and therefore may feasibly give an apparent relationship between v_s and n_H . To investigate these possibilities, we plot the average sound velocities against the refined lattice constants and measured densities in Figure 6.3a and 6.3b respectively. Figure 6.3a shows that v_s generally decreases with rising lattice parameter. Since the magnitude of bond stiffness tends to increase with smaller bond length,^{100, 207} the lattice contraction would if anything be expected to harden the samples. Therefore, the observed changes in a cannot explain the softening. Likewise, Figure 6.3b shows no discernible trend between d and v_s , indicating that changes to the

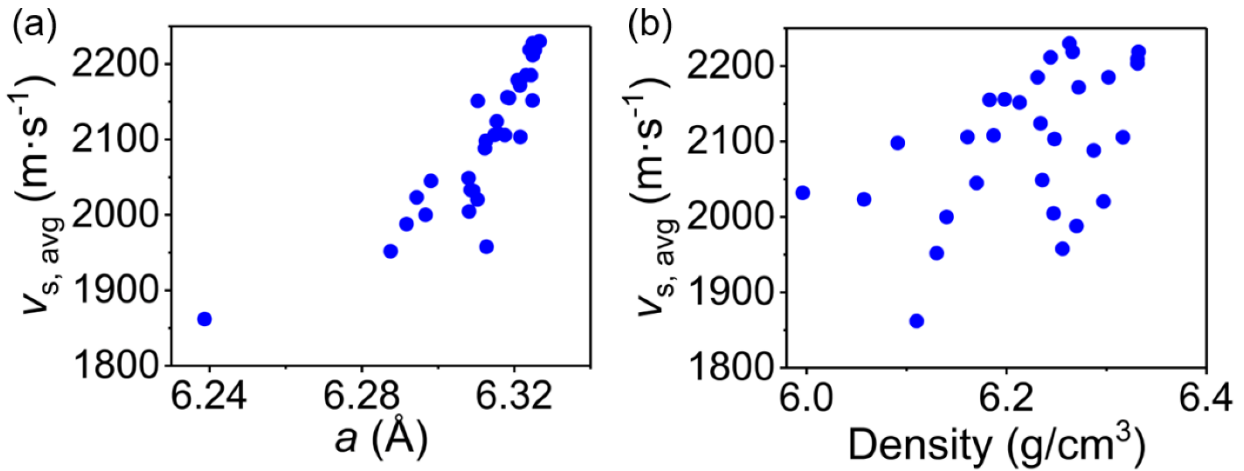


Figure 6.3 (a) Refined lattice parameters for the variably doped SnTe alloys discussed in Figure 6.2. (b) Measured densities for the same SnTe samples.

density are also insufficient to describe the reduction in v_s .

SnTe is well known to crystallize with an intrinsically high concentration of Sn vacancies, each of which introduces two holes into the valence band to maintain charge balance. Because the charge carrier concentration and cation vacancies of SnTe are intimately connected, the vacancies, and not the charge carriers, may feasibly underpin the softening. Indeed, prior work on SnTe-AgSbTe₂ alloys attributes the remarkably low sound velocities found in these materials to an enhanced Sn vacancy concentration.¹⁷⁶ To decouple the charge carriers from the vacancies, we performed density functional theory (DFT) calculations on SnTe, simulating p-type doping with Na and with Sn vacancies. The DFT results are shown in Figure 6.2b. In both cases, the calculations predict a ~15 percent reduction in v_s between intrinsic and doped samples for $n_H \sim 2 \times 10^{21} \text{ cm}^{-3}$, in qualitative agreement with our experimental results. Most importantly, the degree of softening calculated using Na as the dopant is nearly the same as that predicted when

considering the Sn vacancies, suggesting that outside of increasing the hole concentration, the vacancies have little impact on the sound velocities.

To fully assess the individual effects of vacancies and charge carriers, we investigated the doping dependence of v_s in NbCoSb, Pr₃Te₄, and La₃Te₄. NbCoSb is a nominally 19–electron half Heusler material that always crystalizes with a significant fraction of Nb vacancies, moving the electron count closer to the more energetically favored 18, i.e. Nb_{*x*}CoSb ($x \approx 0.8$).²⁰⁸⁻²⁰⁹ The 18–electron form is expected to be semiconducting, and by adding additional Nb, Nb_{0.8+*x*}CoSb, we can simultaneously n-type dope the material and lower the vacancy concentration. Similarly, La₃Te₄ and Pr₃Te₄ are cation deficient compounds that can be varied between semiconducting and metallic forms by altering the La/Pr stoichiometry,²¹⁰⁻²¹¹ where La and Pr-rich phases have high n-type charge carrier concentrations over 10²¹ cm⁻³. Because each of these materials is a cation deficient compound that can be n-type doped by filling the vacancies, any softening observed in these materials cannot be attributed to vacancies.

We conducted analogous Hall effect and pulse-echo measurements on samples with nominal compositions of Nb_{*x*}CoSb ($x = 0.80\text{--}0.84$), and Pr_{*x*}Te₄ ($x = 2.72\text{--}3$). Figure 6.4a and 6.4b display the respective room temperature Hall charge carrier concentrations plotted against nominal Nb or Pr stoichiometry x in Nb_{*x*}CoSb and Pr_{*x*}Te₄. In both systems, the measurements confirm that as x is increased, i.e. the cation vacancy concentration is reduced, the electron concentrations increase, reaching highly degenerate values over 10²¹ cm⁻³. The dependence of the sound velocities on the charge carrier concentration for each material are next presented in Figure 6.4c and 6.4d. Like in SnTe, v_s is increasingly suppressed with greater n_H . In Nb_{*x*}CoSb, the sound velocities decrease ~ 8 percent from 3580 to 3355 m·s⁻¹ as n_H is raised from 5 to 18x10²⁰ cm⁻³.

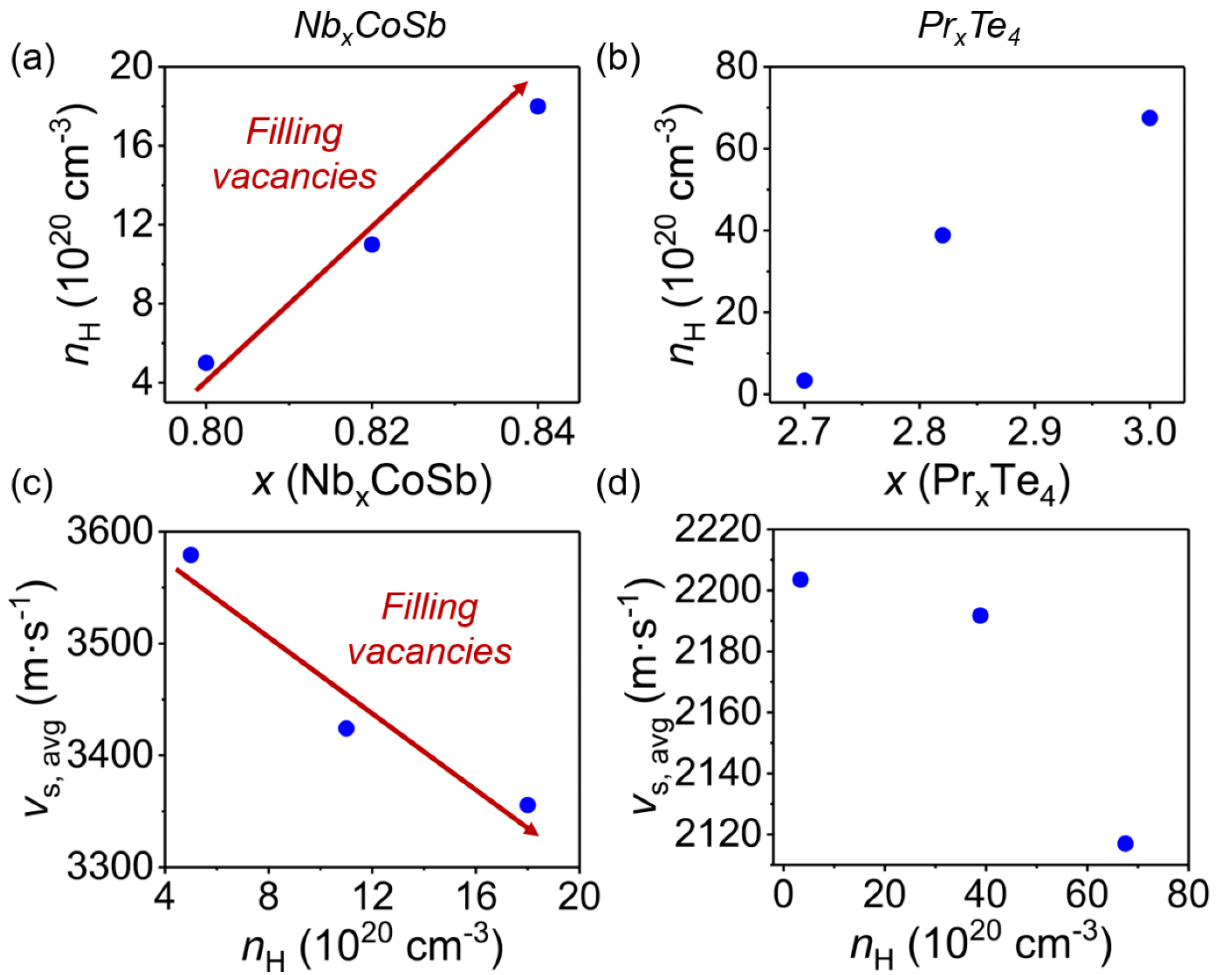


Figure 6.4 Hall charge carrier concentrations plotted against nominal composition x for (a) Nb_xCoSb and (b) Pr_xTe_4 . (c) and (d) are the measured sound velocities plotted against carrier concentration for the same samples.

Likewise, the v_s of Pr_xTe_4 falls from 2210 to 2117 $\text{m}\cdot\text{s}^{-1}$ over the n_H range of 3–64 $\times 10^{20} \text{ cm}^{-3}$.

We furthermore estimated the sound velocities of La_3Te_4 from the Debye temperatures θ_D previously reported by Delaire *et al.* and May *et al.*^{210,212} Figure 6.5a shows the Hall charge carrier concentrations measured for La_xTe_4 plotted against nominal La stoichiometry. As x is raised, n_H clearly increases linearly, indicating that the electron density is greatly enhanced by filling the La

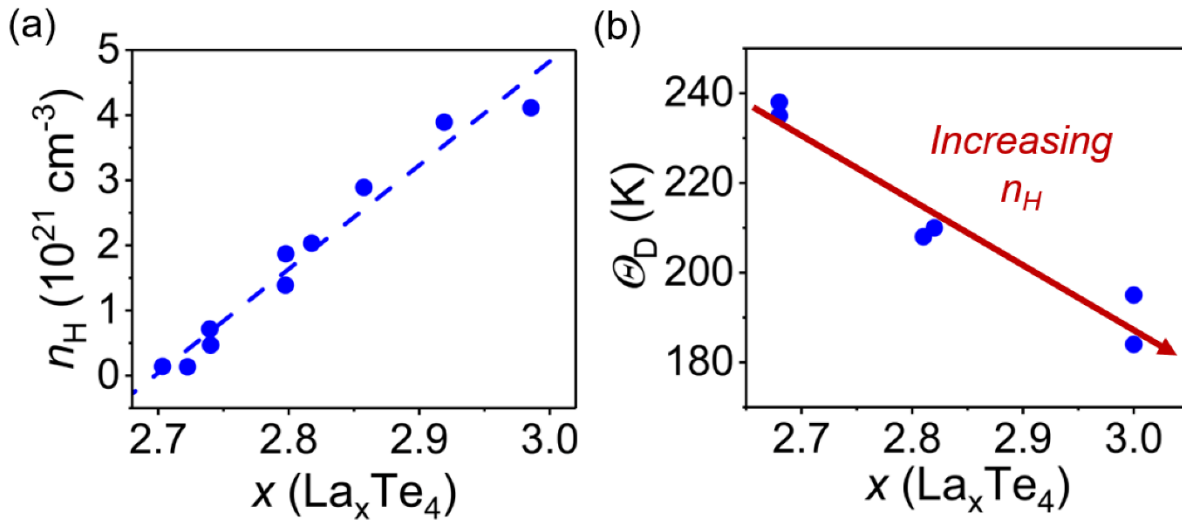


Figure 6.5 (a) Hall charge carrier concentrations plotted against nominal La stoichiometry x in La_xTe_4 . The blue line is a linear fit to the experimental points. (b) Debye temperatures of La_xTe_4 plotted against x . The data shown here was obtained from references 210 and 212.

vacancies. Debye temperatures θ_D estimated from the low temperature specific heat and shown in Figure 6.5b decrease ~20 percent from 238 K to ~190 K as the La stoichiometry is raised from 2.68 to 3. Because θ_D is linearly proportional to v_s ,¹⁹⁸ we can directly compare these results with the sound velocities discussed throughout this work. Together, Figures 6.5a and 6.5b directly show that La_xTe_4 lattice significantly softens with increased charge carrier density. In summary, we find that the sound velocities of Nb_xCoSb , Pr_xTe_4 , and La_xTe_4 , are all suppressed upon increasing n_H . The softening in each occurs in parallel with a *decrease* in the concentration of atomic vacancies, conclusively demonstrating that the vacancies have a negligible impact on v_s .

Another common type of defect found in thermoelectric materials is filler/rattler atoms. Introducing additional atoms into the void sites found in clathrates and skutterudites is well established as an effective way to boost thermoelectric performance. The rattling effect of the

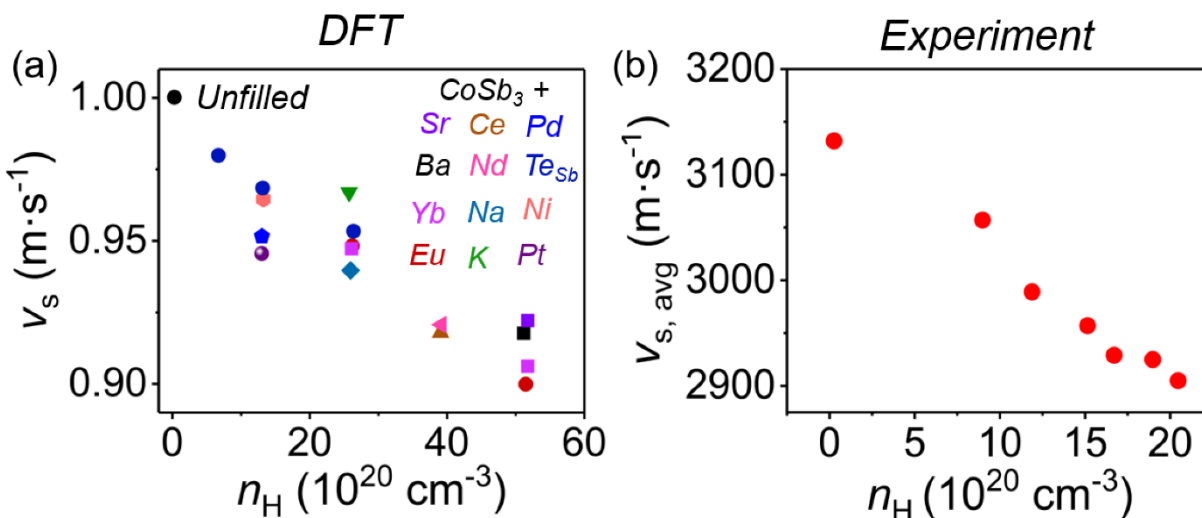


Figure 6.6 (a) DFT calculated sound velocities (normalized to the undoped value v_0) plotted against charge carrier concentration for skutterudite CoSb_3 doped with different filler atoms. (b) Experimental sound velocities and charge carrier concentrations for Yb-filled CoSb_3 (nominally $\text{Yb}_x\text{Co}_4\text{Sb}_{12}$).

weakly bound atom in the void site strongly enhances phonon scattering and has also been shown to lower the sound velocities.^{14, 23-24, 213} Because the filler atoms will also change the charge carrier concentration, we carried out DFT calculations to assess the sound velocities of the skutterudite CoSb_3 upon doping with different fillers.

Figure 6.6a shows the DFT calculated sound velocities for CoSb_3 doped with ten different filler atoms. Our calculations predict a nearly linear dependence of the speed of sound on the charge carrier concentration, with v_s decreasing by ~ 10 percent when doped to $\sim 5 \times 10^{21} \text{ cm}^{-3}$. Like in SnTe , the choice of dopant/filler has only minor impact on the results. Comparing the metals Ni, Pd, and Pt, the sound velocities decrease moving down the periodic table from Ni to Pt as

anticipated by the increasing atomic mass. Nevertheless, this change in v_s is comparably small, and the sound velocities clearly trend most strongly with charge carrier concentration.

To verify the DFT calculations, we carried out measurements of Yb-filled CoSb_3 (nominal compositions $\text{Yb}_x\text{Co}_4\text{Sb}_{12}$), and the data is presented in Figure 6.6b. The experimental data confirms the predicted softening, with a very tight linear reduction of v_s from 3130 to 2900 $\text{m}\cdot\text{s}^{-1}$ over an n_H ranging of 2.5×10^{19} to $2 \times 10^{20} \text{ cm}^{-3}$. In fact, the measured sound velocities as functions of n_H decrease even faster than the DFT prediction. This could feasibly be due to the differences in temperature between experiments (300 K) and calculations (DFT performed at 0K).

Based on the above analysis, we conclude that increasing the charge carrier concentration directly lowers the sound velocities. Using both experiments and computation, we rule out other possibilities such as density, the type of structural defect (vacancies, substitutional and rattler interstitial defects), and the defect concentration. Therefore, we establish increasing n_H as the main cause for the observed suppression of v_s . Considering we measure significant reduction of the sound velocity and/or Debye temperature for both p- and n-type doping and in eight different materials, our work indicates that electron count driven lattice softening is a general phenomenon. Because the sound velocities are a measure of the slope of the acoustic phonon dispersion at low wavevector, our results suggest the acoustic phonons are themselves softened by the enhanced charge carrier concentration. This finding is a significant update to the traditional picture of lattice dynamics which treats the lattice vibrations independently of the electrons and holes, as we clearly show the charge carriers must be considered to properly describe phonon/sound transport and the elastic properties of heavily doped semiconductors.

While a detailed microscopic mechanism for the lattice softening is outside the scope of this work, we propose a simple chemical explanation to rationalize our findings. The sound (and phonon) velocities are fundamentally determined by the interatomic force constants, or the strength of chemical bonding. Because intrinsic semiconductors are generally valence precise compounds in which the atoms transfer or share electrons to achieve energetically favorable 8 or 18 electron configurations for main group and transition metals respectively, increasing or decreasing the total charge carrier concentration changes the number of electrons available for atomic bonding and may feasibly weaken the bonds and give softer vibrational modes.

Several recent publications likewise suggest high charge carrier densities can impact the vibrational properties of semiconductors. For example, recently reported DFT calculations and Raman spectroscopy suggest that raising the electron concentration in mono- and bilayers of MoS₂, WS₂, and WSe₂ increases the electron phonon coupling and softens several optical and acoustic phonon modes.²¹⁴ Theoretical calculations of the vibrational properties of doped PbTe furthermore predict up a strong dependence of the elastic constants and sound velocity for p- and n-type dopants but find no change for neutral alloys.²¹⁵ Lastly, recent theoretical work on doped Si suggests that the strength of phonon scattering will be greatly enhanced from electrons when the charge carrier concentration is raised above $\sim 10^{19} \text{ cm}^{-3}$.²¹⁶⁻²¹⁷

Considering the sound velocity plays a central role determining the electronic, thermal, and mechanical properties of semiconductors, as well the ubiquity of doping in electronic technologies, we anticipate our findings to have broad practical and fundamental implications. Here, we consider the relevance of electron count lattice softening in the context of engineering high performance thermoelectric materials. The maximum energy conversion efficiency of a

thermoelectric module is given by the figure of merit ZT of its semiconductor components, and is given as $ZT = \frac{\sigma S^2}{\kappa_{elec} + \kappa_{lat}}$, where σ is the electrical conductivity, S is the Seebeck coefficient, T is the absolute temperature, and κ_{elec} and κ_{lat} are the electronic and lattice contributions to the total thermal conductivity κ_{tot} . The thermoelectric properties are coupled through both the electronic structure and charge carrier concentration, making improving ZT a complex optimization problem.

We outline the significance of electron count driven lattice softening in Figure 6.7. The red line in Figure 6.7a diagrams the generally accepted picture, which holds that sound velocity and lattice thermal conductivity, are independent of the electron count (phonon–electron scattering may become significant at very high n_H , but this is a separate mechanism from lattice softening and therefore ignored in the present discussion). Because the lattice thermal conductivity scales with the cube of phonon velocity above the Debye temperature,¹⁷ the blue curve shows that changing the n can have a profound impact on κ_{lat} when the electron count driven lattice softening is accounted for. This new picture could significantly renormalize the expected doping dependence of the thermoelectric properties as we illustrate in Figure 6.7b by plotting κ_{tot} , κ_{lat} , and ZT against charge carrier concentration using a single parabolic band (SPB) model. Generally, the total thermal conductivity increases rapidly with doping due to the increasing electronic contribution κ_{elec} , and the need to balance σS^2 and low thermal conductivity normally causes the ZT to be optimized in the range 10^{19} – 10^{20} cm^{-3} .⁹³

The traditional picture can however be significantly different when electron count driven lattice softening is accounted for. As we show in this work, increasing the carrier density also suppresses the sound velocity. This will reduce κ_{lat} and partially offset the increased κ_{elec} . Depending on the details of the band structure, the lattice softening will shift the optimal carrier

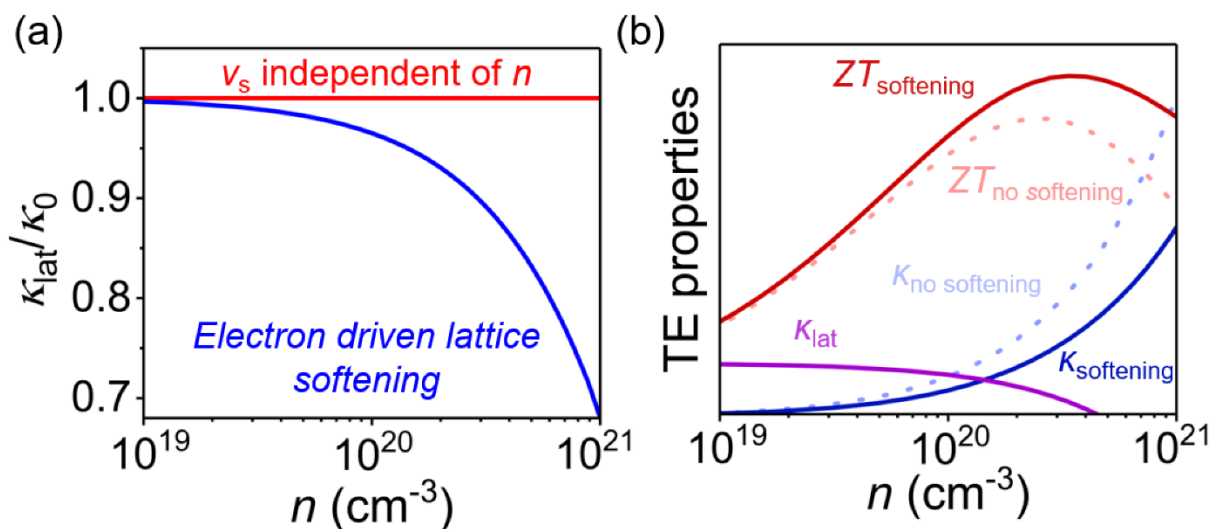


Figure 6.7 (a) Normalized lattice thermal conductivity as a function of charge carrier concentration. The red line is the traditional picture, where κ_{lat} is insensitive to the charge carriers. The blue line shows the relative change of the lattice thermal conductivity assuming that v_s is reduced linearly with n . (b) Thermoelectric properties plotted against charge carrier concentration assuming a single parabolic band (SPB) model with $m^* = 5m_e$. The dashed blue line shows the total thermal conductivity assuming v_s is independent of n , while the solid blue line considers v_s to be linearly dependent on n . If the charge carriers drive lattice softening, κ_{lat} is increasingly suppressed at high n and the total thermal conductivity is reduced, shifting the optimal carrier density needed to maximize ZT to higher values. The scale in (b) is arbitrary.

concentration to higher values and also increase the maximum ZT . Because the figures of merit are generally optimized at higher n_H in compounds with high effective mass, we anticipate the impact of charge carrier driven lattice softening to be most profound in these materials. Since quality thermoelectric materials are generally heavily doped semiconductors with charge carrier

concentrations approaching metallic greater than 10^{19} cm^{-3} , significant softening is likely present and currently overlooked in many materials.

6.3 Summary and Conclusions

We report the doping (Fermi level) dependence of the speed of sound (acoustic phonon velocity) in eight thermoelectric semiconductors. We find the sound velocity of each compound is linearly reduced upon raising the charge carrier concentration. By investigating several different materials and using a combination of experiments and theoretical calculations, we rule out other softening mechanisms such as sample density and defect type (alloy, vacancy, filler/rattler), to conclude that v_s is directly suppressed by raising n_H . In particular, the sound velocities of SnTe and La_3Te_4 are decreased by approximately 16 and 20 percent when n_H is raised from $\sim 10^{19}$ to 10^{21} cm^{-3} . Because the traditional picture of elasticity and lattice dynamics generally treats the atomic vibrations and sound velocity independently of electrons, our work provides a fundamental update, as we demonstrate that considering the electron count is essential to properly describe phonon transport in heavily doped semiconductors. We lastly show how the concept of electron count driven lattice softening may provide a new means of achieving high thermoelectric performance. Furthermore, as doped semiconductors are the foundation of all electronics, the intimate relationship between the sound velocity and electronic, thermal, and mechanical properties of solids suggests our work to have broad technological implications.

6.4 Experimental Details

6.4.1 Synthesis and sample preparation

SnTe based materials: Polycrystalline ingots of SnTe, were first synthesized by weighing stoichiometric quantities of each element along with the dopants into 13 mm diameter fused silica tubes. Nominal compositions generally took the form $A_x\text{Sn}_{1-x}\text{Te}$ where A is the dopant/alloy atom. For the samples containing sodium, the tubes were carbon coated 3 times prior to usage to limit glass attack. The tubes were flame sealed at $\sim 3 \times 10^{-3}$ torr and heated in a box furnace to 1273 K over 12 hours. After dwelling at temperature for 5 hours, the tubes were next brought to room temperature in the furnace over 12 hours. The polycrystalline ingots were next removed from their tubes, and hand ground in an agate mortar and pestle to fine powders. To ensure a relatively uniform particulate size, we passed the powdered samples through a 53 μm mesh sieve. The samples were loaded into 12.7 mm diameter graphite dies and consolidated into dense pellets by spark plasma sintering (SPS) using a SPS-211LX, Fuji Electronic Industrial Co. Ltd. Instrument. During SPS processing, samples were held under dynamic vacuum at 773 K for 10 minutes and under 40 MPa of uniaxial pressure before being cooled to room temperature. After sintering, the pellets were cut and polished in $\sim 6 \times 6 \times 2 \text{ mm}^3$ square prisms for ultra-sound and Hall effect measurements. Cuts were made such that the measurements were made perpendicular to the pressing direction unless otherwise noted.

Nb_xCoSb: Nb_xCoSb samples were prepared using an arc melter using stoichiometric ratios of bulk Nb lumps (99.9% Sigma-Aldrich), Co slugs (99.99% Alpha Aesar), and Sb shot (99.999% Alpha Aesar). Starting elements were cut into small pieces and loaded into an edmund-buehler MAM-1 arc melter where they were melted together 5 times flipping in between each melt. These arc-

melted buttons were sealed in an evacuated fused silica ampule and annealed at 1100 °C for one week. After the anneal the buttons were then pulverized using a in a stainless-steel vial for one hour using a SPEX Sample Prep 800 Series Mixer/Mill. This powder was consolidated using an induction heated rapid hot-press under a flowing argon atmosphere within a 1/2 inch diameter high-density graphite die (POCO). This sample was then pressed at 1100 C for 15 minutes at a pressure of 45 MPa. Once pressed this sample was polished to remove excess graphite from its surface.

Pr_xTe: To synthesize Pr_xTe samples, we combined and sealed elemental Pr (99.9%, Stanford Materials) and Te shot (99.999, 5N Plus) under argon in stainless-steel ball mill vials with stainless-steel balls. The samples were then milled (SPEX SamplePrep 8000) for over 10 hours into homogeneous black powders. The powders were densified in graphite dies through SPS at a pressure of 80 MPa and at temperatures above 1200 °C for 30 min under vacuum. The Archimedes method was used to measure density, and the compacted samples were found to be 97% dense or greater of theoretical values.

6.4.2 Hall effect

Hall effect measurements were conducted using a homebuilt system. The setup utilizes Van der Pauw geometry with magnetic fields of ~2T and currents of 100 mA. The carrier densities were calculated from the Hall coefficient assuming a single carrier band, i.e., $n_H = 1/eR_H$, where R_H is the Hall coefficient.

6.4.3 Sound velocity measurements

The sound velocities of the SnTe–NaSbTe₂ samples were measured using a pulse-echo technique. Typical samples were polished squares similar to the geometry used for the LFA. The samples were coupled to a piezoelectric transducer with a small amount of honey. The transducer sends an initial stress-wave pulse into the sample, and then acts as a detector by receiving and measuring the echoed ultrasound reflections. The time delay t_d between reflections was determined by maximizing the cross-correlation of the two reflections,¹⁷⁶ and the sound velocity calculated as $v = 2d/t_d$ where d is the sample thickness. We measured both longitudinal and transverse components of the sound velocity using 5 MHz longitudinal and transverse transducers (Olympus V1091 and Olympus V157-RM respectively). The crystallographic average sound velocity was then calculated as follows:

$$v_{avg} = \left[\frac{1}{3} \left(\frac{1}{v_L^3} + \frac{2}{v_T^3} \right) \right]^{-1/3} \quad (1)$$

where v_L and v_T are the measured longitudinal and transverse velocities respectively. In this work, v_L and v_T were each measured three times for each sample, and the values reported here are the average of each measurement.

6.4.4 Powder X-ray diffraction

Powder X-ray diffraction (PXRD) patterns were measured with a Rigaku Miniflex 600 instrument using Cu K α radiation with wavelength $\lambda = 1.5406 \text{ \AA}$ and operating at 40 kV and 15 mA and with a K β filter. Using the obtained diffraction patterns, we refined the lattice parameters using the Rietveld method in GSAS-II software.

6.5 Additional and raw data

Table 6.1 Data from the pulse-echo measurements of the sound velocity and Hall effect measurements of the charge carrier concentration for PbTe. Compositions are nominal and p- and n-type doping is denoted by (p or n respectively). The refined lattice parameters and measured sample densities are also given. The uncertainty in v_L and v_T are the standard deviations of 3 measurements obtained on each sample.

Composition	v_L (m·s ⁻¹)	v_T (m·s ⁻¹)	v_{avg} (m·s ⁻¹)	n_H (10 ²⁰ cm ⁻³)	d (g·cm ⁻³)
Pb _{0.99} Na _{0.01} Te (p)	2969	1606	1792	0.5931	8.16
Pb _{0.99} Na _{0.01} Te (p)	2967	1609	1795	0.6964	8.16
Pb _{0.98} Na _{0.02} Te (p)	2947	1559	1743	1.385	8.16
Pb _{0.98} Na _{0.02} Te (p)	2939	1565	1748	1.268	8.16
Pb _{0.96} Na _{0.04} Te (p)	2945	1574	1758	1.402	8.16
Pb _{0.96} Na _{0.04} Te (p)	2955	1593	1779	1.110	7.95
Pb _{0.975} K _{0.02} Te _{1.005} (p)	2912	1582	1766	0.0285	8.07
Pb _{0.99} La _{0.01} Te (n)	3012	1654	1844	0.0865	8.16
Pb _{0.99} La _{0.01} Te (n)	2951	1609	1794	0.506	8.16
Pb _{0.99} La _{0.01} Te (n)	2912	1583	1765	1.09	8.16
PbTe _{0.998} I _{0.012} (n)	2929	1583	1767	1.723	8.128

Table 6.2 Compiled results from the pulse-echo measurements of the sound velocity and Hall effect measurements of the charge carrier concentration for Yb-filled CoSb₃ (Yb_xCo₄Sb₁₂). Compositions are nominal. The data was previously published in a Ph.D. thesis (thesis.library.caltech.edu/9681/55/Tang_Yinglu_2015_thesis_04212016). The original work attributed the softening to the filler alone, not the changed charge carrier density.

Composition	v_L (m·s ⁻¹)	v_T (m·s ⁻¹)	v_{avg} (m·s ⁻¹)	n_H (10 ²⁰ cm ⁻³)	a (Å)	d (g·cm ⁻³)
Co ₄ Sb ₁₂	4743	2830	3132	0.2615	9.034	7.638
Yb _{0.2} Co ₄ Sb ₁₂	4600	2764	3057	8.9796	9.737	7.737
Yb _{0.3} Co ₄ Sb ₁₂	4534	2700	2989	11.8841	9.053	7.769
Yb _{0.4} Co ₄ Sb ₁₂	4469	2672	2957	15.1445	9.058	7.803
Yb _{0.45} Co ₄ Sb ₁₂	4447	2646	2929	16.7033	9.06	7.819
Yb _{0.5} Co ₄ Sb ₁₂	4418	2643	2925	18.972	9.063	7.842
Yb _{0.6} Co ₄ Sb ₁₂	4443	2622	2905	20.4599	9.066	7.860

Table 6.3 Compiled results from the pulse-echo measurements of the sound velocity and Hall effect measurements of the charge carrier concentration for SnTe based alloys. The compositions are nominal. The refined lattice parameters and measured sample densities are also given. The uncertainty in v_L and v_T are the standard deviations of 3 measurements on each sample.

Composition	v_L (m·s ⁻¹)	v_T (m·s ⁻¹)	v_{avg} (m·s ⁻¹)	n_H (10 ²⁰ cm ⁻³)	a (Å)	d (g·cm ⁻³)
Sn _{1.03} Te	3540(13)	2005(8)	2230	0.430	6.3266(1)	6.263
Sn _{1.02} Te	3535(4)	1994(6)	2219	1.284	6.3254(1)	6.266
Sn _{1.01} Te	3504(5)	1989(5)	2212	0.578	6.3248(1)	6.244
SnTe	3468	1932	2151	2.6	6.3104	6.12
Sn _{0.98} Te	3362(18)	1795(7)	2005	6.35	6.3081(1)	6.247
Na _{0.005} Sn _{1.015} Te	3540(11)	1961(6)	2185	1.721	6.3243(1)	6.231
Na _{0.01} Sn _{1.01} Te	3479(4)	1931(5)	2151	2.838	6.3248(2)	6.213
Na _{0.02} SnTe	3434(4)	1887(2)	2103	4.352	6.3215(1)	6.248
Ag _{0.01} Sn _{0.99} Te	3433(5)	1889(2)	2105	0.778	6.3175(1)	-
Ag _{0.02} Sn _{0.98} Te	3462(3)	1871(1)	2088	2.775	6.3123(1)	-
Ag _{0.03} Sn _{0.97} Te	3439(4)	1833.9(6)	2049	5.463	6.3080(2)	-
Ag _{0.05} Sn _{0.95} Te	3445(8)	1809(5)	2023	6.217	6.2944(1)	-
Sn _{0.995} Sb _{0.005} Te	3506(3)	1957(3)	2179	2.379	6.3209(1)	6.577
Sn _{0.99} Sb _{0.01} Te	3482(2)	1951(5)	2172	1.688	6.3215(1)	6.272
Sn _{0.98} Sb _{0.02} Te	3469(4)	1936(1)	2155	2.354	6.3187(1)	6.183
Sn _{0.995} Bi _{0.005} Te	3515.9(0)	1963(3)	2185	1.447	6.3230(1)	6.302
Sn _{0.99} Bi _{0.01} Te	3563(6)	2002(5)	2228	0.988	6.3248(1)	-
Sn _{0.98} Bi _{0.02} Te	3542(8)	1995(1)	2219	0.748	6.3240(1)	6.332
Sn _{0.98} Te _{0.9975} I _{0.0025}	3400.4(2)	1820(2)	2033	5.659	6.3085(1)	-
Sn _{0.98} Te _{0.995} I _{0.005}	3380(2)	1809(0)	2020	3.127	6.3103(1)	6.297
Sn _{0.98} Te _{0.99} I _{0.01}	3307(3)	1752(5)	1958	13.346	6.3126(1)	6.256
Sn _{1.02} Te _{0.9975} I _{0.0025}	3524(1)	1989(6)	2213	0.707	6.3248(1)	-
Sn _{1.02} Te _{0.995} I _{0.005}	3491(8)	1982(5)	2203	0.693	-	6.331
Sn _{1.02} Te _{0.99} I _{0.01}	3521(4)	1986(1)	2209	0.448	-	6.331
SnTe + 2% AgSbTe ₂	3295	1837	2045	5.4	6.2981	6.17
SnTe + 3.8% AgSbTe ₂	3241	1795	2000	7.8	6.2967	6.14
SnTe + 4.8% AgSbTe ₂	3257	1783	1988	8.3	6.2917	6.27
SnTe + 6.5% AgSbTe ₂	3189	1752	1952	9.1	6.2875	6.13
SnTe + 16% AgSbTe ₂	3106	1668	1862	14.5	6.2387	6.11
SnTe + 2% NaSbTe ₂	3456	1937	2156	2.785	6.3181(2)	6.198
SnTe + 3.8% NaSbTe ₂	3497	1905	2124	2.034	6.3154(1)	6.234
SnTe + 4.8% NaSbTe ₂	3386	1894	2108	3.441	6.3157(1)	6.187
SnTe + 6.5% NaSbTe ₂	3398	1891	2106	3.551	6.3148(1)	6.161
SnTe + 9% NaSbTe ₂	3360	1885	2098	4.190	6.3125(1)	6.091
SnTe + 16% NaSbTe ₂	3263	1825	2032	4.571	6.3091(1)	5.996

Table 6.4 Data from the pulse-echo measurements of the sound velocity and Hall effect measurements of the charge carrier concentration for Nb_xCoSb (nominal x)

Composition	ν_L ($\text{m}\cdot\text{s}^{-1}$)	ν_T ($\text{m}\cdot\text{s}^{-1}$)	ν_{avg} ($\text{m}\cdot\text{s}^{-1}$)	n_H (10^{20} cm^{-3})
$\text{Nb}_{0.80}\text{CoSb}$	5697.8	3220(16)	3579	5
$\text{Nb}_{0.82}\text{CoSb}$	5574(8)	3073(8)	3424	11
$\text{Nb}_{0.84}\text{CoSb}$	5496(11)	3010(3)	3356	18

Table 6.5 Data from the pulse-echo measurements of the sound velocity and Hall effect measurements of the charge carrier concentration for Pr_xTe_4 . The uncertainty in ν_L and ν_T are the standard deviations of three measurements obtained on each sample. Due to the very high charge carrier concentrations, the Hall effect measurement of n_H for Pr_3Te_4 has high uncertainty, but independent measurements of the Seebeck coefficient and electrical conductivity confirm the higher charge carrier concentration.

Composition	ν_L ($\text{m}\cdot\text{s}^{-1}$)	ν_T ($\text{m}\cdot\text{s}^{-1}$)	ν_{avg} ($\text{m}\cdot\text{s}^{-1}$)	n_H (10^{20} cm^{-3})
Pr_3Te_4	3578(4)	1894(2)	2117	64(50)
$\text{Pr}_{2.82}\text{Te}_4$	3590(15)	1962(3)	2192	39(3)
$\text{Pr}_{2.70}\text{Te}_4$	3595(18)	1977(2)	2204	3.4(1)

Table 6.6 Data from the pulse-echo measurements of the sound velocity and Hall effect measurements of the charge carrier concentration for $\text{Mg}_{3.2}\text{Sb}_{2-x}\text{Te}_x$.

Composition	ν_L ($\text{m}\cdot\text{s}^{-1}$)	ν_T ($\text{m}\cdot\text{s}^{-1}$)	ν_{avg} ($\text{m}\cdot\text{s}^{-1}$)	n_H (10^{20} cm^{-3})
$\text{Mg}_{3.3}\text{Sb}_2$	4145	2029	2278	0.201
$\text{Mg}_{3.2}\text{Sb}_{1.990}\text{Te}_{0.01}$	4136	2019	2268	0.241
$\text{Mg}_{3.2}\text{Sb}_{1.992}\text{Te}_{0.08}$	4050	1954	2196	1.93
$\text{Mg}_{3.2}\text{Sb}_{1.90}\text{Te}_{0.1}$	3984	1904	2142	3.08

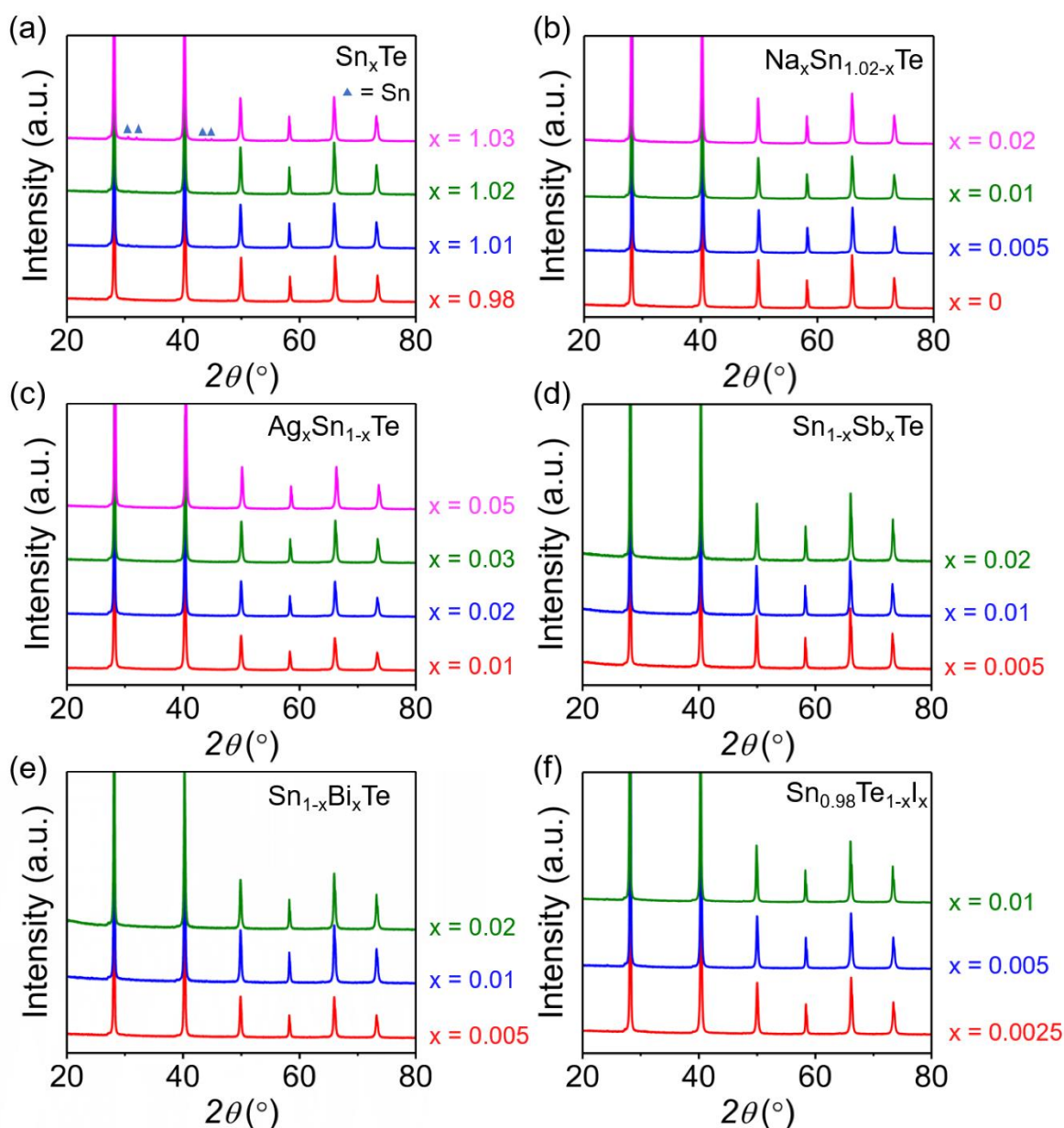


Figure 6.8 Powder X-ray diffraction patterns for the doped/alloyed SnTe samples. Nominal compositions are indicated to the side of each pattern and are as follows: (a) Sn_xTe , (b) $\text{Na}_x\text{Sn}_{1.02-x}\text{Te}$, (c) $\text{Ag}_x\text{Sn}_{1-x}\text{Te}$, (d) $\text{Sn}_{1-x}\text{Sb}_x\text{Te}$, (e) $\text{Sn}_{1-x}\text{Bi}_x\text{Te}$, $\text{Sn}_{0.98}\text{Te}_{1-x}\text{I}_x$. The lattice parameters listed in Table 6.3 are refined from the above powder patterns using the Rietveld method.

Chapter Seven

Conclusions, future work, and outlook

7.1 Summary and conclusions

7.1.1 Absence of nanostructuring in $\text{NaPb}_m\text{SbTe}_{m+2}$: solid solutions with high thermoelectric performance in the intermediate temperature regime

Alloying NaSbTe_2 into PbTe forms quaternary compounds ($\text{NaPb}_m\text{SbTe}_{m+2}$) with microstructures and transport properties that are highly dependent on the synthetic procedure. As-cast ingots are two phase composites, with nano to micron level phase segregation depending on the $\text{NaSbTe}_2:\text{PbTe}$ ratio, and behave as degenerate p-type semiconductors. Grinding the ingots to powder followed by spark plasma sintering or hot pressing causes the secondary phases to dissolve and yields single phase solid solutions that exhibit weakly n-type charge transport. The ability to prepare single phase samples of $\text{NaPb}_m\text{SbTe}_{m+2}$ sets these materials apart from the analogous $\text{AgPb}_m\text{SbTe}_{m+2}$ thermoelectrics, which always form with nanostructures microstructures. Tuning the Na and Sb stoichiometry, i.e. $\text{Na}_{1+x}\text{Pb}_{m-x}\text{Sb}_{0.85}\text{Te}_{m+2}$, allows for recovery of the degenerate p-type charge transport. Facilitated by very low lattice thermal conductivity, optimized samples reach high figures of merit ~ 1.6 at 673 K with high ZT s near room temperature compared to other PbTe -based alloys. The high performance at lower temperatures manifests in excellent $ZT_{\text{avg}} \sim 1.1$ between 323–673 K, indicating $\text{NaPb}_m\text{SbTe}_{m+2}$ may be promising candidates for thermoelectric power generation at low and moderate temperatures.

7.1.2 High thermoelectric performance in PbSe – NaSbSe_2 alloys from valence band convergence and low thermal conductivity

Mixtures of PbSe and NaSbSe_2 ($\text{NaPb}_m\text{SbSe}_{m+2}$) are single phase at the nanoscale and exhibit very minor heterogeneity at the micron level, which increases with NaSbSe_2 fraction.

The NaSbSe₂ lowers the separation between L - and Σ -point valence band, facilitating improved Seebeck coefficient and power factors while simultaneously providing strong point-defect phonon scattering. The high solubility of NaSbSe₂ in PbSe allows access to parallel enhancement of the electronic properties and suppression of the lattice thermal conductivity. As such, properly doped forms of the optimal composition, NaPb₁₀SbSe₁₂ (~9% NaSbSe₂) achieves excellent maximum $ZT \sim 1.4$ at 873 K and $ZT_{\text{avg}} \sim 0.64$ between 423–873 K, a record for tellurium free PbSe thermoelectrics.

7.1.3 Understanding the thermally activated charge transport in NaPb_{*m*}SbQ_{*m+2*} (Q = S, Se, Te) thermoelectrics: weak dielectric screening leads to grain boundary dominated charge carrier scattering

Despite having degenerate hole densities over 10^{20} cm^{-3} , NaPb_{*m*}SbSe_{*m+2*} and NaPb_{*m*}SbS_{*m+2*} exhibit highly irregular thermally activated electrical conductivity below ~500 K with the expected metallic transport above. The NaPb_{*m*}SbTe_{*m+2*} show no irregular transport properties and exhibit the expected degenerate p-type behavior. The unusual transport in the selenide and sulfide compounds is unambiguously demonstrated to stem from charge carrier scattering at the grain boundaries (GBs), and samples prepared with reduced density of GBs recover the expected metallic behavior. The presence and magnitude of GB scattering in each NaPb_{*m*}SbQ_{*m+2*} family can be rationalized and predicted using simple chemical principles that consider the polarizability of the host atoms and relative degree of charge carrier screening in each material. The intuitive chemical framework provided in this chapter furthermore explains the strong GB scattering in the other emerging thermoelectric materials including the Zintl antimonides, half Heuslers, and MgSi.

This work offers new design principles for proper microstructure engineering in ionic thermoelectric materials.

7.1.4 $\text{NaSn}_m\text{SbTe}_{m+2}$ and $\text{NaSn}_m\text{BiTe}_{m+2}$ thermoelectric alloys: high performance facilitated by cation vacancies and lattice softening

SnTe alloys with NaSbTe_2 or NaBiTe_2 form single phase solid solutions for up to ~ 20 percent NaPnTe_2 ($\text{Pn} = \text{Sb}, \text{Bi}$). While qualitatively similar, the two materials have unique thermoelectric properties. SnTe – NaSbTe_2 ($\text{NaSn}_m\text{SbTe}_{m+2}$) has enhanced Seebeck coefficients and powerfactors, as well as lower thermal conductivity, and reaches high $ZT_{\text{max}} \sim 1.2$ at 800–900 K and competitive $ZT_{\text{avg}} \sim 0.7$ between 323–873 K. On the other hand, the thermoelectric properties in SnTe – NaBiTe_2 ($\text{NaSn}_m\text{BiTe}_{m+2}$) are severely limited by bipolar diffusion and only achieve modest ZT s of 0.85. Density functional theory shows both NaSbTe_2 and NaBiTe_2 facilitate valence band convergence in SnTe ; however, each NaPnTe_2 also lowers the band gap, making the resulting alloys more prone to detrimental bipolar diffusion. The band gap closes more rapidly after NaBiTe_2 incorporation, forming a semimetal at high alloy fraction, while remaining finite in the SnTe – NaSbTe_2 family. Moreover, introduction of NaSbTe_2 to SnTe , but not NaBiTe_2 , nearly doubles the fraction of intrinsic vacancies, increasing the hole concentration and suppressing bipolar diffusion in the NaSbTe_2 –based family. The vacancies furthermore enhance phonon scattering and suppress the sound velocity in $\text{NaSn}_m\text{SbTe}_{m+2}$, facilitating glasslike lattice thermal conductivity. The different thermoelectric properties in $\text{NaSn}_m\text{SbTe}_{m+2}$ and $\text{NaSn}_m\text{BiTe}_{m+2}$ underscore the important role played by the intrinsic defects in engineering high performance thermoelectric materials.

7.1.5 Electron count mediated lattice softening in semiconductors

Raising the charge carrier concentration n_H in semiconductors to high values above 10^{20} cm^{-3} directly softens the lattice (reduces the sound or phonon velocities v_s). The sound velocity of SnTe decreases linearly with rising charge carrier concentration, from 2230 to 1860 $\text{m}\cdot\text{s}^{-1}$ over hole densities spanning 4×10^{19} – 1.5×10^{21} cm^{-3} . To decouple the impact of intrinsic vacancies from the carrier concentration, Nb_xCoSb and Pr_xTe_4 , are investigated, as both can be n-type doped by filling the cation vacancies. In each material, the speed of sound decreases upon increasing n_H , conclusively demonstrating the increased carrier density, not the vacancies, drives the softening. Furthermore, ~5–20 percent reduction of the speeds of sound or Debye temperatures is measured in PbTe, La_xTe_4 , and Mo_3Sb_7 . Because we find a decrease in v_s or θ_D in seven different materials and with p- and n-type doping, we conclude that charge carrier driven lattice softening is a general phenomenon. This work provides direct evidence phonons play an important and previously unrecognized role in determining the phonon transport properties in heavily doped semiconductors. Electron count mediated lattice softening is anticipated suppress the lattice thermal conductivity and lead to improved figures of merit at high charge carrier densities, particularly in semiconductors with high effective mass. Outside of thermoelectrics, the importance of both doped semiconductors and phonons to numerous technologies and physical processes indicates the fundamental nature of these results will have broad implications.

7.2 Future work

7.2.1 Mixed chalcogenide forms of $\text{NaPb}_m\text{SbQ}_{m+2}$

The three individual material systems, PbQ-NaSbQ_2 ($\text{Q} = \text{Te, Se, S}$) were extensively investigated, with high thermoelectric performance found in the telluride and sulfide families. Mixtures composed of multiple chalcogenides, i.e. $\text{NaPb}_m\text{Sb}(\text{Te}_{1-x}\text{Se}_x)_{m+2}$, were not explored. Yet, among the pure lead chalcogenides, PbTe-PbS , PbSe-PbTe , and PbT-PbSe-PbS are all known to exhibit superior thermoelectric performance to the binary PbQ phases,^{39, 48, 218} indicating the same may be also true of the $\text{NaPb}_m\text{SbQ}_{m+2}$. In addition to potentially accessing improved performance, the different lead chalcogenide mixtures host a variety of unique microstructures, ranging from shape and size controlled nanoprecipitates to micron level spinodal decomposition.²⁵ While the pure $\text{NaPb}_m\text{SbQ}_{m+2}$ discussed in this thesis all form single phase solid solutions, chalcogenide mixtures may exhibit different microstructures. Investigating the impact of different chalcogenide mixtures on the microstructure and thermoelectric properties will therefore be of practical and fundamental chemical interest.

7.2.2 Potential cation ordering in $\text{NaPb}_m\text{SbQ}_{m+2}$

The $\text{NaPb}_m\text{SbQ}_{m+2}$ and NaPbQ_2 compounds investigated in this thesis crystallize in the rocksalt crystal structure, where the cations randomly occupy the same crystallographic position to maintain cubic symmetry. However, theoretical calculations carried out by collaborators indicate lower symmetry phases with ordered arrangements of cations are more energetically favored than the cubic structures for both ternary and quaternary systems.²¹⁹ Furthermore, while macroscopically cubic, the Ag based analogues, AgSbTe_2 , $\text{AgPb}_m\text{SbTe}_{m+2}$, and $\text{AgPb}_m\text{SbSe}_{m+2}$ are

all reported to exhibit nanoscale regions with superstructure and local deviations from cubic symmetry.⁹⁴ Preliminary electron diffraction studies conducted by collaborating groups and not discussed in this thesis suggest slowly cooled $\text{NaPb}_m\text{SbQ}_{m+2}$ and $\text{NaPb}_m\text{BiQ}_{m+2}$ samples may likewise show local cation order. More detailed investigations are warranted to confirm these results. If ordered forms of $\text{NaPb}_m\text{SbQ}_{m+2}$ can be stabilized, the different symmetries are anticipated to alter the electronic structure and thermoelectric properties.

7.2.3 Exploration of SnSe-NaSbSe_2 and GeTe-NaSbTe_2

This thesis primarily focused on the synthesis and charge/thermal transport characterization of the PbQ-NaSbQ_2 phase space, with additional work on the SnTe-NaPnTe_2 systems. The analogous pseudo-binary SnSe-NaSbSe_2 and GeTe-NaSbTe_2 have yet to be explored and are promising targets for future work. Both base compounds, SnSe and GeTe , are individually outstanding thermoelectrics, and NaSbQ_2 may favorably lower the thermal conductivity and improve the electronic structure. Furthermore, because neither SnSe or GeTe are cubic, it remains to be seen whether the alloys with NaSbQ_2 will crystallize in the lower symmetry structures, form multiphase composites, or stabilize cubic forms of SnSe or GeTe . In addition to being of fundamental chemical interest, each of these possibilities offers promise for favorable manipulation of the thermoelectric properties. If NaSbQ_2 stabilizes cubic quaternaries, the higher symmetry would be anticipated to yield an electronic structure with higher band degeneracy and therefore may provide significant improvements to the power factors.

7.2.4 Optimizing large grained forms of $\text{NaPb}_m\text{SbQ}_{m+2}$ ($\text{Q} = \text{Se}, \text{S}$) and other ionic semiconductors

Work in Chapter Four suggested that large grains are preferable in more ionic thermoelectric materials in order to suppress GB scattering and maintain high charge carrier mobility. The $\text{NaPb}_m\text{SbS}_{m+2}$ semiconductors discussed in this work all have poor ZT owing to their strong GB scattering and poor electronic conductivity. Large grained or single crystal forms should be investigated, as these may have significantly improved charge carrier mobility and figure of merit. Likewise, more work should be directed to optimizing the grain size in the selenides $\text{NaPb}_m\text{SbSe}_{m+2}$ for different NaSbSe_2 fractions and doping levels, as work in Chapter Four indicated the impact of changing the grain size is highly dependent on the charge carrier concentration. Lastly, large grained or single crystal forms of other ionic thermoelectric materials should be explored. Promising examples include Zintl antimonides KAlSb_4 , MCoSb , Sr_3GaSb_3 , NbFeSb , $\text{Ca}_5\text{Al}_2\text{Sb}_6$, and Ca_3AlSb , all of which show promising thermoelectric properties in small grained forms, despite the presence of strong GB scattering. Large grained forms with mitigated GB effects may immediately show improved performance.

7.2.5 Investigating the mechanism of electron count lattice softening

Chapter Six demonstrated that the phonon velocities of many semiconductors is considerably more effected by the electron count, or charge carrier concentration, than previously recognized. Owing to the fundamental nature of phonon transport to nearly all problems in solid state chemistry and condensed matter physics, future work addressing the mechanism of the lattice softening would be of wide interest.

7.3 Outlook

For thermoelectric technology to realize widespread societal usage, both new materials and fresh insight into fundamental charge and thermal transport physics are needed. This thesis makes contributions on both fronts. New quaternary alloys of lead and tin chalcogenides with NaSbQ_2 ($Q = \text{Te, Se, S}$) are synthesized and characterized in detail, with very promising thermoelectric properties found among them. This work furthermore provides an explanation for detrimental grain boundary limited electrical conductivity present in many emerging materials and offers strategies for mitigating its effect. The finding of electron count driven lattice softening lastly constitutes a novel fundamental relationship between charge carriers and phonons which may have significant implication for engineering high performance thermoelectrics and more.

Despite significant progress over the last decade, the field of thermoelectrics still faces significant barriers. Most of the best performing materials, including those developed in this thesis, are composed of toxic or expensive elements such as Pb, Te, and Se. New materials must be made up of more earth abundant and benign atoms while still showing high performance. Towards this goal, the insight and research accomplished in this thesis are likely to be broadly applicable and may provide useful design principles and strategies for engineering next generation thermoelectric materials.

References

- (1) Seebeck, T. J., *Royal Academy of Science, Berlin* **1822**, 265.
- (2) Seebeck, T. J., *Annalen der Physik* **1826**, 82 (2), 133-160.
- (3) Fourier J.; Ørsted H., *Ann. Chim. Phys* **1823**, 375–389.
- (4) Peltier, J., *Annales de chimie et de physique* **1834**, 56, 371.
- (5) Wood, C., *Rep. Prog. Phys.* **1988**, 51 (4), 459.
- (6) DiSalvo, F. J., *Science* **1999**, 285 (5428), 703-706.
- (7) Mahan, G. D.; Sofo, J. O., *Proceedings of the National Academy of Sciences* **1996**, 93 (15), 7436-7439.
- (8) Hicks, L. D.; Dresselhaus, M. S., *Physical Review B* **1993**, 47 (24), 16631-16634.
- (9) Dresselhaus, M. S.; Chen, G.; Tang, M. Y.; Yang, R. G.; Lee, H.; Wang, D. Z.; Ren, Z. F.; Fleurial, J.-P.; Gogna, P., *Adv. Mater.* **2007**, 19 (8), 1043-1053.
- (10) Nolas, G. S.; Morelli, D. T.; Tritt, T. M., *Annu. Rev. Mater. Sci.* **1999**, 29 (1), 89-116.
- (11) Beekman, M.; Morelli, D. T.; Nolas, G. S., *Nature Materials* **2015**, 14 (12), 1182-1185.
- (12) Slack, G. A., *CRC Handbook of Thermoelectrics* **1995**, (CRC Press: Boca Raton), Rowe, D. M., Ed.; CRC Press: Boca Raton.
- (13) Hsu, K. F.; Loo, S.; Guo, F.; Chen, W.; Dyck, J. S.; Uher, C.; Hogan, T.; Polychroniadis, E. K.; Kanatzidis, M. G., *Science* **2004**, 303 (5659), 818-821.
- (14) Keppens, V.; Mandrus, D.; Sales, B. C.; Chakoumakos, B. C.; Dai, P.; Coldea, R.; Maple, M. B.; Gajewski, D. A.; Freeman, E. J.; Bennington, S., *Nature* **1998**, 395 (6705), 876-878.
- (15) Vining, C. B., *Nat Mater* **2009**, 8 (2), 83-85.
- (16) Lee, Y., Northwestern University, Dissertation: 2014.

- (17) Hanus, R.; Agne, M. T.; Rettie, A. J. E.; Chen, Z.; Tan, G.; Chung, D. Y.; Kanatzidis, M. G.; Pei, Y.; Voorhees, P. W.; Snyder, G. J., *Adv. Mater.* **2019**, *31* (21), 1900108.
- (18) Toberer, E. S.; Zevalkink, A.; Snyder, G. J., *J. Mater. Chem.* **2011**, *21* (40), 15843-15852.
- (19) Gurunathan, R.; Hanus, R.; Dylla, M.; Katre, A.; Snyder, G. J., *Physical Review Applied* **2020**, *13* (3), 034011.
- (20) Callaway, J.; von Baeyer, H. C., *Physical Review* **1960**, *120* (4), 1149-1154.
- (21) Abeles, B., *Physical Review* **1963**, *131* (5), 1906-1911.
- (22) Klemens, P. G., *Physical Review* **1960**, *119* (2), 507-509.
- (23) Sales, B. C.; Chakoumakos, B. C.; Mandrus, D.; Sharp, J. W., *Journal of Solid State Chemistry France* **1999**, *146*, 528-532.
- (24) Christensen, M.; Abrahamsen, A. B.; Christensen, N. B.; Juranyi, F.; Andersen, N. H.; Lefmann, K.; Andreasson, J.; Bahl, C. R. H.; Iversen, B. B., *Nature Materials* **2008**, *7* (10), 811-815.
- (25) Girard, S. N.; Schmidt-Rohr, K.; Chasapis, T. C.; Hatzikraniotis, E.; Njegic, B.; Levin, E. M.; Rawal, A.; Paraskevopoulos, K. M.; Kanatzidis, M. G., *Adv. Funct. Mater.* **2013**, *23* (6), 747-757.
- (26) Girard, S. N.; He, J.; Li, C.; Moses, S.; Wang, G.; Uher, C.; Dravid, V. P.; Kanatzidis, M. G., *Nano Lett.* **2010**, *10* (8), 2825-2831.
- (27) Androulakis, J.; Lin, C.-H.; Kong, H.-J.; Uher, C.; Wu, C.-I.; Hogan, T.; Cook, B. A.; Caillat, T.; Paraskevopoulos, K. M.; Kanatzidis, M. G., *J. Am. Chem. Soc.* **2007**, *129* (31), 9780-9788.
- (28) Kanatzidis, M. G., *Chem. Mater.* **2010**, *22* (3), 648-659.

- (29) Sootsman, J. R.; Chung, D. Y.; Kanatzidis, M. G., *Angew. Chem. Int. Ed.* **2009**, *48* (46), 8616-8639.
- (30) Pei, Y.; Lensch-Falk, J.; Toberer, E. S.; Medlin, D. L.; Snyder, G. J., *Adv. Funct. Mater.* **2011**, *21* (2), 241-249.
- (31) Chen, Z.-G.; Han, G.; Yang, L.; Cheng, L.; Zou, J., *Progress in Natural Science: Materials International* **2012**, *22* (6), 535-549.
- (32) Li, J.-F.; Liu, W.-S.; Zhao, L.-D.; Zhou, M., *NPG Asia Materials* **2010**, *2* (4), 152-158.
- (33) Minnich, A. J.; Dresselhaus, M. S.; Ren, Z. F.; Chen, G., *Energy & Environmental Science* **2009**, *2* (5), 466-479.
- (34) Rowe, D. M.; Shukla, V. S., *J. Appl. Phys.* **1981**, *52* (12), 7421-7426.
- (35) Klemens, P. G., *Int. J. Thermophys.* **1994**, *15* (6), 1345-1351.
- (36) Kim, H.-S.; Kang, S. D.; Tang, Y.; Hanus, R.; Jeffrey Snyder, G., *Materials Horizons* **2016**, *3* (3), 234-240.
- (37) Chen, Z.; Ge, B.; Li, W.; Lin, S.; Shen, J.; Chang, Y.; Hanus, R.; Snyder, G. J.; Pei, Y., *Nature Communications* **2017**, *8*, 13828.
- (38) Biswas, K.; He, J.; Blum, I. D.; Wu, C.-I.; Hogan, T. P.; Seidman, D. N.; Dravid, V. P.; Kanatzidis, M. G., *Nature* **2012**, *489* (7416), 414-418.
- (39) Tan, G.; Hao, S.; Cai, S.; Bailey, T. P.; Luo, Z.; Hadar, I.; Uher, C.; Dravid, V. P.; Wolverton, C.; Kanatzidis, M. G., *J. Am. Chem. Soc.* **2019**.
- (40) Zhao, L. D.; Wu, H. J.; Hao, S. Q.; Wu, C. I.; Zhou, X. Y.; Biswas, K.; He, J. Q.; Hogan, T. P.; Uher, C.; Wolverton, C.; Dravid, V. P.; Kanatzidis, M. G., *Energy & Environmental Science* **2013**, *6* (11), 3346-3355.

- (41) Pei, Y.; Tan, G.; Feng, D.; Zheng, L.; Tan, Q.; Xie, X.; Gong, S.; Chen, Y.; Li, J.-F.; He, J.; Kanatzidis, M. G.; Zhao, L.-D., *Advanced Energy Materials* **2017**, *7* (3), 1601450.
- (42) Zhao, L.-D.; He, J.; Wu, C.-I.; Hogan, T. P.; Zhou, X.; Uher, C.; Dravid, V. P.; Kanatzidis, M. G., *J. Am. Chem. Soc.* **2012**, *134* (18), 7902-7912.
- (43) Cahill, D. G.; Pohl, R. O., *Solid State Commun.* **1989**, *70* (10), 927-930.
- (44) Cahill, D. G.; Watson, S. K.; Pohl, R. O., *Physical Review B* **1992**, *46* (10), 6131-6140.
- (45) Pei, Y.; LaLonde, A. D.; Wang, H.; Snyder, G. J., *Energy & Environmental Science* **2012**, *5* (7), 7963-7969.
- (46) Pei, Y.; Wang, H.; Snyder, G. J., *Adv. Mater.* **2012**, *24* (46), 6125-6135.
- (47) Pei, Y.; Shi, X.; LaLonde, A.; Wang, H.; Chen, L.; Snyder, G. J., *Nature* **2011**, *473* (7345), 66-69.
- (48) Girard, S. N.; He, J.; Zhou, X.; Shoemaker, D.; Jaworski, C. M.; Uher, C.; Dravid, V. P.; Heremans, J. P.; Kanatzidis, M. G., *J. Am. Chem. Soc.* **2011**, *133* (41), 16588-16597.
- (49) Tan, G.; Shi, F.; Hao, S.; Zhao, L.-D.; Chi, H.; Zhang, X.; Uher, C.; Wolverton, C.; Dravid, V. P.; Kanatzidis, M. G., *Nature Communications* **2016**, *7*, 12167.
- (50) Hodges, J. M.; Hao, S.; Grovogui, J. A.; Zhang, X.; Bailey, T. P.; Li, X.; Gan, Z.; Hu, Y.-Y.; Uher, C.; Dravid, V. P.; Wolverton, C.; Kanatzidis, M. G., *J. Am. Chem. Soc.* **2018**.
- (51) Wang, H.; Gibbs, Z. M.; Takagiwa, Y.; Snyder, G. J., *Energy & Environmental Science* **2014**, *7* (2), 804-811.
- (52) Zhao, L.-D.; Tan, G.; Hao, S.; He, J.; Pei, Y.; Chi, H.; Wang, H.; Gong, S.; Xu, H.; Dravid, V. P.; Uher, C.; Snyder, G. J.; Wolverton, C.; Kanatzidis, M. G., *Science* **2016**, *351* (6269), 141-144.

- (53) Wu, D.; Zhao, L.-D.; Hao, S.; Jiang, Q.; Zheng, F.; Doak, J. W.; Wu, H.; Chi, H.; Gelbstein, Y.; Uher, C.; Wolverton, C.; Kanatzidis, M.; He, J., *J. Am. Chem. Soc.* **2014**, *136* (32), 11412-11419.
- (54) Tan, G.; Shi, F.; Hao, S.; Chi, H.; Zhao, L.-D.; Uher, C.; Wolverton, C.; Dravid, V. P.; Kanatzidis, M. G., *J. Am. Chem. Soc.* **2015**, *137* (15), 5100-5112.
- (55) Tang, Y.; Gibbs, Z. M.; Agapito, L. A.; Li, G.; Kim, H.-S.; Nardelli, Marco B.; Curtarolo, S.; Snyder, G. J., *Nature Materials* **2015**, *14* (12), 1223-1228.
- (56) Zhang, J.; Song, L.; Pedersen, S. H.; Yin, H.; Hung, L. T.; Iversen, B. B., *Nature Communications* **2017**, *8*, 13901.
- (57) Tan, G.; Zhao, L.-D.; Kanatzidis, M. G., *Chem. Rev.* **2016**, *116* (19), 12123-12149.
- (58) Mishra, S. K.; Satpathy, S.; Jepsen, O., *J. Phys.: Condens. Matter* **1997**, *9* (2), 461-470.
- (59) Liu, W.; Tan, X.; Yin, K.; Liu, H.; Tang, X.; Shi, J.; Zhang, Q.; Uher, C., *Phys. Rev. Lett.* **2012**, *108* (16), 166601.
- (60) Cutler, M.; Mott, N. F., *Physical Review* **1969**, *181* (3), 1336-1340.
- (61) Hicks, L. D.; Dresselhaus, M. S., *Physical Review B* **1993**, *47* (19), 12727-12731.
- (62) Hicks, L. D.; Harman, T. C.; Sun, X.; Dresselhaus, M. S., *Physical Review B* **1996**, *53* (16), R10493-R10496.
- (63) Dresselhaus, M. S.; Dresselhaus, G.; Sun, X.; Zhang, Z.; Cronin, S. B.; Koga, T., *Physics of the Solid State* **1999**, *41* (5), 679-682.
- (64) Heremans, J. P.; Wiendlocha, B.; Chamoire, A. M., *Energy & Environmental Science* **2012**, *5* (2), 5510-5530.

- (65) Heremans, J. P.; Jovovic, V.; Toberer, E. S.; Saramat, A.; Kurosaki, K.; Charoenphakdee, A.; Yamanaka, S.; Snyder, G. J., *Science* **2008**, *321* (5888), 554-557.
- (66) Jaworski, C. M.; Kulbachinskii, V.; Heremans, J. P., *Physical Review B* **2009**, *80* (23), 233201.
- (67) Poudeu, P. F. P.; D'Angelo, J.; Downey, A. D.; Short, J. L.; Hogan, T. P.; Kanatzidis, M. G., *Angew. Chem. Int. Ed.* **2006**, *45* (23), 3835-3839.
- (68) Kuo, J. J.; Kang, S. D.; Imasato, K.; Tamaki, H.; Ohno, S.; Kanno, T.; Snyder, G. J., *Energy & Environmental Science* **2018**.
- (69) Mao, J.; Shuai, J.; Song, S.; Wu, Y.; Dally, R.; Zhou, J.; Liu, Z.; Sun, J.; Zhang, Q.; dela Cruz, C.; Wilson, S.; Pei, Y.; Singh, D. J.; Chen, G.; Chu, C.-W.; Ren, Z., *Proceedings of the National Academy of Sciences* **2017**, *114* (40), 10548-10553.
- (70) Ortiz, B. R.; Gorai, P.; Krishna, L.; Mow, R.; Lopez, A.; McKinney, R.; Stevanović, V.; Toberer, E. S., *Journal of Materials Chemistry A* **2017**, *5* (8), 4036-4046.
- (71) Qiu, Q.; Liu, Y.; Xia, K.; Fang, T.; Yu, J.; Zhao, X.; Zhu, T., *Advanced Energy Materials* **2019**, *9* (11), 1803447.
- (72) Zevalkink, A.; Zeier, W. G.; Pomrehn, G.; Schechtel, E.; Tremel, W.; Snyder, G. J., *Energy & Environmental Science* **2012**, *5* (10), 9121-9128.
- (73) He, R.; Kraemer, D.; Mao, J.; Zeng, L.; Jie, Q.; Lan, Y.; Li, C.; Shuai, J.; Kim, H. S.; Liu, Y.; Broido, D.; Chu, C.-W.; Chen, G.; Ren, Z., *Proceedings of the National Academy of Sciences* **2016**, *113* (48), 13576-13581.
- (74) Toberer, E. S.; Zevalkink, A.; Crisosto, N.; Snyder, G. J., *Adv. Funct. Mater.* **2010**, *20* (24), 4375-4380.

- (75) Zeier, W. G.; Zevalkink, A.; Schechtel, E.; Tremel, W.; Snyder, G. J., *J. Mater. Chem.* **2012**, 22 (19), 9826-9830.
- (76) de Boor, J.; Dasgupta, T.; Kolb, H.; Compere, C.; Kelm, K.; Mueller, E., *Acta Mater.* **2014**, 77, 68-75.
- (77) Kim, H. S.; Liu, W.; Ren, Z., *Energy & Environmental Science* **2017**, 10 (1), 69-85.
- (78) Mehdizadeh Dehkordi, A.; Zebarjadi, M.; He, J.; Tritt, T. M., *Materials Science and Engineering: R: Reports* **2015**, 97, 1-22.
- (79) Yang, J.; Xi, L.; Qiu, W.; Wu, L.; Shi, X.; Chen, L.; Yang, J.; Zhang, W.; Uher, C.; Singh, D. J., *Npj Computational Materials* **2016**, 2, 15015.
- (80) Zhang, X.; Zhao, L.-D., *Journal of Materiomics* **2015**, 1 (2), 92-105.
- (81) Wu, D.; Zhao, L.-D.; Tong, X.; Li, W.; Wu, L.; Tan, Q.; Pei, Y.; Huang, L.; Li, J.-F.; Zhu, Y.; Kanatzidis, M. G.; He, J., *Energy & Environmental Science* **2015**, 8 (7), 2056-2068.
- (82) Zhao, L.-D.; Lo, S.-H.; Zhang, Y.; Sun, H.; Tan, G.; Uher, C.; Wolverton, C.; Dravid, V. P.; Kanatzidis, M. G., *Nature* **2014**, 508 (7496), 373-377.
- (83) Zhao, L.-D.; Tan, G.; Hao, S.; He, J.; Pei, Y.; Chi, H.; Wang, H.; Gong, S.; Xu, H.; Dravid, V. P.; Uher, C.; Snyder, G. J.; Wolverton, C.; Kanatzidis, M. G., *Science* **2015**.
- (84) Duong, A. T.; Nguyen, V. Q.; Duvjir, G.; Duong, V. T.; Kwon, S.; Song, J. Y.; Lee, J. K.; Lee, J. E.; Park, S.; Min, T.; Lee, J.; Kim, J.; Cho, S., *Nature Communications* **2016**, 7, 13713.
- (85) Zhou, M.; Li, J.-F.; Kita, T., *J. Am. Chem. Soc.* **2008**, 130 (13), 4527-4532.
- (86) Biswas, K.; He, J.; Zhang, Q.; Wang, G.; Uher, C.; Dravid, V. P.; Kanatzidis, M. G., *Nat Chem* **2011**, 3 (2), 160-166.
- (87) He, J.; Kanatzidis, M. G.; Dravid, V. P., *Mater. Today* **2013**, 16 (5), 166-176.

- (88) He, J.; Sootsman, J. R.; Girard, S. N.; Zheng, J.-C.; Wen, J.; Zhu, Y.; Kanatzidis, M. G.; Dravid, V. P., *J. Am. Chem. Soc.* **2010**, *132* (25), 8669-8675.
- (89) Zhao, L.-D.; Dravid, V. P.; Kanatzidis, M. G., *Energy & Environmental Science* **2014**, *7* (1), 251-268.
- (90) Pei, Y.; Wang, H.; Gibbs, Z. M.; LaLonde, A. D.; Snyder, G. J., *NPG Asia Mater* **2012**, *4*, e28.
- (91) Hendricks, T.; Choate, W. T. *Engineering Scoping Study of Thermoelectric Generator Systems for Industrial Waste Heat Recovery*; None; Other: 4528 United States 10.2172/1218711 Other: 4528 EE-LIBRARY English; ; Pacific Northwest National Lab. (PNNL), Richland, WA (United States): 2006; p Medium: ED; Size: 74 p.
- (92) Lee, Y.; Lo, S.-H.; Androulakis, J.; Wu, C.-I.; Zhao, L.-D.; Chung, D.-Y.; Hogan, T. P.; Dravid, V. P.; Kanatzidis, M. G., *J. Am. Chem. Soc.* **2013**, *135* (13), 5152-5160.
- (93) Snyder, G. J.; Toberer, E. S., *Nat Mater* **2008**, *7* (2), 105-114.
- (94) Quarez, E.; Hsu, K.-F.; Pcionek, R.; Frangis, N.; Polychroniadis, E. K.; Kanatzidis, M. G., *J. Am. Chem. Soc.* **2005**, *127* (25), 9177-9190.
- (95) Lioutas, C. B.; Frangis, N.; Todorov, I.; Chung, D. Y.; Kanatzidis, M. G., *Chem. Mater.* **2010**, *22* (19), 5630-5635.
- (96) Hoang, K.; Desai, K.; Mahanti, S. D., *Physical Review B* **2005**, *72* (6), 064102.
- (97) Barabash, S. V.; Ozolins, V.; Wolverton, C., *Phys. Rev. Lett.* **2008**, *101* (15), 155704.
- (98) Perdew, J. P.; Ruzsinszky, A.; Csonka, G. I.; Vydrov, O. A.; Scuseria, G. E.; Constantin, L. A.; Zhou, X.; Burke, K., *Phys. Rev. Lett.* **2008**, *100* (13), 136406.

- (99) Zunger, A.; Wei, S. H.; Ferreira, L. G.; Bernard, J. E., *Phys. Rev. Lett.* **1990**, *65* (3), 353-356.
- (100) Zeier, W. G.; Zevalkink, A.; Gibbs, Z. M.; Hautier, G.; Kanatzidis, M. G.; Snyder, G. J., *Angew. Chem. Int. Ed.* **2016**, *55* (24), 6826-6841.
- (101) Pei, Y.; LaLonde, A. D.; Heinz, N. A.; Shi, X.; Iwanaga, S.; Wang, H.; Chen, L.; Snyder, G. J., *Adv. Mater.* **2011**, *23* (47), 5674-5678.
- (102) Ioffe, A. F., Infosearch: London, 1957.
- (103) Salvador, J. R.; Cho, J. Y.; Ye, Z.; Moczygemba, J. E.; Thompson, A. J.; Sharp, J. W.; Koenig, J. D.; Maloney, R.; Thompson, T.; Sakamoto, J.; Wang, H.; Wereszczak, A. A., *PCCP* **2014**, *16* (24), 12510-12520.
- (104) Xiao, Y.; Yang, J.-y.; Jiang, Q.-h.; Fu, L.-w.; Luo, Y.-b.; Liu, M.; Zhang, D.; Zhang, M.-y.; Li, W.-x.; Peng, J.-y.; Chen, F.-q., *Journal of Materials Chemistry A* **2014**, *2* (47), 20288-20294.
- (105) Borup, K. A.; de Boor, J.; Wang, H.; Drymiotis, F.; Gascoin, F.; Shi, X.; Chen, L.; Fedorov, M. I.; Muller, E.; Iversen, B. B.; Snyder, G. J., *Energy & Environmental Science* **2015**, *8* (2), 423-435.
- (106) Blachnik, R.; Igel, R., *Zeitschrift für Naturforschung B*, 1974; Vol. 29, p 625.
- (107) Pei, Y.-L.; Liu, Y., *J. Alloys Compd.* **2012**, *514*, 40-44.
- (108) She, X.; Su, X.; Du, H.; Liang, T.; Zheng, G.; Yan, Y.; Akram, R.; Uher, C.; Tang, X., *Journal of Materials Chemistry C* **2015**, *3* (46), 12116-12122.
- (109) Johnsen, S.; He, J.; Androulakis, J.; Dravid, V. P.; Todorov, I.; Chung, D. Y.; Kanatzidis, M. G., *J. Am. Chem. Soc.* **2011**, *133* (10), 3460-3470.

- (110) May, A. F.; Toberer, E. S.; Saramat, A.; Snyder, G. J., *Physical Review B* **2009**, *80* (12), 125205.
- (111) Ravich, I. U. I.; Efimova, B. A.; Smirnov, I. A., Plenum Press: New York, 1970; p xv, 377 pages.
- (112) Perdew, J. P.; Burke, K.; Ernzerhof, M., *Phys. Rev. Lett.* **1997**, *78* (7), 1396-1396.
- (113) Kresse, G.; Furthmüller, J., *Physical Review B* **1996**, *54* (16), 11169-11186.
- (114) Champier, D., *Energy Convers. Manage.* **2017**, *140*, 167-181.
- (115) Zhang, Y., *ACS Energy Letters* **2018**, *3* (7), 1523-1524.
- (116) Zhao, L.-D.; Hao, S.; Lo, S.-H.; Wu, C.-I.; Zhou, X.; Lee, Y.; Li, H.; Biswas, K.; Hogan, T. P.; Uher, C.; Wolverton, C.; Dravid, V. P.; Kanatzidis, M. G., *J. Am. Chem. Soc.* **2013**, *135* (19), 7364-7370.
- (117) El-Sharkawy, A. A.; Abou El-Azm, A. M.; Kenawy, M. I.; Hillal, A. S.; Abu-Basha, H. M., *Int. J. Thermophys.* **1983**, *4* (3), 261-269.
- (118) Luo, Z.-Z.; Hao, S.; Zhang, X.; Hua, X.; Cai, S.; Tan, G.; Bailey, T. P.; Ma, R.; Uher, C.; Wolverton, C.; Dravid, V. P.; Yan, Q.; Kanatzidis, M. G., *Energy & Environmental Science* **2018**, *11* (11), 3220-3230.
- (119) Qian, X.; Xiao, Y.; Chang, C.; Zheng, L.; Zhao, L., *Progress in Natural Science: Materials International* **2018**, *28* (3), 275-280.
- (120) Wu, C.-F.; Wei, T.-R.; Sun, F.-H.; Li, J.-F., *Advanced science (Weinheim, Baden-Wurttemberg, Germany)* **2017**, *4* (11), 1700199-1700199.
- (121) Lee, Y.; Lo, S.-H.; Chen, C.; Sun, H.; Chung, D.-Y.; Chasapis, T. C.; Uher, C.; Dravid, V. P.; Kanatzidis, M. G., *Nature Communications* **2014**, *5*, 3640.

- (122) You, L.; Liu, Y.; Li, X.; Nan, P.; Ge, B.; Jiang, Y.; Luo, P.; Pan, S.; Pei, Y.; Zhang, W.; Snyder, G. J.; Yang, J.; Zhang, J.; Luo, J., *Energy & Environmental Science* **2018**, *11* (7), 1848-1858.
- (123) Poudeu, P. F. P.; Guéguen, A.; Wu, C.-I.; Hogan, T.; Kanatzidis, M. G., *Chem. Mater.* **2010**, *22* (3), 1046-1053.
- (124) Slade, T. J.; Grovogui, J. A.; Hao, S.; Bailey, T. P.; Ma, R.; Hua, X.; Guéguen, A.; Uher, C.; Wolverton, C.; Dravid, V. P.; Kanatzidis, M. G., *J. Am. Chem. Soc.* **2018**, *140* (22), 7021-7031.
- (125) He, J.; Zhao, L.-D.; Zheng, J.-C.; Doak, J. W.; Wu, H.; Wang, H.-Q.; Lee, Y.; Wolverton, C.; Kanatzidis, M. G.; Dravid, V. P., *J. Am. Chem. Soc.* **2013**, *135* (12), 4624-4627.
- (126) Hua, X.; Hegde, V.; Wolverton, C., *Chem. Mater.* **2019**, *31* (22), 9445-9452.
- (127) Chen, N.; Gascoin, F.; Snyder, G. J.; Müller, E.; Karpinski, G.; Stiewe, C., *Appl. Phys. Lett.* **2005**, *87* (17), 171903.
- (128) Wang, H.; Pei, Y.; LaLonde, A. D.; Snyder, G. J., *Proceedings of the National Academy of Sciences* **2012**, *109* (25), 9705-9709.
- (129) Chasapis, T. C.; Lee, Y.; Hatzikraniotis, E.; Paraskevopoulos, K. M.; Chi, H.; Uher, C.; Kanatzidis, M. G., *Physical Review B* **2015**, *91* (8), 085207.
- (130) Allgaier, R. S.; Jr., B. B. H., *J. Appl. Phys.* **1966**, *37* (1), 302-309.
- (131) Allgaier, R. S., *J. Appl. Phys.* **1965**, *36* (8), 2429-2434.
- (132) Allgaier, R. S., *J. Appl. Phys.* **1961**, *32* (10), 2185-2189.
- (133) Harwell, J. R.; Baikie, T. K.; Baikie, I. D.; Payne, J. L.; Ni, C.; Irvine, J. T. S.; Turnbull, G. A.; Samuel, I. D. W., *PCCP* **2016**, *18* (29), 19738-19745.

- (134) Spanopoulos, I.; Hadar, I.; Ke, W.; Tu, Q.; Chen, M.; Tsai, H.; He, Y.; Shekhawat, G.; Dravid, V. P.; Wasielewski, M. R.; Mohite, A. D.; Stoumpos, C. C.; Kanatzidis, M. G., *J. Am. Chem. Soc.* **2019**, *141* (13), 5518-5534.
- (135) Baikie, I. D.; Grain, A.; Sutherland, J.; Law, J., *physica status solidi c* **2015**, *12* (3), 259-262.
- (136) Wang, H.; Cao, X.; Takagiwa, Y.; Snyder, G. J., *Materials Horizons* **2015**, *2* (3), 323-329.
- (137) Jood, P.; Ohta, M.; Yamamoto, A.; Kanatzidis, M. G., *Joule* **2018**, *2* (7), 1339-1355.
- (138) Hu, X.; Jood, P.; Ohta, M.; Kunii, M.; Nagase, K.; Nishiate, H.; Kanatzidis, M. G.; Yamamoto, A., *Energy & Environmental Science* **2016**, *9* (2), 517-529.
- (139) Snyder, G. J.; Snyder, A. H., *Energy & Environmental Science* **2017**, *10* (11), 2280-2283.
- (140) Cai, K. F.; He, X. R.; Avdeev, M.; Yu, D. H.; Cui, J. L.; Li, H., *J. Solid State Chem.* **2008**, *181* (6), 1434-1438.
- (141) Pan, L.; Mitra, S.; Zhao, L.-D.; Shen, Y.; Wang, Y.; Felser, C.; Berardan, D., *Adv. Funct. Mater.* **2016**, *26* (28), 5149-5157.
- (142) Wang, S.; Hui, S.; Peng, K.; Bailey, T. P.; Zhou, X.; Tang, X.; Uher, C., *Journal of Materials Chemistry C* **2017**, *5* (39), 10191-10200.
- (143) Seto, J. Y. W., *J. Appl. Phys.* **1975**, *46* (12), 5247-5254.
- (144) Orton, J. W.; Powell, M. J., *Rep. Prog. Phys.* **1980**, *43* (11), 1263-1307.
- (145) Hohenberg, P.; Kohn, W., *Phys. Rev.* **1964**, *136*, B864.
- (146) Kohn, W.; Sham, L. J., *Phys. Rev.* **1965**, *140*, A1133.
- (147) Kresse, G.; Hafner, J., *Physical Review B* **1994**, *49* (20), 14251-14269.
- (148) Kresse, G.; Hafner, J., *Physical Review B* **1993**, *47* (1), 558-561.

- (149) Kresse, G.; Furthmüller, J., *Phys. Rev. B: Condens. Matter Mater. Phys.* **1996**, *54* (16), 11169.
- (150) Blöchl, P. E., *Physical Review B* **1994**, *50* (24), 17953-17979.
- (151) Perdew, J. P.; Burke, K.; Ernzerhof, M., *Phys. Rev. Lett.* **1996**, *77*, 3865.
- (152) Monkhorst, H. J.; Pack, J. D., *Physical Review B* **1976**, *13* (12), 5188-5192.
- (153) Zhang, Q.; Liao, B.; Lan, Y.; Lukas, K.; Liu, W.; Esfarjani, K.; Opeil, C.; Broido, D.; Chen, G.; Ren, Z., *Proceedings of the National Academy of Sciences* **2013**, *110* (33), 13261-13266.
- (154) Fu, L.; Yin, M.; Wu, D.; Li, W.; Feng, D.; Huang, L.; He, J., *Energy & Environmental Science* **2017**, *10* (9), 2030-2040.
- (155) Liu, H.; Shi, X.; Xu, F.; Zhang, L.; Zhang, W.; Chen, L.; Li, Q.; Uher, C.; Day, T.; Snyder, G. J., *Nature Materials* **2012**, *11*, 422.
- (156) Zhao, L. D.; Berardan, D.; Pei, Y. L.; Byl, C.; Pinsard-Gaudart, L.; Dragoë, N., *Appl. Phys. Lett.* **2010**, *97* (9), 092118.
- (157) Kraemer, D.; Sui, J.; McEnaney, K.; Zhao, H.; Jie, Q.; Ren, Z. F.; Chen, G., *Energy & Environmental Science* **2015**, *8* (4), 1299-1308.
- (158) Slade, T. J.; Bailey, T. P.; Grovogui, J. A.; Hua, X.; Zhang, X.; Kuo, J. J.; Hadar, I.; Snyder, G. J.; Wolverton, C.; Dravid, V. P.; Uher, C.; Kanatzidis, M. G., *Advanced Energy Materials* **2019**, *9* (30), 1901377.
- (159) Wei, T.-R.; Tan, G.; Zhang, X.; Wu, C.-F.; Li, J.-F.; Dravid, V. P.; Snyder, G. J.; Kanatzidis, M. G., *J. Am. Chem. Soc.* **2016**, *138* (28), 8875-8882.
- (160) Lipskis, K.; Sakalas, A.; Višćakas, J., *physica status solidi (a)* **1971**, *5* (3), 793-801.
- (161) Orton, J. W., *Thin Solid Films* **1981**, *86* (4), 351-357.

- (162) Grovenor, C. R. M., *Journal of Physics C: Solid State Physics* **1985**, *18* (21), 4079.
- (163) Levinson, J.; Shepherd, F. R.; Scanlon, P. J.; Westwood, W. D.; Este, G.; Rider, M., *J. Appl. Phys.* **1982**, *53* (2), 1193-1202.
- (164) Lee, Y. K.; Luo, Z.; Cho, S. P.; Kanatzidis, M. G.; Chung, I., *Joule* **2019**, *3* (3), 719-731.
- (165) He, J.; Blum, I. D.; Wang, H.-Q.; Girard, S. N.; Doak, J.; Zhao, L.-D.; Zheng, J.-C.; Casillas, G.; Wolverton, C.; Jose-Yacamán, M.; Seidman, D. N.; Kanatzidis, M. G.; Dravid, V. P., *Nano Lett.* **2012**, *12* (11), 5979-5984.
- (166) Blum, I. D.; Isheim, D.; Seidman, D. N.; He, J.; Androulakis, J.; Biswas, K.; Dravid, V. P.; Kanatzidis, M. G., *J. Electron. Mater.* **2012**, *41* (6), 1583-1588.
- (167) Kim, Y.-J.; Zhao, L.-D.; Kanatzidis, M. G.; Seidman, D. N., *ACS Applied Materials & Interfaces* **2017**, *9* (26), 21791-21797.
- (168) Madelung, O.; Rössler, U.; Schulz, M., Eds. Springer Berlin Heidelberg: Berlin, Heidelberg, 1998; pp 1-10.
- (169) Madelung, O.; Rössler, U.; Schulz, M., Eds. Springer Berlin Heidelberg: Berlin, Heidelberg, 1998; pp 1-10.
- (170) Madelung, O.; Rössler, U.; Schulz, M., Eds. Springer Berlin Heidelberg: Berlin, Heidelberg, 1998; pp 1-6.
- (171) Ko, J.; Kim, J.-Y.; Choi, S.-M.; Lim, Y. S.; Seo, W.-S.; Lee, K. H., *Journal of Materials Chemistry A* **2013**, *1* (41), 12791-12796.
- (172) Nielsch, K.; Bachmann, J.; Kimling, J.; Böttner, H., *Advanced Energy Materials* **2011**, *1* (5), 713-731.

- (173) Kanno, T.; Tamaki, H.; Sato, H. K.; Kang, S. D.; Ohno, S.; Imasato, K.; Kuo, J. J.; Snyder, G. J.; Miyazaki, Y., *Appl. Phys. Lett.* **2018**, *112* (3), 033903.
- (174) Wood, M.; Kuo, J. J.; Imasato, K.; Snyder, G. J., *Adv. Mater.* **2019**, *31* (35), 1902337.
- (175) Kohn, W.; Becke, A. D.; Parr, R. G., *The Journal of Physical Chemistry* **1996**, *100* (31), 12974-12980.
- (176) Tan, G.; Hao, S.; Hanus, R. C.; Zhang, X.; Anand, S.; Bailey, T. P.; Rettie, A. J. E.; Su, X.; Uher, C.; Dravid, V. P.; Snyder, G. J.; Wolverton, C.; Kanatzidis, M. G., *ACS Energy Letters* **2018**, *3* (3), 705-712.
- (177) Moshwan, R.; Yang, L.; Zou, J.; Chen, Z.-G., *Adv. Funct. Mater.* **2017**, *27* (43), 1703278.
- (178) Tang, J.; Gao, B.; Lin, S.; Li, J.; Chen, Z.; Xiong, F.; Li, W.; Chen, Y.; Pei, Y., *Adv. Funct. Mater.* **2018**, *28* (34), 1803586.
- (179) Tan, G.; Zhao, L.-D.; Shi, F.; Doak, J. W.; Lo, S.-H.; Sun, H.; Wolverton, C.; Dravid, V. P.; Uher, C.; Kanatzidis, M. G., *J. Am. Chem. Soc.* **2014**, *136* (19), 7006-7017.
- (180) Tan, G.; Shi, F.; Doak, J. W.; Sun, H.; Zhao, L.-D.; Wang, P.; Uher, C.; Wolverton, C.; Dravid, V. P.; Kanatzidis, M. G., *Energy & Environmental Science* **2015**, *8* (1), 267-277.
- (181) Zhang, X.; Wang, D.; Wu, H.; Yin, M.; Pei, Y.; Gong, S.; Huang, L.; Pennycook, S. J.; He, J.; Zhao, L.-D., *Energy & Environmental Science* **2017**, *10* (11), 2420-2431.
- (182) Moshwan, R.; Liu, W.-D.; Shi, X.-L.; Wang, Y.-P.; Zou, J.; Chen, Z.-G., *Nano Energy* **2019**, *65*, 104056.
- (183) Zhou, M.; Gibbs, Z. M.; Wang, H.; Han, Y.; Xin, C.; Li, L.; Snyder, G. J., *PCCP* **2014**, *16* (38), 20741-20748.

- (184) Tan, G.; Shi, F.; Hao, S.; Chi, H.; Bailey, T. P.; Zhao, L.-D.; Uher, C.; Wolverton, C.; Dravid, V. P.; Kanatzidis, M. G., *J. Am. Chem. Soc.* **2015**, *137* (35), 11507-11516.
- (185) Li, W.; Zheng, L.; Ge, B.; Lin, S.; Zhang, X.; Chen, Z.; Chang, Y.; Pei, Y., *Adv. Mater.* **2017**, *29* (17), 1605887.
- (186) Dimmock, J. O.; Melngailis, I.; Strauss, A. J., *Phys. Rev. Lett.* **1966**, *16* (26), 1193-1196.
- (187) Tan, G.; Shi, F.; Sun, H.; Zhao, L.-D.; Uher, C.; Dravid, V. P.; Kanatzidis, M. G., *Journal of Materials Chemistry A* **2014**, *2* (48), 20849-20854.
- (188) Gibbs, Z. M.; LaLonde, A.; Snyder, G. J., *New Journal of Physics* **2013**, *15* (7), 075020.
- (189) Xiao, Y.; Wu, H.; Wang, D.; Niu, C.; Pei, Y.; Zhang, Y.; Spanopoulos, I.; Witting, I. T.; Li, X.; Pennycook, S. J.; Snyder, G. J.; Kanatzidis, M. G.; Zhao, L.-D., *Advanced Energy Materials* **2019**, *9* (17), 1900414.
- (190) Tan, G.; Zeier, W. G.; Shi, F.; Wang, P.; Snyder, G. J.; Dravid, V. P.; Kanatzidis, M. G., *Chem. Mater.* **2015**, *27* (22), 7801-7811.
- (191) Ratsifaritana, C. A.; Klemens, P. G., *Int. J. Thermophys.* **1987**, *8* (6), 737-750.
- (192) Hoffmann, R., VCH Publishers: New York, NY, 1988.
- (193) Gopal, E. S. R., Springer US: Boston, MA, 1966; pp 20-54.
- (194) Tan, G.; Liu, W.; Chi, H.; Su, X.; Wang, S.; Yan, Y.; Tang, X.; Wong-Ng, W.; Uher, C., *Acta Mater.* **2013**, *61* (20), 7693-7704.
- (195) Kresse, G.; Furthmüller, J., *Computational Materials Science* **1996**, *6* (1), 15-50.
- (196) Kresse, G.; Joubert, D., *Physical Review B* **1999**, *59* (3), 1758-1775.
- (197) Okhotnikov, K.; Charpentier, T.; Cadars, S., *Journal of Cheminformatics* **2016**, *8* (1), 17.
- (198) Anderson, O. L., *J. Phys. Chem. Solids* **1963**, *24* (7), 909-917.

- (199) Callaway, J., *Physical Review* **1959**, *113* (4), 1046-1051.
- (200) Holland, M. G., *Physical Review* **1963**, *132* (6), 2461-2471.
- (201) Bardeen, J.; Shockley, W., *Physical Review* **1950**, *80* (1), 72-80.
- (202) Herring, C.; Vogt, E., *Physical Review* **1956**, *101* (3), 944-961.
- (203) Costato, M.; Reggiani, L., *physica status solidi (b)* **1973**, *58* (2), 471-482.
- (204) Schlem, R.; Ghidui, M.; Culver, S. P.; Hansen, A.-L.; Zeier, W. G., *ACS Applied Energy Materials* **2020**, *3* (1), 9-18.
- (205) Muy, S.; Voss, J.; Schlem, R.; Koerver, R.; Sedlmaier, S. J.; Maglia, F.; Lamp, P.; Zeier, W. G.; Shao-Horn, Y., *iScience* **2019**, *16*, 270-282.
- (206) Zeier, W. G.; Zevalkink, A.; Gibbs, Z. M.; Hautier, G.; Kanatzidis, M. G.; Snyder, G. J., *Angew. Chem., Int. Ed.* **2016**, *55*, 6826.
- (207) Zevalkink, A.; Smiadak, D. M.; Blackburn, J. L.; Ferguson, A. J.; Chabynyc, M. L.; Delaire, O.; Wang, J.; Kovnir, K.; Martin, J.; Schelhas, L. T.; Sparks, T. D.; Kang, S. D.; Dylla, M. T.; Snyder, G. J.; Ortiz, B. R.; Toberer, E. S., *Applied Physics Reviews* **2018**, *5* (2), 021303.
- (208) Zeier, W. G.; Anand, S.; Huang, L.; He, R.; Zhang, H.; Ren, Z.; Wolverton, C.; Snyder, G. J., *Chem. Mater.* **2017**, *29* (3), 1210-1217.
- (209) Anand, S.; Xia, K.; I. Hegde, V.; Aydemir, U.; Kocevski, V.; Zhu, T.; Wolverton, C.; Snyder, G. J., *Energy & Environmental Science* **2018**, *11* (6), 1480-1488.
- (210) May, A. F.; Fleurial, J.-P.; Snyder, G. J., *Physical Review B* **2008**, *78* (12), 125205.
- (211) Cheikh, D.; Hogan, B. E.; Vo, T.; Von Allmen, P.; Lee, K.; Smiadak, D. M.; Zevalkink, A.; Dunn, B. S.; Fleurial, J.-P.; Bux, S. K., *Joule* **2018**, *2* (4), 698-709.

- (212) Delaire, O.; May, A. F.; McGuire, M. A.; Porter, W. D.; Lucas, M. S.; Stone, M. B.; Abernathy, D. L.; Ravi, V. A.; Firdosy, S. A.; Snyder, G. J., *Physical Review B* **2009**, *80* (18), 184302.
- (213) Zebarjadi, M.; Esfarjani, K.; Yang, J.; Ren, Z. F.; Chen, G., *Physical Review B* **2010**, *82* (19), 195207.
- (214) Sohler, T.; Ponomarev, E.; Gibertini, M.; Berger, H.; Marzari, N.; Ubrig, N.; Morpurgo, A. F., *Physical Review X* **2019**, *9* (3), 031019.
- (215) Joseph, E.; Amouyal, Y., *J. Appl. Phys.* **2015**, *117* (17), 175102.
- (216) Liao, B.; Qiu, B.; Zhou, J.; Huberman, S.; Esfarjani, K.; Chen, G., *Phys. Rev. Lett.* **2015**, *114* (11), 115901.
- (217) Fang, T.; Xin, J.; Fu, C.; Li, D.; Zhao, X.; Felser, C.; Zhu, T., *Annalen der Physik n/a* (n/a), 1900435.
- (218) Korkosz, R. J.; Chasapis, T. C.; Lo, S.-h.; Doak, J. W.; Kim, Y. J.; Wu, C.-I.; Hatzikraniotis, E.; Hogan, T. P.; Seidman, D. N.; Wolverton, C.; Dravid, V. P.; Kanatzidis, M. G., *J. Am. Chem. Soc.* **2014**, *136* (8), 3225-3237.
- (219) Hua, X.; I. Hegde, V.; Wolverton, C., *Chem. Mater.* **2019**.

Curriculum Vita**Tyler J. Slade**

Department of Chemistry, Northwestern University
715-820-3123, tylerslade2020@u.northwestern.edu

Education

- Ph.D. Materials Chemistry** expected completion–2020
Northwestern University
Advisor: Professor Mercuri G. Kanatzidis
- B.S. Chemistry** 2015
University of Wisconsin–Madison
Advisor: Professor Song Jin

Research Experience

- Northwestern University, Kanatzidis Research Group** 2015–2020
- Synthesis and characterization of the thermoelectric properties of $\text{NaPb}_m\text{SbQ}_{m+2}$ ($Q = \text{S, Se, Te}$), $\text{ASn}_m\text{PnTe}_{m+2}$ ($A = \text{Na, Ag}$; $\text{Pn} = \text{Sb, Bi}$).
 - Determined the impact of grain boundaries on the charge transport properties of lead chalcogenide alloys.
 - Established a relationship between sound velocity and charge carrier concentration in heavily doped semiconductors.
- University of Wisconsin-Madison, Jin Research Group** 2013–2015
- Developed a low temperature synthesis of silicon by electrochemical reduction of silicates in molten salt fluxes.
 - Developed a scalable synthesis for nano metal-silicides by magnesiothermal reduction of SiO_2 and metal-oxide precursors in a molten LiCl/KCl eutectic flux.

Teaching Experience

- Center for the Integration of Research, Teaching, and Learning (CIRTL)**
- Introduction to Evidence-Based Undergraduate STEM Teaching 2019
Understanding and Addressing Bias in STEM Classes 2019
- Teaching Assistant, Northwestern University** 2015–2016
Chemistry 101, 103, 123, 181, 182
Experience teaching recitation and laboratory classes
- Academic Tutor, Center for Educational Opportunity–U.W. Madison** 2012–2014
Tutored students in general chemistry, inorganic chemistry, organic chemistry and calculus
Focused on first-generation and underrepresented students.

Service and Outreach Activities

Journal Reviewer

Reviewed manuscripts for *JACS*, *ACS Nano*, *Acta Crystallographica*, *Materials Today*, *ACS Applied Materials & Interfaces*

Basolo-Ibers-Pearson (BIP) seminar leader **2019–2020**
Organized and lead the department's student-run weekly inorganic chemistry seminars.

Kanatzidis Group safety officer **2019–2020**

Science in the City (SITC) **2017–2019**
Conducted science lessons and demonstrations at Chicago public elementary schools.

Lincolnwood Partnership **2015–2017**
Science outreach for 4th and 5th graders at Lincolnwood Elementary School in Evanston, IL.

Awards and Honors

- | | |
|---|-------------|
| 8) IIN Outstanding Researcher Award | 2019 |
| 7) Northwestern Hierarchical Materials Cluster Program Fellowship | 2016 |
| 6) UW-Madison Sustainability Innovation in Research and Education-Research Experience for Undergraduates (SIRE-REU) Grant | 2014 |
| 5) Wayland Noland Undergraduate Scholarship | 2014 |
| 4) Undergraduate Student Support in Chemistry Scholarship | 2014 |
| 3) Prohaska Family Foundation Scholarship | 2011 |
| 2) Wisconsin State Telecommunications Foundation Scholarship | 2011 |
| 1) Price County UW Madison Alumni Scholarship | 2011 |

Presentations

- 6) **North American Solid State Chemistry Conference (NASSCC)**, Golden, CO, (2019)
“Insight into the high thermoelectric performance and unorthodox charge transport in PbSe-NaSbSe₂ alloys” (Oral presentation)
- 5) **International Conference on Thermoelectrics (ICT)**, Pasadena, CA, (2017)
“Exploration of the NaPb_mSbTe_{m+2} system for thermoelectric applications” (Poster presentation)
- 4) **Electronic Materials Conference**, South Bend, IN (2017)
“Exploration of the NaPb_mSbTe_{m+2} system for thermoelectric applications” (Oral presentation)
- 3) **UW-Madison Department of Chemistry Board of Directors Session**, Madison, WI, (2014)
“Sustainable synthesis of metal silicide nanoparticles by magnesiothermal reduction in eutectic LiCl/KCl” (Poster presentation)
- 2) **UW-Madison Department of Chemistry Undergraduate Poster Session**, Madison, WI, (2014)
“Sustainable synthesis of metal silicide nanoparticles by magnesiothermal reduction in eutectic LiCl/KCl” (Poster presentation)
- 1) **UW-Madison Sustainability Fair**, Madison, WI, (2014)
“Sustainable synthesis of metal silicide nanoparticles by magnesiothermal reduction in eutectic LiCl/KCl” (Oral Presentation)

Publications

- 9) Lin, Y.; Wood, M.; Imasato K.; Kuo J. J.; Lam D.; Mortazavi, N.; **Slade, T. J.**; Xi, K.; Hodge, S. A.; Kanatzidis, M. G.; Clarke, D. R.; Hersam M. C.; G. Snyder, G. J.; Energy Filtering Effect in Mg₃Sb₂ through Grain Boundary Engineering with Graphene. *Submitted*
- 8) Xie, H.; Hao, S.; Bao, J.; **Slade, T. J.**; Snyder, G. J.; Wolverton, C.; Kanatzidis, M. G.; All-inorganic halide perovskites as potential thermoelectric materials: Dynamic cation off-centering induces ultralow thermal conductivity. *J. Am. Chem. Soc.* **2020**.
- 7) **Slade, T. J.**; Grovogui, J. A.; Kuo J. J.; Anand, S.; Bailey, T. P.; Wood, M.; Uher, C.; Snyder, G. J.; Dravid, V. P.; Kanatzidis, M. G. Understanding the thermally activated charge transport in NaPb_mSbQ_{m+2} (Q = S, Se, Te) thermoelectrics: weak dielectric screening leads to grain boundary dominated charge carrier scattering. *Energy & Environmental Science.* **2020**. DOI: 10.1039/d0ee00491j
- 6) Kuo J. J.; Wood M.; **Slade, T. J.**; Kanatzidis, M. G.; Snyder, G. J. Systematic over-estimation of lattice thermal conductivity in materials with electrically-resistive grain boundaries. *Energy & Environmental Science.* **2020**. DOI: 10.1039/c9ee03921j
- 5) **Slade, T. J.**; Bailey, T. P.; Grovogui, J. A.; Hua, X.; Zhang, X.; Kuo, J. J.; Hadar, I., Snyder, G. J.; Wolverton, C.; Dravid, V. P., Uher; C., Kanatzidis; M. G.; High Thermoelectric Performance in PbSe–NaSbSe₂ Alloys from Valence Band Convergence and Low Thermal Conductivity. *Adv. Energy Mater.* **2019**, 9, (30), 1901377
- 4) Grovogui, J., **Slade, T.J.**, Pan, Y., Witting, I., Snyder, G., Kanatzidis, M., & Dravid, V. **2018**. Multiscale Microstructural Features in Thermoelectric Materials. *Microscopy and Microanalysis.* 24(S1), 384-385
- 3) **Slade, T. J.**; Grovogui, J. A.; Hao, S.; Bailey, T. P.; Ma, R.; Hua, X.; Guéguen, A.; Uher, C.; Wolverton, C.; Dravid, V. P.; Kanatzidis, M. G., Absence of Nanostructuring in NaPb_mSbTe_{m+2}: Solid Solutions with High Thermoelectric Performance in the Intermediate Temperature Regime. *J. Am. Chem. Soc.* **2018**, 140 (22), 7021-7031.
- 2) Khoury, J. F.; Hao, S.; Stoumpos, C. C.; Yao, Z.; Malliakas, C. D.; Aydemir, U.; **Slade, T. J.**; Snyder, G. J.; Wolverton, C.; Kanatzidis, M. G., Quaternary Pavanites A_{1+x}Sn_{2-x}Bi_{5+x}S₁₀ (A⁺ = Li⁺, Na⁺): Site Occupancy Disorder Defines Electronic Structure. *Inorg. Chem.* **2018**, 57 (4), 2260-2268.
- 1) Yifan, D.; **Slade, T. J.**; J., S. M.; Linsen, L.; Girard. S. N.; Liqiang, M.; Song, J., Low-Temperature Molten-Salt Production of Silicon Nanowires by the Electrochemical Reduction of CaSiO₃. *Angew. Chem. Int. Ed.* **2017**, 56 (46), 14453-14457.

Patents

- 1) Jin, S.; Dong, Y.; **Slade, T.**; “Low Temperature Electrochemical Production of Silicon” US Patent filed on April 11, 2017